REPORT DOCUMENTATION PAGE

Form Approved
OMB NO. 0704-0188

Public Reporting burden for this collection of information is estimated to average 1 hour per response, including the time for reviewing instructions, searching existing data sources, gathering and maintaining the data needed, and completing and reviewing the collection of information. Send comment regarding this burden estimates or any other aspect of this collection of information, including suggestions for reducing this burden, to Washington Headquarters Services, Directorate for information Operations and Reports, 1215 Jefferson Davis Highway, Suite 1204, Arlington, VA 22202-4302, and to the Office of Management and Budget, Paperwork Reduction Project (0704-0188,) Washington, DC 20503.

1. AGENCY USE ONLY (Leave Blank)

2. REPORT DATE

3. REPORT TYPE AND DATES COVERED
FINAL ~~July~~ 1998 to ~~July~~ 2002
01 June 31 May

4. TITLE AND SUBTITLE
Active/Passive Structural Damping Control for Rotorcraft Systems

5. FUNDING NUMBERS
DAAG55-98-1-0339

6. AUTHOR(S)
Norman M. Wereley

7. PERFORMING ORGANIZATION NAME(S) AND ADDRESS(ES)
DEPT. OF AEROSPACE ENGINEERING
UNIVERSITY OF MARYLAND
COLLEGE PARK MD 20742

8. PERFORMING ORGANIZATION REPORT NUMBER N/A

9. SPONSORING / MONITORING AGENCY NAME(S) AND ADDRESS(ES)

U. S. Army Research Office
P.O. Box 12211
Research Triangle Park, NC 27709-2211

10. SPONSORING / MONITORING AGENCY REPORT NUMBER

38856.4-EG-YIP

11. SUPPLEMENTARY NOTES
The views, opinions and/or findings contained in this report are those of the author(s) and should not be construed as an official Department of the Army position, policy or decision, unless so designated by other documentation.

12 a. DISTRIBUTION / AVAILABILITY STATEMENT

Approved for public release; distribution unlimited.

12 b. DISTRIBUTION CODE

13. ABSTRACT (Maximum 200 words)

Our primary objective is to augment the aeromechanical stability of bearingless and articulated rotor systems. We will focus on two damping strategies: (1) dampers based on magnetorheological fluids, (2) Hybrid elastomeric-magnetorheological fluid-based dampers. The flexbeam and torque tube substructure of the model-scale rotor will incorporate adaptive dampers based on MRF technology. Key aspects of the damper design will be undertaken utilizing quasi-steady constitutive models. MR fluids exhibit a reversible change in yield stress as magnetic field is applied. This change in yield stress can be exploited in the design of a damper with an electromagnet. The key performance criterion will be the damping coefficient, or the field dependent damping over the damping in the absence of applied field. The test data will be used to validate analysis, and demonstrate utility of smart active/passive damping control concepts.

14. SUBJECT TERMS

15. NUMBER OF PAGES
71

16. PRICE CODE

17. SECURITY CLASSIFICATION OR REPORT **UNCLASSIFIED**	18. SECURITY CLASSIFICATION ON THIS PAGE **UNCLASSIFIED**	19. SECURITY CLASSIFICATION OF ABSTRACT **UNCLASSIFIED**	20. LIMITATION OF ABSTRACT **UL**

NSN 7540-01-280-5500

Standard Form 298 (Rev.2-89)
Prescribed by ANSI Std. 239-18
298-102

20030310 034

FINAL REPORT

Active/Passive Structural Damping Control for Rotorcraft Systems

Contract Number DAAG55-98-1-0339

Norman M. Wereley
Associate Professor
Smart Structures Laboratory
Alfred Gessow Rotorcraft Center
Dept. of Aerospace Engineering
University of Maryland
College Park MD 20742 USA
Tele:(301) 405-1927,
Fax:(301) 314-9001,
E-mail: wereley@eng.umd.edu

Submitted to:
Dr. Gary Anderson
U.S. Army Research Office

Active/Passive Structural Damping Control for Rotorcraft Systems

INTRODUCTION

Based on the DoD Rotary Wing Technology Development Approach (RVW-TDA), the objective of this task is to augment inherent lag mode damping by at least 50% by the year 2000 and to strive for an ultimate increase in lag mode damping of 100% by 2005. Aeromechanical stability of helicopters is a nonlinear phenomenon involving complex interactions of aerodynamic, inertial and elastic forces. Current advanced rotor designs tend towards hingeless and bearingless rotors due to reduced life cycle costs (fewer parts), improved hub designs, and superior handling qualities. For example, RAH-66 Comanche helicopter incorporates a bearingless main rotor (BMR). Due to stress and weight considerations, advanced rotors are soft-inplane, and are susceptible to aeromechanical instabilities. Classical ground resonance, caused by the coupling of blade lag motion and landing gear modes, is mitigated in conventional articulated rotors using mechanical lag dampers. However, lag damper effectiveness is reduced for advanced rotors due to small displacements near blade roots. This reduced effectiveness, coupled with high maintenance cost, and weight/drag of mechanical dampers, and high cost of elastomeric dampers, make alternative rotor stability augmentation schemes attractive. High pay-off may result from application of magnetorheological damper technology to the bearingless main rotor.

RESEARCH OBJECTIVES

Our primary objective is to augment the aeromechanical stability of bearingless and articulated rotor systems. We will focus on two damping strategies: (1) dampers based on magnetorheological fluids, (2) Hybrid elastomeric-magnetorheological fluid-based dampers. The flexbeam and torque tube substructure of the model-scale rotor will incorporate adaptive dampers based on MRF technology. Key aspects of the damper design will be undertaken utilizing quasi-steady constitutive models. MR fluids exhibit a reversible change in yield stress as magnetic field is applied. This change in yield stress can be exploited in the design of a damper with an electromagnet. The key performance criterion will be the damping coefficient, or the field dependent damping over the damping in the absence of applied field. The test data will be used to validate analysis, and demonstrate utility of smart active/passive damping control concepts.

APPROACH

This research involves analytical and experimental studies of lag mode damping augmentation strategies using smart materials and structures technology.

An electro-rheological fluid (ERF) undergoes dramatic reversible changes in dynamic yield stress when electric field is applied. ERF behavior is similar to elastomeric materials whose damping varies nonlinearly as a function of frequency and amplitude. ERFs have a disadvantage in that high electric field strengths (≈ 3 kV/mm) are required to fully activate ER effects. New revolutionary magneto-rheological fluids (MRFs) developed can be activated using low voltages (e.g. 28V) with order of magnitude higher dynamic yield stress. We are developing dampers that can adapt to changing flight condition in place of passive mechanical lag dampers for articulated rotors and passive elastomeric snubber dampers used in bearingless rotors. Augmentation of passive damping with an elastomeric damping components. MRF-based adaptive dampers will be developed and implemented. The performance, analysis, and dynamic behavior of this class of dampers will be characterized.

KEY ACCOMPLISHMENTS

The accomplishments of this project are presented as a collection of journal publications in the appendices. Theses are also available for many of these projects as pdf files. The manuscripts are listed below:

N.M. Wereley, Li Pang, and G.M. Kamath (1998). "Idealized hysteresis modeling of electrorheological and magnetorheological dampers." *Journal of Intelligent Material Systems and Structures*. Vol. 9, No. 8, August, pp. 642–649.

G.M. Kamath, N.M. Wereley, and M.R. Jolly (1999). "Characterization of magnetorheological helicopter lag dampers." *Journal of the American Helicopter Society*. Vol. 44, Number 3, July, pp. 234–248.

J. Lindler and N.M. Wereley (1999). "Analysis and Testing of Electrorheological Bypass Dampers." *Journal of Intelligent Material Systems and Structures*. Vol. 10, No. 5, May, pp. 363-376.

J. Lindler and N.M. Wereley (1999). "Double Adjustable Shock Absorbers Using Electrorheological Fluids." *Journal of Intelligent Material Systems and Structures*. Vol. 10, No. 8, August, pp. 652–657.

N.M. Wereley, G.M. Kamath, V. Madhavan (1999). "Hysteresis Modeling of Semi-active Magnetorheological Helicopter Lag Dampers." *Journal of Intelligent Material Systems and Structures*. Vol. 10, No. 8, August, pp. 624–633.

R. Snyder, G.M. Kamath, and N.M. Wereley (2001). "Characterization and Analysis of Magnetorheological Damper Behavior Under Sinusoidal Loading," *AIAA Journal*, Vol. 39, No. 7, July 2001, pp. 1240-1253.

N.M. Wereley, R. Snyder, R. Krishnan, and T. Sieg (2001). "Helicopter Damping." Encyclopedia of Vibration. Editors: S.G. Braun, D.J. Ewins and S.S. Rao, Academic Press, London, UK, Volume 2, pp. 629-642.

G. Dimock, J.-H. Yoo, and N.M. Wereley (2002). "Bingham Biplastic Analysis of ER and MR Dampers." *Journal of Intelligent Material Systems and Structures*. In Press.

TECHNOLOGY TRANSFER

1. Provided quasi-steady design tool to General Dynamics for use in air bag combustion gas flow control.
2. Developed design tools for damper design and tested a preliminary design under Army-Aberdeen SBIR project (Dr. Csaba Zoltani as technical monitor).
3. Met with Mr. Eric Kathe at Benet Laboratories to discuss recoil systems using MR dampers (August 2000).
4. Met with Dr. Frank Hoogterp of Army TACOM (Warren, Michigan) to discuss automotive shock absorber applications.

STAFFING

During this reporting period, Drs. Young-Tai Choi, Dr. J.-S. Jeon, and Prof. N.M. Wereley contributed to the progress in this report. Also, numerous students contributed to the progress in this effort as listed below.

1. Gopal M. Kamath completed his Ph.D.
2. Li Pang completed her M.S.
3. Vijay Madhavan completed his M.S.
4. Rebecca Snyder (partially supported) completed her M.S.
5. Jason Lindler completed his M.S.
6. Radhakumar Radhakrishnan completed his M.S.
7. Glen Dimock completed his B.S.

SUMMARY

If the reader of this report has any questions, please contact the author via email: Wereley@eng.umd.edu.

Idealized Hysteresis Modeling of Electrorheological and Magnetorheological Dampers

NORMAN M. WERELEY,* LI PANG AND GOPALAKRISHNA M. KAMATH
Smart Structures Laboratory, Alfred Gessow Rotorcraft Center,
Department of Aerospace Engineering, University of Maryland, College Park, MD 20742

ABSTRACT: The hysteresis behavior of a linear stroke magnetorheological damper is characterized for sinusoidal displacement excitation at 2.0 Hz (nominal). Four different modeling perspectives are discussed for purposes of system identification procedures, including: (1) equivalent viscous damping, (2) nonlinear Bingham plastic model, (3) nonlinear biviscous model, and (4) nonlinear hysteretic biviscous model. By progressively adding model parameters with which to better represent pre-yield damper behavior, the force vs. velocity hysteresis model is substantially improved. The three nonlinear models represent the force vs. displacement hysteresis behavior nearly equally well. Thus, any of the three nonlinear damper models could be used equally successfully if only a prediction of energy dissipation or damping were of interest. The nonlinear hysteretic biviscous model provides the best representation of force vs. velocity hysteresis of the four models examined here.

1. INTRODUCTION

ELECTRORHEOLOGICAL (ER) and magnetorheological (MR) fluids belong to the class of smart materials that have the unique ability to change properties when electric or magnetic field is applied. When field is applied to an ER or MR fluid, this change is primarily manifested as a substantial increase in the dynamic yield stress of the fluid, while the viscosity remains relatively constant (Carlson et al., 1996). When compared to ER fluids, MR fluids have superior properties, including an order of magnitude higher yield stress, typically 50–100 kPa, and a much wider operational temperature range, typically –40 to 150°C. Because the rheological behavior of ER fluids is qualitatively similar to that of MR fluids, these results can also be extended to ER dampers.

First, we present the hysteresis behavior of a linear stroke magnetorheological damper for sinusoidal displacement excitation at 2.0 Hz (nominal). The sinusoidal steady state behavior is of interest primarily because of the benefits of damping in reducing the detrimental effects of resonance conditions in a structure. We discuss four perspectives with which to describe the behavior of MR dampers subjected to oscillatory sinusoidal shaft motion: (1) linear or equivalent viscous damping model, (2) nonlinear Bingham plastic model (Prager, 1961; Phillips, 1969), (3) nonlinear biviscous model (Stanway et al., 1996), and (4) nonlinear hysteretic biviscous model. These models describe MR damper hysteresis behavior using piecewise continuous functions of velocity, and increase in complexity by adding progressively more parameters. It should be noted that other generalized hysteresis models have been proposed for MR dampers of this type, such as Bouc-Wen hysteresis models (Dyke et al., 1996) or the viscoelastic-plastic model (Kamath and Wereley, 1997a–c). The piecewise continuous nonlinear hysteretic biviscous model can be used to motivate our nonlinear piecewise smooth viscoelastic-plastic model (Kamath and Wereley, 1997a–c), and to improve the parameter optimization procedures used to identify its parameters.

The proposed class of piecewise continuous models is intended to improve understanding of steady state force vs. displacement and force vs. velocity damper behavior due to a sinusoidal velocity input by developing a mechanisms-based modeling perspective. Each of the mechanisms used is linear and piecewise continuous. The appropriateness of the models is examined in two ways. First, we examine the accuracy of damping prediction, or its corollary, accuracy of each model when reconstructing the force versus displacement hysteresis cycle, which is related to the energy dissipation per cycle. Second, we examine the accuracy in reconstructing the force versus velocity hysteresis cycle, which is related to the rheology of the MR fluid in terms of its shear stress versus shear strain rate behavior.

2. DAMPER TESTING

An experimental prototype of a magnetorheological (MR) linear stroke damper was provided by the Lord Corporation. A cross-sectional schematic of the nominal MR damper is shown in Figure 1. Typical quasi-steady (constant) force vs. velocity behavior is shown in Figure 2. The hydraulic cylinder of the damper is nominally 102 mm (4″) in length and 45 mm (1.75″) in diameter. The hydraulic cylinder houses the damper piston, in which is mounted a magnetic circuit. At the base and inside the hydraulic cylinder is an accumulator that is used to pressurize the approximately 50 ml of MR fluid to

---

Reprinted with permission of IOP Publishing Ltd.

*Author to whom correspondence should be addressed.

1045-389X/98/08 0642-08 $10.00/0

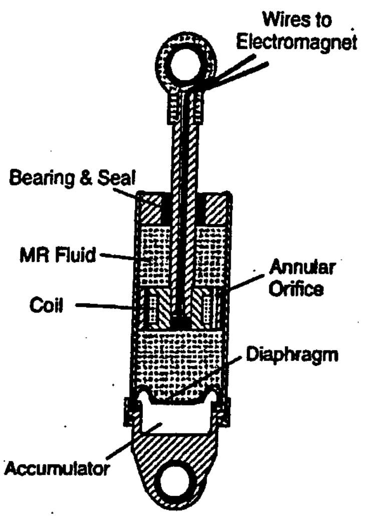

Figure 1. *Cross section of Rheonetics SD-1000-2 MR damper. Damper body is nominally 102 mm long, with a stroke of 60 mm. Courtesy of Lord Corporation.*

above atmospheric pressure. This is a standard technique to prevent cavitation on the low pressure side of the piston while it is in motion. The MR fluid flows through an annular orifice in the piston head, where it can be activated by a current applied to the magnetic circuit.

The MR damper was tested for its steady state dynamic characteristics at different magnetic field strengths (current was applied in the range of 0–0.7 A in increments of 0.1 A) and varying displacement amplitudes of ±1.25 mm, ±2.54 mm, ±5.08 mm, ±7.62 mm (±0.05, ±0.10, ±0.20, and ±0.30 inches) using a sinusoidal displacement input at a frequency of 2.0 Hz (nominal). A Fourier analysis shows the actual frequency of oscillation to be $\Omega = 1.95$ Hz, which will be used in the remainder of paper. The data was then filtered to remove high frequency noise by retaining the first five harmonics of Ω in the reconstructed displacement signals. The force signal, conservatively, was not filtered, because it contained nonlinear information. An Interlaken 100 kN (22 kip) servo-hydraulic testing machine was used to apply the desired damper shaft sinusoidal displacement. The MR damper was mounted in the testing machine using clevises at each damper end designed to prevent relative motion between the clevis pin and damper rod eye using a set screw arrangement. A smooth rod extended from the clevis and was inserted into the hydraulic collet grips of the testing machine. During each test, we measured nominally 20 cycles of force vs. displacement and calculated the force vs. velocity hysteresis cycles for each of these test conditions. Typical hysteresis data, for a nominal displacement amplitude of ±5 mm, is shown in Figure 3.

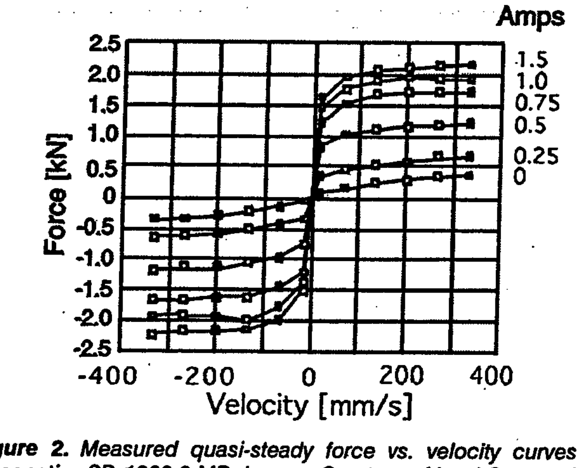

Figure 2. *Measured quasi-steady force vs. velocity curves for Rheonetics SD-1000-2 MR damper. Courtesy of Lord Corporation.*

(a) Force vs. Displacement at 1.95 Hz

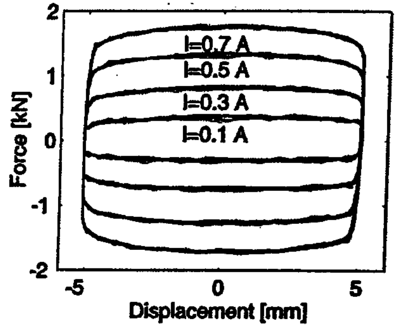

(b) Force vs. Velocity at 1.95 Hz

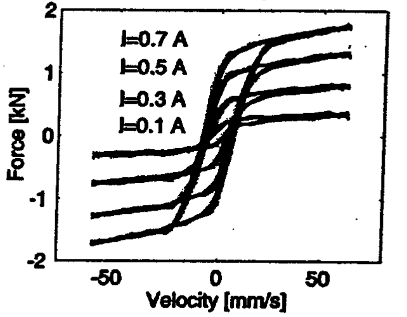

Figure 3. *Hysteresis cycles for MR damper under 2.0 Hz sinusoidal displacement excitation. Data was taken at current levels of 0 to 0.7 A in 0.1 A increments, but is shown only for I = 0.1, 0.3, 0.5 and 0.7 A.*

3. EQUIVALENT VISCOUS DAMPING

Equivalent viscous damping is a standard linearization technique that could be applied to a nonlinear damper such as the MR damper. This approach is useful when comparing the nonlinear MR damper to a linear viscous device. The equivalent viscous damping is computed by equating the energy dissipated, E, over a cycle of frequency, Ω,

$$E = \oint F(t)dx = \int_0^{2\pi/\Omega} F(t)v(t)dt \qquad (1)$$

where $F(t)$ is the measured force, $x(t)$ is the measured shaft displacement, and $v(t)$ is the measured shaft velocity of the damper. Equating the dissipated energy of the nonlinear device to that of an equivalent viscous damper leads to an expression for the equivalent viscous damping, C_{eq},

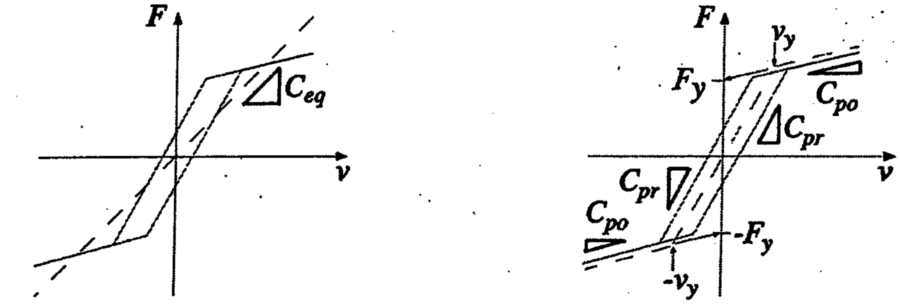

(a) Equivalent Viscous Damping (c) Nonlinear Biviscous

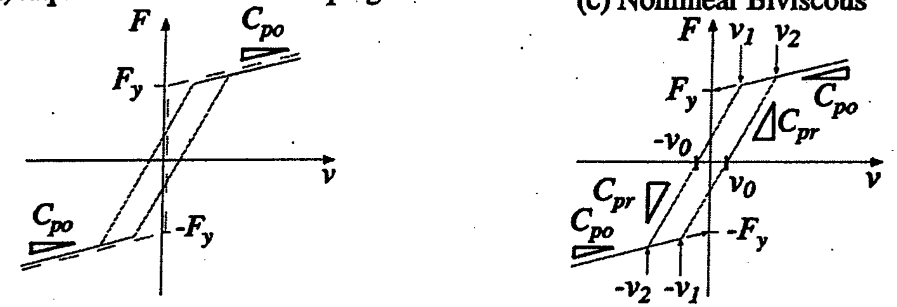

(b) Nonlinear Bingham-plastic (d) Nonlinear Hysteretic Biviscous

Figure 4. Schematics of piecewise continuous damper models used in this study. The idealized model force vs. velocity behavior is represented by a dashed line, while the actual damper behavior is represented by the solid line.

$$C_{eq} = \frac{E}{\pi \Omega X_0^2} \tag{2}$$

where X_0 is the sinusoidal displacement input amplitude. A schematic of this model is shown in Figure 4(a).

4. BINGHAM PLASTIC MODEL

By adding a yield force to a linear damping model, the Bingham plastic model results. This shear flow mechanism has been used to develop predictive models assuming parallel plate geometry (Wereley and Pang, 1998; Makris et al., 1996) or axisymmetric geometry (Kamath, Hurt and Wereley, 1996; Gavin et al., 1996a–b). Yield force, F_y, and post-yielding damping, C_{po}, are included in the model, a schematic of what is shown in Figure 4(b). The equations describing this constitutive model are

$$F(t) = \begin{cases} C_{po}v + F_y & v > 0 \\ -F_y < F < F_y & v = 0 \\ C_{po}v - F_y & v < 0 \end{cases} \tag{3}$$

The Bingham plastic damper model is often expressed as

$$F(t) = F_y \operatorname{sgn}(v(t)) + C_{po}v(t) \tag{4}$$

The model assumes that in the pre-yield condition, the material is rigid and does not flow, hence, when $|F(t)| < F_y$, the shaft velocity, $v = 0$. Once the force applied to the damper exceeds the yield force, then the fluid begins to flow, and the material is essentially a Newtonian fluid with a non-zero yield stress, as shown in Figure 4(b). In this model, the yield force is obtained from the post-yield force vs. velocity asymptote intercept with the force axis, as shown in Figure 4(b).

5. NONLINEAR BIVISCOUS MODEL

Rather than assuming that the material is rigid in the pre-yield condition, the material is assumed to be plastic in both the pre-yield and the post-yield conditions as in Stanway et al. (1996). However, the pre-yield damping, C_{pr}, is assumed to be much greater than the post-yielding damping, C_{po}, or $C_{pr} > C_{po}$, in order to obtain the yield force over a small change in shaft velocity. In this model, the yield force is determined from the post-yield force vs. velocity asymptote intercept with the force axis, as shown in Figure 4(c). This model can be represented by

$$F(t) = \begin{cases} C_{po}v + F_y & v \geq v_y \\ C_{pr}v & -v_y \geq v \leq v_y \\ C_{po}v - F_y & v \leq -v_y \end{cases} \tag{5}$$

where the yield velocity, v_y, is defined as

$$v_y = \frac{F_y}{C_{pr} - C_{po}} \tag{6}$$

This model attempts to model the pre-yield behavior in the force vs. velocity diagram as a highly viscous behavior. Rather than representing a true material property, this pre-yield damping is due to leakage in the damper, which is a Newtonian flow between the piston head and the hydraulic cylinder, designed to smooth the force versus displacement response.

6. NONLINEAR HYSTERETIC BIVISCOUS MODEL

Based on damper behavior observed during testing, the force vs. velocity behavior shows a distinct pre-yield hysteresis loop or bilinear hysteresis. The force versus velocity behavior of the MR damper is reminiscent of the force versus displacement behavior of a bilinear spring (Caughey, 1960). A four parameter nonlinear hysteretic biviscous model, a schematic of which is shown in Figure 4(d), is introduced that has a clear physical motivation. The nonlinear hysteretic biviscous model is an extension of the nonlinear biviscous model (Stanway et al., 1996) with an improved representation of the pre-yield hysteresis. This is accomplished by adding another parameter, that is, the zero force velocity intercept, v_0, to the three prior parameters: the pre-yield viscous damping, C_{pr}, the post-yield viscous damping, C_{po}, and the yield force, F_y. The equations of the piecewise continuous nonlinear hysteretic biviscous model are

$$F = \begin{cases} C_{po}v - F_y & v \le -v_1 & \dot{v} > 0 \\ C_{pr}(v - v_0) & -v_1 \le v \le v_2 & \dot{v} > 0 \\ C_{po}v + F_y & v_2 \le v & \dot{v} > 0 \\ C_{po}v + F_y & v_1 \le v & \dot{v} < 0 \\ C_{pr}(v + v_0) & -v_2 \le v \le v_1 & \dot{v} < 0 \\ C_{po}v - F_y & v \le -v_2 & \dot{v} < 0 \end{cases} \qquad (7)$$

where we have introduced the decelerating yield velocity v_1, and the accelerating yield velocity, v_2, given by

$$v_1 = \frac{F_y - C_{pr}v_0}{C_{pr} - C_{po}} \quad \text{and} \quad v_2 = \frac{F_y + C_{pr}v_0}{C_{pr} - C_{po}} \qquad (8)$$

The hysteresis cycle is separated into two groups of equations. The first group of three equations are for positive acceleration, while the second three are for negative acceleration.

7. PARAMETER OPTIMIZATION

The parameters of the latter three models were identified using a constrained least mean squared error minimization procedure using MATLAB subroutines. A cost function, J, was defined as

$$\min J = \sum_{k=1}^{N} [F(t_k) - \hat{F}(t_k, C_{pr}, C_{po}, F_y, v_0)]^2 \qquad (9)$$

where $\hat{F}(t_k)$ is the force calculated using the equations of the nonlinear hysteretic biviscous model from Equation (7), $F(t_k)$ is the measured force (raw data), and t_k is the time at which the kth sample was taken. The four parameters of C_{pr}, C_{po}, F_y, and v_0, are selected so as to minimize the cost function, J. Only a single optimization procedure is required to identify the parameters of the nonlinear hysteretic biviscous model, the parameters of which are used for all three nonlinear models: Bingham-plastic, biviscous, and hysteretic biviscous. The values of C_{pr}, C_{po}, F_y, and v_0 are all constrained to be greater than zero, and $C_{pr} > C_{po}$. The parameter optimization is performed for each testing condition of applied current and sinusoidal displacement input amplitude.

8. RESULTS

8.1 Linearized Damping

The equivalent viscous damping was calculated using the measured force vs. displacement hysteresis data and Equation (1), and the results are shown in Figure 5. Essentially, the equivalent viscous damping varies as a (third order) polynomial function of current. However, this characterization approach linearizes the damper as an ideal dashpot at every operating condition, so that C_{eq} is a function of both the input current I, and the displacement amplitude, X_0.

8.2 Parameter Identification for Nonlinear Models

In Figure 6, the four parameters of pre-yield damping, C_{pr}, post-yield damping, C_{po}, zero force velocity intercept, v_0, and yield force, F_y, are plotted vs. current for the four 2.0 Hz sinusoidal amplitudes of 1.25 mm, 2.54 mm, 5.08 mm, and 7.62 mm (0.05″, 0.1″, 0.2″, and 0.3″) tested in this study. Although there is a dependence of these parameters on the amplitude, it is interesting to note that the variation of the yield force with amplitude is relatively small. This suggests that yield force as a function of current is strongly related to the yield stress as a function of field. As a function of applied

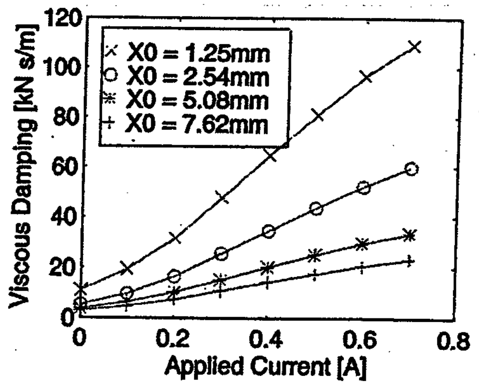

Figure 5. Equivalent viscous damping is plotted vs. applied current for different sinusoidal displacement amplitudes at a test frequency of 2.0 Hz.

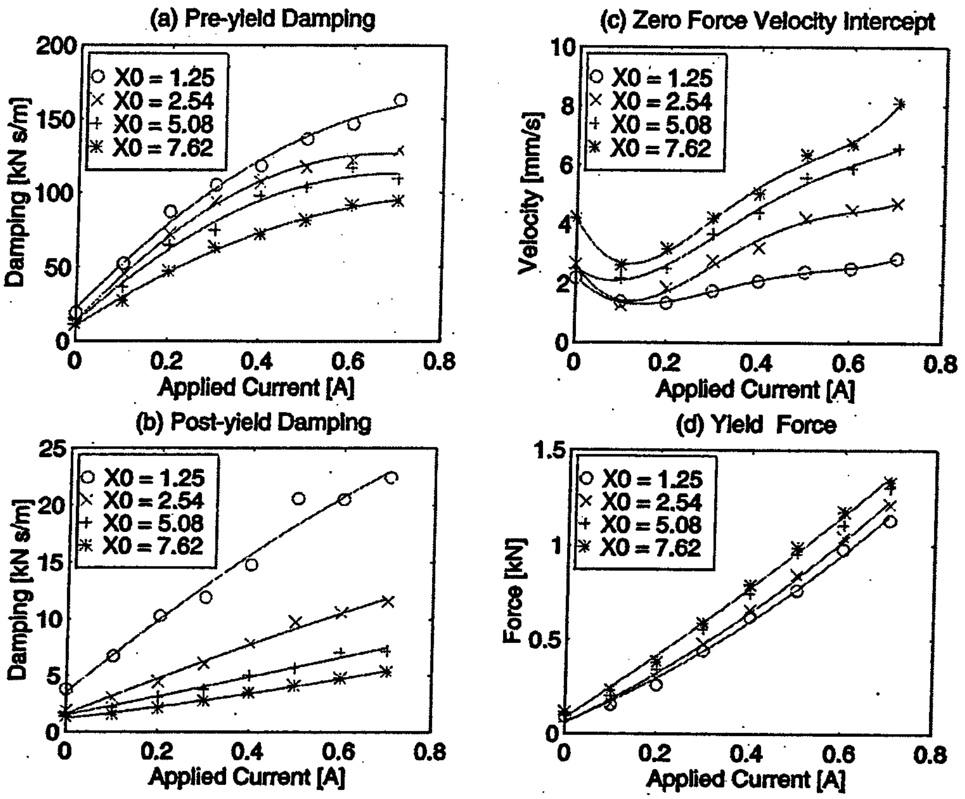

Figure 6. The four parameters of pre-yield damping, C_{pr}, post yield damping, C_{po}, zero force velocity intercept, v_0, and yield force, F_y, are plotted vs. applied current for the linear stroke MR damper. X_0 is in units of [mm].

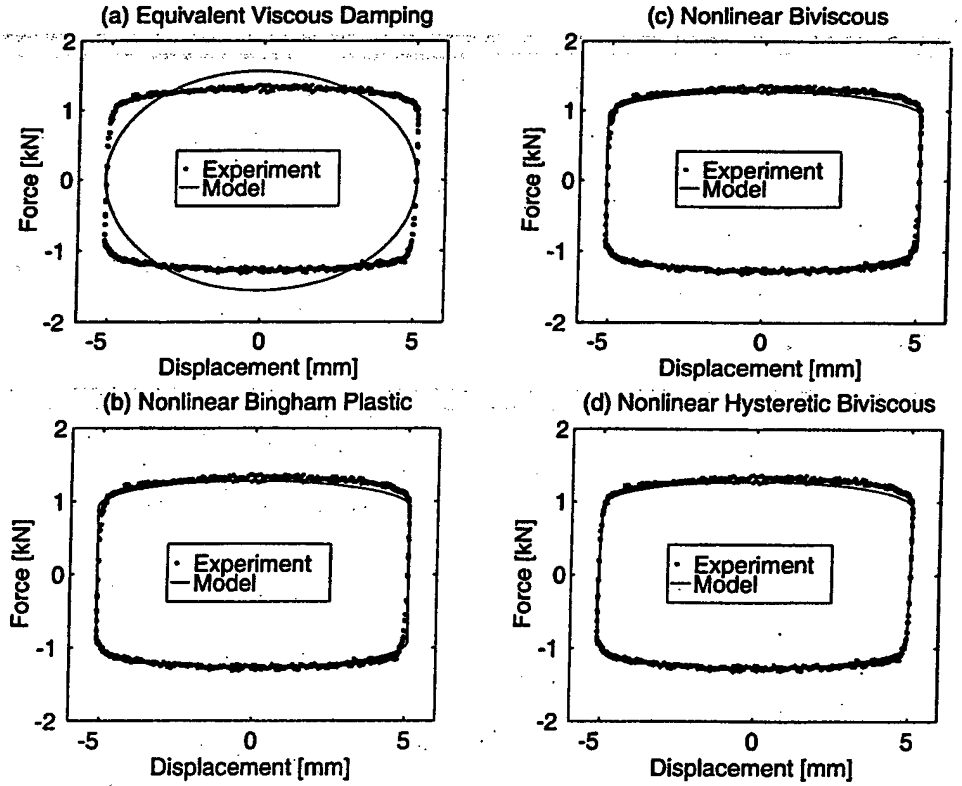

Figure 7. At same conditions of current, I = 0.5 Amps, and displacement, X_0 = 5.08 mm (0.2"), force vs. displacement hysteresis data (dots) are compared with force calculated using identified models (solid line).

current, a simple second-order polynomial accurately fits the parameters of C_{pr}, C_{po}, and F_y, while the velocity intercept, v_0 requires a fourth-order polynomial.

8.3 Energy Diagram

The parameters identified above can be used in the various models to predict the hysteresis cycles of both force vs. displacement and force vs. velocity for the testing conditions of $I = 0.5$ Amps, and $X_0 = 5.08$ mm (0.2″). In Figure 7, typical force vs. displacement hysteresis cycle data are plotted against the predicted hysteresis cycles from the simulation of each model.

The hysteresis cycle predicted by the linearized model, or the equivalent viscous damping model, is shown in Figure 7(a). The linear model is the least accurate in representing the force versus displacement nonlinear hysteresis cycle shape. The linearized model will always predict an ellipsoidal hysteresis cycle shape, so that it cannot capture the Coulomb or friction damper behavior represented the yield force. However, the area inside the linear (ellipsoidal) energy diagram is identical to that inside the nonlinear energy diagram, by definition.

In contrast, the force vs. displacement hysteresis cycle behavior, shown in Figures 7(b)–(d), is more accurately represented by the three nonlinear models. This improvement is achieved because each of the nonlinear models has introduced a friction component or yield force into the model. This allows for the prediction of a more rectangular hysteresis cycle shape reminiscent of Coulomb friction.

In Figure 8, the energy calculated from test data in plotted against the energy calculated using the simulated velocity and force, for all test conditions at $\Omega = 1.95$ Hz. Again, as shown in Figure 8(a), the energy dissipation per cycle predicted by the analysis matches the measured values exactly, by definition. The nonlinear models accurately match the energy dissipation per cycle, even though, as shown in the next section, the force vs. velocity hysteresis behavior varies significantly between the models. Essentially, the post-yield behavior of the damper plays the largest role in describing the energy dissipation, where the velocity magnitude is greatest. All of the pre-yield behavior occurs at relatively lower velocity, making less of an impact on the damping performance.

8.4 Force vs. Velocity Hysteresis Cycles

In Figure 9, typical force vs. velocity hysteresis cycle data are plotted against the predicted hysteresis cycles from the simulation of each model. Figure 9(a) shows the approximate linearized behavior expected of the single parameter linearized equivalent viscous damping model. In Figure 9(b), by adding a yield force to the post-yield viscous damping, the Bingham plastic model accurately represents the post-yield behavior, with a rigid pre-yield characteristic. In the nonlinear biviscous model shown in Figure 9(c), the rigid pre-yield of the Bingham plastic model is replaced by a vis-

(a) Equivalent Viscous Damping

(c) Nonlinear Biviscous

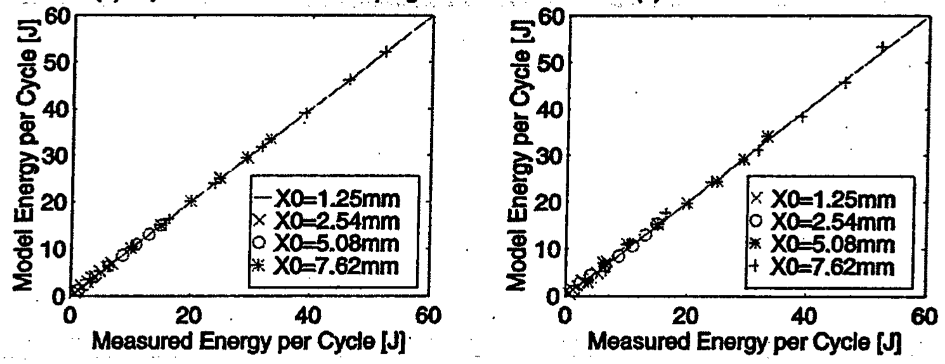

(b) Nonlinear Bingham Plastic

(d) Nonlinear Hysteretic Biviscous

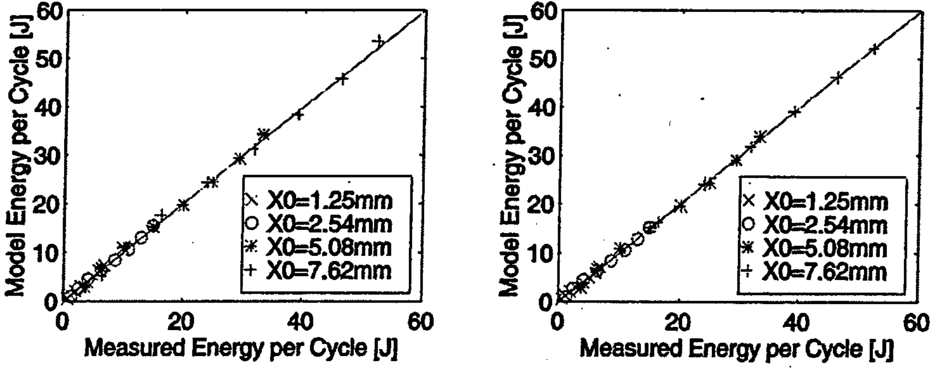

Figure 8. *The energy calculated from test data for all test conditions at 2.0 Hz, is plotted against the energy predicted using a simulation of each model.*

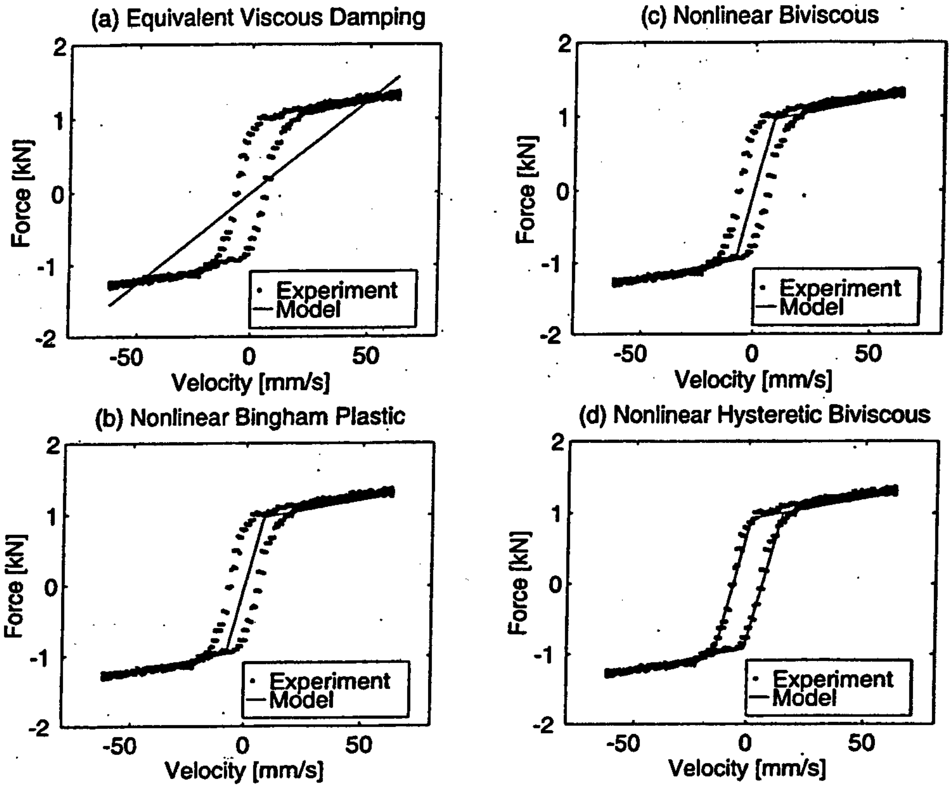

Figure 9. *For testing conditions of current, I = 0.5 Amps, and displacement, X_0 = 5.08 mm (0.2"), force vs. velocity hysteresis data (dots) are compared with force calculated using identified models (solid line).*

cous pre-yield mechanism in order to have a more realistic pre-yield behavior. However, the pre-yield hysteresis is still not captured by the model, only the average slope of the pre-yield hysteresis is represented. The nonlinear hysteretic biviscous models, shown in Figure 9(d), most accurately represents the force vs. velocity behavior, including the pre-yield hysteresis. The force vs. displacement hysteresis cycle behavior, shown in Figure 7, is accurately represented by the three nonlinear models, and the linearized model is the least accurate in representing the hysteresis cycle shape.

9. CONCLUSIONS

Four models were proposed as the underlying model structure of a system identification procedure based on experimental hysteresis cycle data from measured steady state force due to sinusoidal displacement inputs. The four models are piecewise continuous models of force vs. velocity hysteresis cycle behavior.

1. The linearized equivalent viscous damping (EVD) model appropriately accounts for energy dissipated over one oscillation cycle. This model describes the MR damper as an equivalent linear passive hydraulic damper via a single parameter, the equivalent viscous damping, C_{eq}. C_{eq} was shown to be a function of both the applied magnetic field (current) and sinusoidal displacement amplitude. However, the EVD model does not accurately account for either the steady state force vs. displacement or velocity hysteresis cycle behavior. Thus, the strong nonlinear behavior of the MR damper renders the linearized model nearly useless as a simulation model. However, C_{eq} is useful when comparing energy dissipation characteristics of passive hydraulic or elastomeric dampers to MR dampers.
2. The nonlinear Bingham-plastic model uses parameters of yield force, F_y, and post-yield damping, C_{po}. The model accounts for force vs. displacement hysteresis behavior and energy dissipated over each cycle, but does not account for force vs. velocity hysteresis behavior because the pre-yield behavior is assumed to be rigid, and the observed viscoelastic pre-yield damper behavior is neglected.
3. The nonlinear biviscous model uses three parameters: yield force, F_y; pre-yield damping, C_{pr}; post-yield damping, C_{po}. An improved representation of pre-yield viscoelastic behavior is introduced via a pre-yield plastic mechanism. The model accounts for energy dissipated over each cycle, and accounts for force vs. displacement. However, the pre-yield force vs. velocity hysteresis behavior is represented only as a linear damping mechanism.
4. The nonlinear hysteretic biviscous model uses four parameters: yield force, F_y; zero force velocity intercept, v_0; pre-yield damping, C_{pr}; post-yield damping, C_{po}. This model accounts for the force vs. displacement and veloc-

ity hysteresis cycle behavior, as well as the energy dissipation in each cycle. This model would be the most appropriate as a simulation model for steady state oscillations.

5. All of the above nonlinear damper models use the same post-yield viscous damping mechanism. Because the damping predictions depends mostly on this post-yield viscous damping, all of the above nonlinear models perform equally well in damping predictions.
6. The nonlinear hysteretic biviscous (NHBV) model is a piecewise continuous version of our nonlinear viscoelastic-plastic (NVEP) model (Kamath and Wereley, 1997a–c), which differs in that it is piecewise smooth. The parameters of the NHBV model can be estimated graphically from the experimental data, whereas the NVEP model requires an optimization procedured as outlined in Kamath and Wereley (1997c).

ACKNOWLEDGEMENTS

This research was supported primarily by the U.S. Army Research Office (ARO) under the FY96 MURI on Active Control of Rotorcraft Vibration and Acoustics (Dr. Tom Doligalski). ARO provided support to NMW under an FY96 Defense University Research Instrumentation Program grant (Dr. Gary Anderson, technical monitor). ARO provided additional support under an Army Young Investigator Program grant to NMW (Dr. Gary Anderson, technical monitor). The authors thank Dr. Mark Jolly of Lord Corporation (Cary, NC) for providing the prototype MR damper used in this study, and for his technical assistance.

REFERENCES

Carlson, J. D., D. M. Catanzarite and K. A. St. Clair. 1996. "Commercial magnetorheological fluids devices," *Proceedings of the 5th International Conference on Electrorheological Fluids, Magnetorheological Suspensions, and Associated Technology*, World Scientific Publishing Co., River Edge, New Jersey.

Caughey, T. K. 1960. "Sinusoidal excitation of a system with bilinear hysteresis," *ASME Journal of Applied Mechanics*, 27:640–643.

Dyke, S. J., B. F. Spencer Jr., M. K. Sain and J. D. Carlson. 1996. "Modeling and control of magnetorheological dampers for seismic response reduction," *Smart Materials and Structures*, 5(5): 565–575.

Gavin, H. P., R. D. Hanson and F. E. Filisko. 1996. "Electrorheological dampers, part I: analysis and design," *Journal of Applied Mechanics*, 63:669–675.

Gavin, H. P., R. D. Hanson and F. E. Filisko. 1996. "Electrorheological dampers, part II: testing and modeling," *J. Applied Mechanics*, 63:676–682.

Kamath, G. M., M. K. Hurt and N. M. Wereley. 1996. "Analysis and testing of Bingham plastic behavior in semi-active electrorheological fluid dampers," *Smart Materials and Structures*, 5(5): 576–590.

Kamath, G. M. and N. M. Wereley. 1997a. "A nonlinear viscoelastic-plastic model for electrorheological fluids," *Smart Materials and Structures*, 6(3):351–358.

Kamath, G. M. and N. M. Wereley. 1997b. "Modeling the damping mechanism in electrorheological fluid based dampers," *M3DIII: Mechanics and Mechanisms of Material Damping*, ASTM STP 1304, 331–348.

Kamath, G. M. and N. M. Wereley. 1997c. "Nonlinear viscoelastic-plastic mechanisms-based model of an electrorheological damper," *AIAA J. Guidance, Control, and Dynamics*, 20(6):1225–1332.

Markis, N., S. A. Burton, D. Hill and M. Jordan. 1996. "Analysis and design of ER damper for seismic protection of structures," *ASCE J. Engineering Mechanics*, 122:1003–1011.

Phillips, R. W. 1969. *Engineering Applications of Fluids with a Variable Yield Stress*, Ph.D. thesis, Mech. Eng., U. California at Berkeley.

Prager, W. 1961. *Introduction to Mechanics of Continua*. Ginn and Company, New York.

Stanway, R., J. L. Sproston and A. K. El-Wahed. 1996. "Application of electrorheological fluids in vibration control: a survey," *Smart Materials and Structures*, 5(4):464–482.

Wereley, N. M. and Li Pang. 1998. "Nondimensional analysis of semi-active electrorheological and magnetorheological dampers using approximate parallel plate models," *Smart Materials and Structures*, 7(5):732–743.

Characterization of Magnetorheological Helicopter Lag Dampers

Gopalakrishna M. Kamath*
Graduate Research Asst.
Norman M. Wereley
Associate Professor
Alfred Gessow Rotorcraft Center
Department of Aerospace Engineering
University of Maryland
College Park, MD 20742

Mark R. Jolly
Senior Engineering Specialist
Lord Corporation
Thomas Lord Research Center
110 Lord Drive
Cary, NC 27511

Magnetorheological fluid dampers are attractive candidates for augmentation of lag mode damping in helicopter rotors, where additional damping is required to avert instabilities only during specific flight conditions. Magnetorheological (MR) fluids change properties dramatically with application of a magnetic field. This active damping component presents an advantage over passive elastomeric and fluid-elastomeric dampers. An extensive comparative study of fluid-elastomeric and MR dampers is presented. The study was conducted with four (a pair each) 1/6th Froude scale dampers. The MR dampers were tested with the magnetic field turned off (OFF condition) and with the magnetic field turned on (ON condition). The dampers were tested individually and in pairs, under different preloads, and under single and dual frequency excitation conditions. The fluid-elastomeric and MR (OFF) damper behavior was linear, while the MR (ON) behavior was nonlinear with the stiffness and damping varying with the displacement amplitude. Under dual frequency conditions, the MR dampers (ON condition) showed a significant degradation in damping and stiffness as the dual frequency excitation was increased. The MR (OFF) dampers showed no change in properties. The fluid-elastomeric dampers showed a mild degradation in stiffness and damping under dual frequency excitation conditions. The MR (ON) damper hysteresis was modeled using a nonlinear viscoelastic-plastic model. The model captures the nonlinear behavior accurately. Using the single frequency parameters, the dual frequency hysteresis behavior was predicted, and it correlates well with experimental data.

Introduction

Aeromechanical instabilities such as air and ground resonance phenomena are serious concerns in helicopter rotor systems (Ref. 1). In conventional articulated rotors, ground resonance is mitigated using hydraulic and elastomeric dampers. In hingeless and bearingless rotors, which are designed to be soft-inplane rotors due to stress and weight considerations, elastomeric lag dampers are used to mitigate these instabilities. Elastomeric dampers have the advantage of having no moving parts and eliminating the leakage problems that are present in hydraulic dampers. However, elastomeric damper behavior is nonlinear and highly dependent on frequency, temperature and loading conditions such as preload and excitation amplitudes. The lag motion in helicopter rotors occurs at two frequencies: the lead-lag frequency and the 1/rev frequency. Under these conditions, the damping in elastomers has been shown to degrade substantially at low amplitudes, thus causing undesirable limit cycle oscillations (Ref. 2). In order to circumvent the problems associated with the elastomeric dampers, Fluidlastic® dampers have been proposed (Refs. 3-5). Fluidlastic® dampers use elastomers in conjunction with fluids. The fluid adds a viscous component to the energy dissipation mechanism in the dampers. Moreover, the inclusion of the fluid expands the dynamic range of forces generated by the damper (Ref. 3). Panda et al. tested Fluidlastic® lead-lag dampers in a 1/6th Froude-scale rotor model and showed that the limit-cycle instabilities that were observed with elastomeric dampers can be eliminated (Ref. 4). A comparison between elastomeric and Fluidlastic® dampers shows that the former has stiffness and damping properties that are nonlinear functions of the displacement amplitude whereas the latter exhibits relatively constant properties (Ref. 5). The mechanical properties of lag mode dampers can vary as much as 5% from one damper to the next, so that they are carefully matched sets for a given rotor. Matched sets of dampers are used to minimize the impact of varying damper mechanical properties on rotor tracking conditions. Therefore, a damper that could adapt its properties to a fixed mechanical property specification would be of tremendous benefit. Moreover, damping augmentation is required only in flight regimes where there is a potential for instabilities to occur, which highlights the need for damping strategies that can be tailored to the specific flight condition, such as while spooling up the rotor or while the rigid body modes in forward flight coalesce with the lag mode. Thus, controllable fluid dampers are attractive choices for augmenting lag mode damping in helicopter rotor systems.

Controllable fluids such as electrorheological (ER) and magnetorheological (MR) fluids belong to the class of *smart* materials that have the ability to change properties when acted upon by an electric or magnetic field. This change is mainly manifested as a substantial increase in

---

Presented at the SPIE's 5th Annual International Symposium on Smart Structures and Materials, San Diego, CA, 1-5 March, 1998. Manuscript received October 1998; accepted April 1999.

*Currently Asst. Research Scientist.

namic yield stress of the fluid. ER fluid applications have so far outnumbered those of MR fluids primarily due to the wider commercial availability of ER fluids (Refs. 6-8). MR fluids have captured the attention of researchers only recently, on account of their higher dynamic yield stresses (Ref. 9). Moreover, while ER fluids require very high electric field strengths (of the order of 3 kV/mm), MR fluids can be activated using standard circuit board voltages of 28 Volts or less. Despite the superior performance of MR fluids, ER and MR fluids are mechanistically similar such that phenomenological models used to describe ER fluids can be applied to MR fluids (Refs. 10-11). In order to describe ER and MR fluid damper behavior, various models have been proposed (Refs. 11-17). The classical Bingham plastic model describes ER fluid force vs. displacement damper behavior well, from which the damping can be calculated accurately (Refs. 11-13). The force vs. velocity hysteresis characteristics are better modeled using nonlinear functions or hysteretic models (Refs. 11, 14-17). In order to incorporate ER and MR dampers in a system, the hysteresis cycles need to be modeled accurately. Linearized constants such as equivalent damping and complex modulus are not sufficient to uniquely define the hysteresis behavior (Refs. 11, 14, 18-19).

Numerous models have been proposed to describe the behavior of hydraulic and elastomeric lag dampers and their effects on the rotor system dynamics (Refs. 20-22). Gandhi and Chopra proposed a nonlinear elastomeric damper model wherein the damper was represented by a combination of linear and nonlinear springs and dashpots (Ref. 20). The model parameters were estimated based on the experimental values of the components of the complex modulus. Smith et al. proposed a thermomechanical approach based on Anelastic Displacement Fields (ADF) whose mechanical analog is a combination of nonlinear springs and dashpots (Ref. 21). Here, the model coefficients were determined by minimizing the error between model predictions and experimental stress-strain hysteresis cycles. Tarzanin and Panda proposed a nonlinear lead-lag damper model which consisted of nonlinear spring and Coulomb friction elements (Ref. 22). The element coefficients were determined using the current velocity and the corresponding local peak velocity. Kunz showed that linearized complex modulus coefficients do not capture the hysteresis behavior correctly (Ref. 23)

This paper presents a detailed characterization and comparison studies of semi-active MR fluid and passive Fluidlastic® dampers, and presents a model to describe their hysteresis behavior. The objective of this study is to demonstrate the feasibility of semi-active magnetorheological dampers that can maintain constant properties even at low amplitude levels. The results presented here were obtained using a pair each of 1/6th Froude-scale MR fluid and Fluidlastic® dampers. The dampers are similar to those tested by Panda et al. for the Boeing-Sikorsky Comanche helicopter wind tunnel model (Refs. 4-5). Dynamic tests were conducted to characterize individual dampers as well as like pairs of dampers. The dampers were tested individually to measure and compare linearized properties such as equivalent viscous damping and complex modulus for each damper, and ensure that they were similar before testing them in pairs. The damper pairs were tested under zero preload and preloaded conditions. The damper pairs were also tested under single frequency and dual frequency excitation conditions. A nonlinear viscoelastic-plastic model was used to describe the single frequency behavior. This model uniquely describes the force vs. displacement hysteresis cycles, from which the linearized complex modulus components can be calculated. This model was extended to describe the dual frequency behavior and was shown to be fairly accurate.

Damper Characterization

Individual Damper Characterization

A pair each of Fluidlastic® and MR fluid dampers was tested to measure the force vs. displacement hysteresis. The MR fluid dampers could be operated either with the magnetic field turned off or the magnetic field turned on. Thus, there was a pair each of three damper configurations: Fluidlastic,® MR (OFF) and MR (ON). The OFF and ON conditions define the boundaries of the operating envelope of the MR dampers, but it is possible to conceptualize an MR damper design wherein the magnetic field can be varied continuously between the two conditions. The individual damper characterization was done to make sure that the properties of the dampers belonging to each configuration pair were similar. The bench-top experimental setup in Fig. 1 was used to test the individual dampers. The damper to be tested was mounted such that it would be excited in the shear direction. The excitation force was provided by a 4 lbf Ling Dynamic Systems electromagnetic shaker. A Sensotec load cell was placed between the damper clasp and the shaker to measure the force input to the damper. A Lucas Schaevitz non-contacting laser sensor measured displacement. The force and displacement time histories for all the test cases were collected using a Tektronix TDS 420A digital oscilloscope. Each damper was tested for a range of amplitudes at a frequency of 10 Hz, which is the first lead-lag frequency of the 1/6th model-scale rotor. There was no preload on the dampers. The test conditions for the individual damper characterizations are given in Table 1.

Table 1. Test displacements for individual damper characterization. Fluidlastic, MR (OFF), and MR (ON) damper pairs tested with zero preload at 10 Hz frequency.

Amplitudes	
inches	(mm)
0.005	(0.127)
0.0075	(0.190)
0.01	(0.254)
0.015	(0.381)
0.02	(0.508)
0.03	(0.762)
0.04	(1.016)
0.05	(1.270)

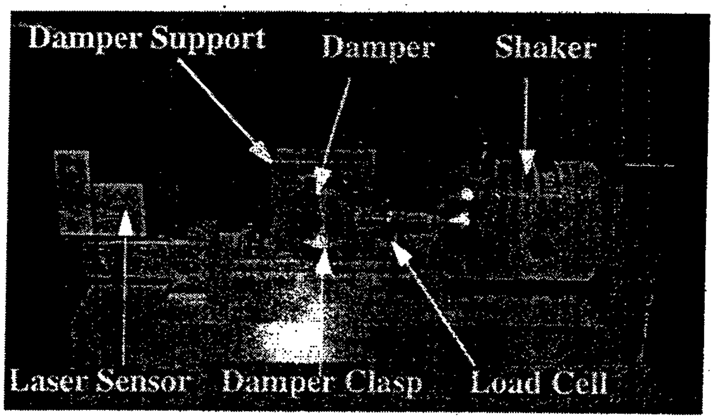

Fig. 1. Experimental setup for individual damper characterization.

Damper Pair Characterization

The lag dampers are usually mounted in pairs onto the rotor system with a compressive preload acting on them (Refs. 4-5). To test the dampers under these conditions and measure the force vs. displacement hysteresis, a setup was designed and built (Fig. 2a). In this setup the dampers were placed face to face with a connecting piece between the faces which was then connected to the shaker. The preload in the dampers was achieved using preload plates that held the two damper support blocks by means of dowel pins at a precise distance, L – ΔL (Fig.2b). A set of preload plates

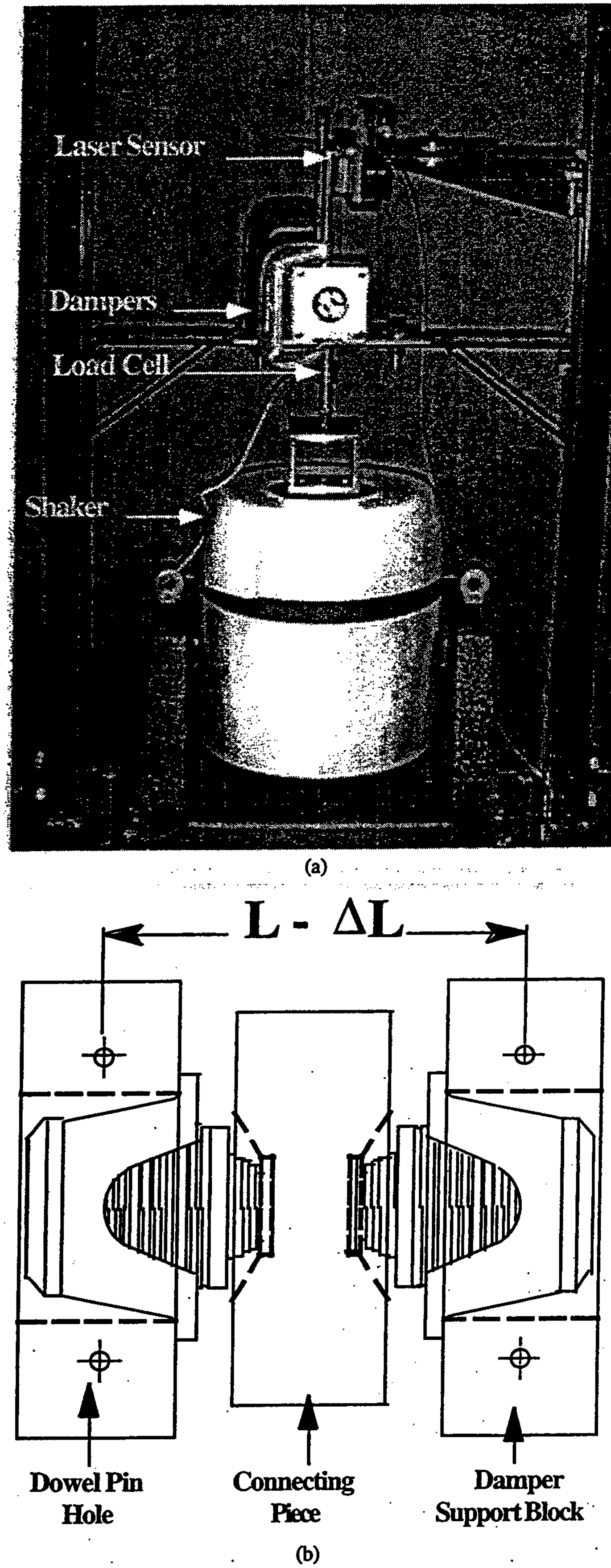

Fig. 2. Experimental setup for damper pair characterization.

were machined for each value of ΔL. A zero value for ΔL implied zero preload and a ΔL value of 0.04 inches (0.02 inches for each damper) was applied for the preloaded condition. A 110 lbf Ling Dynamic Systems shaker was used to excite the dampers, and a load cell mounted between the shaker and the connecting piece measured the force input. The displacements were measured using the non-contacting laser sensor placed above the damper assembly. For each of the preload conditions, the damper pairs were tested for single frequency excitation and dual frequency excitation conditions. The single frequency excitation was at 10 Hz. The dual frequencies were 10 and 15 Hz and for a matrix of amplitudes. The two frequencies correspond to the lag frequency and the 1/rev rotor frequency, respectively, of the model-scale rotor. The complete array of tests for the damper pair characterization is given in Table 2; the symbols x and * represent the single frequency and dual frequency test conditions, respectively.

Table. 2. Matrix of test displacements for damper pair characterization. x and * indicate single frequency and dual frequency excitation conditions, respectively. Fluidlastic, MR (OFF) and MR (ON) damper pairs tested for both zero preload and preload conditions.

		Matrix of Amplitudes							
		10 Hz Amplitudes, inches (mm)							
		0.005 (0.127)	0.0075 (0.190)	0.01 (0.254)	0.015 (0.381)	0.02 (0.508)	0.03 (0.762)	0.04 (1.016)	0.05 (1.270)
15 Hz Amplitudes, inches (mm)	0.0 (0.0)	x	x	x	x	x	x	x	x
	0.005 (0.127)	*	*	*	*	*	*	*	*
	0.01 (0.254)	*	*	*	*	*	*	*	*
	0.02 (0.508)	*	*	*	*	*	*	*	*

Single Frequency Excitation Results

The force vs. displacement hysteresis curves for the damper pairs are shown in Figs. 3, 4 and 5. For brevity, the hysteresis data for the individual dampers is not shown. However, the hysteresis curves for individual dampers of each pair are very similar to those in Figs. 3, 4 and 5 (Ref. 24). Moreover, the linearized constants such as equivalent damping and the complex modulus components associated with a pair of dampers are very close to the sum of the linearized constants associated with the individual dampers (Ref. 24).

The hysteresis curves for the Fluidlastic® dampers are elliptical in shape indicating distinct stiffness and damping components (Fig. 3). Figure 3a shows the hysteresis curves for the zero preload condition, and Fig 3b for the preloaded condition. The inclination of the curves remains constant with amplitude for both cases, which clearly indicates linear behavior. The hysteresis curves for the MR dampers with no applied magnetic field (OFF condition) are shown in Fig. 4. For the zero preload case (Fig. 4a), the hysteresis behavior shows a predominant stiffness component and zero damping. When preloaded, the damping increases as seen by the increase in the area within the hysteresis loops (Fig. 4b). However, the force levels drop with preload indicating a reduction in stiffness. When the magnetic field is applied (ON condition), the MR damper behavior changes drastically, with a distinct nonlinearity (Fig. 5). An apparent increase in stiffness at low amplitudes is seen (Fig. 5a). The shapes of the hysteresis curves remain the same for the preloaded condition although, as in the case of the MR (OFF) damper, an increase in damping and a drop in stiffness is observed (Fig. 5b).

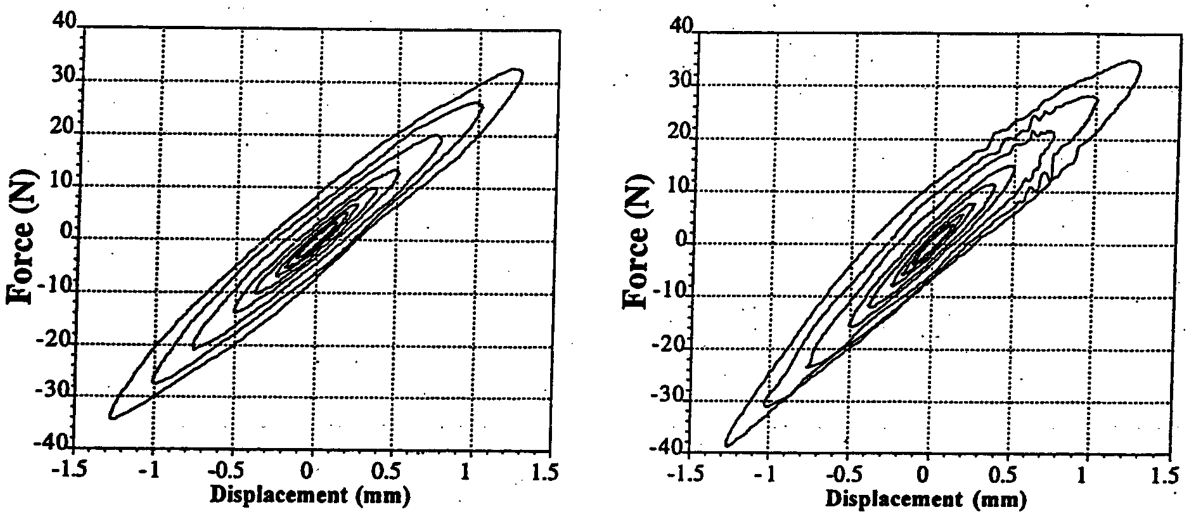

(a) (b)

Fig. 3. Single frequency hysteresis data for Fluidlastic® dampers: (a) with zero preload, and (b) preloaded.

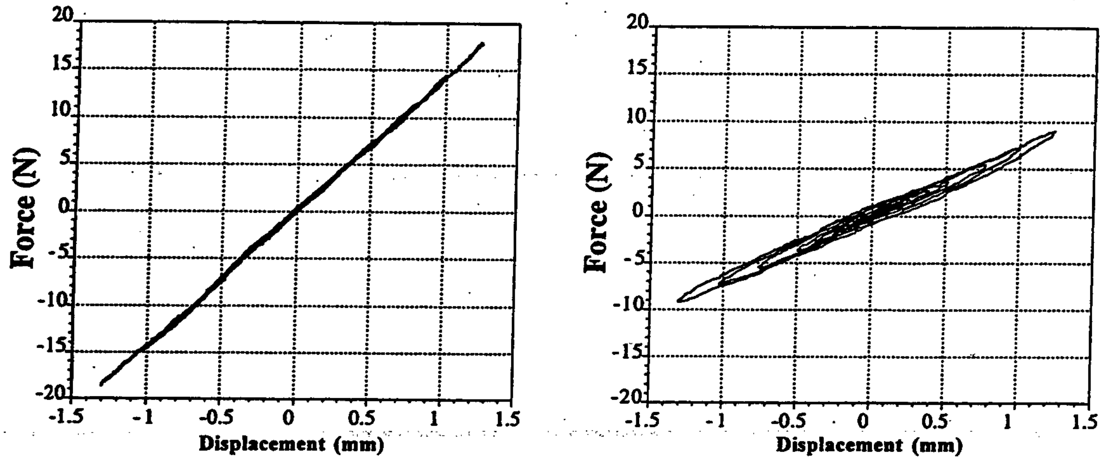

(a) (b)

Fig. 4. Single frequency hysteresis data for MR (OFF) dampers: (a) with zero preload, and (b) preloaded.

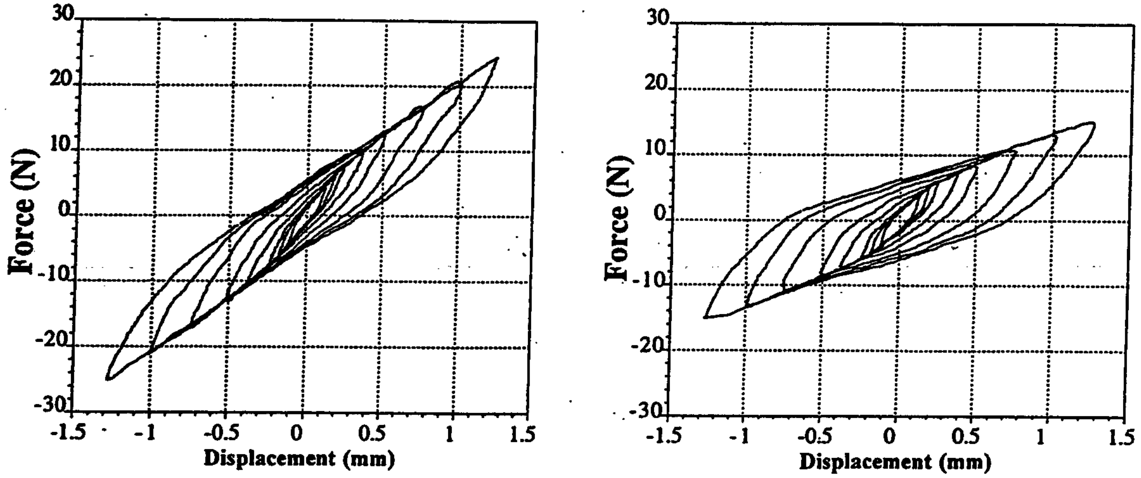

(b)

Fig. 5. Single frequency hysteresis data for MR (ON) dampers: (a) with zero preload, and (b) preloaded.

Linearization of Damper Characteristics

Figures 3 and 4 indicate that the hysteresis behavior is linear in the case of the Fluidlastic® and MR (OFF) dampers. Only the MR (ON) dampers show a nonlinear behavior. In order to compare the three different configurations, a linearization technique is adopted and equivalent linear constants that serve as comparison metrics are calculated. One such linearization constant is the equivalent viscous damping based on the energy dissipated over one cycle. This measure of damping is convenient to compare with conventional hydraulic dampers. Another popular approach is to calculate the complex modulus, which is useful to compare with elastomeric dampers. However, the linearized constants are insufficient to accurately describe the force vs. displacement hysteresis of nonlinear dampers (Ref. 23). Keeping this caveat in mind, the linearization constants are calculated and used to accurately predict the linear hysteresis behavior in the Fluidlastic® and MR (OFF) dampers. However, for the MR (ON) dampers, where the behavior is nonlinear, the linearized constants serve only to compare with the linear dampers and a nonlinear model is used to describe the hysteresis.

Equivalent Viscous Damping

If U is the energy dissipated per cycle, then the equivalent viscous damping coefficient is given by

$$C_{eqv} = \frac{U}{\pi \Omega X_0^2} \tag{1}$$

where Ω is the excitation frequency, X_0 is the displacement amplitude, and U is given by

$$U = \oint F\,dx = \int_0^{\frac{2\pi}{\Omega}} Fv\,dt \tag{2}$$

For the damper pair tests, the C_{eqv} values for the six configurations are plotted in Fig. 6b. The MR (OFF) zero preload case is very close to zero as expected from the hysteresis plots in Fig. 4a. As the damper is preloaded, the C_{eqv} values increase to approximately 10 Ns/m. An increase in damping with the preload is also observed with the Fluidlastic® and MR (ON) dampers. The C_{eqv} values for the Fluidlastic® dampers remain relatively constant at around 100 Ns/m for the zero preload case. This value is close to the sum of the C_{eqv} values for the individual Fluidlastic® dampers. For the MR (ON) dampers, C_{eqv} decreases with the amplitude. The difference between the MR (ON) and MR (OFF) C_{eqv} values shows that the damping in the MR damper can be increased substantially by applying a magnetic field.

The C_{eqv} values for the individual damper tests are not shown here for brevity. The individual dampers of each pair show similar trends in the C_{eqv} values (Ref. 24). The MR (OFF) values were very close to zero since these dampers show a predominant stiffness term. The Fluidlastic® damper values showed that the damping remains close to a constant value of $C_{eqv} = 55$ Ns/m. The equivalent damping for the two MR (ON) dampers exhibited the same decreasing trend with amplitude. However, the quantitative values were slightly different from each other. The C_{eqv} for low amplitudes were close to that of the Fluidlastic® dampers. For amplitudes higher than 0.8 mm, the MR (ON) values dropped below that of the Fluidlastic® dampers.

For completeness, the equivalent spring constant, K_{eqv}, for the damper pair tests are calculated. The equivalent spring constant is defined as the spring constant of a linear spring such that, for a given displacement amplitude, the elastic energy stored in the linear spring is the same as the elastic energy of the damper. In order to determine the equivalent spring constant, the damping component of the force was subtracted from the total force using the damping constant C_{eqv} calculated from Eq. (1). Thus,

$$F_{elastic} = F_{total} - C_{eqv}\dot{X} \tag{3}$$

Using the $F_{elastic}$ versus X data, a curve was fit such that

$$F_{elastic} = K_1 X + K_3 X^3 \tag{4}$$

Thus, from the above definition of the equivalent spring constant, the following relation for K_{eqv} was obtained:

$$K_{eqv} = K_1 + \tfrac{1}{2} K_3 X_0^2 \tag{5}$$

where, X_0 is the displacement amplitude.

In the cases of Fluidlastic® dampers and MR (OFF) dampers, the constant K_3 was zero due to the linear behavior of the two dampers. The constant K_3 was non-zero only for the case of MR (ON) dampers. The K_{eqv} values thus calculated are plotted for the different damper pair configurations in Fig. 6a.

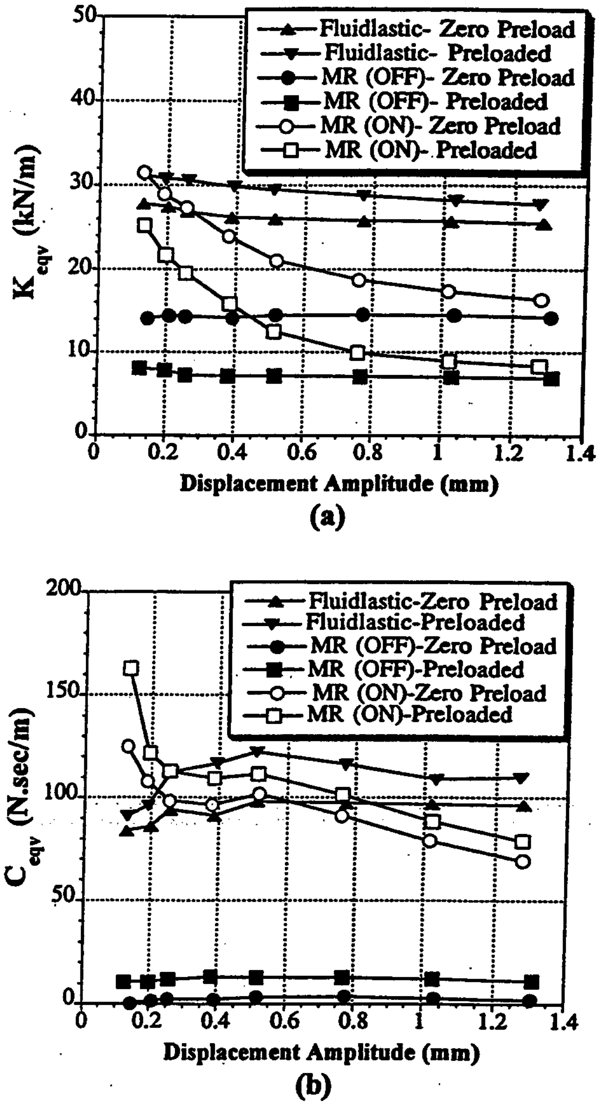

(a)

(b)

Fig. 6. Linearized constants obtained from the damper pair characterization: (a) equivalent spring constant, K_{eqv} (b) equivalent viscous damping constant, C_{eqv}.

Complex Modulus

If the force input to the damper can be expressed as a harmonic function of the first dominant frequency (10 Hz) and if the displacement response is also written as a harmonic function of that frequency, the in-phase components determine the equivalent stiffness (real part of the complex modulus), G', and the quadrature components (90 deg out of phase) determine the damping (imaginary part of the complex modulus), G''.

Thus, the force input is expressed as $F = F_s \sin(\Omega t) + F_c \cos(\Omega t)$, and the displacement response as $X = X_s \sin(\Omega t) + X_c \cos(\Omega t)$. The force-displacement relation is given by

$$F = G'X + \frac{G''}{\Omega}\dot{X} \tag{6}$$

Substituting for F and X in Eq. (6), and equating the coefficients of the sine and cosine terms gives the following expressions for G' and G''.

$$G' = \frac{F_c X_c + F_s X_s}{X_s^2 + X_c^2} \tag{7}$$

$$G'' = \frac{F_c X_s + F_s X_c}{X_s^2 + X_c^2} \tag{8}$$

A Fourier decomposition was done with the force and displacement time histories as obtained from the load cell and laser sensor measurements, respectively, and the coefficients of the dominant frequency (10 Hz) were used to calculate the G' and G'' values.

The G' and the G'' calculations for the individual damper configurations are not shown for brevity. The G' and G'' values for the Fluidlastic® and MR (OFF) dampers remained constant with amplitude, and the values for the individual dampers of a pair matched well with each other (Ref. 24). These G' and G'' values for the Fluidlastic® dampers also compared well with those obtained by Panda, et al. in Ref. 5. For the MR (ON) damper, G' and G'' decrease with amplitude. The values for the individual MR (ON) dampers followed the same trend but are slightly different from each other.

The G' and the G'' values for the damper pairs are shown in Figs. 7a and 7b respectively. For the Fluidlastic® dampers, the stiffness G' and the damping G'' increase when a preload is applied. For the MR dampers (OFF) and (ON), the stiffness decreases, but the damping increases as the dampers are preloaded. As in the case of the individual damper test results, the stiffness and damping remain fairly constant for the MR (OFF) case, and decrease with amplitude for the MR (ON) case.

Thus, the individual dampers of a particular configuration pair show identical qualitative and quantitative trends in properties (Ref. 24). Furthermore, the sum of the linearization constants as obtained for a particular pair from the individual damper tests match well with the constants obtained from the pair under zero preload condition from the damper pair test results. Therefore, the rest of this study will focus only on the damper pair configurations and their characterization.

Single Frequency Hysteresis Modeling

The Fluidlastic® dampers show a linear behavior which can be modeled using a simple Kelvin chain model (a linear spring and a linear dashpot in parallel) (Ref. 25). Similarly, the MR dampers in the OFF condition can be also be modeled using the Kelvin chain. The spring constants and the damping coefficients are obtained by averaging the G' and the G'' values (plotted in Fig. 7) and using the relations $K = G'$ and $C = G''/\Omega$. The correlation obtained using the simple Kelvin element is shown for the Fluidlastic® damper (zero preload) and the MR (OFF) damper (preloaded) in Figs. 8a and 8b, respectively. Good correlation was also obtained for the Fluidlastic® damper (preloaded) and the MR (OFF) damper (zero preload). However, they have not been shown here for brevity.

The MR dampers in the ON condition, in contrast to the Fluidlastic® and MR (OFF) dampers, are very nonlinear with amplitude. It has been shown that the viscoelastic-plastic model is an accurate and physically motivated approach to electrorheological (ER) fluid modeling (Refs. 11, 14, 18-19). Since the phenomenology of MR fluid behavior is similar to that of ER fluid behavior (Ref. 10), the viscoelastic-plastic model is used in this study to describe the MR (ON) damper hysteresis. This model has been used to model both ER (Ref. 14) and MR (Ref. 11) dampers. The linear Kelvin chain model for the Fluidlastic® and MR (OFF) dampers is but a special case of the nonlinear viscoelastic-plastic model.

So, in order to first extract the magnetorheological effect caused by the application of the magnetic field from the experimental built-up damper-force data, the stiffness and damping forces for the MR (OFF) condition were subtracted from the MR (ON) force time histories. Thus,

$$F^{e}_{mr\_effect} = F_{mr\_on} - F_{mr\_off} \tag{9}$$

where,

$$F_{mr\_off} = G'X + \frac{G''}{\omega}\dot{X}$$

and G' and G'' are corresponding zero preload and preloaded MR (OFF) values plotted in Figs. 7a and b.

The resulting force vs. displacement hysteresis corresponding to the extracted magnetorheological effect as obtained from Eq.(9) is shown in Fig. 9. Figures 9a and 9b show the MR effect hysteresis for the zero preload and the preloaded condition, respectively. An interesting result is the qualitative

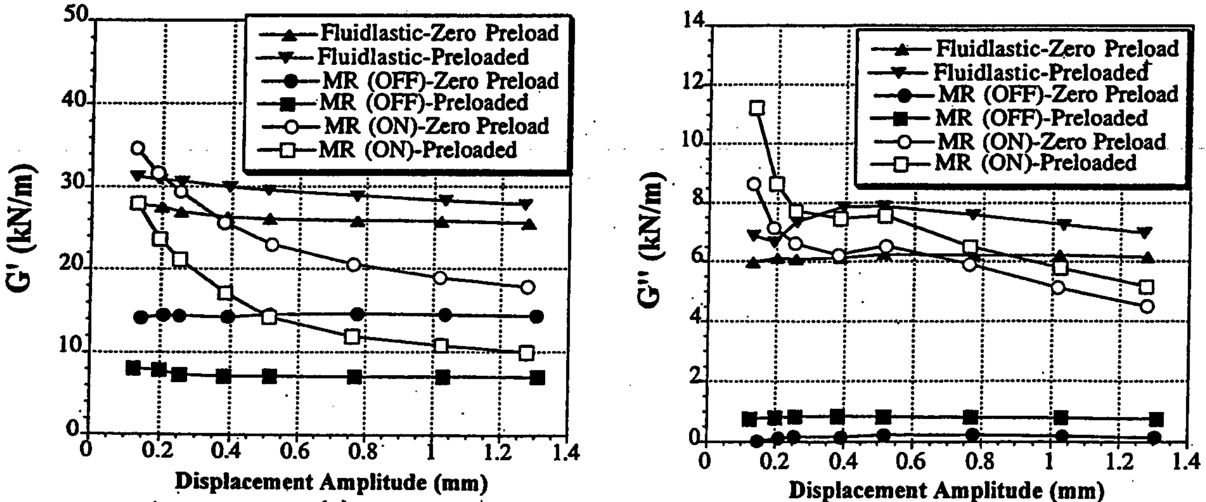

(a) (b)

Fig. 7. Linearized constants obtained from the damper pair characterization: (a) stiffness modulus, G', and (b) damping modulus, G''.

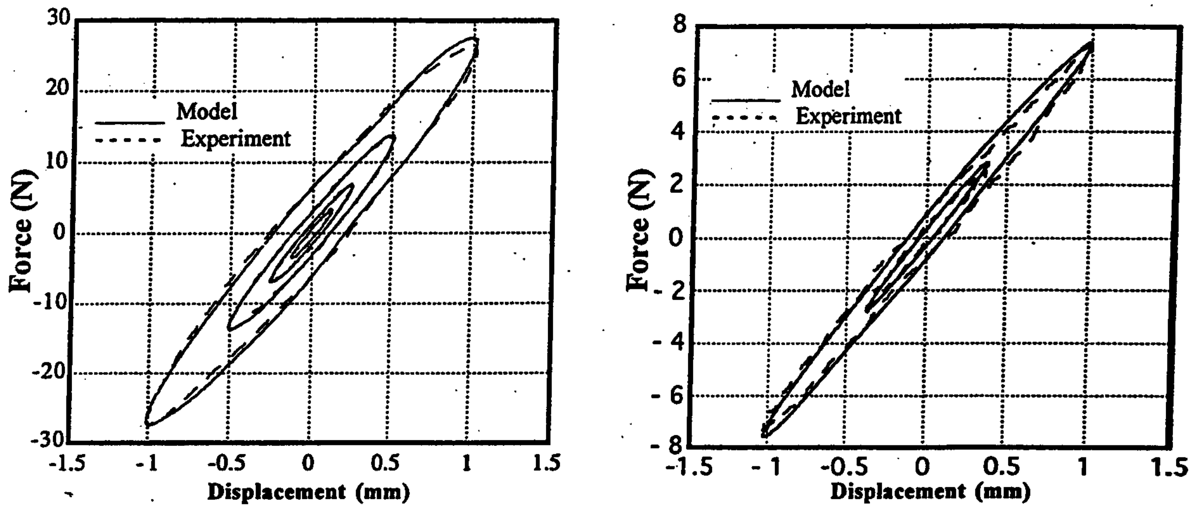

(a) (b)

Fig. 8. Comparison of model hysteresis with single frequency experimental data for a few amplitude cases for (a)Fluidlastic® dampers with zero preload, and (b) MR (OFF) dampers preloaded.

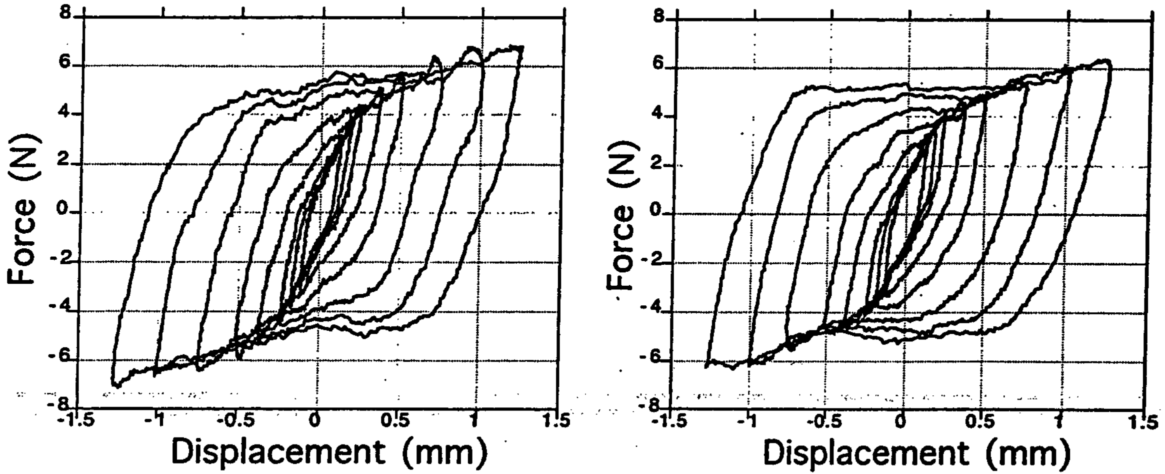

(a) (b)

Fig. 9. Force vs. displacement hysteresis curves for the magnetorheological effect extracted from the MR (ON condition) hysteresis data: (a) zero preload (b) preloaded.

and quantitative similarity between the groups of hysteresis cycles for the zero preload and preloaded cases. This indicates that the preload has a significant effect only on the elastomeric component that dominates MR (OFF) behavior, and has no effect on the internal geometry of the dampers (such as gap sizes and hence the volume of MR fluid that is energized by the magnetic field) which would have caused a change in the MR effect. The corresponding MR effect force vs velocity hysteresis for the two preload conditions are plotted in Figs. 10a and 10b, respectively. The curves show the slow transition from the pre-yield behavior at low amplitudes to the post-yield behavior at high amplitudes. The yield velocity is approximately 50 mm/sec. Dashed lines representing the idealized Bingham plastic damper model are drawn to highlight the onset of yield at high amplitudes. These observations reaffirm the validity of using the viscoelastic-plastic model which incorporates this transition from pre-yield to post-yield behavior.

The schematic of the viscoelastic-plastic model used for this study is shown in Fig. 11. The model is a network that comprises two branches: the pre-yield and the post-yield branches. Each branch consists of a shape function and a linear mechanism. The linear mechanisms model the phenomenology of their respective rheological domains. The pre-yield behavior is modeled using a linear Kelvin chain to represent the viscoelastic stiffness (K_{ve}) and damping (C_{ve}) components. The post-yield behavior is modeled as a viscous dashpot element (C_{vi}). The two shape functions, S_{ve} and S_{vi}, act as switches to turn on and turn off the two mechanisms depending on whether the fluid is in the pre-yield or post-yield region. This transition yield point is located at the yield velocity, V_y. V_y is only a model parameter, and does not physically reflect the velocity at which the fluid yields in the damper. Thus, the MR effect as predicted by the model is given by

$$F^{m}_{mr\_effect} = S_{ve}F_{ve} + S_{vi}F_{vi} \tag{10}$$

where,

$$S_{ve} = \frac{1}{2}\left\{1 - \tanh\left(\frac{|\dot{X}| - V_y}{4\varepsilon}\right)\right\} \tag{11}$$

$$F_{ve} = K_{ve}X + C_{ve}\dot{X} \tag{12}$$

$$S_{vi} = \frac{1}{2}\left\{1 + \tanh\left(\frac{|\dot{X}| - V_y}{4\varepsilon}\right)\right\} \tag{13}$$

$$F_{vi} = C_{vi}\dot{X} \tag{14}$$

The parameter ε determines the rate at which the transition through yield occurs. For example, $\varepsilon = 0$ would result in a step jump at V_y, and as it is

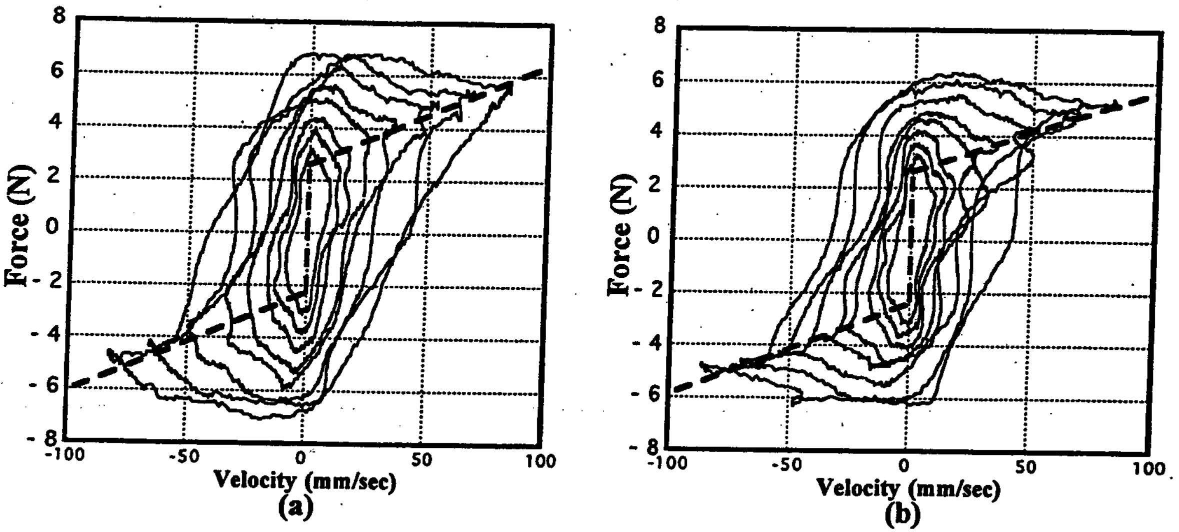

Fig. 10. Force vs. velocity hysteresis curves for magnetorheological effect extracted from the MR (ON condition) hysteresis data: (a) zero preload (b) preloaded. The dashed line represents an idealized Bingham plastic behavior.

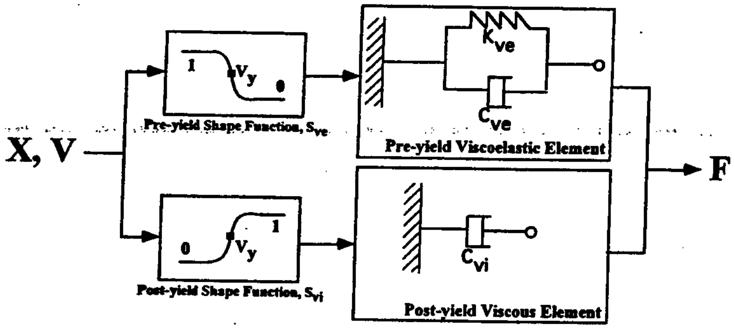
X, V
1
V_y
0
Pre-yield Shape Function, S_{ve}
K_{ve}
C_{ve}
Pre-yield Viscoelastic Element
F
0
V_y
1
Post-yield Shape Function, S_{vi}
C_{vi}
Post-yield Viscous Element

Fig. 11. Schematic of the nonlinear viscoelastic-plastic model.

increased, the transition occurs in a more gradual manner. Thus, the 5 unknown parameters in the model are K_{ve}, C_{ve}, C_{vi}, V_y and ε. The parameters are estimated by minimizing the error between the experimental hysteresis data, which in this case is the MR effect experimental data, $F^{e}_{mr\_effect}$ given by Eq. (9) and the model prediction, $F^{m}_{mr\_effect}$ given by Eq. (10) (Refs. 11, 14, 18-19). The parameters were estimated for the zero preload and the preloaded MR effect hysteresis data, and for each amplitude condition separately. The estimated parameters are denoted by the circles and squares in Figs. 12 and 13. The figures show that some of the identified parameters are different for the zero preload and preloaded cases although the responses are similar. This is an artifact of the optimization procedure. The sensitivity of the response to each of the parameters varies significantly. Thus, a large change in a weakly influential parameter would be compensated for in the optimization process by a small change in a strongly influential parameter.

Using the estimated parameters, the hysteresis curves are reconstructed. The reconstructed MR effect hysteresis curves are plotted with the experimental data in Fig. 14. Figure 14a shows the correlation for the force vs. displacement hysteresis for the zero preload case, and Fig. 14b shows the force vs. velocity correlation for the zero preload case. In order to correlate the built-up damper hysteresis for the MR (ON) damper, Eq. (9) was used to calculate F_{mr_on}, and plotted against experimental built-up damper data. The force vs. displacement correlations for the zero preload and the preloaded cases are shown in Figs. 15a and 15b, respectively. It can be seen that the model captures the nonlinear behavior of the MR (ON) damper quite accurately.

Dual Frequency Characterization

In addition to testing the dampers at a single frequency of 10 Hz, experiments were conducted at dual frequencies of 10 Hz, which is the first lead-lag frequency of the 1/6 scale Comanche rotor blade, and 15 Hz which is the 1/rev rotor frequency. This was done to assess the potential loss of damping at the lag frequency due to dual frequency motion (Ref. 2). The range of 10 Hz amplitudes was the same as for the single frequency tests, and the 15 Hz amplitudes tested were 0.005, 0.01 and 0.02 inches, marked as *'s in Table 2. An HP 8904A multifunction synthesizer was used to generate and sum the signals with the two individual frequencies. The force input and the displacement response were measured using a load cell and a laser sensor, respectively, as in the single frequency characterization tests. In order to characterize the dampers under dual frequency excitation conditions, the components of the complex modulus G^* were determined at the two frequencies. The stiffness modulus component G' at 10 Hz for the three damper configurations, and for the two preload conditions is shown in Fig. 16. Figures 16a and 16b show the variation of G' for the Fluidlastic® damper under zero preload and preloaded condition, respectively. For the zero preload case (Fig. 16a), the stiffness modulus increases with increase in the 15 Hz amplitude and then decreases. The change is between +3% to –7% at low 10 Hz amplitudes. At high amplitudes the dual frequency excitation does not have a significant effect on the stiffness which remains at around 25.5 kN/m. For the Fluidlastic® preloaded case (Fig. 16b), the stiffness drops by a maximum of 15% at low amplitudes, and by about 7% at high amplitudes. Figures 16c and 16d show the variation of G' for the MR (OFF) damper under zero preload and preloaded conditions, respectively. The stiffness remains constant for all 10 Hz and 15 Hz amplitudes, so that there is no effect of dual frequency excitation. Figures 16e and 16f show the variation of G' for the MR (ON) damper under zero preload and preloaded condition, respectively. The effect of dual frequency excitation is most significant for the zero preload MR (ON) damper (Fig. 16e) at low 10 Hz amplitudes, where there is a 50% drop in stiffness from 35 kN/m to 18 kN/m. However, as the 10 Hz amplitude is increased, there is no effect of dual frequency excitation on the stiffness, which remains at 18 kN/m. The trends are the same for the MR (ON) damper in the preloaded condition (Fig. 16f), where there is a 64% drop in stiffness from 28 kN/m to 10 kN/m at a 10 Hz amplitude of 0.005 inches (0.125 mm). For high amplitudes, the stiffness is insensitive to dual frequency excitation, and remains at 10 kN/m.

Figure 17 shows the damping modulus component G'' at 10 Hz for the

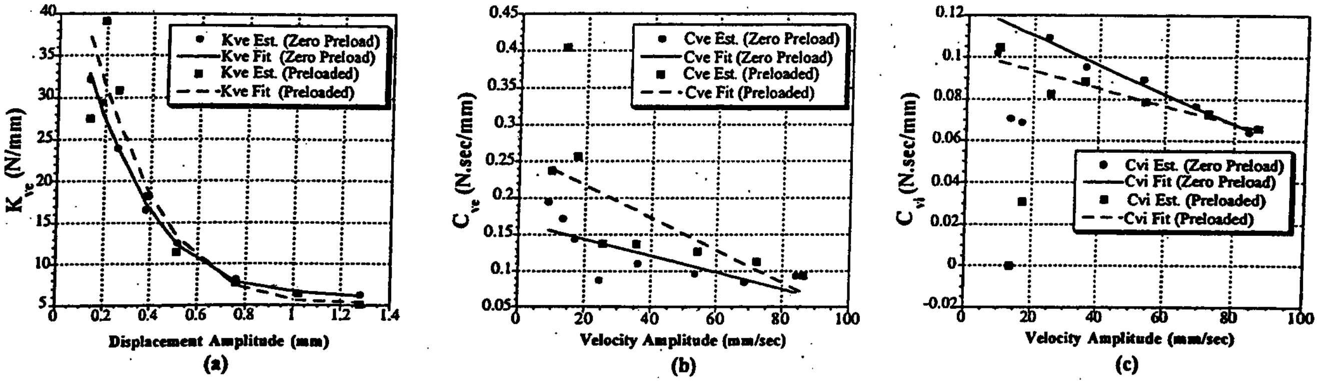

Fig. 12. Parameter estimation results and the fits through the individual viscoelastic and viscous parameters: (a) K_{ve}, (b) C_{ve}, and (c) C_{vi}.

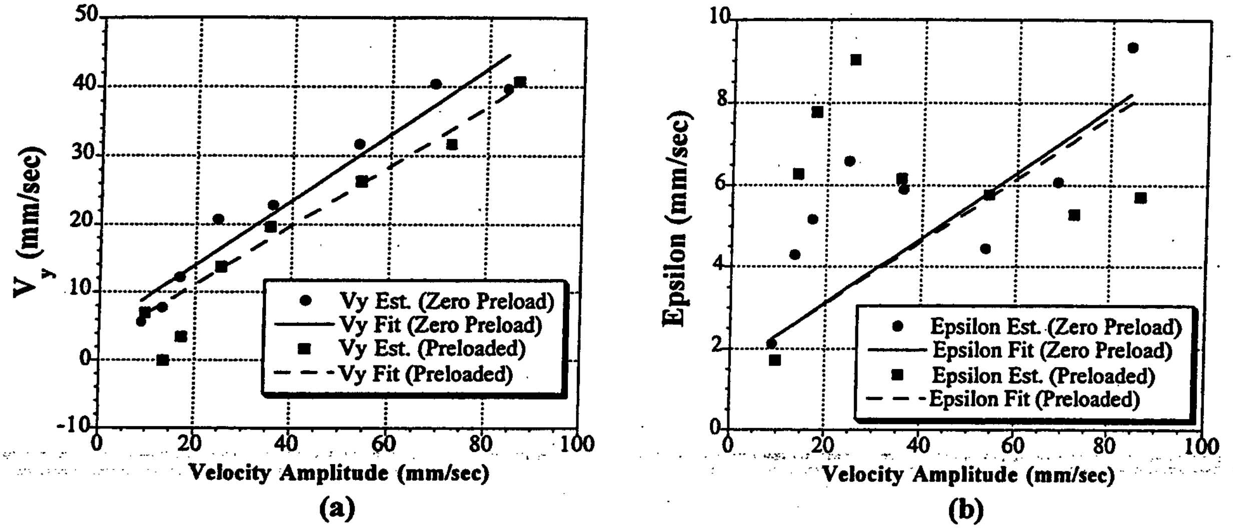

Fig. 13. Parameter estimation results and the fits through the shape function parameters: (a) V_y, and (b) ε.

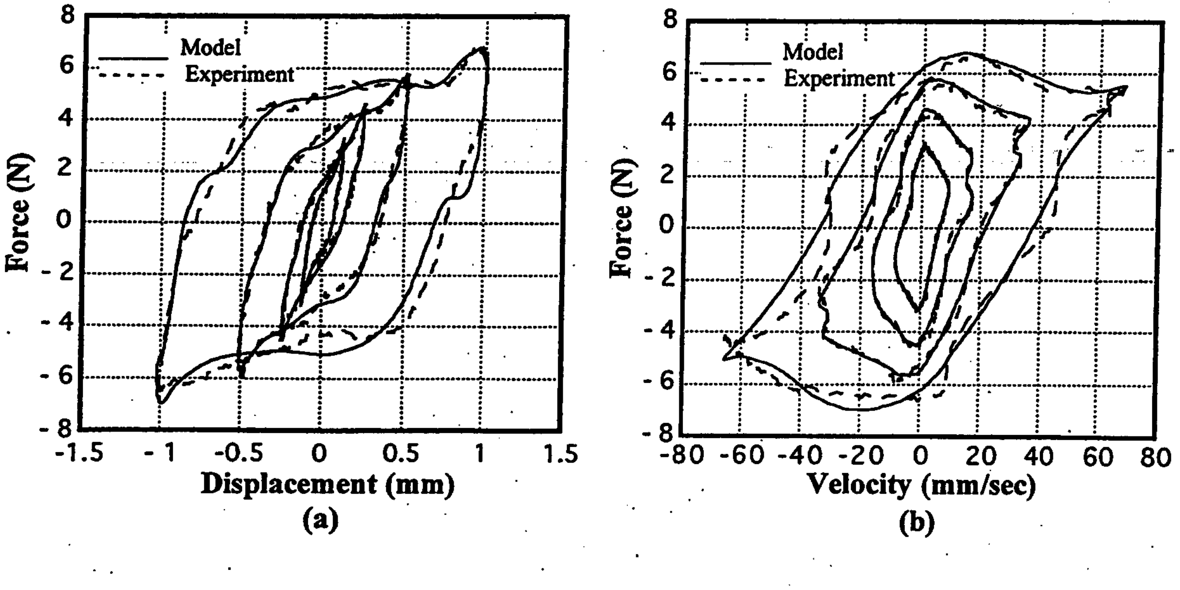

Fig. 14. Model correlation for the MR effect hysteresis curves for zero preload condition: (a) force vs. displacement (b) force vs. velocity.

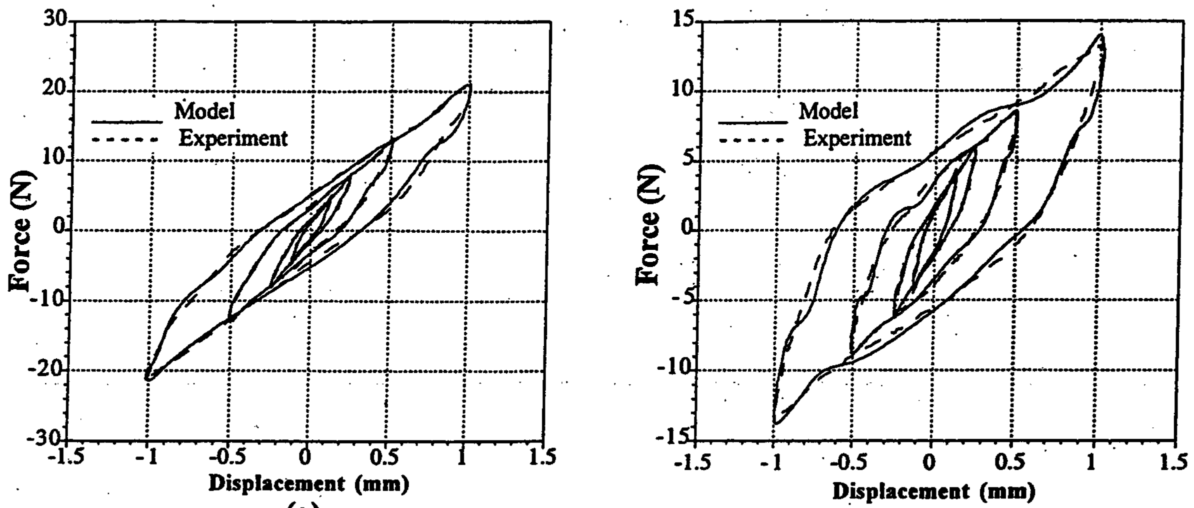

(a) (b)

Fig. 15. Model correlation for the MR (ON) built-up damper hysteresis for (a) zero preload, and (b) preloaded cases.

three damper configurations under the two preload conditions. Figures 17a and 17b show the variation of G'' for the Fluidlastic® damper under zero preload and preloaded condition, respectively. It can be seen that the dual frequency excitation has a small to almost zero effect on the damping modulus values. Similar trends are seen in Figs. 17c and 17d, which show the variation of G'' for the MR (OFF) damper under zero preload and preloaded condition, respectively. Figures 17e and 17f show the variation of G'' for the MR (ON) damper under zero preload and preloaded condition, respectively. The damping modulus shows a significant drop (50 to 60%) as the 15 Hz amplitude is increased at low 10 Hz amplitudes. For high amplitudes of 10 Hz frequency, the change in damping is almost zero.

Thus, the characterization results show that the MR (ON) dampers, due to their nonlinear behavior, are significantly affected by dual frequency excitation at low amplitudes (0.005 inches (0.125 mm)), where they show 50 to 60% degradation in stiffness and damping. However at high 10 Hz amplitudes (0.05 inches (1.25 mm)), there is almost no effect of dual frequency excitation on the stiffness or damping. These effects of dual frequency excitation are similar to the effects observed by Felker et al. in their study of elastomeric dampers (Ref. 2).

Dual Frequency Hysteresis Modeling

The single frequency excitation experiment results showed that the Fluidlastic® dampers and the MR (OFF) dampers behavior is linear. The dual frequency characterization results discussed in the previous section confirmed to a large extent this linear behavior. Thus the Kelvin element with the spring constant and the damping coefficient used for the single frequency excitation was used to predict the dual frequency results. Sample correlation plots for the Fluidlastic® dampers (zero preload) and the MR (OFF) dampers (preloaded) are shown in Figs. 18 and 19, respectively. It can be seen that the linear models predict the dual frequency behavior quite well.

For the MR (ON) dampers, the nonlinear viscoelastic-plastic model was used to predict the dual frequency hysteresis behavior. The maximum values (amplitudes) were first determined from the displacement and the velocity time histories of the dual frequency measurements for each case. Using these values, the model constants, K_{ve}, C_{ve}, C_{vi}, V_y and ε were determined from the polynomial fits denoted by the solid and dashed lines in Figs. 12 and 13. Using these model constants, the hysteresis cycles were predicted for all the damper configurations and dual frequency test cases.

The model predictions for 10 Hz amplitude = 0.127 mm (0.005″) cases using these parameters are compared with the experimental data in Fig. 20 for the zero preload case and in Fig. 21 for the preloaded case. These cases are in fact the worst cases because, as Figs. 16e and 16f, and Figs. 17e and 17f show, the 10 Hz amplitude = 0.127 mm (0.005″) cases are the ones most severely affected by dual frequency excitation. Yet, the correlation results in Figs. 20 and 21 show that the parameters as obtained from an approximate fit of the single frequency parameters perform fairly well in predicting the dual frequency behavior. Better correlation was obtained for higher 10 Hz amplitudes, but is not shown here for the sake of brevity.

Conclusions

1. Fluidlastic® and MR (OFF) dampers are linear, with the equivalent damping and the complex modulus components, G' and G'', remaining constant with varying displacement amplitude. Thus, the Fluidlastic® and MR (OFF) dampers can be modeled as Kelvin chains.
2. A substantial increase in damping can be achieved by applying a magnetic field in the MR dampers. However, MR (ON) dampers are nonlinear with G' and G'' decreasing with amplitude under single frequency excitation conditions. Although the dampers used in this study were tested in the ON and OFF conditions, it is feasible to continuously vary the magnetic field between these two operating conditions so as to tune the damping and stiffness properties, albeit not independently, to a desired level.
3. The effect of the magnetic field on the MR damper behavior can be extracted from the difference in MR (OFF) and MR (ON) hysteresis data. This extracted data reveals the phenomenology of the MR effect with a transition from pre-yield to post-yield behavior. This yield transition behavior is captured well by the nonlinear viscoelastic-plastic model.
4. Under dual frequency excitation conditions, the Fluidlastic® dampers exhibit a mild degradation (about 7% decrease) in stiffness, but no change in damping. While MR (OFF) dampers show no effect of dual frequency excitation on the stiffness or damping, the MR (ON) dampers show a substantial degradation (about 50 to 60% decrease) in both stiffness and damping.
5. Since the Fluidlastic® and MR (OFF) dampers show fairly linear behavior under dual frequency excitation conditions, the single frequency linear Kelvin chain models predict the dual frequency behavior fairly

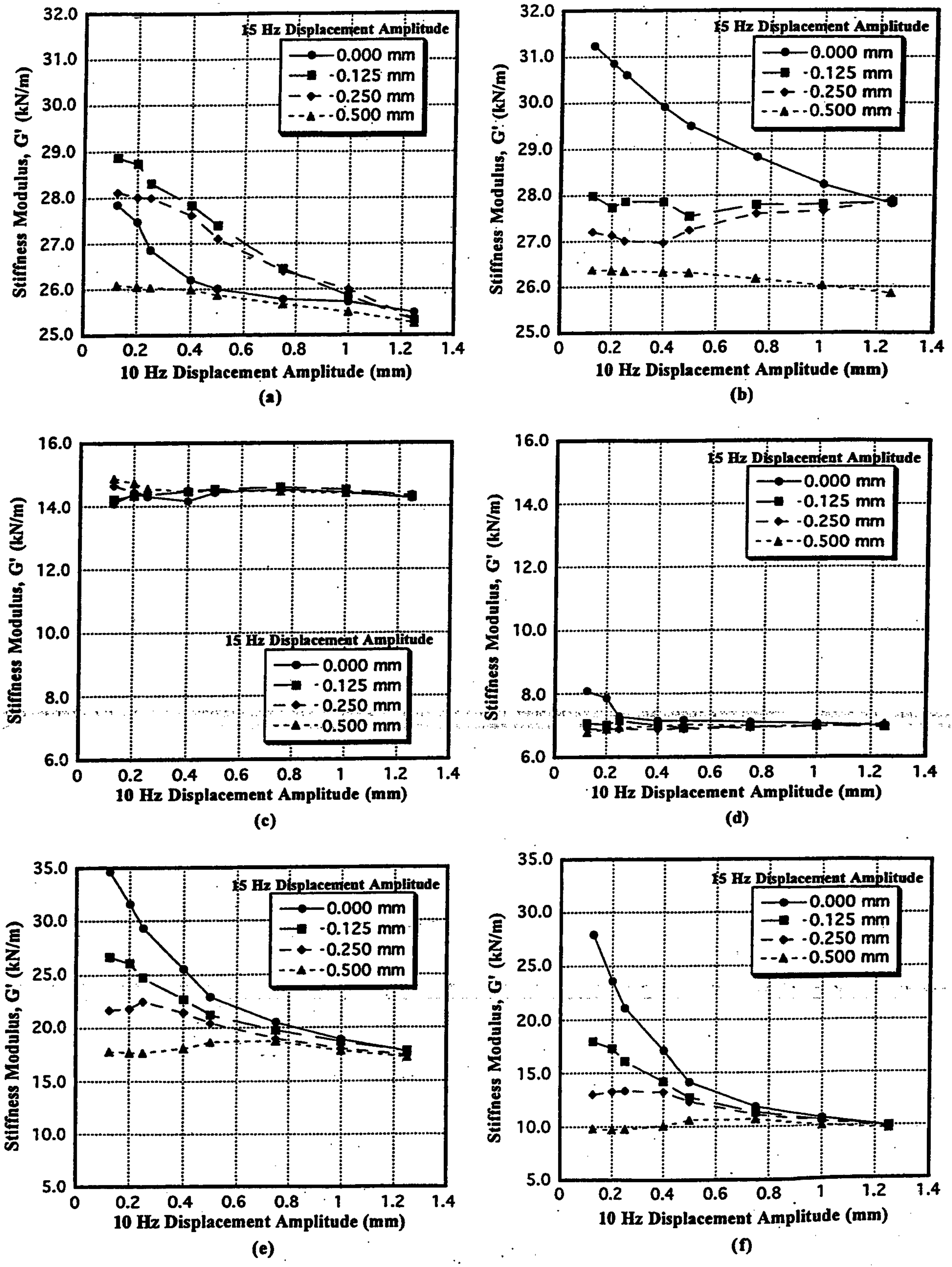

Fig. 16. Stiffness modulus variation under dual frequency conditions for (a) Fluidlastic®, zero preload (b) Fluidlastic®, preloaded (c) MR damper (OFF), zero preload (d) MR damper (OFF), preloaded (e) MR damper (ON), zero preload (f) MR damper (ON), preloaded.

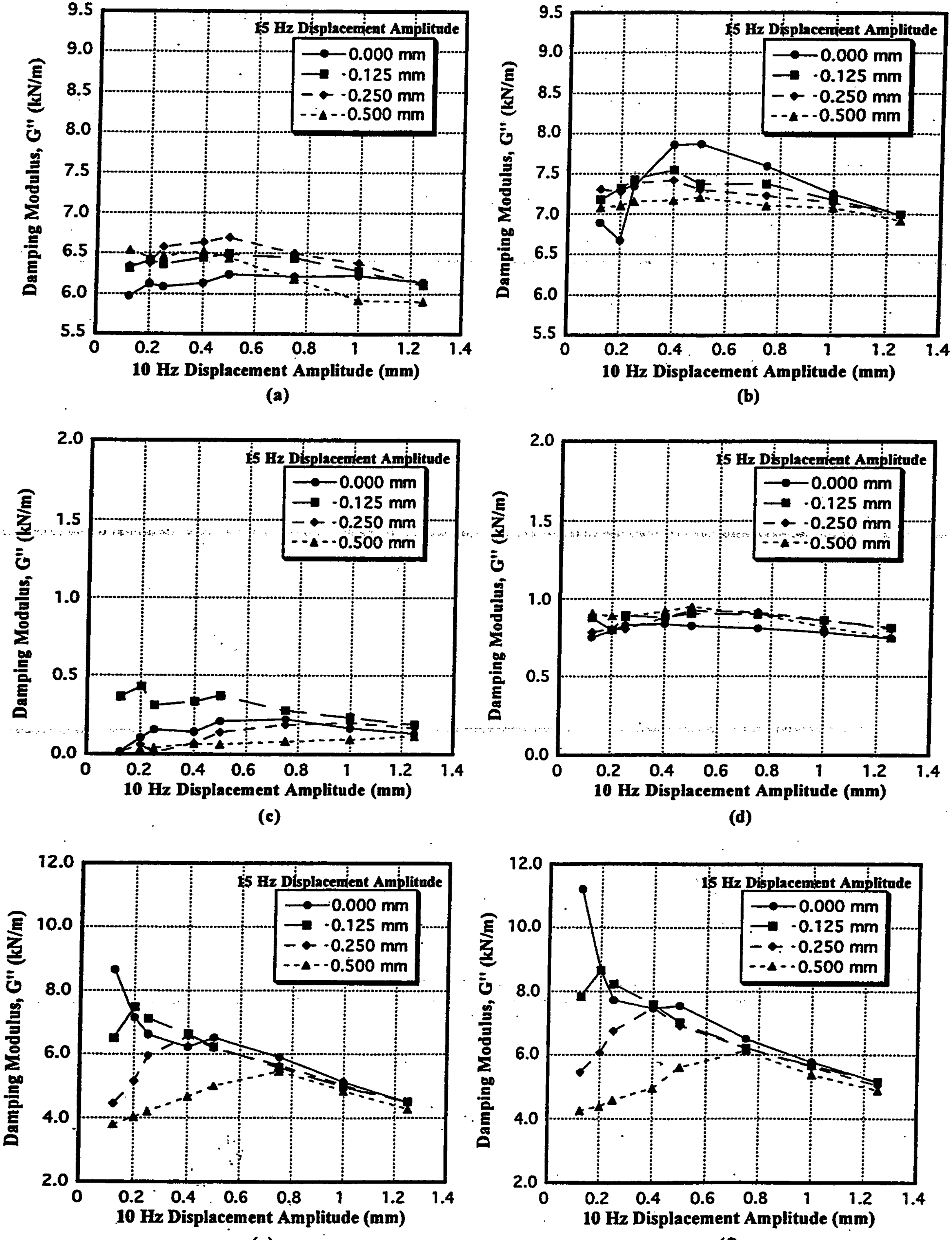

(a) (b)

(c) (d)

(e) (f)

Fig. 17. Damping modulus variation under dual frequency conditions for (a) Fluidlastic®, zero preload (b) Fluidlastic®, preloaded (c) MR damper (OFF), zero preload (d) MR damper (OFF), preloaded (e) MR damper (ON), zero preload (f) MR damper (ON), preloaded.

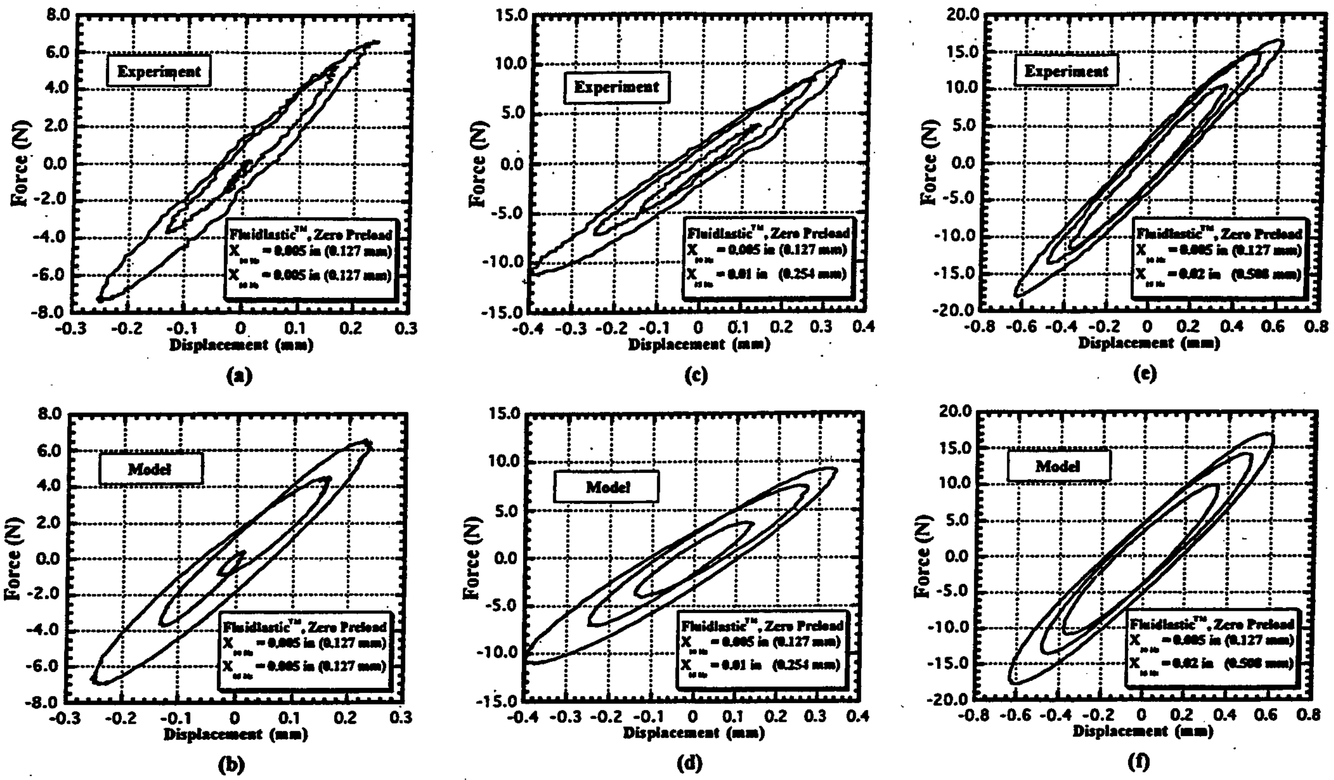

(a) (c) (e)

(b) (d) (f)

Fig. 18. Comparison of dual frequency Fluidlastic®, zero preload experimental data with hysteresis prediction using model with parameters obtained from single frequency data: (a), (c), and (e) experimental data; (b), (d), and (f) model predictions.

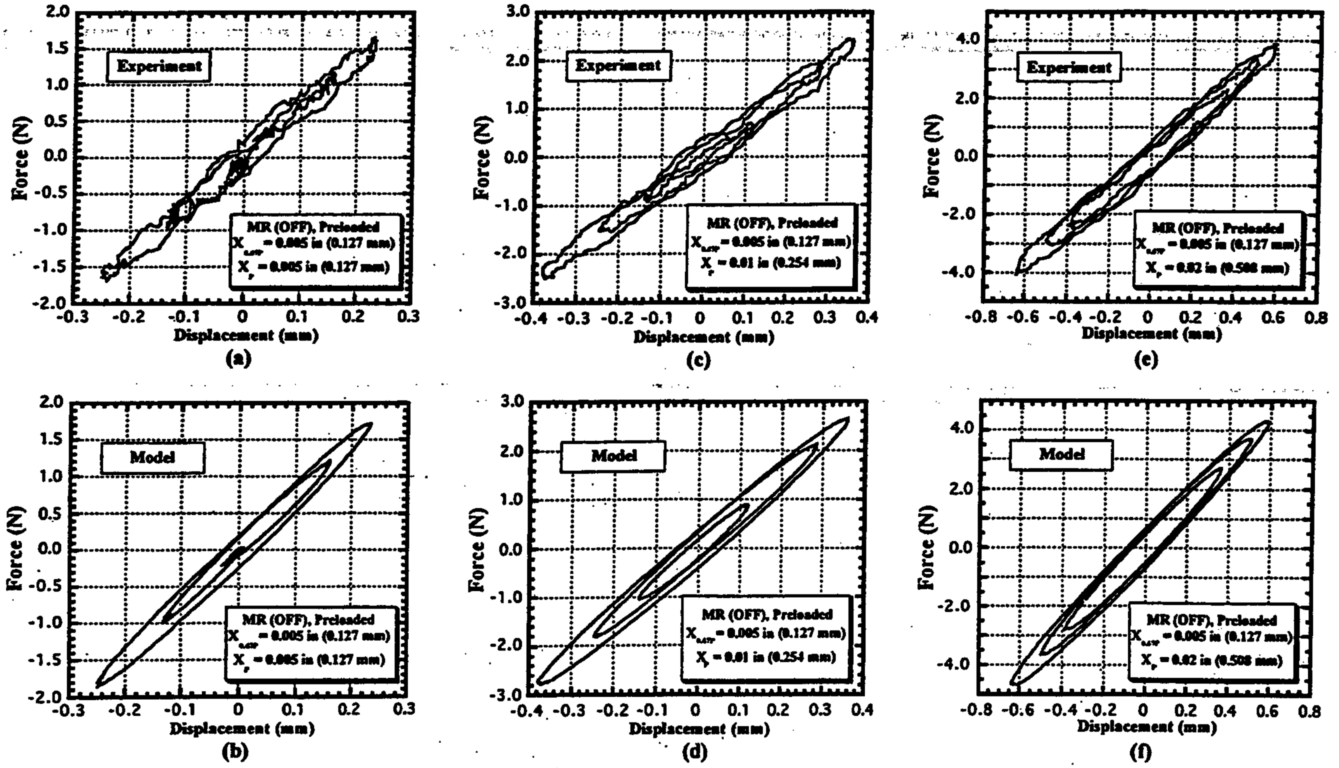

(a) (c) (e)

(b) (d) (f)

Fig. 19. Comparison of dual frequency MR (OFF) preloaded experimental data with hysteresis prediction using model with parameters obtained from single frequency data: (a), (c), and (e) experimental data; (b), (d), and (f) model predictions.

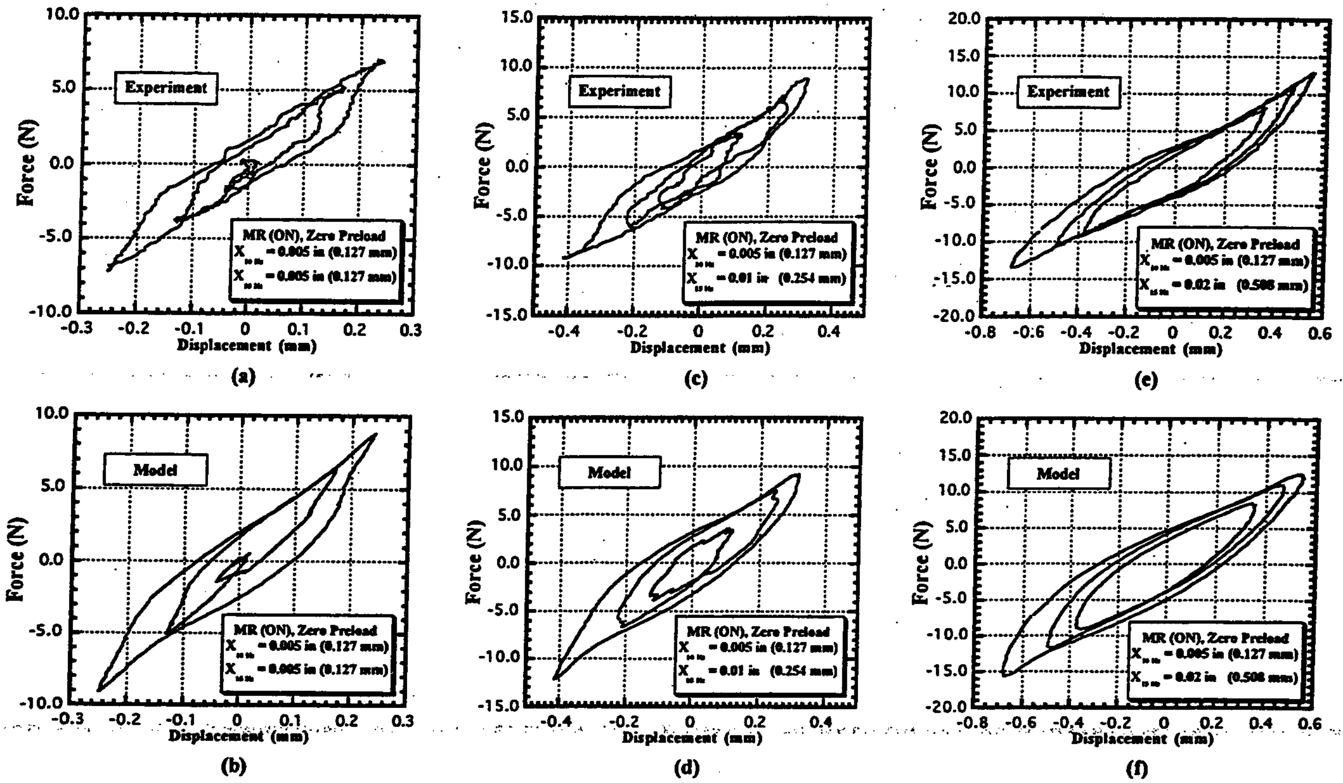

Fig. 20. Comparison of dual frequency MR (ON) zero preload experimental data with hysteresis prediction using nonlinear viscoelastic plastic model with parameters obtained from single frequency data: (a), (c), and (e) experimental data; (b), (d), and (f) model predictions.

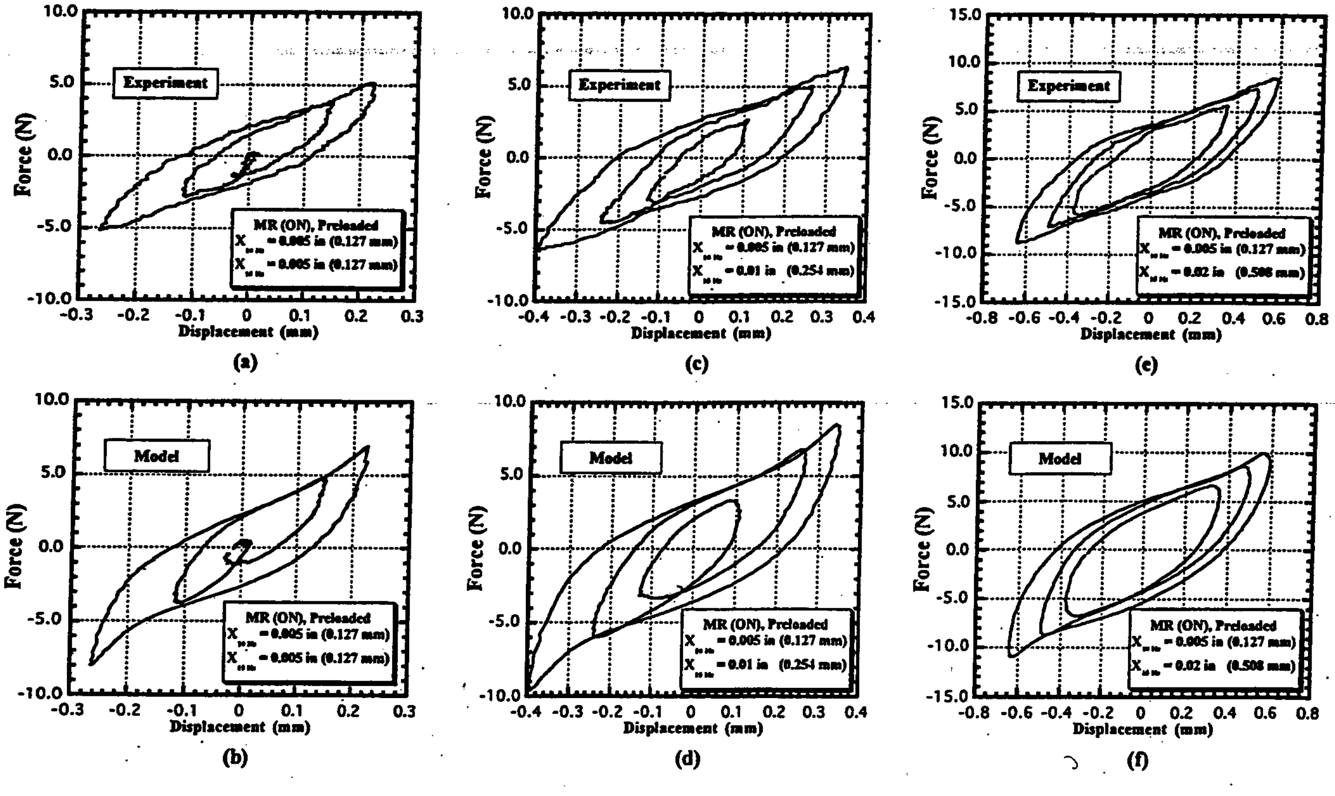

Fig. 21. Comparison of dual frequency MR (ON) preloaded experimental data with hysteresis prediction using nonlinear viscoelastic plastic model with parameters obtained from single frequency data: (a), (c), and (e) experimental data; (b), (d), and (f) model predictions.

well. The nonlinear viscoelastic-plastic model with parameters estimated from the single frequency hysteresis data was used to predict the dual frequency hysteresis behavior. The model predictions correlate well with the experimental data. However, the model can only be used to predict the forced response of a damper. So, the displacement and velocity amplitudes of motion are needed *a priori* to determine the appropriate model parameters. This represents a limitation in that the model is not suited for capturing transient behavior wherein the amplitude is continuously changing, or responses where steady state is not reached in a short span of time.

This study demonstrates the feasibility of using MR dampers for lag mode damping applications wherein a substantial increase in damping can be effected by applying a magnetic field. Tracking problems arise due to dissimilarities in dynamic properties of rotor blades. Lag dampers, which exert a strong influence on blade dynamics, thus can give rise to tracking problems if they are dissimilar. Thus, it seems feasible that the properties of a set of dampers in a helicopter rotor system could be tuned to match each other thereby helping to improve the tracking of the rotor blades. Although the MR dampers in the ON condition show a degradation in damping and stiffness due to inherent nonlinearities, this problem can be circumvented by varying the magnetic field continuously such that damping and stiffness levels are kept constant. However, a more detailed study of the effects of continuous variation of magnetic field needs to be conducted before a conclusive strategy for lag mode damping augmentation is proposed.

Acknowledgments

This work was initiated by the U.S. Army Research Office under a Short Term Innovative Research Award to Norman M. Wereley, Contract No. DAAH-4496-10078 with Dr. Gary Anderson serving as the technical monitor. Gopalakrishna M. Kamath received fellowship support from the Minta Martin Fund for Aeronautical Research at the University of Maryland, and a Vertical Flight Foundation Scholarship. Additional support to Norman M. Wereley was obtained under the Defense University Research Instrumentation Program (Contract No. DAAH-0496-10301), and under the Army Young Investigator Program (Contract No. DAAG-5598-10339), both with Dr. Gary Anderson serving as the technical monitor. The authors gratefully acknowledge the technical assistance of Mr. Pat Sheridan of Lord Corporation.

Fluidlastic® is a registered trademark of Lord Corporation.

References

[1] Chopra, I., "Perspectives in Aeromechanical Stability of Helicopter Rotors," *Vertica*, Vol. 14, (4), 1990, pp. 457-508.

[2] Felker, F. F., Lau, B. H., McLaughlin, S., and Johnson, W., "Nonlinear Behavior of an Elastomeric Lag Damper Undergoing Dual-Frequency Motion and its Effect on Rotor Dynamics," *Journal of the American Helicopter Society*, Vol. 34, (4), Oct 1987, pp. 45-53.

[3] McGuire, D. P., "Fluidlastic® Dampers and Isolators for Vibration Control in Helicopters," Proceedings of the 50th Annual Forum of American Helicopter Society, Washington D.C., May 1994, pp. 295-303.

[4] Panda, B. and Mychalowycz, E., "Aeroelastic Stability Wind Tunnel Testing with Analytical Correlation of the Comanche Bearingless Main Rotor," *Journal of the American Helicopter Society*, Vol. 42, (3), Jul 1997, pp. 207-217.

[5] Panda, B., Mychalowycz, E., and Tarzanin, F J., "Application of Passive Dampers to Modern Helicopters," *Smart Materials & Structures*, Vol. 5, (5), Oct 1996, pp. 509-516.

[6] Stanway, R., Sproston, J. L., and El-Wahed, A. K., "Application of Electro-Rheological Fluids in Vibration Control: a Survey," *Smart Materials & Structures*, Vol. 5, (5), 1996, pp. 464-482.

[7] Brooks, D. A., "Design and Development of Flow Based Electro-Rheological Devices," *Int. J. Modern Physics B*, Vol. 6, (15 and 16), 1992, pp. 2705-30.

[8] Duclos, T. G., "Design of Devices using Electrorheological Fluids," *Society of Automotive Engineering Transactions*, Vol. 97, Sec. 2, SAE Paper No. 881134, 1988, pp. 2.532-2.536.

[9] Carlson, J. D., Catanzarite, D. M., and St. Clair, K. A., "Commercial Magneto-Rheological Fluid Devices," Presented at the 5th Int. Conf. on Electro-Rheological, Magneto-Rheological Suspensions and Associated Technology, Sheffield, U.K., Jul 1995, pp. 20-28.

[10] Weiss, K. D., Carlson, J. D., and Nixon, D. A., "Viscoelastic Properties of Magneto- and Electro-Rheological Fluids," *J. Intelligent Material Systems and Structures*, Vol. 5, (11), Nov 1994, pp. 772-775.

[11] Pang, L., Kamath, G. M., and Wereley, N. M., "Dynamic Characterization and Analysis of Magnetorheological Damper Behavior," 5th Symposium on Smart Structures and Materials, Passive Damping and Isolation Conference, San Diego, CA, Mar 1-5, 1998, SPIE Paper No. 3327-25, pp. 284-302.

[12] Kamath, G. M., Hurt, M. K., and Wereley, N. M., "Analysis and Testing of Bingham Plastic Behavior in Semi-Active Electrorheological Fluid Dampers," *Smart Materials & Structures*, Vol. 5, (5), Oct 1996, pp. 576-590.

[13] Lou, Z., Ervin, R. D., and Filisko, F. E., "A Preliminary Parametric Study of Electrorheological Dampers," *Developments in Electrorheological Flows and Measurement Uncertainty*, FED 205/AMD 190, American Society for Mechanical Engineers, Nov 1994, pp. 143-156.

[14] Kamath, G. M. and Wereley, N. M., "Nonlinear Viscoelastic-Plastic Mechanisms-Based Model of an Electrorheological Damper," *AIAA J. Guidance, Control, and Dynamics*, Vol. 20, (6), Nov-Dec 1997, pp. 1125-1132.

[15] Stanway, R., Sproston, J., and Stevens, N. G., "Non-Linear Modelling of an Electro-rheological Vibration Damper," *Journal of Electrostatics*, Vol. 20, 1987, pp. 167-184.

[16] Gavin, H. P., Hanson, R. D., and Filisko, F. E., "Electrorheological Dampers, Part II: Testing and Modeling," *ASME Journal of Applied Mechanics*, Vol. 63, (3), Sep 1996, pp. 676-682.

[17] Spencer, B. F., Dyke, S. J., Sain, M. K., and Carlson, J. D., "Phenomenological Model of a Magnetorheological Damper," *ASCE Journal of Engineering Mechanics*, Vol. 123, (3), May 1997, pp. 230-238.

[18] Kamath G. M. and Wereley, N. M., "Modeling the Damping Mechanism in ER Fluid Based Dampers," M3DIII: *Mechanics and Mechanisms of Material Damping*, ASTM STP 1304, A. Wolfenden and V. K. Kinra, Eds., American Society for Testing and Materials, 1997, pp. 331-348.

[19] Kamath, G. M. and Wereley, N. M., "A Nonlinear Viscoelastic-Plastic Model for Electrorheological Fluids," *Smart Materials & Structures*, Vol. 6, (3), Jun 1997, pp. 351-359.

[20] Gandhi, F. and Chopra, I., "Analysis of Bearingless Main Rotor Dynamics with the Inclusion of an Improved Time Domain Nonlinear Elastomeric Damper Model," Proceedings of the 51st Annual Forum of American Helicopter Society, Fort Worth, TX, May 9-11, 1995, pp. 403-420.

[21] Smith, E. C., Beale, M .R., Govindswamy, K., Vascsinec, M. J., and Lesieutre, G. A., "Formulation and Validation of a Finite Element Model for Elastomeric Lag Dampers," Proceedings of the 51st Annual Forum of American Helicopter Society, Fort Worth, TX, May 9-11, 1995, pp. 1101-1116.

[22] Tarzanin, F. J., and Panda, B., "Development and Application of Nonlinear Elastomeric and Hydraulic Lag Damper Models," Proceedings of the 36th Structures, Structural Dynamics and Materials Conference, New Orleans, Louisiana, Apr 1995, pp. 2534-2544.

[23] Kunz, D. L., "Influence of Elastomeric Damper Modeling on the Dynamic Response of Helicopter Rotors," *AIAA Journal*, Vol. 35, (2), Feb 1997, pp. 349-354.

[24] Kamath, G.M., "Electrorheological and Magnetorheological Fluid Lag Dampers for Helicopter Rotor Systems," Ph.D Dissertation, University of Maryland, College Park, 1998.

[25] Flugge, W., *Viscoelasticity*, Blaisdell Publishing Company, 1967.

Analysis and Testing of Electrorheological Bypass Dampers

JASON LINDLER AND NORMAN M. WERELEY*
Smart Structures Laboratory, Alfred Gessow Rotorcraft Center, Dept. of Aerospace Engineering, University of Maryland, College Park, MD 20742

ABSTRACT: We experimentally validate nonlinear quasi-steady electrorheological (ER) and magnetorheological (MR) damper models, using an idealized Bingham plastic shear flow mechanism, for the flow mode of damper operation. An electrorheological valve or bypass damper was designed, and fabricated using predominantly commercial off-the-shelf hydraulic components. Both the hydraulic cylinder and the bypass duct have cylindrical geometry, and damping forces are developed in the annular bypass via Poiseuille (flow mode) flow. Damper models assume parallel plate geometry. Three nondimensional groups are used for damper analysis, namely, the Bingham number, Bi, the nondimensional plug thickness, $\bar{\delta}$, and the area coefficient defined as the ratio of the piston head area, A_p, to the cross-sectional area of the annular bypass, A_d. In the flow mode case, the damping coefficient, which is defined as the ratio of equivalent viscous damping of the Bingham plastic material, C_{eq}, to the Newtonian viscous damping, C, is a function only of the nondimensional plug thickness. The damper was tested using a mechanical damper dynamometer for sinusoidal stroke of 2 in., over a range of frequencies below 0.63 Hz. The damping coefficient vs. nondimensional plug thickness diagram was experimentally validated using these data over a range of damper shaft velocities or frequencies and applied electric fields. Because the behavior of ER and MR fluids are qualitatively similar, these ER damper modeling results can be extended to analysis of flow mode MR dampers.

INTRODUCTION

ELECTRORHEOLOGICAL (ER) and magnetorheological (MR) fluids have been utilized in controllable valves, clutches, brakes, suspensions, and engine mounts (Stanway et al., 1996; Duclos, 1988; Brooks, 1992). Several advantages may result from applying these controllable fluids in dampers for aerospace systems, such as helicopter lag mode dampers (Kamath, Wereley and Jolly, 1999), dampers for landing gear to semi-actively control nose shimmy and enhance crashworthiness (Ervin et al., 1996; Lou et al., 1993a), and semi-active shock and vibration mounts for avionics systems, especially in naval aircraft. These advantages include damper adjustability to account for varying disturbance spectra, and tuning of damping levels at resonance.

ER fluids exhibit complex characteristics and nonlinear effects due to applied electric field, applied load, strain amplitude and frequency of excitation in dynamic conditions (Kamath and Wereley, 1997b). In steady fully developed flow, ER and MR fluids tend to behave like idealized Bingham plastic shear flows (Kamath et al., 1996; Gavin et al., 1996a–b). For a Bingham plastic material, the onset of flow does not occur until the applied shear stress exceeds the dynamic yield stress. Once the local shear stress exceeds the dynamic yield stress, the ER fluid flows like a Newtonian fluid with a constant plastic viscosity. Because of its simplicity, the Bingham plastic model has been widely used to describe ER and MR fluid behavior (Atkin et al., 1991; Brooks, 1992; Kamath et al., 1996). In addition, several studies strongly support the Bingham shear flow model as a simplified constitutive model for ER and MR fluids (Duclos, 1988; Brooks, 1992; Kamath et al., 1996; Gavin et al., 1996a). However, the Bingham plastic model is a steady state model and assumes that the fluid is in the post-yield phase and is flowing at a constant shear rate. The model does not account for the pre-yield viscoelastic behavior which is important in dynamic studies (Kamath et al., 1997a–b). We developed a 1D axisymmetric model for ER and MR dampers using the Bingham plastic model of ER fluid behavior (Kamath et al., 1996). The design variables accounted for dimensions such as electrode length, electrode gap, piston area, and piston diameter. Dynamic yield stress and plastic viscosity, as a function of applied field, are required material properties for the model.

To describe the dynamic behavior of ER fluids, alternative models have been suggested. In our prior work (Kamath and Wereley, 1997a–c; Kamath, Wereley and Jolly, 1999), we used a mechanisms-based model to describe pre-yield and post-yield characteristics using linear viscoelastic and viscous elements, respectively. The parameters of the nonlinear viscoelastic plastic model were identified from experimental hysteresis cycle data. Makris et al. (1996) developed an alternative elastic-viscoplastic model to account for pre-yield and post-yield behavior. Although the dynamic models more accurately describe fluid behavior under oscillatory loads, the Bingham plastic model, because of its simplicity, serves as a better starting point in the design of ER fluid-based devices.

---

*Author to whom correspondence should be addressed. E-mail: wereley@eng.umd.edu

1045-389X/99/05 0363-14 $10.00/0
© 2000 Technomic Publishing Co., Inc.

It is advantageous to develop nondimensional analysis to test design concepts at model-scale before moving to full-scale prototypes. Several efforts have been made to develop a set of nondimensional groups with which to characterize damper performance in a concise way. Phillips (1969) developed a set of nondimensional groups and corresponding polynomial solutions to determine the pressure gradient in flow and mixed mode dampers given the volume flux due to piston motion. This approach is well-known and was further refined in recent studies by Gavin et al. (1996a–b) and Makris et al. (1996). This approach leads to damper design procedures that are very useful, but can be simplified using the nondimensional groups described in this paper.

Stanway et al. (1996) developed an alternative non-dimensional scheme for flow mode dampers utilizing a friction coefficient, the Reynolds number, and the Hedstrom number. The solution procedure also reduces to a root finding problem for a polynomial.

We utilize alternative non-dimensional groups, based on an approximate parallel plate analysis, to characterize the field dependent damping in ER and MR dampers. The three non-dimensional numbers are the Bingham number, Bi (Prager, 1961; Leek et al., 1994a–b; Peel and Bullough, 1994), the nondimensional plug thickness, $\bar{\delta}$, and the area coefficient defined as the ratio of the piston head area, A_p, to the annular area between the electrodes, A_d. The relationship between the damping coefficient, C_{eq}/C, vs. non-dimensional plug thickness, $\bar{\delta}$, is validated experimentally, using an ER bypass damper designed and fabricated at the University of Maryland.

FLOW MODE DAMPER ANALYSIS

There are three modes of damper operation: (1) shear mode or Couette flow, (2) flow mode or Poiseuille flow, and (3) mixed mode as in a dashpot damper (Wereley and Pang, 1998; Lou et al., 1993b). The flow mode of damper operation is the focus of this paper. Thus, we will develop an analysis of an ER valve or bypass damper that operates in the flow mode. An ER damper was designed and fabricated to experimentally validate this analysis. A schematic of a flow mode damper is shown in Figure 1(a). The damper consists of a hydraulic cylinder, where a bypass is fitted to its side. The bypass consists of two concentric tubular electrodes, and forms the annulus through which the ER fluid flows. The ER fluid is activated by electric field created by applying a voltage across these electrodes. The flow mode damper develops rate dependent damping forces because of the pressure drop through the electrode gap as velocity is applied to the damper shaft.

The quasi-steady governing equation obtained from force equilibrium is well known (acceleration terms are neglected):

$$\frac{\partial \tau}{\partial r} + \frac{\tau}{r} = \frac{\partial p}{\partial z} \tag{1}$$

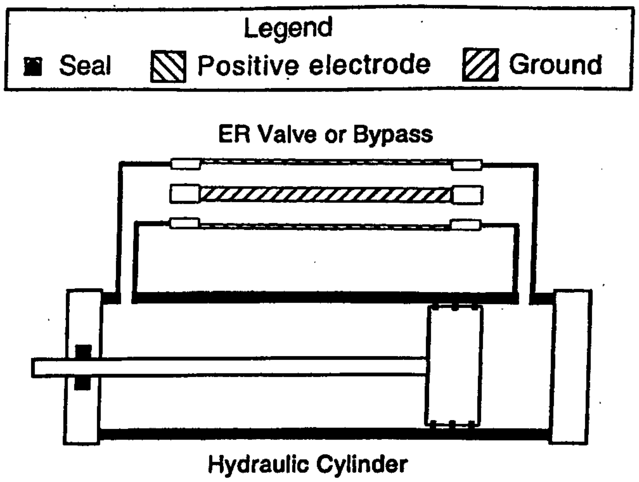

a) Flow Mode Damper

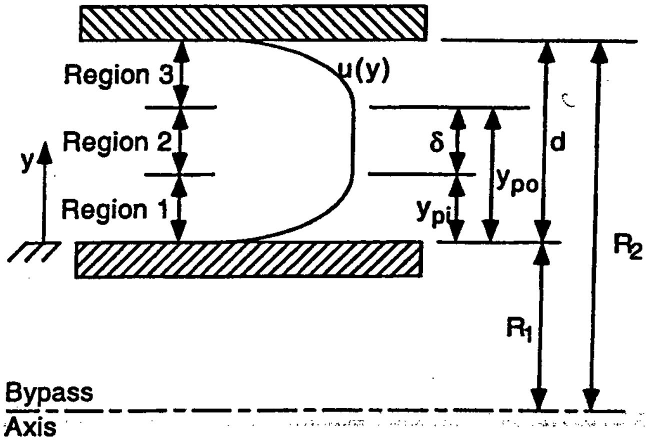

b) Coordinate System in ER Bypass or Valve

Figure 1. The flow mode damper. (a) Schematic of the electrorheological (ER) flow mode or bypass damper. (b) Typical velocity profile through an electrode gap for an ER fluid in the presence of an axial (bypass axis) linear pressure gradient.

Note that u is the velocity, τ is the shear stress, r is the radial coordinate, z is the longitudinal (bypass axial) coordinate, and p is the pressure developed via piston head motion. For the flow mode damper, the pressure gradient is assumed to vary linearly along the length of the electrodes. Equation (1) can be rewritten as

$$\frac{d\tau}{dr} + \frac{\tau}{r} = \frac{\Delta P}{L} \tag{2}$$

Note that $\Delta P = -F/A_p$, where A_p is the piston head area, and F is the applied force. If we approximate 1D axisymmetric geometry by parallel plate geometry, Equation (2) simplifies to

$$\frac{d\tau}{dy} = \frac{\Delta P}{L} \tag{3}$$

We will examine both Newtonian and Bingham-plastic shear flow mechanisms. In the case of Newtonian flow, the shear mechanism is

$$\tau = \mu \frac{du}{dy} \tag{4}$$

Here, μ is the plastic viscosity. A Bingham plastic material is characterized by a dynamic yield stress. In the pre-yield condition, the fluid in the annular electrode gap does not flow because the shear stress in the fluid has not exceeded the yield stress, or $|\tau| < \tau_y$. When the shear stress exceeds the dynamic yield stress, $|\tau| > \tau_y$, then the material begins to flow, and the velocity gradient is greater than zero, or $|du/dy| > 0$. Therefore, the shear stress can be expressed as

$$\tau = \tau_y \operatorname{sign}\left(\frac{du}{dy}\right) + \mu \frac{du}{dy} \tag{5}$$

Thus, a Newtonian fluid can be viewed as a Bingham plastic material with a dynamic yield stress of zero. For the ER fluid, the dynamic yield stress is usually approximated by a quadratic function of electric field.

NEWTONIAN FLOW

For Newtonian flow, and assuming parallel plate geometry (Wereley and Pang, 1998), the viscous damping is

$$C = \mu \frac{12 A_p^2 L}{A_d d^2} \tag{6}$$

where A_d is the cross sectional area of the annulus formed between the two electrodes of the bypass, A_p is the piston head area, d is the electrode gap, and L is the wetted electrode length.

BINGHAM PLASTIC FLOW

We now consider the approximate parallel plate analysis of the flow mode damper containing an ER or MR fluid. The 1D axisymmetric analysis is given in Kamath, Hurt and Wereley (1996). To predict damping in ER and MR dampers, we must predict velocity and shear stress profiles between the two tubular electrodes of the bypass, as a function of the damper shaft force or velocity. A schematic of the velocity profile is given in Figure 1(b). There are three flow regions in the gap between the electrodes. Regions 1 and 3 are postyield regions where $|\tau| > \tau_y$, while Region 2 is the preyield or plug flow region where $|\tau| < \tau_y$. The velocity profile must be symmetric about the center of the annular duct because we assume that (1) the pressure is uniform across the gap, and (2) cylindrical or axisymmetric geometry may be approximated by parallel plate geometry.

Several conditions must be satisfied by the velocity and shear stress profiles: boundary conditions, compatibility conditions and symmetry conditions. For convenience, we denote the velocity profile in the ith region as $u_i(y)$. First the velocity boundary conditions at the inner electrode, $y = 0$, and the outer electrode, $y = d$, are

$$\begin{aligned} u_1(0) &= 0 \\ u_3(d) &= 0 \end{aligned} \tag{7}$$

The velocity compatibility conditions are

$$u_1(y_{pi}) = u_2(y_{pi}) = u_2(y_{po}) = u_3(y_{po}) \tag{8}$$

Velocity gradient compatibility conditions arise from the plug flow moving at a constant velocity, so that

$$u_1'(y_{pi}) = u_2'(y_{pi}) = u_2'(y_{po}) = u_3'(y_{po}) = 0 \tag{9}$$

Finally, the following velocity symmetry condition must hold:

$$u_1(d - y) = u_3(y) \tag{10}$$

Preyield Region

The width of the preyield region or the plug thickness, δ, and its location in the annular gap, y_{pi} and y_{po}, as shown in Figure 1(b), are required to predict the damping. From the symmetry and compatibility conditions, the following equations must hold:

$$\begin{aligned} y_{po} - y_{pi} &= \delta \\ y_{pi} + y_{po} &= d \end{aligned} \tag{11}$$

Solving for the location of the plug leads to

$$\begin{aligned} y_{pi} &= \frac{d}{2}(1 - \bar{\delta}) \\ y_{po} &= \frac{d}{2}(1 + \bar{\delta}) \end{aligned} \tag{12}$$

where the nondimensionalized plug thickness,

$$\bar{\delta} = \frac{\delta}{d} \tag{13}$$

has been introduced. According to approximate parallel plate analysis, the plug is symmetric about the center of the annulus, which is only approximately true for the case of cylindrical geometry (Kamath et al., 1996).

The nondimensional plug thickness, $\bar{\delta}$, is determined from the shear stress boundary conditions. In the preyield region, the shear stress is given by

$$\tau = \frac{\Delta P}{L} y + A_2 \qquad (14)$$

The boundary conditions are $\tau(y_{pi}) = \tau_y$, and $\tau(y_{po}) = -\tau_y$, which yields an expression for the nondimensional plug thickness

$$\bar{\delta} = \frac{2L\tau_y}{|\Delta P| d} \qquad (15)$$

The nondimensional plug thickness increases as the electric field increases due to the field dependence of the dynamic yield stress, τ_y. Thus, the field dependence of the nondimensional plug thickness can be interpreted in a similar fashion to the opening and closing of a mechanical valve: for the highest electric fields, the valve is "closed" and damping force is maximized, whereas, in the absence of electric field, the valve is "open" and the damping force is minimized.

Velocity Profile

For Bingham plastic flow, we substitute Equation (5) into Equation (3) and obtain the velocity profile by direct integration, so that

$$u(y) = \frac{\Delta P}{2\mu L} y^2 + Ay + B \qquad (16)$$

The velocity profile in each region of flow is determined by satisfying the boundary conditions from Equation (7), and the compatibility conditions from Equation (8) and Equation (9). These regions are illustrated in the typical velocity profile shown in Figure 1(b).

The boundary conditions for Region 1 (post-yield) are $u_1(0) = 0$, and $u_1'(y_{po}) = 0$, which leads to the velocity profile

$$u_1(y) = \frac{\Delta P}{2\mu L}(y^2 - 2y_{pi} y) \qquad (17)$$

Region 3 is a post-yield region, and the boundary conditions are $u_3(d) = 0$ and $u_3'(y_{po}) = 0$, so that the velocity profile is

$$u_3(y) = \frac{\Delta P}{2\mu L}[y^2 - d^2 + 2y_{po}(d - y)] \qquad (18)$$

The velocity of the plug or the preyield region, u_2 is constant and is given by

$$u_2(y) = u_1(y_{pi}) = u_3(y_{po}) \qquad (19)$$

Using these values for the plug location, the complete velocity profile is

$$\begin{aligned} u_1(y) &= \frac{\Delta P}{2\mu L}[y^2 - (d - \delta)y] \\ u_2(y) &= -\frac{\Delta P}{8\mu L}(d - \delta)^2 \\ u_3(y) &= \frac{\Delta P}{2\mu L}[y^2 - (d + \delta)y + d\delta] \end{aligned} \qquad (20)$$

Shear Stress Profile

The shear stress profile through the gap is determined by substituting the velocity profile into the Bingham-plastic constitutive equation to obtain:

$$\begin{aligned} \tau_1(y) &= \tau_y + \frac{\Delta P}{2L}[2y - (d - \delta)] \\ \tau_2(y) &= \frac{\Delta P}{2L}(2y - d) \\ \tau_3(y) &= -\tau_y + \frac{\Delta P}{2L}[2y - (d + \delta)] \end{aligned} \qquad (21)$$

DAMPING

We will develop an expression for the equivalent viscous damping constant, C_{eq}, in terms of the nondimensional plug thickness, $\bar{\delta}$, and the Bingham number, Bi. The average velocity in the bypass, v_d, is given by

$$v_d = \frac{A_p}{A_d} v_0 \qquad (22)$$

where v_0 is the constant piston velocity.

A second nondimensional group, the Bingham number, Bi, is defined as (Prager, 1961; Leek et al., 1994a–b; Peel and Bullough, 1994; Wereley and Pang, 1998)

$$\text{Bi} = \frac{\tau_y d}{\mu v_d} \qquad (23)$$

The Bingham number is the ratio of dynamic shear stress to Newtonian shear stress developed by a fluid of viscosity μ under direct shear between two parallel plates separated by a distance, d. Alternatively, the Bingham number is the ratio of nonlinear to linear shear or the ratio of the sum of the active and passive (field dependent) shear stress over the passive (zero field) shear stress.

Thus, the average velocity of the flow in the bypass can be expressed in terms of the Bingham number as

$$v_d = \frac{\tau_y d}{\mu \text{Bi}} \qquad (24)$$

The dynamic yield stress can be expressed as

$$\tau_y = \frac{\bar{\delta} F d}{2 A_p L} \tag{25}$$

so that

$$v_d = \frac{\bar{\delta} F d^2}{2\mu A_p L}\frac{1}{\mathrm{Bi}} \tag{26}$$

Thus,

$$C_{eq} = \frac{F}{v_0} = \frac{2\mu A_p^2 L}{d^2 A_d}\frac{\mathrm{Bi}}{\bar{\delta}} \tag{27}$$

The ratio of the equivalent viscous damping constant, C_{eq}, to the Newtonian damping constant, C, is

$$\frac{C_{eq}}{C} = \frac{\mathrm{Bi}}{6\bar{\delta}} \tag{28}$$

The Bingham number can be expressed in terms of the nondimensional plug thickness by noting that the total volume flux through the annulus must equal the volume flux displaced by the piston. The volume flux in each region of the annulus is

$$\begin{aligned} Q_1 &= b\int_0^{y_{pi}} u_1(y)dy = -\frac{bd^3\Delta P}{24\mu L}(1-\bar{\delta})^3 \\ Q_2 &= b\int_{y_{pi}}^{y_{po}} u_2(y)dy = -\frac{bd^3\Delta P}{8\mu L}(1-\bar{\delta})^2\bar{\delta} \\ Q_3 &= b\int_{y_{po}}^{d} u_3(y)dy = -\frac{bd^3\Delta P}{24\mu L}(1-\bar{\delta})^3 \end{aligned} \tag{29}$$

The total volume flux is thus

$$\left|Q_f\right| = \frac{bd^3\Delta P}{12\mu L}(1-\bar{\delta})^2\left(1+\frac{\bar{\delta}}{2}\right) \tag{30}$$

so that

$$\left|Q_f\right| = Q_p = A_p v_0 \tag{31}$$

From these relationships it is easily shown that

$$\mathrm{Bi} = 6\frac{\bar{\delta}}{(1-\bar{\delta})^2\left(1+\frac{\bar{\delta}}{2}\right)} \tag{32}$$

Let us consider two damper experiments: (1) quasi-steady load is applied to the damper, F, and the resultant shaft velocity, v_0, is measured, and (2) the damper shaft is translated with constant velocity, v_0, and the resultant force, F, is measured.

Constant Force Input

Noting that $\Delta P = -F/A_p$ leads to

$$F = C_{eq} v_0 \tag{33}$$

where the ratio of the equivalent viscous damping constant, C_{eq}, to the Newtonian damping constant, C, is

$$\frac{C_{eq}}{C} = \frac{1}{(1-\bar{\delta})^2\left(1+\frac{\bar{\delta}}{2}\right)} \tag{34}$$

The nondimensional plug thickness, $\bar{\delta}$, is given explicitly in terms of the input force. When the Bingham number tends to zero, as in the case of strongly post-yield or high shaft velocity, then the nondimensional plug thickness also tends to zero, so that

$$\frac{\mathrm{Bi}}{\bar{\delta}} = 6 \tag{35}$$

and

$$\lim_{\mathrm{Bi}\to 0}\frac{C_{eq}}{C} = \lim_{\bar{\delta}\to 0}\frac{C_{eq}}{C} = 1 \tag{36}$$

or the equivalent viscous damping constant tends to the Newtonian damping constant when the flow mode damper operates in a strongly post-yield condition.

Constant Velocity Input

Here, we rewrite Equation (33) as a polynomial in $\bar{\delta}$ as

$$\frac{1}{2}\bar{\delta}^3 - \left[\frac{3}{2}+\frac{6}{\mathrm{Bi}}\right]\bar{\delta} + 1 = 0 \tag{37}$$

Given the input velocity, v_0, the Bingham number, Bi is calculated, and the nondimensional plug thickness, $\bar{\delta}$, can be determined either using a root finding algorithm or analytically. The physically sensible root is the root that satisfies $0 < \bar{\delta} < 1$. This is an alternative solution methodology to the well-known nondimensional polynomial introduced by Phillips (1969), and utilized by others (Gavin et al., 1996a; Makris et al., 1996).

ER BYPASS DAMPER

To validate this nondimensional analysis using the nonlinear Bingham-plastic shear flow, a high force (≈ 2000 N) and high stroke (≈ 5 cm) ER damper was constructed. The damper consists of three main parts: a hydraulic cylinder, industrial tube fittings, and an ER bypass, as pictured in Figure 2. In Figure 3, a 3D solid model schematic of the damper is

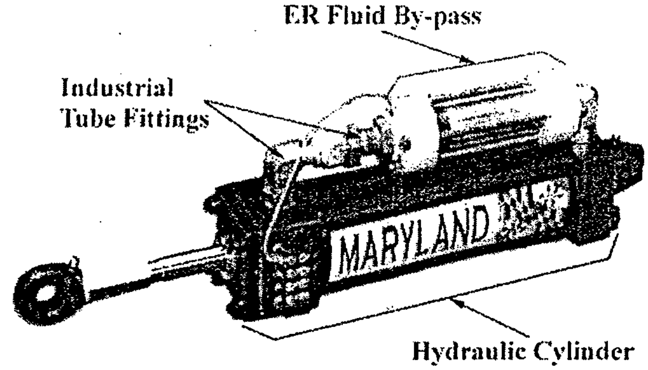

Figure 2. The electrorheological bypass damper consists of a hydraulic cylinder on which is fitted a bypass duct having two concentric aluminum tubular electrodes. The ER fluid is activated by applying voltage across the two electrodes.

shown, with a cutaway of the ER bypass and hydraulic cylinder.

To reduce damper cost, commercial-off-the-shelf parts, such as a hydraulic cylinder and industrial tube fittings, were utilized in the design of the damper. The steel hydraulic cylinder is a modified hydraulic actuator with a 3.08 cm (2 inch) bore and a maximum stroke of 15.24 cm (6 inches). The ends of the hydraulic cylinder are capped by two steel blocks that have standard SAE threaded ports. Inside of the hydraulic cylinder is a piston head connected to a piston rod. The piston head is encircled by lip seals that prevent fluid from flowing between the piston head and the interior wall of the hydraulic cylinder. The plastic end caps of the ER bypass use standard SAE threaded ports, so that they can be fitted to the hydraulic cylinder with standard tube fittings. The main element of the bypass is made from two concentric aluminum tubes that are held in place by the two plastic end caps, which retain O-rings seals used to prevent leakage of the fluid. The inner tube is 57.7 mm long and the outer tube has a diameter of 18.6 mm. The outer tube is 80.0 mm long and has an inner diameter such that the gap between the two tubes is 0.5 mm. These two aluminum tubes serve as the two electrodes by which electric field is applied to the ER fluid.

The damper operates by using the piston head to force ER fluid out of the hydraulic cylinder on one side, through the bypass, and back into the other side of the hydraulic cylinder. Pushed by the piston head, the ER fluid flows from one side of the hydraulic cylinder through the industrial tube fittings and enters the plastic cap. Inside the plastic caps, the fluid flow is split by an array of six diverging pipe channels that direct the fluid between the two concentric aluminum tubular electrodes that form the bypass. Upon exiting the ER bypass, the flow is recombined via a similar arrangement of six converging pipe channels in the opposite plastic end cap. The fluid returns to the hydraulic cylinder on the opposite side of the piston head via the opposite set of tube fittings. The damping force results from the pressure required for the piston head to push the ER fluid through the bypass.

EXPERIMENTAL SETUP

In this section, we present the experimental setup for the ER damper testing, including filling of the damper and testing of the damper using the damper dynamometer.

Damper Filling

Charging the damper with ER fluid is a key design and ex-

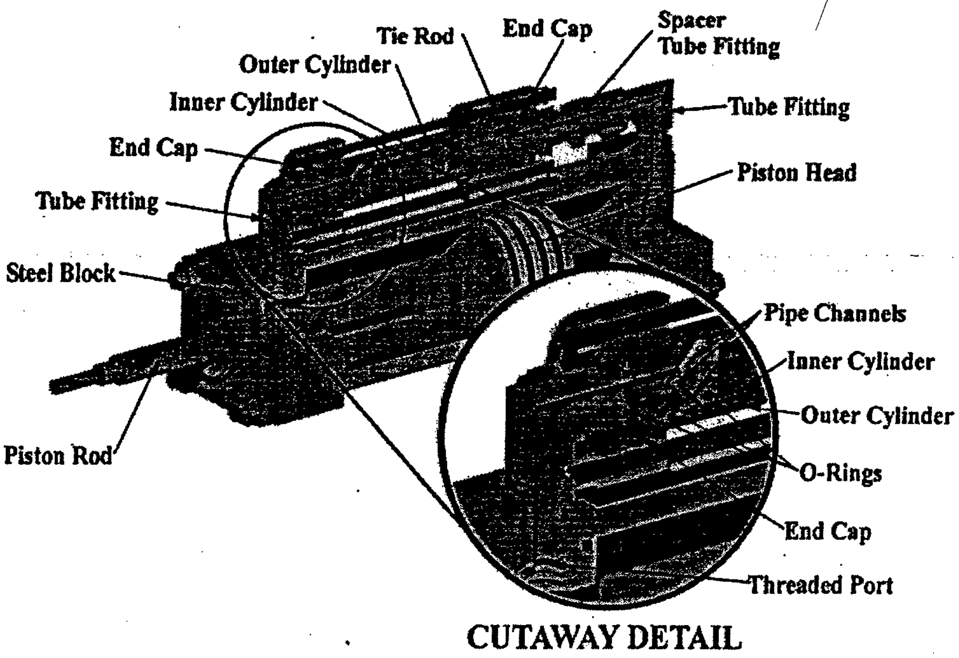

Figure 3. Solid model of the electrorheological damper with a cutaway detail showing how the fluid is channeled through the plastic caps into the electrode gap.

perimental issue. The damper is charged with ER fluid, Bayer Rheobay 3565. The ER fluid is highly viscous and cannot be easily poured into the device. Furthermore, trapping excess air in the hydraulic cylinder during the filling process creates a compliant air bubble and this should be minimized to successfully validate our Bingham plastic analysis. Also, no provision was made for an inert gas accumulator with which to pressurize the ER fluid and prevent cavitation in the design or the analysis. The piston rod volume in the hydraulic cylinder changes throughout the damper stroke and some air in the hydraulic cylinder was necessary to permit piston rod travel in and out of the hydraulic cylinder. Thus, a small necessary amount air was injected into the hydraulic cylinder for this purpose (Dixon, 1999). To control the excess air in the damper and to help fill the damper, a filling station was constructed. To prevent trapping excess air in the hydraulic cylinder, the filling station evacuates the air in the damper before the ER fluid is allowed to flow into the damper. In addition, evacuating the air from the damper supplies the pressure gradient needed to push the viscous ER fluid into the damper. The filling station consists of two polycarbonate plastic reservoirs that are 15.24 cm (6 inches) in diameter. To fill the damper, two polypropylene tubes with needle valves connect each reservoir to one end of the hydraulic cylinder. ER fluid is poured in one of the reservoirs and a vacuum pump removes the air from the other reservoir. Next, the needle valve between the hydraulic cylinder and evacuated reservoir is opened, evacuating the air from the damper. Then, the needle valve between the ER fluid filled reservoir and the hydraulic cylinder is opened, so that the ER fluid fills the damper. Some air in the damper is needed to allow for the change in piston rod volume in the hydraulic cylinder. This is controlled by moving the piston to the beginning of its stroke, and then allowing air to enter the hydraulic cylinder as the piston completes its stroke. The air bubble is maintained in the top of the hydraulic cylinder during testing by keeping the damper vertical, so that the air bubble does not travel through the ER valve (Dixon, 1999).

Damper Testing

For the experimental validation of the flow mode equations, force measurements from sinusoidal displacement cycles were recorded on a Roehrig Engineering 5 HP scotch yoke mechanical damper dynamometer at the University of Maryland. The damper dynamometer, shown in Figure 4 with the ER bypass damper mounted in the clevises, sinusoidally oscillates the shaft of the damper, measures the shaft displacement using an LVDT and measures the applied load using a 5000 lb load cell.

A matrix of tests for 5.08 cm (2 inches) of stroke, consisting of 320 different experimental conditions, was collected on the damper dynamometer for experimental validation of the quasi-steady flow mode damper analysis. The damper dynamometer proved to be a rapid and convenient testing instrument for damper testing under these numerous operating conditions. Oscillation frequency ranged from 0.03 to 0.63 Hz, in increments of nominally 0.03 Hz. The applied voltage ranged from 0.0 kV to 1.5 kV in increments of 0.1 kV. This translated to a range of electric field of 0 kV/mm to 3 kV/mm in increments 0.2 kV/mm because the gap was 0.5 mm. The electric field range was based on the ER fluid manufacturers' recommended maximum field of 4 kV/mm for shear mode testing, beyond which the ER fluid tends to experience dielectric breakdown. Above 3 kV/mm, the yield stress no longer increases substantially as a function of field, so that the damper properties begin to saturate. The operating frequency was varied, so that the model could be validated over a larger range of velocities, although the highest frequency tested was 0.63 Hz. It is desirable to use as low a velocity as possible, as long as the input signal is sinusoidal, in order to ascertain the applicability of the quasi-steady assumption as a function of frequency or damper shaft speed.

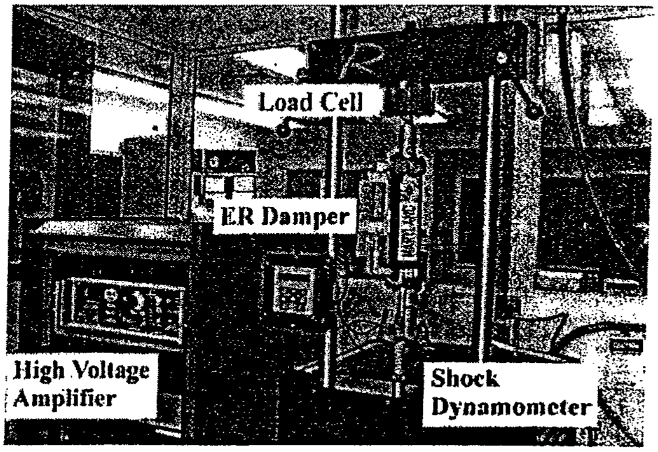

Figure 4. A mechanical scotch-yoke type damper dynamometer was used for ER bypass damper testing in the Smart Structures Laboratory of the Alfred Gessow Rotorcraft Center at the University of Maryland.

EXPERIMENTAL RESULTS

Effect of Electric Field and Shaft Frequency

In Figure 5, the experimental force vs. displacement hysteresis cycles are plotted. In Figure 5(a), these force vs. displacement hysteresis cycles are plotted as electric field increases in value. As the electric field increases the area within the hysteresis cycle increases, indicating that the damping or energy dissipated by the damper is also increasing. For zero field, 0 kV/mm, the force vs. displacement hysteresis cycle is nearly ellipsoidal, indicating that the behavior of the damper is nearly Newtonian, or linear, in nature. As the field increases up to a maximum of 3 kV/mm, the force vs. displacement characteristic becomes very rectangular, indicative of the nonlinear Coulomb-like behavior of ER fluids at full field. However, as shown in Figure 5(b), if the root mean square (RMS) velocity or frequency of the sinusoidal shaft excitation is increased, the force vs. displacement becomes more ellipsoidal, indicating that the damper behavior is be-

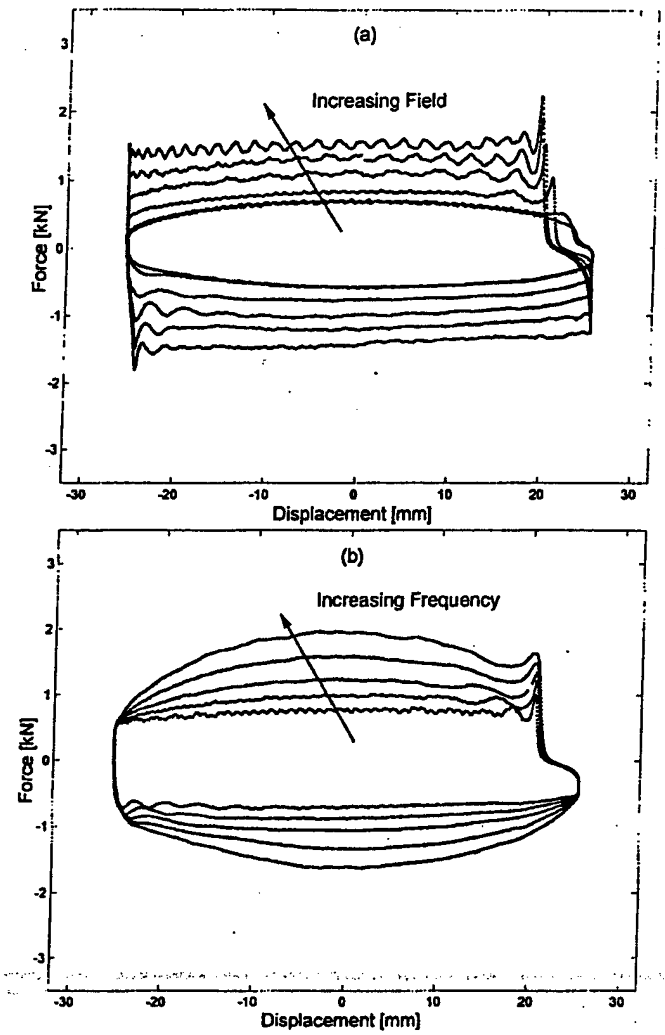

Figure 5. Typical force vs. displacement hysteresis cycle data measured using the damper dynamometer. (a) As the electric field increases, the area inside the hysteresis cycle, and hence the damping level, also increases. Shown are data for 0.22 Hz as electric field ranges from 0 to 3 kV/mm in increments of 0.6 kV/mm. (b) As the shaft velocity or frequency increases, the force vs. displacement hysteresis cycle diagram begins to resemble more Newtonian (ellipsoidal) than the Coulomb (rectangular) hysteresis cycle shape. Shown are data for applied electric field of 1.4 kV/mm as frequency ranges through 0.12, 0.25, 0.38, 0.50, and 0.63 Hz.

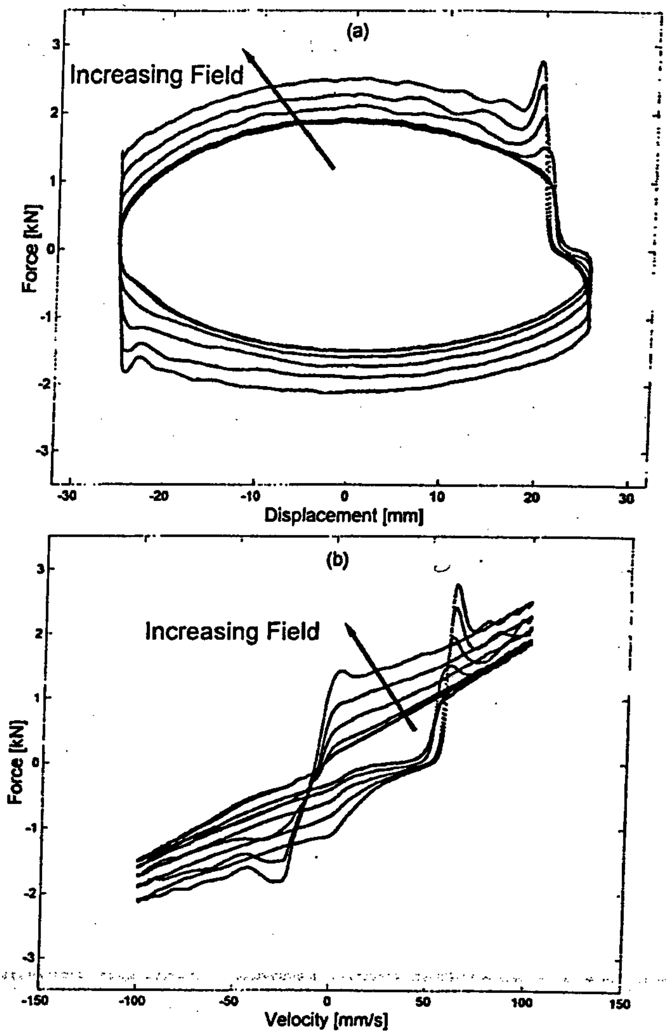

Figure 6. Typical force vs. displacement and force vs. velocity hysteresis cycle data measured using the damper dynamometer. Data is shown for $\Omega = 0.63$ Hz, and is plotted for applied electric field of 0 kV/mm, 0.6 kV/mm, 1.2 kV/mm, 1.8 kV/mm, 2.4 kV/mm and 3.0 kV/mm. (a) As electric field increases, the area inside the hysteresis cycle, and hence the damping also increases. (b) As the electric field increases, the yield force also increases, which is directly related to the dynamic yield stress property of the ER fluid.

coming more linear or Newtonian, although the behavior still remains quite nonlinear.

Nonlinear Damper Response

In Figure 6, the force vs. displacement and force vs. velocity are plotted for a 2 inch stroke, for electric field values of 0 kV/mm, 0.6 kV/mm, 1.2 kV/mm, 1.8 kV/mm, 2.4 kV/mm and 3.0 kV/mm. These data are shown for a frequency of oscillation of 0.63 Hz. As the electric field increases, the area enclosed by the force vs. displacement hysteresis cycle, shown Figure 6(a), also increases implying that both the damping and energy dissipation over a single cycle also increase. As the electric field increases, the Coulomb-like damping behavior tends to be accentuated, as evidenced by the change from a near-ellipsoidal force vs. displacement characteristic, to one that is more rectangular in nature. The force vs. velocity behavior, shown in Figure 6(b), is reminiscent of Bingham-plastic shear flow as expected, and the presence of the compliant air bubble in the hydraulic cylinder damper is manifested by the force impulses at intermediate to high positive shaft velocities (greater than 50 mm/s) as the air bubble is fully compressed. A smaller less significant force impulse can be seen in the force vs. velocity diagram for negative velocities.

Energy Dissipation and Damping

Equivalent linearization is a standard linearization technique that can be applied to a nonlinear damper such as this

ER damper. The damper restoring force, $f(t)$, is proportional to the damper shaft velocity, $v(t)$, as

$$f(t) = C_{eq} v(t) \tag{38}$$

where C_{eq} is the equivalent viscous damping.

The equivalent viscous damping, C_{eq}, is computed by equating the energy dissipated over a cycle, E, at frequency Ω using

$$E = \oint F(t)dx = \int_0^{2\pi/\Omega} F(t)v(t)dt \tag{39}$$

and equating the dissipated energy of the nonlinear device to that of an equivalent viscous damper

$$C_{eq} = \frac{E}{\pi \Omega X_0^2} \tag{40}$$

where Ω is the sinusoidal test frequency, and X_0 is the sinusoidal displacement input amplitude. The energy dissipated over one cycle is computed using a Riemann sum. We calculated equivalent viscous damping using the measured force vs. displacement hysteresis data, and the results are shown in Figure 7. However, this approach to characterizing the damper linearizes the damper to be an ideal dashpot at every operating condition, so that C_{eq} is a function of both the applied electric field, E, and the frequency.

Complex Stiffness

A second approach is to characterize the complex damper stiffness, K^*, as the in-phase or storage stiffness, K', and quadrature or loss stiffness, K'', so that

$$K^* = K' + jK'' = K'(1 + j\eta) \tag{41}$$

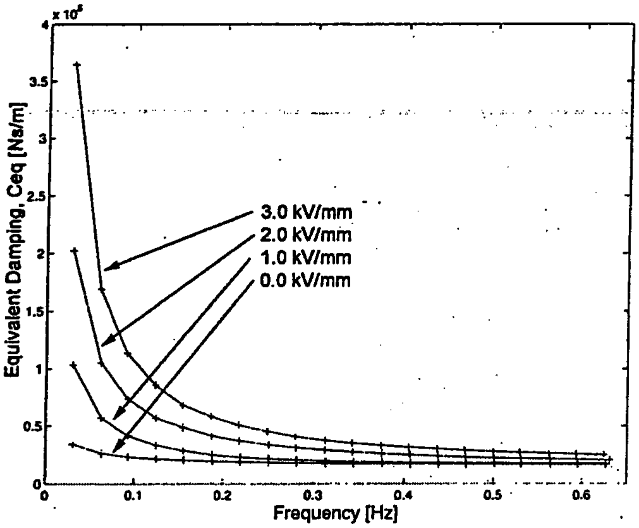

Figure 7. *The equivalent viscous damping of the electrorheological bypass damper is plotted vs. frequency.*

where η is the loss factor. This is a common approach in the characterization of elastomeric dampers (Kamath, Wereley and Jolly, 1999; Felker et al., 1987; McGuire, 1994; Panda et al., 1996; Kunz, 1997). Alternatively, K' is the effective or equivalent stiffness, while K'' is related to the equivalent viscous damping in an approximate way by

$$C_{eq} \approx \frac{K''}{\Omega} \tag{42}$$

The relation is approximate because the complex stiffness considers only the harmonic at frequency Ω as will be shown below. To determine the damper force,

$$f(t) = F_{1c} \cos \Omega t + F_{1s} \sin \Omega t = K'x(t) + \frac{K''}{\Omega} v(t) \tag{43}$$

Here F_{1c} and F_{1s} are the cosine and sine Fourier coefficients of $f(t)$ at frequency Ω. We assume that the displacement is sinusoidal

$$x(t) = X_{1c} \cos \Omega t + X_{1s} \sin \Omega t \tag{44}$$

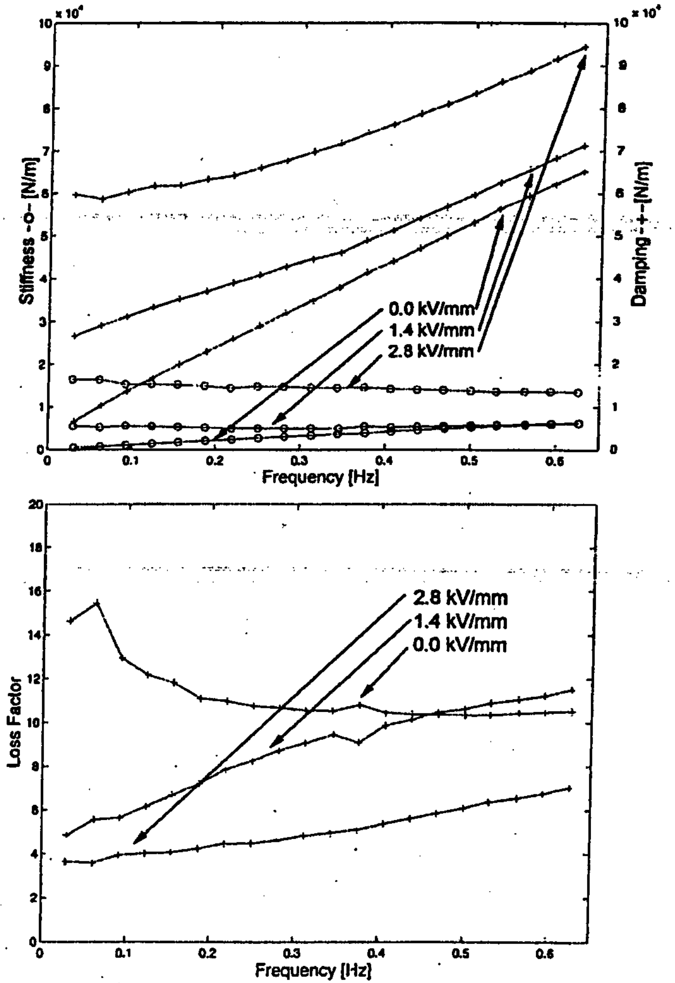

Figure 8. *The complex stiffness, or the stiffness and damping, and the loss factor of the ER damper are plotted vs. frequency.*

where X_{1c} and X_{1s} are the cosine and sine Fourier coefficients of $x(t)$ at frequency Ω. Substituting $x(t)$ into the force equation and equating the sine and cosine terms, yields the in-phase and quadrature stiffnesses as

$$K' = \frac{F_{1c}X_{1c} + F_{1s}X_{1s}}{X_{1c}^2 + X_{1s}^2}$$
$$K'' = \frac{F_{1c}X_{1s} - F_{1s}X_{1c}}{X_{1c}^2 + X_{1s}^2} \tag{45}$$

In general, this calculation would be performed for a sweep in the oscillation frequency, Ω.

The results for such a complex stiffness calculation is plotted versus frequency in Figure 8 for the ER damper. The linearized perspective is not convenient because this approach characterizes the damper behavior as a simple viscoelastic element at every operating condition, so that K' and K'' are a function of both the applied electric field, E, and the frequency. These results reflect the same trends as the equivalent viscous damping calculations above.

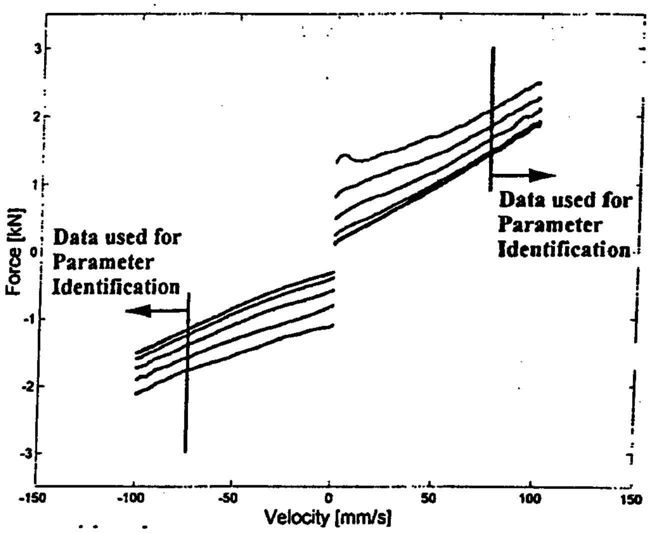

Figure 9. The force vs. velocity hysteresis diagrams, shown for a frequency of $\Omega = 0.63$ Hz, has been truncated to include only those data corresponding to operating conditions where the damper shaft is decelerating in order to eliminate the compliant air bubble effects from the Bingham plastic analysis.

PARAMETER IDENTIFICATION

The two critically important material properties used in developing the nondimensional analysis are the plastic viscosity, μ, and dynamic yield stress, τ_y. Both material properties can be functions of electric field. In Figure 9, the force vs. velocity behavior is plotted for the same conditions shown in Figure 6, however, the data is plotted only for decelerating damper shaft motion. The data clearly show that the damper behavior may be approximated by the Bingham-plastic model. If the high velocity (i.e., v greater than 75 mm/s), force vs. velocity linear asymptote is projected back to the force axis, its intercept with the force axis determines the value of the yield force, F_y, from which the dynamic yield stress, τ_y, can be determined. The slope of this linear asymptote provides the post-yield damping, C_{po}, from which the plastic viscosity may be determined.

The Bingham plastic model results from adding a yield force to a linear viscous damping model. This shear flow mechanism was used to develop predictive models assuming both parallel plate geometry (Lou et al., 1993b; Makris et al., 1996; Wereley and Pang, 1998) or axisymmetric geometry (Kamath et al., 1996; Gavin et al., 1996a–b). Yield force, F_y, and postyield damping, C_{po}, are included in the model.

$$f(t) = \begin{cases} C_{po}v + F_y & v > 0 \\ -F_y < f(t) < F_y & v = 0 \\ C_{po}v - F_y & v < 0 \end{cases} \tag{46}$$

Here, v is the shaft velocity. The damper model assumes that in the preyield condition, the ER fluid is rigid and does not flow, hence, when $|f(t)| < F_y$ the shaft velocity, $v = 0$. Once the force applied to the damper exceeds the yield force, then the fluid begins to flow, and the material is essentially a Newtonian fluid with a non-zero yield stress.

Clearly, from Figure 9, the force vs. velocity response is not symmetric. For shaft inward motion, the piston head area is given by A_p, whereas during outward shaft motion, the piston head area is given by $A_p - A_s$, where A_s is the damper shaft cross-sectional area. A parameter identification was developed to produce estimates of the yield force for shaft inward, F_y^i, and shaft outward motion, F_y^o, and postyield damping for both shaft inward, C_{po}^i, and shaft outward motion, C_{po}^o, separately.

These parameters of Bingham plastic model, C_{po}^i, C_{po}^o, F_y^i, and F_y^o were identified as a function of applied electric field, using a constrained least mean squared (LMS) error minimization procedure using MATLAB subroutines. A cost function, J, was defined as

$$J(C_{po}^i, C_{po}^o, F_y^i, F_y^o) = \sum_{k=1}^{N} [f(t_k) - \hat{f}(t_k)]^2 \tag{47}$$

where $\hat{f}(t_k)$ is the force calculated using the equations of the nonlinear Bingham-plastic model in Equation (46), $f(t_k)$ is the measured force, and t_k is the time at which the kth sample was taken. The parameters of C_{po}^i, C_{po}^o, F_y^i, and F_y^o are estimated so as to minimize the cost function, J, and are constrained to be greater than zero. Force vs. velocity data corresponding only to decelerating phase of the damper shaft motion is included in the optimizer for shaft speeds greater than 75 mm/s, as shown in Figure 9.

In this constitutive model, the yield force, F_y, is obtained from the postyield force vs. velocity asymptote intercept with the force axis. Recall that the dynamic yield stress is given by

$$\tau_y = \frac{\bar{\delta} F d}{2 A_p L} \tag{48}$$

At the yield point, the force applied to the damper is the yield force, F_y, and the plug fills the annulus, so that $\bar{\delta} = 1$. From Equation (48), the yield stress can then be estimated as

$$\tau_y = \frac{F_y^i d}{2 A_p L} \quad \text{or} \quad \tau_y = \frac{F_y^o d}{2(A_p - A_s)L} \tag{49}$$

The post yield damping, C_{po} is given by the slope of the high velocity asymptote. Recall that the Newtonian damping is given by

$$C = \mu \frac{12 A_p^2 L}{A_d d^2} \tag{50}$$

Recognizing that for non-zero electric field, the above damping constant is the postyield damping, C_{po}, leads to an estimate of the plastic viscosity,

$$\mu = \frac{A_d d^2}{12 A_p^2 L} C_{po}^i \quad \text{or} \quad \mu = \frac{A_d d^2}{12(A_p - A_s)^2 L} C_{po}^o \tag{51}$$

The results of the parameter identification procedures are shown in Figure 10. The dynamic yield stress calculations are shown on the top as symbols in Figure 10(a), and a second order polynomial function is fitted to these data. In addition, the manufacturer quotes only the high electric field linear asymptote, and its intercept with the electric field axis for zero yield stress, as a function of temperature (Bayer, 1997). These lines are plotted as dashed lines in Figure 10(a). The quadratic function fitted to the identified parameters falls between the asymptotes for 40 and 20°C. Given that the damper was tested at ambient room temperature for relatively low speeds, and the damper model developed above does not account for built up damper effects such as dynamic shaft and piston seals, the dynamic yield stress function identified by this procedure is reasonably accurate.

The viscosity of the ER fluid can vary substantially based on the volume fraction of carrier fluid. The manufacturer quoted nominal plastic viscosity values of $\mu = 73$ mPa s at 20°C and $\mu = 55$ mPa s at 40°C for its Rheobay 3565 product (Bayer, 1997). In Figure 10(b), the plastic viscosity identified by the parameter identification techniques is nearly constant. The mean value of plastic viscosity estimates was $\mu = 43$ mPa s, which is used in the remainder of the paper.

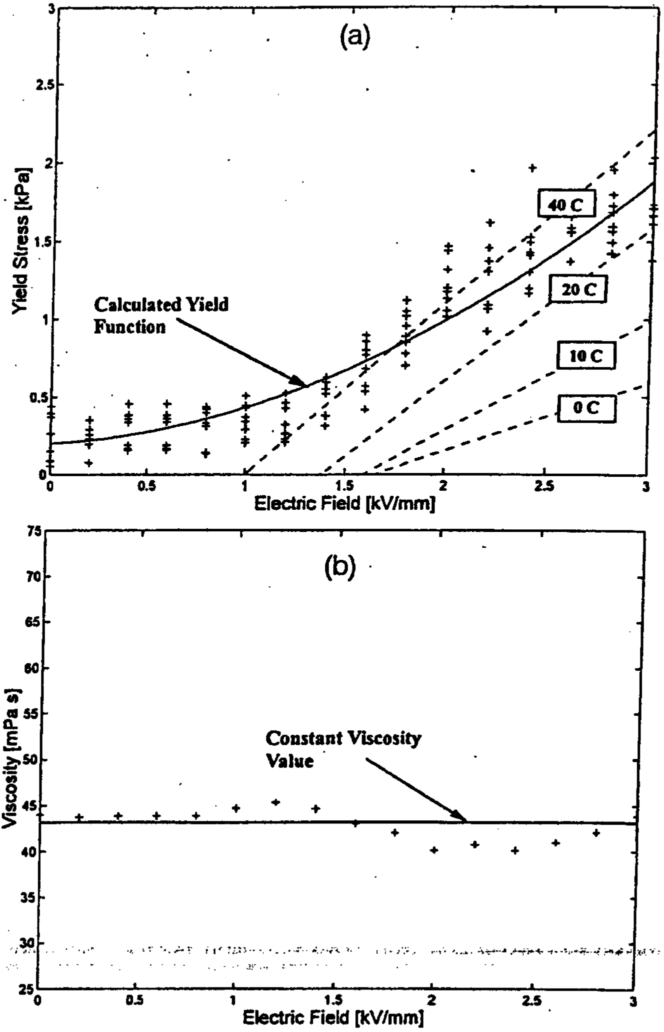

Figure 10. *The required properties of the yield stress, $\tau_y(E)$, and the plastic viscosity, $\mu(E)$, are shown as a function of electric field. The plastic viscosity was assumed to be a constant value, $\mu = 43$ mPa s, which is the mean value of the estimates shown here.*

ANALYSIS RESULTS

Damping Coefficient vs. Nondimensional Plug Thickness

Using the material properties of dynamic yield stress as a function of electric field, $\tau_y(E)$ and plastic viscosity, μ, we can construct the damping coefficient, C_{eq}/C vs. non-dimensional plug thickness, $\bar{\delta}$, diagram. For each of the 320 operating conditions tested in this study, the RMS velocity, v_p, was determined from the measured sinusoidal velocity, $v(t)$. The RMS shaft velocity was used in place of the constant shaft velocity, v_0, in our analysis. The Bingham number, Bi, was then calculated. The nondimensional plug thickness was determined by numerically solving for the roots of the polynomial

$$\frac{1}{2}\bar{\delta}^3 - \left[\frac{3}{2} + \frac{6}{\text{Bi}}\right]\bar{\delta} + 1 = 0 \qquad (52)$$

and selecting the feasible root, or $0 \le \bar{\delta} \le 1$. The Newtonian damping. constant, C, is calculated for each operating condition, which is then used to normalize the corresponding measured equivalent viscous damping, C_{eq}, to obtain the damping coefficient for each operating condition, C_{eq}/C. The equivalent viscous damping was calculated using

$$C_{eq} = \frac{1}{\pi \Omega X_0^2} \int_0^{2\pi/\Omega} F(t)v(t)dt \qquad (53)$$

The measured damping coefficient is plotted vs. the nondimensional plug thickness as symbols in Figure 11. The quasi-steady analysis result is shown as a solid line. The analysis correlates well with experiment.

Effect of Frequency or Damper Shaft Speed

To explain the trend of decreasing dynamic range of damping coefficient as frequency increases, the force vs. displacement hysteresis diagrams are shown in Figure 12 for four frequencies of damper shaft oscillation: 0.06 Hz, 0.25 Hz, 0.44 Hz and 0.63 Hz. For clarity, only the electric field conditions of OFF (0 kV/mm) and ON (3.0 kV/mm) are shown in the force vs. displacement hysteresis cycle diagrams.

For the lowest speed case or an oscillation frequency of 0.03 Hz, the force increases dramatically from the OFF to the ON condition. The damper has a large dynamic range for both force and damping coefficient. The damping coefficient is 22.2 for the ON condition at $\Omega = 0.03$ Hz. For the frequency of 0.06 Hz shown in Figure 12, the damping coefficient is 10.3. For these low speed operating conditions, the damper is operating closest to the yield condition and has the highest dynamic range or damping coefficient. For the high speed case or an oscillation frequency of 0.63 Hz, the force vs. displacement hysteresis cycles are shown in Figure 12. The difference in energy dissipation between the OFF and ON conditions, represented by the area enclosed by the force vs. displacement hysteresis cycle, is reduced from the lowest speed case. The dynamic range for this operating condition is 1.54. Due to the small dynamic range, this device is a relatively poor semi-active damper at 0.63 Hz compared to the lower frequencies tested. Finally, the damper performance at the mid range frequencies of oscillation, 0.44 Hz demonstrates the performance of this device for moderate speed or frequency. The force vs. displacement diagram is shown in Figure 12. The force in the full field or ON condition is more than two times that of the OFF condition. For a frequency of operation of 0.44 Hz, the maximum damping coefficient, C_{eq}/C, is 1.85. For a frequency of operation of 0.25 Hz, the maximum damping coefficient, C_{eq}/C, is 2.76 demonstrating moderate dynamic range at moderate frequencies.

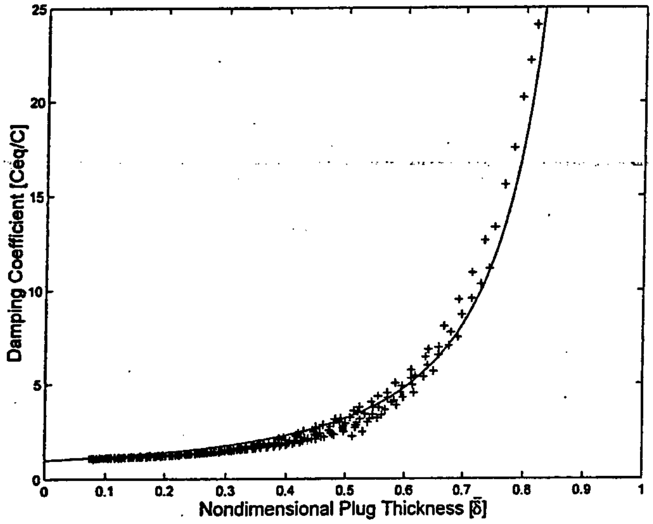

Figure 11. The damping coefficient, C_{eq}/C, is plotted vs. the nondimensional plug thickness for the 320 test conditions examined in this paper. The experimental results agree well with the quasi-steady analysis, shown as a solid line.

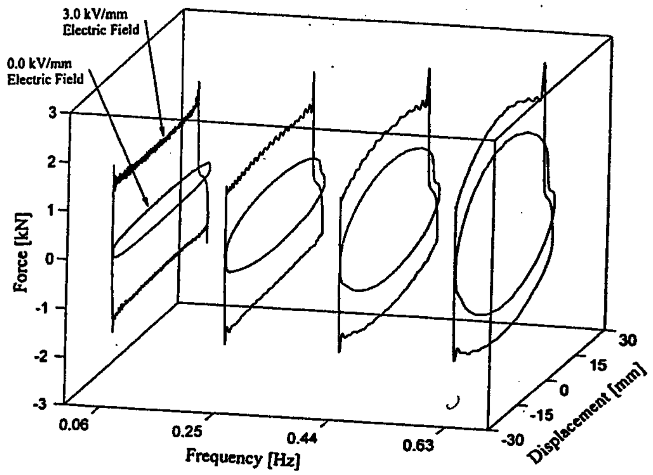

Figure 12. Force vs. displacement hysteresis diagrams at four frequencies of damper shaft oscillation: 0.06 Hz, 0.25 Hz, 0.44 Hz and 0.63 Hz. For clarity, only the electric field conditions of OFF (0 kV/mm) and ON (3 kV/mm) are shown in the force vs. displacement hysteresis cycle diagram.

Limitations of the Analysis

The analysis presented above is of limited scope, but was shown to be useful in the design of ER dampers. The analysis does not account for numerous effects that might manifest themselves in a fabricated damper. Some of these limitations are described below:

1. The analysis assumes constant or quasi-steady loading and fully developed flow. The analysis neglects fluid mass. This may be an important factor in MR fluid applications, where the specific gravity is substantially higher than that of ER fluids. This increased specific gravity

would reduce the range of frequencies over which the quasi-steady assumption is valid.

2. The damper used to experimentally validate the analysis described in this paper has only a single acting piston rod, so that the piston rod volume inside the damper varies throughout the stroke. Although our analysis neglects the resulting compressibility effects that result from this changing rod volume, this spring effect does not affect the prediction of the damping coefficient, C_{eq}/C.
3. Contributions of piston rod seals, piston head rings, and sources of friction and damping present in the damper other than the controllable fluid effects, are neglected. The overall force levels are sufficiently high that these parasitic damping effects are small relative to the controllable damping effects.
4. Dampers are often pressurized to avoid cavitation effects (Dixon, 1999). Pressurization tends to squeeze out adsorbed gas in the fluid, resulting in a small increase in the yield stress of the fluid at a given field level. The pressurization is typically set at a fixed or static pressure. Thus, the parameter identification procedures outlined in this paper can easily account for quasi-steady variations in yield stress and plastic viscosity as a function of quasi-steady variations in temperature.
5. ER fluids tend to experience changes in properties as temperature varies, however, these temperature effects are neglected in the model. Since the dependence of these material properties on temperature can be measured, this analysis can be applied to quasi-steady temperature variations.

In spite of these limitations, this analysis predominantly accounts for the ER damper behavior over the range of electric field, stroke and quasi-steady frequency experimentally tested in this paper.

CONCLUSIONS

Approximate parallel plate analysis of an ER flow mode damper was presented based on well known prior work by Phillips (1969). The approximate parallel plate analysis was modified to emphasize the central role that the nondimensional plug thickness plays in determination of the equivalent viscous damping levels in an ER fluid damper. To validate this analysis, an ER bypass damper was designed, fabricated, and tested on a damper dynamometer. A preliminary experimental validation of the damping coefficient vs. nondimensional plug thickness analysis was presented using low frequency hysteresis cycle data. Based on this work, the following conclusions can be drawn:

1. For the flow mode damper, the nondimensional damping coefficient, C_{eq}/C, is a function of only the nondimensional plug thickness, $\bar{\delta}$.
2. The feasibility of designing ER dampers using a Bingham plastic analysis was demonstrated using the simple relationship between the damping coefficient, C_{eq}/C and the nondimensional plug thickness, $\bar{\delta}$.
3. The dynamic yield stress, τ_y, was shown to be an increasing quadratic function of increasing electric field for the Rheobay ER fluid used in this study. In addition, the plastic viscosity was shown to be nearly constant as a function of electric field.
4. The damping coefficient, C_{eq}/C, vs. nondimensional plug thickness, $\bar{\delta}$ diagram determined via analysis correlated with experimental data. The C_{eq}/C vs. diagram measures if an ER damper will provided an adequate dynamic range of forces and energy dissipation for a given operating frequency range. This diagram can also show if the damper is operating in essentially the Newtonian or passive condition, that is, $C_{eq}/C \approx 1$.
5. Although the Bingham plastic model does not precisely describe the force vs. velocity hysteresis cycle, it was shown to be an excellent predictor of energy dissipation over a cycle.

Thus, the analysis presented here is useful in designing ER flow mode dampers in order to meet a specification of damping performance.

NOMENCLATURE

b = Inner electrode circumference ($b = 2\pi R_1$)
d = Electrode gap
$u(y)$ = Velocity profile
v_d = Mean RMS flow velocity in annulus
v_0 = Constant (quasi-steady) shaft velocity
v_p = RMS shaft velocity
y = Radial coordinate referenced to inner electrode of bypass
y_{pi} = Inner location of plug
y_{po} = Outer location of plug
A_d = Cross sectional area of annulus ($A_d = b_d$)
A_p = Cross sectional area of piston head
A_s = Cross sectional area of shaft
Bi = Bingham number (non-dimensional)
C = Viscous damping (Newtonian)
C_{eq} = Equivalent viscous damping (Bingham-plastic)
E = Electric field
F = Force applied to damper shaft
L = Wetted inner electrode length
Q = Total volume flux through annulus
Q_1 = Volume flux in region 1 of gap where $\tau > \tau_y$
Q_2 = Volume flux in region 2 of gap where $\tau < \tau_y$
Q_3 = Volume flux in region 3 of gap where $\tau > \tau_y$
Q_p = Volume flux due to piston motion
δ = Plug thickness
$\bar{\delta}$ = Ratio of plug thickness to gap
μ = Plastic viscosity
τ = Shear stress
τ_y = Dynamic yield shear stress

ACKNOWLEDGMENT

Research supported under a grant by the U.S. Army Research Office Young Investigator Program, contract no. 38856-EG-YIP (Dr. Gary Anderson, technical monitor). Laboratory equipment support was provided under a grant by the FY96 Defense University Research Instrumentation Program (DURIP), contract no. DAAH-0496-10301 (Dr. Gary Anderson, technical monitor). We also thank Bayer AFG (Dr. Eckhard Wendt) for providing the electrorheological fluid used in this study. Mr. Lindler was supported in part by an ASPIRE undergraduate research fellowship from the Engineering Research Center at the University of Maryland.

REFERENCES

Atkin, R. J., Shi, X., and Bullough, W. A. (1991). "Solutions of the Constitutive Equations for the Flow of an Electrorheological Fluid in Radial Configurations," *Journal of Rheology,* Vol. 35, No. 7, pp. 1441–1461.

Bayer AFG (1997). "Rheobay Electrorheological Fluid: Provisional Product Information."

Brooks, D. A. (1992). "Design and Development of Flow Based Electro-Rheological Devices," *InternationalJournal of Modern Physics B.* Vol. 6, pp. 2705–2730.

Dixon, J. C. (1999). *Shock Absorber Handbook.* Society of Automotive Engineers, Warrendale, PA.

Duclos, T. G. (1988). "Design of Devices Using Electrorheological Fluids." *Society of Automotive Engineers,* Paper 881134, pp. 2.532–2.536.

Ervin, R. D., Lou, Z., Filisko, F. E., and Winkler, C. B. (1996). "Electrorheology for Smart Landing Gear," NASA-CR2000883 (N96-25313), 30 April.

Felker, F. F., Lau, B. H., McLaughlin, S. and Johnson, W. (1987). "Nonlinear Behavior of an Elastomeric Lag Damper Undergoing Dual-Frequency Motion and its Effect on Rotor Dynamics," *Journal of the American Helicopter Society,* Vol. 32, No. 4, 1987, pp. 45–53.

Gavin, H. P., Hanson, R. D., and Filisko, F. E. (1996a). "Electrorheological Dampers, Part I: Analysis and Design," *ASME Journal of Applied Mechanics,* Vol. 63, Sept., pp. 669–675.

Gavin, H. P., Hanson, R. D., and Filisko, F. E. (1996b). "Electrorheological Dampers, Part II: Testing and Modeling," *ASME Journal of Applied Mechanics,* Vol. 63, Sept., pp. 676–682.

Kamath, G.M., Hurt, M. K., and Wereley, N. M. (1996). "Analysis and Testing of Bingham Plastic Behavior in Semi-Active Electrorheological Fluid Dampers," *Smart Materials and Structures,* Vol. 5, No. 5, pp. 576–590.

Kamath, G. M., and Wereley, N. M. (1997a). "A Nonlinear Viscoelastic-Plastic Model for Electrorheological Fluids," *Smart Materials and Structures,* Vol. 6, No. 3, 1997, pp. 351–358.

Kamath, G. M., and N. M. Wereley (1997b). "Modeling the Damping Mechanism in Electrorheological Fluid Based Dampers," *M3DIII: Mechanics and Mechanisms of Material Damping,* edited by V. K. Kinra and A. Wolfenden, American Society for Testing and Materials, pp. 331–348 (STP1304).

Kamath, G. M., and Wereley, N. M. (1997c). "Nonlinear Viscoelastic-Plastic Mechanisms-Based Model of an Electrorheological Damper," *AIAA J. Guidance, Control, and Dynamics,* Vol. 20, No. 6, 1997, pp. 1225–1332.

Kamath, G. M., Wereley, N. M. and Jolly, M. R. (1999). "Characterization of Magnetorheological Helicopter Lag Dampers," *Journal of the American Helicopter Society,* Vol. 44, No. 3, pp. 234–248.

Kunz, D. L. (1997). "Influence of Elastomeric Damper Modeling on the Dynamic Response of Helicopter Rotors," *AIAA Journal,* Vol. 35, No. 2, February, pp. 349–354.

Leek, T. H., Lingard, S., Bullough, W. A., and Atkin, R. J. (1994a). "Hydrodynamic Pressure Generation With an Electrorheological Fluid—Part I Unexcited Fluid," *Electrorheological Fluids. Mechanisms, Properties, Technology and Applications,* World Scientific, New Jersey, pp. 609–624.

Leek, T. H., Lingard, S., Bullough, W. A., and Atkin, R. J. (1994b). "Hydrodynamic Pressure Generation With an Electrorheological Fluid— Part II Excited Fluid," *Electrorheological Fluids: Mechanisms, Properties, Technology and Applications,* World Scientific, New Jersey, pp. 625–642.

Lou, Z., Ervin, R. D., Filisko, F. E., and Winkler, C. B. (1993a). "An Electrorheologically Controlled Semi-Active Landing Gear," SAE publication 93-1403.

Lou, Z., R. D. Ervin, and F. E. Filisko (1993b). "A Preliminary Parametric Study of Electrorheological Dampers," *Electro-Rheological Flows,* ASME, FED-Vol. 164, 1993, pp. 143–156.

Makris, N., Burton, S. A., Hill, D., and Jordan, M. (1996). "Analysis and Design of ER Damper for Seismic Protection of Structures," *Journal of Engineering Mechanics,* Vol. 122, No. 10, pp. 1003–1011.

McGuire, D. P. (1994). "Fluidlastic Dampers and Isolators for Vibration Control in Helicopters," Presented at the 50th Annual Forum of American Helicopter Society, Washington D.C., May 1994.

Panda B., and Mychalowycz, E. (1996). "Aeroelastic Stability Wind Tunnel Testing with Analytical Correlation of the Comanche Bearingless Main Rotor," Presented at the 52nd Annual Forum of American Helicopter Society, Washington D.C., June.

Peel, D. J. and Bullough, W. A. (1994). "Bingham Plastic Analysis of ER Valve Flow," *Electrorheological Fluids: Mechanisms, Properties, Technology and Applications,* World Scientific, New Jersey, pp. 538–567.

Phillips, R. W. (1969). *Engineering Applications of Fluids with a Variable Yield Stress,* Ph.D. Thesis, Mechanical Engineering, U. California at Berkeley.

Prager, W. (1961). *Introduction to Mechanics of Continua,* Ginn and Company, New York.

Stanway, R., Sproston, J. L., and El-Wahed, A. K. (1996). "Application of Electrorheological Fluids in Vibration Control: A Survey," *Smart Materials and Structures,* Vol. 5, No.4, 1996, pp. 464–482.

Wereley, N. M., and Pang, Li (1998). "Nondimensional Analysis of Semi-Active Electrorheological and Magnetorheological Dampers Using Approximate Parallel Plate Models," *Smart Materials and Structures,* Vol. 7, No. 5, pp. 732–743.

Double Adjustable Shock Absorbers Using Electrorheological Fluid

J. E. LINDLER AND N. M. WERELEY*

Smart Structures Laboratory, Dept. of Aerospace Engineering, University of Maryland, College Park, MD 20742

ABSTRACT: Double adjustable shock absorbers allow for adjustment of their yield force and post-yield damping. To emulate the performance of a conventional double adjustable shock absorber, an electrorheological (ER) automotive shock absorber was designed and fabricated at the University of Maryland. An applied electric field between two tubular electrodes, located in the piston head, increases the force required for a given piston rod velocity. Two different shaped gaps between the electrodes, meet the controllable performance requirements of a double adjustable shock. A uniform gap primarily adjust the yield force of the shock absorber, as opposed to a non-uniform gap which allow for control of the post-yield damping. Force measurements from sinusoidal displacement cycles, recorded on a 5 HP mechanical dynamometer, validate the performance of uniform and non-uniform gaps for yield force and post-yield damping adjustments.

INTRODUCTION

To adjust for optimal performance, mechanisms on the main piston head and in the pneumatic reservoir independently control the yield force and damping of double adjustable shocks. However, manual adjustment of the shock requires time consuming disassembly of the device. In contrast, electrorheological fluids (ER), with an electric field dependent yield stress, can vary the amount of damping without disassembly of the device [1,2,3]. To emulate the performance of a conventional double adjustable shock absorber, an electrorheological (ER) automotive shock absorber was designed and fabricated at the University of Maryland. During piston rod motion, ER fluid flows through the piston head in a gap between tubular electrodes. An applied electric field in the gap increases the yield stress, $\tau_y(E)$, of the ER fluid between the electrodes. The yield stress alters the velocity profile of the fluid and raises the pressure required for a given flow rate. Different electrode configurations are developed and modeled to control the shock's yield force and post-yield damping. Force measurements from sinusoidal displacement cycles, recorded on a 5 HP mechanical dynamometer, validate the performance of uniform and non-uniform gaps for yield force and post-yield damping adjustment without disassembly of the damper.

DOUBLE ADJUSTABLE SHOCK ABSORBER

Due to its adjustable performance, an 8100 series Penske double adjustable shock represents the baseline design criterion for the performance of a semiactive automotive shock absorber. The force vs. velocity cycles of many automotive shocks may be separated into four distinct regions: low-speed compression, high-speed compression, low-speed rebound and high-speed rebound. A unique damping constant characterizes each region, and a distinct yield force divides the low and high-speed regions [4] (Figure 1).

The Penske damper consists of a main hydraulic cylinder connected to a remote pneumatic reservoir via a hydraulic hose. The main hydraulic cylinder contains a piston head assembly, piston rod and conventional hydraulic fluid. The remote pneumatic reservoir contains a floating piston that separates compressed nitrogen from the hydraulic fluid. Mechanisms on the main piston head, and in the pneumatic reservoir, allow for independent control of the shock absorber's yield force and damping during the compression and rebound strokes.

A typical cycle of the Penske damper begins with low-speed compression of the piston rod, during which fluid flows through small orifices in the piston head. In addition, the increasing rod volume within the damper body forces an equal volume of fluid through an orifice into the pneumatic reservoir. Changing the orifice size in the pneumatic reservoir controls the compression damping [Figure 2(a)]. As compression speed increases, fluid pressure on the compression valve stack increases. Each valve stack consists of a series of steel shims that collectively act as a preloaded spring [Figure 2(b)]. As a result, high fluid pressure causes the valve stack to snap open, which allows fluid to flow directly through large ports in the piston head. This parallel flow greatly decreases the damping during high-speed compression. Changing the thickness of the shims alters the critical pressure required to open the valve stack and therefore adjusts the yield force of the shock absorber.

---

*Author to whom correspondence should be addressed. E-mail: wereley@eng.umd.edu

1045-389X/99/08 0652-06 $10.00/0 DOI: 10.1106/468R-DHQM-076W-MAF6
© 2000 Technomic Publishing Co., Inc.

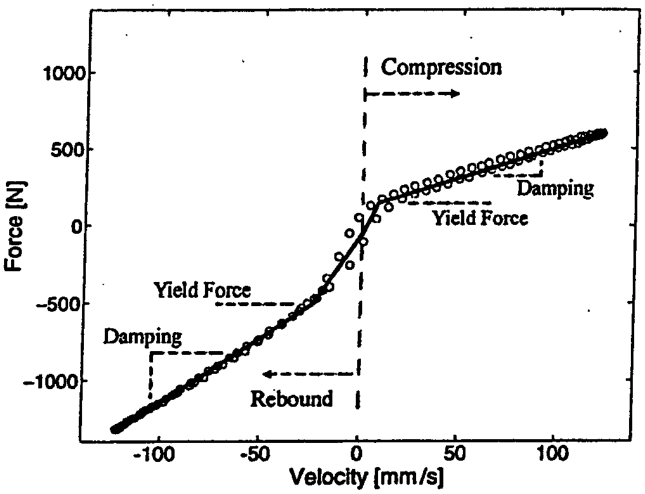

Figure 1. Typical force versus velocity response of a double adjustable shock absorber due to sinusoidal excitation.

During the rebound stroke, fluid bypasses the piston head through a needle and jet valve in the piston rod [Figure 2(b)]. The location of the jet determines the rebound damping. Similar to high compression speeds, at high rebound speeds the fluid pressure yields the rebound valve stack which allows fluid to easily pass through the piston head.

ER FLUID BEHAVIOR

Electrorheological fluids (ER) are normally composed of non-conducting particles dispersed in a carrier fluid. In the presence of an electric field, the particles become polarized and orient themselves as particle chains (Figure 3).

The particle chains induce a yield stress in the fluid which results in a Bingham plastic behavior during shear (Figure 4). The process is completely reversible and removing the field disperses the particles back into the disordered state. Due to their field dependent yield stress, ER fluids are a possible replacement for variable damping systems using mechanical valves.

In the case of Newtonian flow, the shear stress is proportional to the shear rate.

$$\tau = \mu \frac{du}{dy} \tag{1}$$

For a Bingham plastic, a dynamic yield stress characterizes the material. In the pre-yield condition, no shearing occurs because the local shear stress, τ, is less than the fluid's yield stress, $\tau_y(E)$. When the shear stress exceeds the yield stress, the material flows like a Newtonian fluid.

$$\tau = \tau_y(E)\ \mathrm{sgn}\left(\frac{du}{dy}\right) + \mu \frac{du}{dy} \tag{2}$$

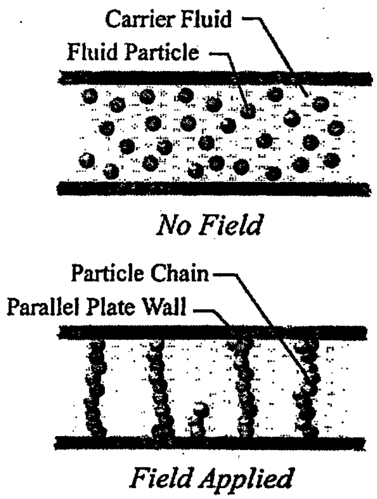
Carrier Fluid
Fluid Particle
No Field
Particle Chain
Parallel Plate Wall
Field Applied

Figure 3. In the presence of an electric field, the ER particles orient themselves into particle chains.

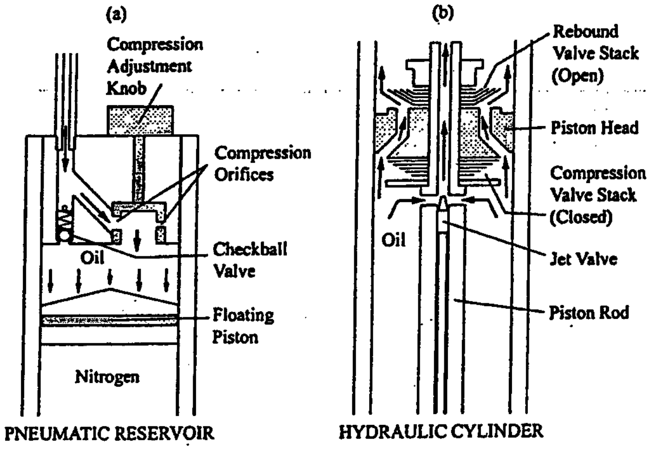
(a)
Compression Adjustment Knob
Compression Orifices
Oil
Checkball Valve
Floating Piston
Nitrogen
PNEUMATIC RESERVOIR
(b)
Rebound Valve Stack (Open)
Piston Head
Compression Valve Stack (Closed)
Oil
Jet Valve
Piston Rod
HYDRAULIC CYLINDER

Figure 2. Schematics of a double adjustable shock absorber. (a) Cross section of the pneumatic reservoir that contains the compression adjuster. (b) Cross section of the main hydraulic cylinder that contains the piston head assembly.

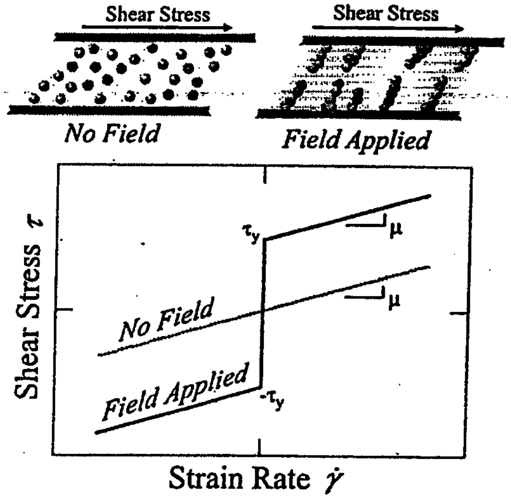
Shear Stress
Shear Stress
No Field
Field Applied
Shear Stress τ
τ_y
μ
μ
No Field
Field Applied
$-\tau_y$
Strain Rate $\dot{\gamma}$

Figure 4. The particle chains induce a yield stress in the fluid which results in a Bingham plastic behavior during shear.

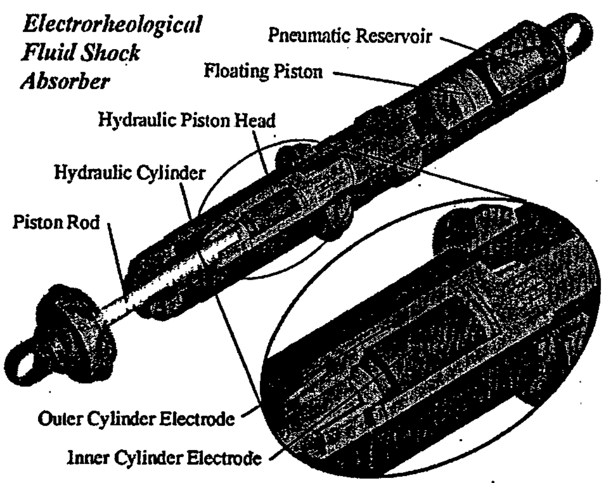

Figure 5. *Cutaway drawing of the electrorheological fluid automotive shock absorber designed and fabricated at the University of Maryland. The shock absorber, composed of hydraulic and pneumatic reservoirs separated by a floating piston, is a monotube, single rod design.*

ER FLUID SHOCK ABSORBER

An electrorheological (ER) automotive shock absorber, was designed and fabricated at the University of Maryland, to emulate the performance of a double adjustable shock absorber. Composed of hydraulic and pneumatic reservoirs separated by a floating piston, the shock absorber is a monotube, single rod design (Figure 5). As the piston rod moves in and out of the hydraulic cylinder the floating piston head compresses the pneumatic reservoir to accommodate the changing rod volume within the hydraulic cylinder. Inside the hydraulic cylinder, the piston rod attaches to a piston head containing two tubular electrodes. During piston rod motion, ER fluid flows through the piston head in a gap between the tubular electrodes.

To achieve semi-active properties, the hydraulic cylinder is filled with Bayer Rheobay 3565 electrorheological fluid. An electrical voltage potential between the electrodes creates an electric field in the gap perpendicular to the ER fluid flow direction. The electric field increases the yield stress of the ER fluid between the electrodes. This increase in yield stress alters the velocity profile of the fluid in the gap and raises the pressure required for a given flow rate.

VELOCITY PROFILE BETWEEN PARALLEL PLATE ELECTRODES

This section determines the velocity profile of the ER fluid in the gap between two parallel plate electrodes due to a pressure gradient. The pressure gradient creates a region of low shear stress in the center of the gap and high shear stress along the plate walls. An applied voltage potential between the parallel plate electrodes creates an electric field in the gap that increases the yield stress of the ER fluid. Assuming a Bingham plastic material, the increase in the fluid's yield stress creates three distinct flow regions (Figure 6) [1]. Two post-yield regions occur along the wall of the electrodes, where the shear stress exceeds the yield stress of the ER fluid. A pre-yield region occurs in the center of the gap, where the shear stress is less than the yield stress of the ER fluid.

Quasi-steady damper analysis and the boundary conditions determine the velocity profile of the fluid between the parallel plates [1]. The non-dimensional plug thickness, $\bar{\delta}$, which is the ratio of the plug thickness, δ, to the gap between the plates, d, simplifies the velocity profile equations for each region.

$$
\begin{aligned}
u_1(y) &= \frac{\Delta P}{2\mu L}\left(y^2-(1-\bar{\delta})dy\right)\\
u_2(y) &= \frac{-\Delta P}{8\mu L}(1-\bar{\delta})^2 d^2 \qquad (3)\\
u_3(y) &= \frac{\Delta P}{2\mu L}\left(y^2-(1-\bar{\delta})dy+\bar{\delta}d^2\right)
\end{aligned}
$$

The shear stress profile between parallel plates relates the non-dimensional plug thickness to the pressure drop [1].

$$\bar{\delta} = \frac{2L\tau_y}{d|\Delta P|} \qquad (4)$$

Integrating the velocity profile equations solves for the flow rate per unit width for each region in terms of the pressure gradient and the non-dimensional plug thickness. Summing the flow rate per unit width for each region gives the total flow rate per unit width in the gap between the parallel plates [1]

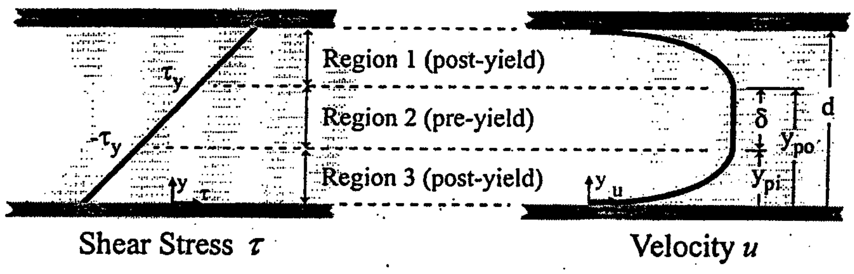

Figure 6. *Application of an electric field creates three regions in the shear stress and velocity profile of a electrorheological fluid.*

$$q = \frac{d^3 \Delta P}{12 \mu L}(1-\bar{\delta})^2 \left(1+\frac{\bar{\delta}}{2}\right) \qquad (5)$$

FLOW RATE IN THE GAP BETWEEN THE ELECTRODES

Uniform Gap

This section derives equations that relate the required pressure drop to the flow rate of ER fluid through a uniform gap between electrodes. The derived analysis assumes that the radius of the electrodes is much larger than that of the gap between the electrodes. As a result, the velocity profile between parallel plates depicts the uniform gap velocity profile [Figure 7(a)]. Equation 5 gives the flow rate per unit width between parallel plates in terms of the pressure drop and the non-dimensional plug thickness, $\bar{\delta}$. Equation (4) replaces the non-dimensional plug thickness in Equation (5) and gives the flow rate per unit width in terms of the pressure drop. Then integrating the flow rate per unit width around the circumference of the inner electrode solves for the total flow rate [3].

$$Q_c = \left(\frac{bd^3}{12 \mu L}\right)\Delta P - \left(\frac{bd^2 \tau_y}{4 \mu}\right) - \left(\frac{bL^2 \tau_y^3}{3 \mu}\right)\frac{1}{\Delta P^2} \qquad (6)$$

Addition of Piston Leakage

Similar to a double adjustable shock absorber, a small orifice allows a controlled amount of leakage through the piston head. Laminar fluid dynamic equations relate the leakage damping, C_l, to the geometry of the orifice.

$$C_l = \frac{8 \mu L_l}{\pi r_l^4} \qquad (7)$$

As a result, the leakage flux in terms of the pressure drop, damping coefficient and piston head area is given by

$$Q_l = \left(\frac{A_p^2}{C_l}\right)\Delta P \qquad (8)$$

The continuity equation for steady incompressible flow requires that the flow rate through the piston head is equal to the sum of the flow rate through the electrodes and the leakage orifice, $Q_t = Q_c + Q_l$. Summing Equation (8) and Equation (6) gives the total flow rate as a function of the pressure drop across the piston head. Then multiplying by ΔP^2 and rearranging produces a polynomial function of the pressure drop in terms of the total flow rate.

$$\left(\frac{bd^3}{12 \mu L} + \frac{A_p^2}{C_l}\right)\Delta P^3 - \left(Q_t + \frac{bd^2 \tau_y}{4 \mu}\right)\Delta P^2 - \left(\frac{bL^2 \tau_y^3}{3 \mu}\right) = 0 \qquad (9)$$

The roots of Equation (9) degenerate three values of required pressure. The correct pressure corresponds to a valid non-dimensional plug thickness, $0 \le \bar{\delta} \le 1$, calculated using Equation 4. Finally, the piston head area, A_p, relates the piston rod force to the pressure drop, $F = \Delta P A_p$, and the piston rod velocity to the flow rate, $v_o = Q_t / A_p$.

Non-Uniform Gap

Experimental testing and Equation (9) demonstrate that increasing the yield stress in the annulus increases the yield force of the device while incurring little change in the post-yield damping. However, double adjustable shocks can alter the post-yield damping independently of their yield force. To emulate the performance of a double adjustable shock, an eccentricity between the inner and outer electrodes is introduced to create an electric field dependent post-yield damping. The eccentricity creates a small gap region and a large gap region between the tubular electrodes. With the application of an electric field, the yield stress restricts flow in the small gap region and thereby increases the pressure required for a given flow rate. At the same time, the large gap region permits flow for any given pressure and eliminates the damper's yield force. The combination of the small gap region, to restrict the flow, and a large gap region, that allows flow for any given pressure, creates a field dependent post-yield damping.

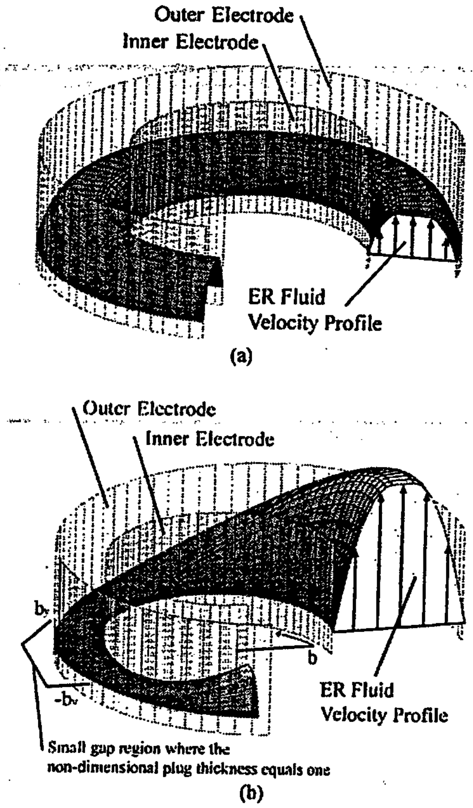
Outer Electrode
Inner Electrode
ER Fluid Velocity Profile
(a)
Outer Electrode
Inner Electrode
b_s
b
$-b_s$
ER Fluid Velocity Profile
Small gap region where the non-dimensional plug thickness equals one
(b)

Figure 7. Velocity profile of ER fluid between electrodes due to a pressure gradient. (a) Concentric electrodes having a uniform gap. (b) Eccentric electrodes having a non-uniform gap.

Depending on the pressure drop, the addition of an applied voltage, which creates a yield stress, prevents flow in the small gap region, $-b_y < b < b_y$, of the eccentric electrodes [Figure 7(b)]. Integrating the velocity profile around the remaining portion of the gap determines the flow rate through the non-uniform gap. The boundaries of the pre-yield region, where $\tau < \tau_y$, set the limits of the integration. Setting the non-dimensional plug thickness [Equation (4)] equal to one solves for the location of the yield point, b_y, and generates the limits of the integration. With the limits of the integration known, integrating the velocity profile around the large gap region of the gap solves for the flow rate as a function of the non-dimensional plug thickness and the pressure drop.

$$Q_e = \int_{-b_y}^{b_y} q\,db = \int_{-b_y}^{b_y} \frac{d^3\Delta P}{12\mu L}(1-\bar{\delta})^2\left(1+\frac{\bar{\delta}}{2}\right)db \qquad (10)$$

EXPERIMENTAL VALIDATION

Force measurements from sinusoidal displacement cycles, recorded on a 5 HP mechanical dynamometer, validate the derived equations. The dynamometer, with the ER damper mounted in its clevises, excites the piston rod while a load cell measures the force on the damper and a LVDT measures the piston rod displacement. Testing of multiple gaps, for concentric and eccentric electrode configurations, validate the utility of the derived equation to accurately predict performance of an ER shock absorber.

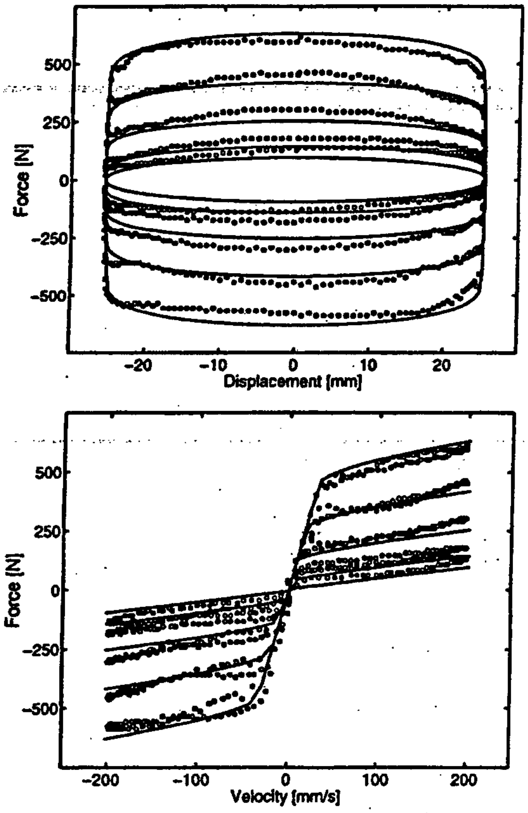

Figure 8. Predicted (shown as solid lines) and experimental (shown as circles) results of force versus displacement and force versus velocity response of the uniform gap configuration due to sinusoidal excitation of the piston rod.

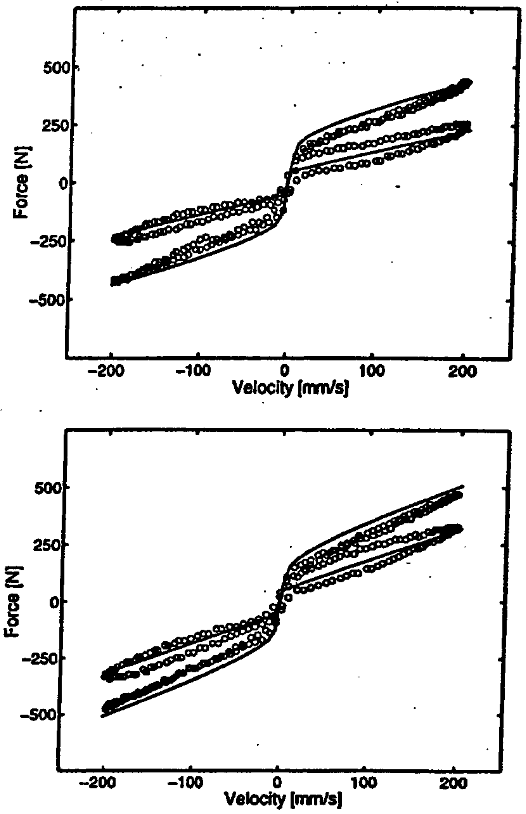

Figure 9. Predicted (shown as solid lines) and experimental (shown as circles) results of the force versus velocity response of the non-uniform gap configuration due to sinusoidal excitation of the piston rod.

For uniform gaps, at a constant frequency, the applied electric field increases the area within the force vs. displacement cycle, which is proportional to the damping. The force vs. velocity cycles demonstrate that an increasing electric field, for concentric electrodes, raises the yield force of the device without greatly affecting the post-yield damping (Figure 8). The force vs. velocity cycles show that increasing the electric field, for a non-uniform gap, raises the post-yield damping of the device without incurring a large change in the yield force (Figure 9).

CONCENTRIC AND ECCENTRIC ELECTRODES IN SERIES

To allow for optimal performance, mechanisms on the main piston head and in the pneumatic reservoir independently control the yield force and damping of double adjustable shocks. To emulate the performance of a conventional double adjustable shock absorber, an electrorheological (ER) automotive shock absorber was designed and fabricated at the University of Maryland (Figure 10). The force vs. velocity cycles demonstrate that an increasing electric

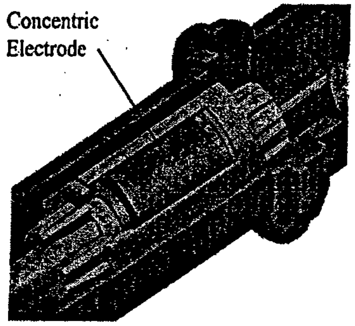

Single Concentric Cylinder

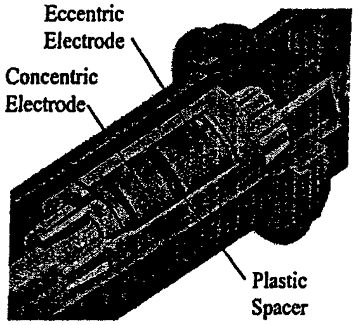

Concentric and Eccentric in Series

Figure 10. *Schematics of electrorheological double adjustable shock absorbers. (a) Cross section of the piston head that contains only a uniform gap. (b) Cross section of the piston head that contains uniform and non-uniform gaps in series.*

field, for concentric electrodes, raises the yield force of the device without greatly affecting the post-yield damping (Figure 8). The force vs. velocity cycles show that increasing the electric field, for eccentric electrodes, raises the post-yield damping of the device without incurring a yield force (Figure 9). The combination of concentric and eccentric electrodes in series demonstrates the ability of a ER damper with independently adjustable yield force and post-yield damping (Figure 11).

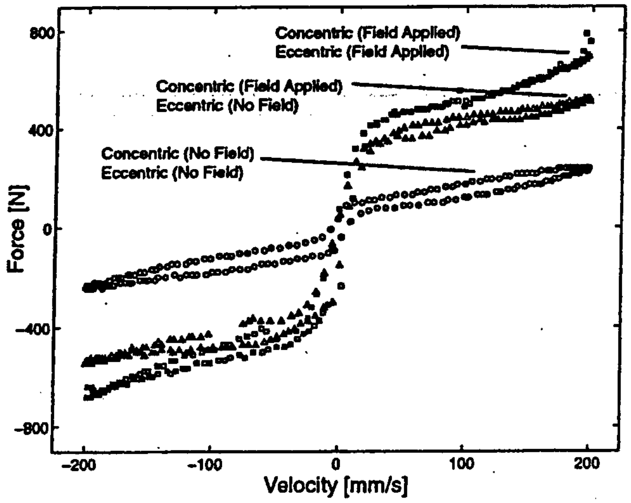

Figure 11. *Experimental results of force versus velocity response of the concentric and eccentric electrodes in series.*

CONCLUSIONS

Force vs. velocity hysteresis cycles of many shocks may be separated into four distinct regions: low-speed compression, high-speed compression, low-speed rebound and high-speed rebound. A unique damping coefficient characterizes each region, and a distinct yield force divides the low and high-speed regions. To emulate the performance of a conventional double adjustable shock absorber, an electrorheological (ER) automotive shock absorber was designed and fabricated at the University of Maryland. An applied electric field in the gap, between two concentric electrodes, increases the yield stress of the ER fluid between the cylinders, which alters the velocity profile of the fluid and raises the pressure required for a given flow rate. Both the experimental data and the derived equations demonstrate that increasing the voltage across the concentric gap controls the yield force of the device. In addition, the experimental data demonstrates that an eccentricity between the two electrodes allows for a post-yield damping controlled by an electric field. Finally, the combination of both concentric and eccentric cylinders in series demonstrate the ability of an ER damper with independently adjustable yield force and post-yield damping.

ACKNOWLEDGMENTS

Research was supported primarily by the National Science Foundation under a NSF Career Award CMS-9734244 (Dr. Ken Chong, technical monitor). Additional support was provided under a grant by the U.S. Army Research Office Young Investigator Program, contract no. 38856-EG-YIP (Dr. Gary Anderson, technical monitor). Laboratory equipment was provided under a grant by the FY96 Defense University Research Instrumentation Program (DURIP), contract no. DAAH-0496-10301 (Dr. Gary Anderson, technical monitor). We also thank Bayer AFG (Dr. Eckhard Wendt) for providing the electrorheological fluid used in this study. Mr. Lindler was supported in part under fellowships from the Vertical Flight Foundation, and the Minta Martin Fund for Aeronautical Research at the University of Maryland.

REFERENCES

1. Wereley, N. M. and Pang, L., "Nondimensional Analysis of Semi-Active Electrorheological and Magnetorheological Dampers using an Approximate Parallel Plate Model," *Smart Materials and Structures,* Vol 7, pp. 732–743.
2. Kamath, G. M., Hurt, M. K. and Wereley, N. M., "Analysis and Testing of Bingham Plastic Behavior in Semi-Active Electrorheological Fluid Dampers," *Smart Materials and Structures,* Vol. 5, No. 5, 1996, pp. 576–590.
3. Lindler, J. E. and Wereley, N. M., "Parametric Analysis and Testing of an Electrorheological Fluid Damper," *Smart Structures and Integrated Systems, Proceedings of SPIE,* Vol. 3668, 1999, pp. 474–486.
4. Dixon, J. C., *Shock Absorber Handbook,* Society of Automotive Engineers Inc., Warrendale, PA, 1999.

Hysteresis Modeling of Semi-Active Magnetorheological Helicopter Dampers

NORMAN M. WERELEY,[1] GOPALAKRISHNA M. KAMATH[2] AND VIJAY MADHAVAN
Alfred Gessow Rotorcraft Center, Department of Aerospace Engineering, University of Maryland, College Park, MD 20742

ABSTRACT: MR dampers in soft-inplane rotors such as hingeless and bearingless rotors have potential benefits including semi-active control of aeromechanical instabilities, such as ground and air resonance. An experimental performance characterization of hybrid elastomeric/MR dampers for the 1/6th scale Comanche wind tunnel model rotor is presented. These dampers are similar to prior fluid-elastomeric Comanche wind tunnel model dampers, except that the passive fluid is replaced by an MR fluid. MR lag dampers were tested under a compressive preload with the magnetic field turned on (ON condition) and off (OFF condition). Damping was characterized for single frequency sinusoidal excitation at the lag/rev (10 Hz) frequency; that is, the lightly damped inplane rotor blade bending mode that plays a dominant role in aeromechanical instabilities. Dual frequency testing was also carried out at 10 Hz and 15 Hz corresponding to the model rotor lag/rev and 1/rev or rotor RPM frequencies respectively. In all of these tests, the force versus displacement hysteresis cycle or energy diagram was measured for the MR dampers. Two nonlinear models are compared: (1) a stiffness plus viscoelastic-plastic model, and (2) a stiffness-viscosity-elasto-slide model. These models were developed to capture the nonlinear behavior of these dampers. The model parameters were identified by minimizing the mean squared error between the predicted and measured MR damper force time histories due to a lag/rev harmonic excitation. Model validation for both single and dual frequency data was carried out. A key conclusion is that both models accurately predict damping performance, which suggests that the underlying hysteresis model is not unique when only damping is the performance metric.

INTRODUCTION

AEROMECHANICAL stability of helicopters is a nonlinear phenomenon involving complex interactions of aerodynamic, inertial and elastic forces. Advanced rotor designs are tending towards hingeless and bearingless rotor systems that have lower parts count, maintenance costs and superior handling qualities. Due to stress and weight considerations, these rotor systems are designed to be soft-inplane, that is, the first inplane natural frequency of the blade is less than the rotor RPM. Since the inplane bending mode or lag mode tends to be very lightly damped, these rotors are susceptible to ground and air resonance instabilities that are serious concerns in helicopter rotor systems (Chopra, 1990). Existing hingeless or bearingless helicopter rotor hub designs use elastomeric or hybrid fluid-elastomeric lag dampers (Panda et al., 1996). The inplane motion in helicopter systems occurs at two frequencies: (1) lead-lag frequency or inplane rotor blade bending or lag/rev frequency and (2) rotor RPM or 1/rev. Under these conditions, the lag/rev damping in elastomers has been shown to degrade substantially at low amplitudes (Felker et al., 1987) due to the 1/rev excitation. Moreover, mechanical properties of lag dampers can vary as much as 5% due to manufacturing variations. Matched sets of dampers are used to minimize the impact of varying damper mechanical properties on rotor tracking conditions. Moreover, damping augmentation is only required in certain flight regimes. Therefore, an MR damper that could adapt its properties to a fixed mechanical property specification would be of tremendous benefit. MR fluids are examined in this study because MR fluids require smaller excitation voltages and have greater dynamic yield stresses than ER fluids (Carlson et al., 1995). MR damper behavior is highly nonlinear. Linear models do not accurately capture the single and dual-frequency hysteresis behavior, but this accuracy is essential for aeroelastic stability analysis. The modeling of force vs. velocity hysteresis characteristics of MR dampers can be improved using nonlinear hysteretic models (Kamath and Wereley, 1997; Spencer et al., 1997; Wereley et al., 1998; Kamath et al., 1999).

This paper presents a comparison of two nonlinear mechanisms-based models that can be used to characterize semi-active MR fluid dampers for the 1/6th Froude-scaled Comanche wind tunnel model rotor, the hub of which is shown in Figure 1. These dampers were fabricated and provided by the Lord Corporation. Dynamic single frequency tests were conducted for damper pairs under a compressive preload at 10 Hz which corresponds to lag/rev frequency of the model rotor. Dual frequency tests at 10 Hz and 15 Hz (corresponding

---

Substantially revised version of a paper presented at the 7th International Conference on ER/MR Fluids, Honolulu, HI, July, 1999.

[1] Author to whom correspondence should be addressed. E-mail: wereley@eng.umd.edu

[2] Currently: National Aerospace Laboratories, Bangalore, India.

1045-389X/99/08 0624-10 $10.00/0 DOI: 10.1106/NHLE-FNDL-U243-L8U0
© 2000 Technomic Publishing Co., Inc.

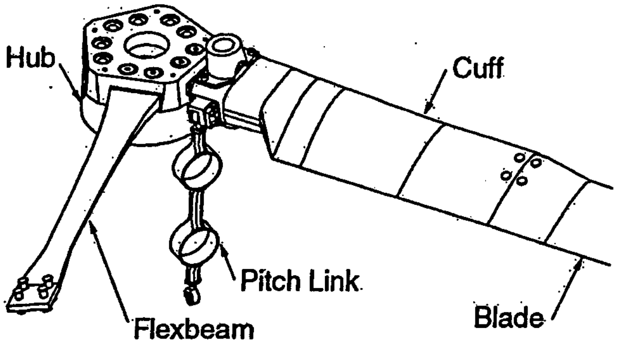

***Figure 1.** Wind tunnel model of the Comanche helicopter rotor hub from Panda et al. (1996).*

to the rotor RPM) were also conducted and these conditions mirrored the excitation of lag dampers in-flight. Test results for the single and dual frequency preloaded cases with the magnetic field ON are presented in this paper. A comprehensive characterization of the damper behavior including factors such as various loading conditions, amplitudes, frequencies and magnetic fields and comparison with similar fluidlastic dampers is provided in Kamath et al. (1999). Two hysteresis models are compared in this paper: (1) a stiffness plus nonlinear viscoelastic-plastic (NVEP) model (Kamath et al., 1999), and (2) a stiffness-viscosity-elasto-slide (SVES) model. The NVEP model uses a nonlinear combination of linear mechanisms to capture the hysteresis behavior of the dampers. The SVES model uses a linear combination of nonlinear mechanisms and is based on ideas in elastomeric damper literature (Panda et al., 1996 and 1997). In this paper, single frequency test data at the lag/rev frequency are used to identify model parameters based on minimizing the mean squared error between the predicted amd measured damper force due to sinusoidal displacements. The performances of these two models are assessed via comparisons of: (1) the linear characterization results at 10 Hz or lag/rev frequency, (2) the experimental and predicted force vs. displacement hysteresis cycle behavior in both the single and dual frequency conditions. Both models are nonlinear models and capture the damper hysteresis behavior reasonably accurately.

DAMPER TESTING

The setup shown in Figure 2 was used to measure force vs. displacement hysteresis. A 110 lb Ling dynamics shaker was used to excite the damper pairs. Lag dampers are usually mounted in a rotor system in pairs with a compressive preload acting on them (Panda and Mychalowycz, 1997). The test setup had a provision for applying preload by using preload plates that held the two damper support blocks by means of dowel pins at a precise distance, $L-\Delta L$. A value of $\Delta L = 0.04$ inches was used for the preload condition. A load cell between the shaker and the connecting piece measured the force input and displacements were measured using a non-contacting laser sensor placed above the damper assembly. Single frequency sinusoidal excitation was applied at 10 Hz at amplitudes ranging from 0.127 mm (0.005 in) to 1.27 mm (0.05 in). Dual frequency excitation was applied at 10 Hz and 15 Hz over a suitably selected matrix of amplitudes. The 10 Hz and 15 Hz frequencies correspond to the lag/rev frequency and 1/rev rotor frequency, respectively, of the model-scale rotor. A HP 8904A multifunction synthesizer was used to generate and sum the signals with the two discrete frequencies.

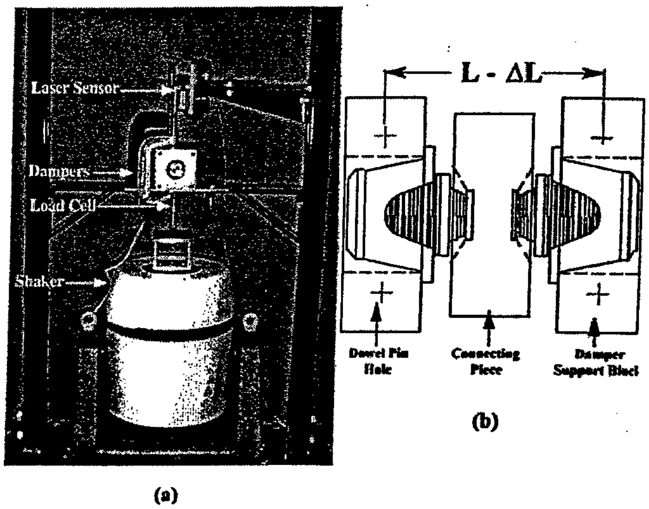

***Figure 2.** Experimental setup for damper testing.*

SINGLE FREQUENCY CHARACTERIZATION

The force vs. displacement hysteresis data were collected for the MR ON and MR OFF preloaded cases at 10 Hz, the data for which is shown in Figure 3. Linearization of damper characteristics was carried out using a complex stiffness given by

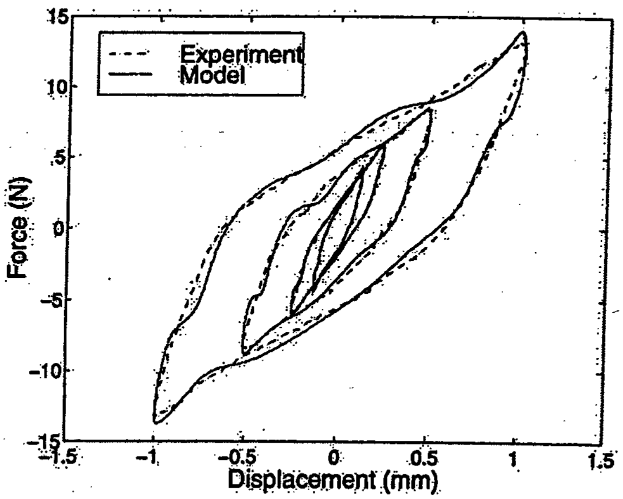

***Figure 3.** Measured force vs. displacement hysteresis cycles are compared to those predicted by the nonlinear viscoelastic-plastic model for the MR helicopter lag dampers.*

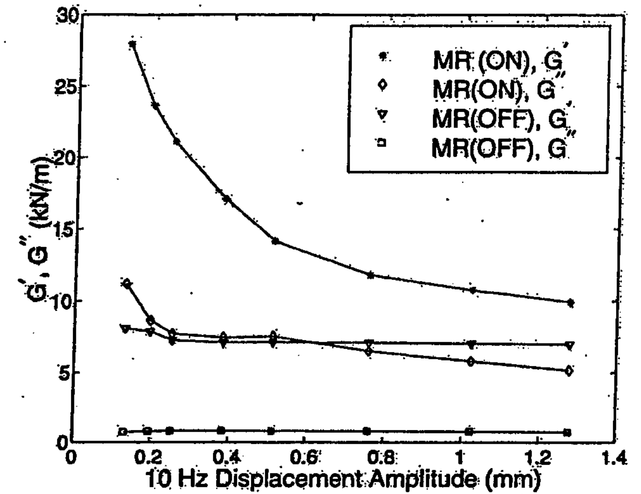

Figure 4. Linear characterization using complex stiffness for the MR lag dampers.

$$G^* = G' + jG'' \tag{1}$$

The linearized stiffness, G', and damping, G'', were obtained by transforming the measured displacement, $x(t)$, and force, $F(t)$, into the frequency domain using a Fourier series expansion,

$$x(t) = x_c \cos \Omega_{lag} t + x_s \sin \Omega_{lag} t \tag{2}$$

$$F(t) = F_c \cos \Omega_{lag} t + F_s \sin \Omega_{lag} t \tag{3}$$

and then using first harmonics as follows:

$$G' = \frac{F_c x_c + F_s x_s}{x_s^2 + x_c^2} \tag{4}$$

$$G'' = \frac{F_c x_s - F_s x_c}{x_s^2 + x_c^2} \tag{5}$$

Here, F_c and F_s are the first Fourier force cosine and sine coefficients, respectively, and x_c and x_s are the corresponding displacement Fourier cosine and sine coefficients (Kamath, Wereley and Jolly, 1999). Linearized stiffness, G', and damping, G'', are plotted versus amplitude of harmonic excitation in Figure 4 and clearly illustrate the MR effect. In the MR OFF, preloaded condition, the MR dampers show an almost linear behavior with a marginal damping and a predominant stiffness component. From this data, it can be seen that application of a magnetic field results in an increase in both the stiffness and the damping levels.

SINGLE FREQUENCY HYSTERESIS MODELING

We will consider two models: (1) the viscoelastic plastic model, and (2) the stiffness-viscosity-elasto-slide model.

Viscoelastic-Plastic Model

The MR dampers in the ON condition are nonlinear with amplitude. In our prior work we have shown that the nonlinear viscoelastic-plastic (NVEP) model is an accurate and physically motivated approach to electrorheological (ER) fluid modeling (Kamath and Wereley, 1997a), as well as damper modeling (Kamath and Wereley, 1997b, 1997c). Because the phenomenology of MR fluid behavior is similar to that of ER fluid behavior (Weiss, Carlson and Nixon, 1994), the viscoelastic-plastic model is used in this study to describe the MR ON damper hysteresis. The viscoelastic-plastic model has also been used to model linear stroke MR dampers (Pang, Kamath and Wereley, 1998).

We first extract the MR effect caused by the application of the magnetic field from the experimental built-up damper force data. To do this, the stiffness and damping forces for the MR OFF condition were subtracted from the MR ON force time histories. Thus,

$$F^e_{mr\_effect} = F_{mr\_on} - \hat{F}_{mr\_off} \tag{6}$$

Here

$$\hat{F}_{mr\_off} = G'x(t) + \frac{G''}{\omega}\dot{x}(t) \tag{7}$$

where G' and G'' are the preloaded MR OFF values plotted in Figure 4.

A schematic of the NVEP model is shown in Figure 5. The model is a network comprising two branches: the preyield and the postyield branches. Each branch consists of a shape function and a linear mechanism. The linear mechanisms model the phenomenology of their respective rheological domains. The preyield behavior is modeled using a linear Kelvin chain to represent the viscoelastic stiffness (K_{ve}) and damping (C_{ve}) components. The postyield behavior is modeled as a viscous dashpot element (C_{vi}). The two shape functions, S_{ve} and S_{vi}, act as switches to turn on and turn off the two mechanisms depending on whether the fluid is in the preyield or postyield region. This transition yield point is located at the yield velocity, V_y. V_y is only a model parameter, and does not physically reflect the velocity at which the fluid yields in the damper. Thus, the predicted MR effect is

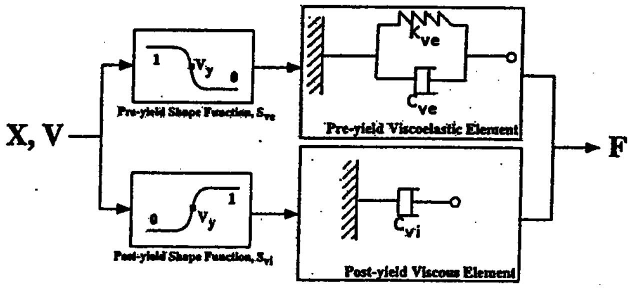
X, V
1
V_y
0
Pre-yield Shape Function, S_ve
K_ve
C_ve
Pre-yield Viscoelastic Element
F
0
V_y
1
Post-yield Shape Function, S_vi
C_vi
Post-yield Viscous Element

Figure 5. Schematic of the nonlinear viscoelastic plastic model (NVEP).

$$\hat{F}_{mr\_effect} = S_{ve}F_{ve} + S_{vi}F_{vi} \tag{8}$$

where

$$S_{ve} = \frac{1}{2}\left\{1 - \tanh\left(\frac{|\dot{x}| - V_y}{4\varepsilon}\right)\right\} \tag{9}$$

$$F_{ve} = K_{ve}x + C_{ve}\dot{x} \tag{10}$$

$$S_{vi} = \frac{1}{2}\left\{1 + \tanh\left(\frac{|\dot{x}| - V_y}{4\varepsilon}\right)\right\} \tag{11}$$

$$F_{vi} = C_{vi}\dot{x} \tag{12}$$

The parameter ε determines the rate at which the transition through yield occurs. For example, $\varepsilon = 0$ would result in a step jump at V_y, and as it is increased, the transition occurs in a more gradual manner. Thus, the 5 unknown parameters in the model are K_{ve}, C_{ve}, C_{vi}, V_y and ε. The parameters are estimated by minimizing the error between the experimental hysteresis data, which in this case is the MR effect experimental data, F_{mr_effect} given by Equation (6) and the model prediction, $\hat{F}_{mr\_effect}$ given by Equation (8). The identified parameters for the preloaded case are detailed in Kamath, Wereley and Jolly (1999). The model validations are presented for the total predicted force, that is,

$$\hat{F}_{mr\_on} = \hat{F}^{e}_{mr\_effect} + F_{mr\_off} \tag{13}$$

Stiffness-Viscosity-Elasto-Slide Model

The nonlinear stiffness-viscosity-elasto-slide model (SVES) consists of a linear combination of nonlinear mechanisms. Figure 6 shows a schematic of the SVES model used to describe the hysteretic behavior of the MR dampers. The model has the following three amplitude-dependent mechanisms in parallel: (1) a linear stiffness, (2) a linear viscous dashpot, and (3) a nonlinear elasto-slide element (consisting of a stiffness and Coulomb element in series). Figure 7 shows the effect of each of these mechanisms on the hysteresis cycles of the dampers. The linear stiffness and linear dashpot parameters give the necessary slope and linear damping to the hysteresis curve. The elasto-slide element represents a stiffness in the region where the velocity of the damper changes its sign and the displacement from the extreme position is less than a certain value $2X_s$. In the remaining portion of the hysteresis cycle, the elasto-slide element is equivalent to a Coulomb element. Two parameters are required to completely characterize the elasto-slide element. The linear stiffness and linear viscous damping elements require 1 parameter each for complete characterization. Thus, the SVES model is a 4-parameter model. Having established the model structure and model components, the parameters in the model need to be identified. The predicted force from the model is given by:

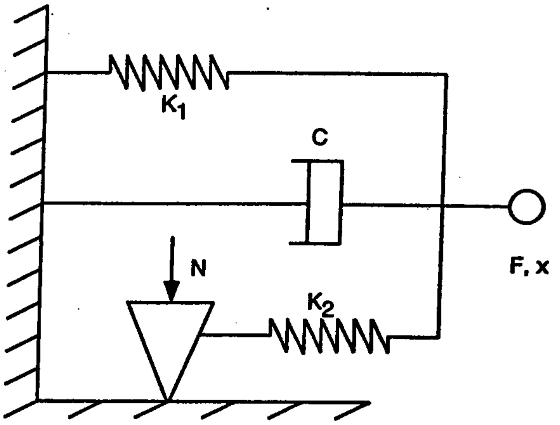

Figure 6. Schematic of the stiffness-viscosity-elasto-slide (SVES) model.

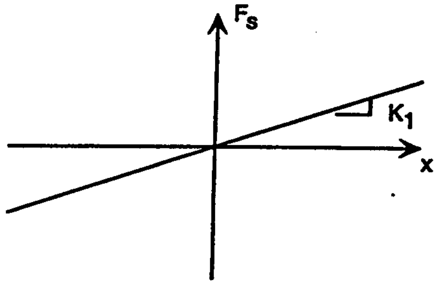

(a) Stiffness Element

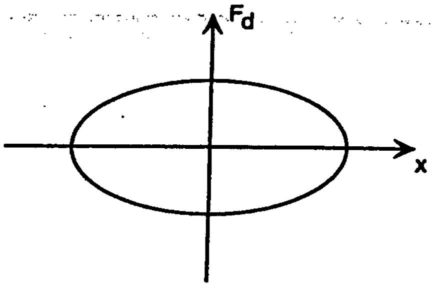

(b) Damping Element

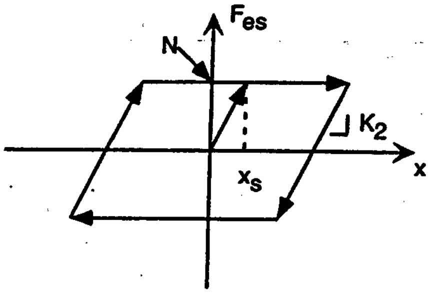

(C) Elasto-slide Element (Lazan, 1968)

Figure 7. Mechanisms in the stiffness-viscosity-elasto-slide (SVES) model and their effect on hysteresis cycle shape.

$$F(t) = F_s(t) + F_d(t) + F_{es}(t) \tag{14}$$

where F_s, F_d and F_{es} are the forces in the stiffness, viscous dashpot and elasto-slide element at any time t. The stiffness and damping forces are linear spring and linear viscous as follows:

$$F_s = K_1 x \tag{15}$$

$$F_d = C\dot{x} \tag{16}$$

The elasto-slide element has four branches as

$$F_{es} = \left\{ \begin{array}{lll} -N & x = -\bar{x} & \dot{x} = 0 \\ -N + K_2(x + \bar{x}) & x < -\bar{x} + 2X_s & \dot{x} > 0 \\ N & x > -\bar{x} + 2X_s & \dot{x} > 0 \\ N & x = \bar{x} & \dot{x} = 0 \\ N + K_2(x - \bar{x}) & x > \bar{x} - 2X_s & \dot{x} < 0 \\ -N & x < \bar{x} - 2X_s & \dot{x} < 0 \end{array} \right. \tag{17}$$

where the slide force is given by

$$N = K_2 X_s \tag{18}$$

Here, $\bar{x}$ is the amplitude over the cycle. The unknown parameters are estimated on the basis of minimizing the error between the predicted force, $\hat{F}$, and the measured force, F, obtained from experiments. The parameters of the model are obtained from a constrained minimization of the objective function, J, given by

$$J = \sum_{k=1}^{N} [\hat{F}(t_k) - F(t_k)]^2 \tag{19}$$

where N is the number of data points for each hysteresis cycle. A constrained minimization was performed using MATLAB optimization tools to minimize the above objective function in Equation (19). Using this system identification technique, and to obtain physically meaningful results, the identified parameters are constrained to have positive values: $K_1 > 0$, $K_2 > 0$, $C > 0$ and $N > 0$. The identified parameters are plotted versus excitation amplitude in Figure 8. A

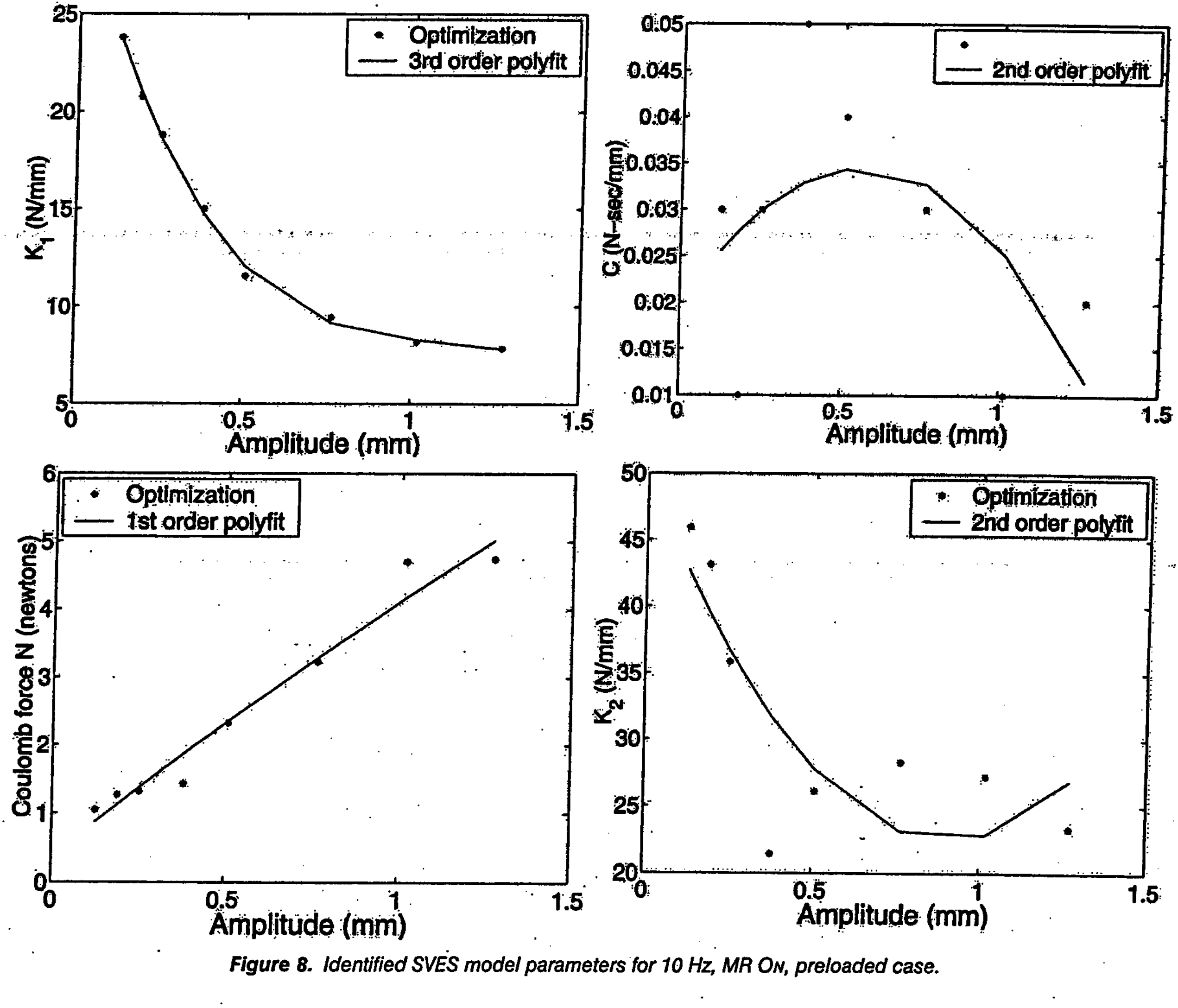

Figure 8. Identified SVES model parameters for 10 Hz, MR On, preloaded case.

similar procedure was used to identify the viscoelastic-plastic model parameters as detailed in Kamath, Wereley and Jolly (1999).

SINGLE FREQUENCY VALIDATION

The force vs. displacement correlations for the NVEP model for the preloaded, MR ON case are shown in Figure 4, and those for the SVES model are shown in Figure 9. It can be seen that both models capture the nonlinear behavior of the MR ON damper quite accurately. Figure 10 shows a comparison of the prediction errors at various amplitudes for both models. The error measure used for purposes of comparing the two models is given by

$$\varepsilon = \sqrt{\frac{1}{N\bar{F}^2}\sum_{k=1}^{N}[\hat{F}(t_k) - F(t_k)]^2} \qquad (20)$$

where $\hat{F}$ and F are the predicted force and the measured force, respectively. $\bar{F}$ is the maximum value of the force in the data set at a given excitation amplitude. From Figure 10, the SVES model has lower errors compared to the NVEP model in the single frequency case. Note that the force versus displacement hysteresis cycle shape is that of a parallelogram, as shown in Figure 9, indicating a piecewise smooth force time history for sinusoidal damper motion. The measured force versus displacement hysteresis cycle shape is smooth as shown in Figure 4. Therefore, qualitatively, the NVEP model is able to better capture the nuances of the force time history and the associated force versus displacement hysteresis cycle shape.

Dual Frequency Hysteresis Modeling

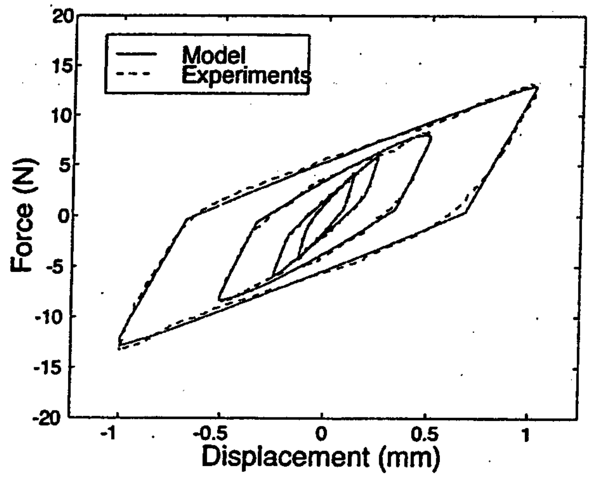

Figure 9. *Single frequency validation of SVES hysteresis model for the MR ON, preloaded case.*

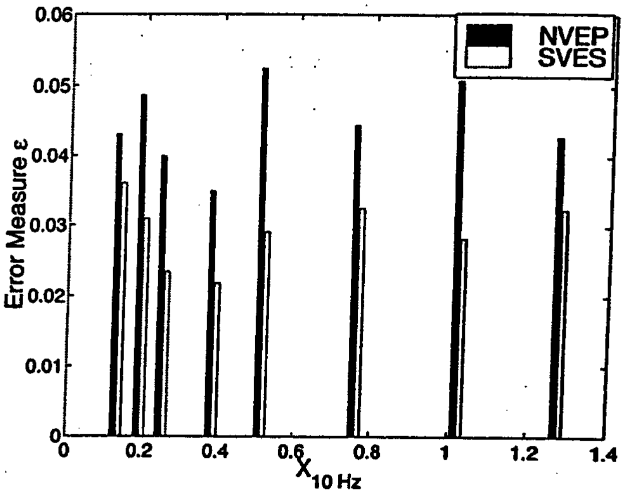

Figure 10. *Single frequency validation error for the two hysteresis models for the MR ON, preloaded case.*

For the MR ON preloaded dampers, the nonlinear viscoelastic-plastic (NVEP) model and the nonlinear stiffness-viscosity-elasto-slide (SVES) model were used to predict the dual frequency behavior. A detailed description of the dual-frequency modeling approach for the NVEP model can be seen in our prior work (Kamath, Wereley and Jolly, 1999). For dual frequency modeling, using the SVES model, the maximum values of the displacement were determined from the experimental force-displacement hysteresis cycles. Since the two frequencies are close to each other, it was hypothesised that the parameters identified from single frequency tests at 10 Hz would yield sufficiently accurate validations for the dual frequency test results. The model constants K_1, K_2, C and N were fitted as functions of amplitude at the lag frequency, $\Omega_{lag} = 10$ Hz by using appropriate polynomials. The values for a given data set were then determined by computing the values of these fitted functions at the effective amplitude of the dual frequency signal. These parameter values were then used to validate the model.

The dual frequency correlation results for three dual frequency excitation conditions are shown in Figures 11, 12 and 13. In Figure 11, the lag amplitude, $X_{10Hz} = 0.254$ mm is twice the 1/rev amplitude of $X_{15Hz} = 0.127$ mm. This results in two loops. The viscoelastic-plastic model does an excellent job of capturing the dual frequency hysteresis behavior of the MR damper. Because of the nature of the SVES model, the model does not capture the higher order derivatives of the force as well as the NVEP model. The correlation results for both models show that the parameters obtained from appropriate curve-fits for the single frequency parameters perform fairly well in predicting dual frequency results. Similar results were obtained for the case where the lag amplitude, $X_{10Hz} = 0.254$ mm equaled the 1/rev amplitude of $X_{15Hz} = 0.254$ mm as shown in Figure 12. In the case where the lag amplitude, $X_{10Hz} = 0.254$ mm, is less than the 1/rev amplitude of $X_{15Hz} = 0.508$ mm, good correlations were obtained by both models, as shown in Figure 13. Many more cases were analyzed, and similar correlations were obtained for all the dual frequency data sets, but only these representative results

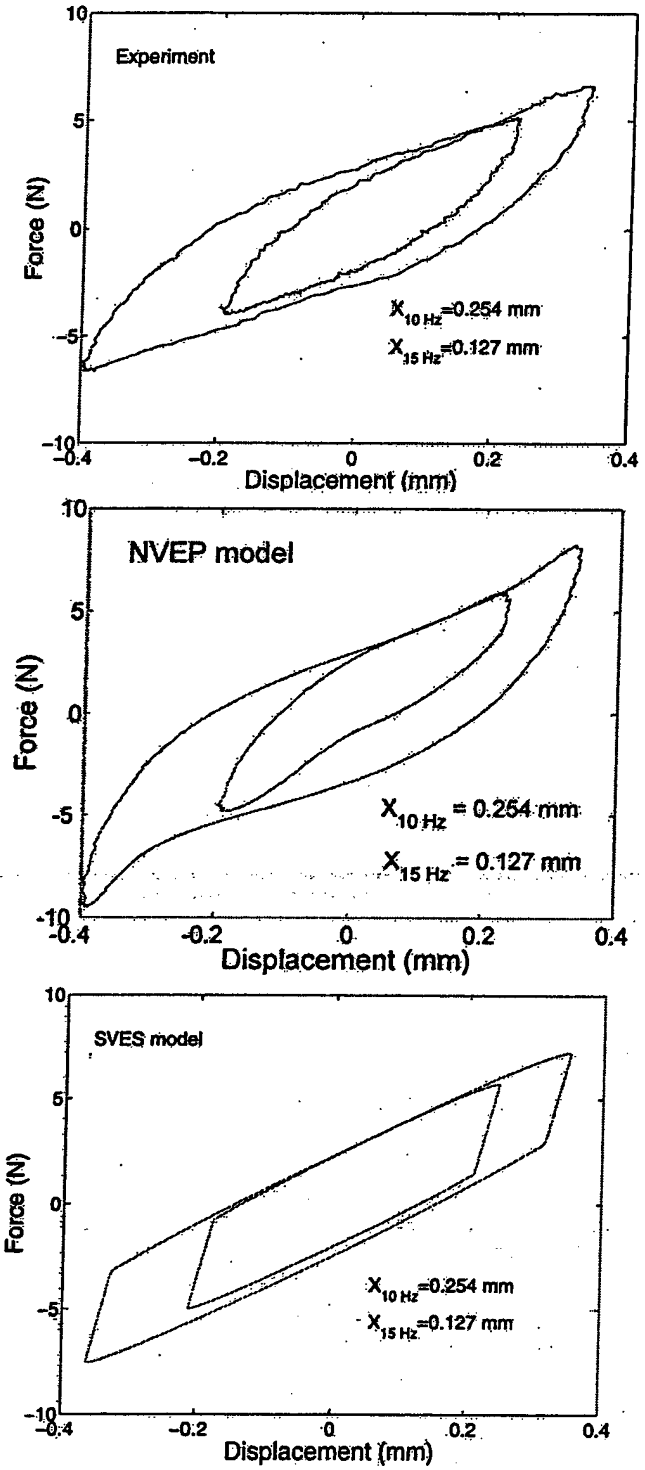

Figure 11. Dual frequency validation of SVES and NVEP hysteresis models for the preloaded MR ON case for a 10 Hz amplitude of 0.254 mm and a 15 Hz amplitude of 0.127 mm.

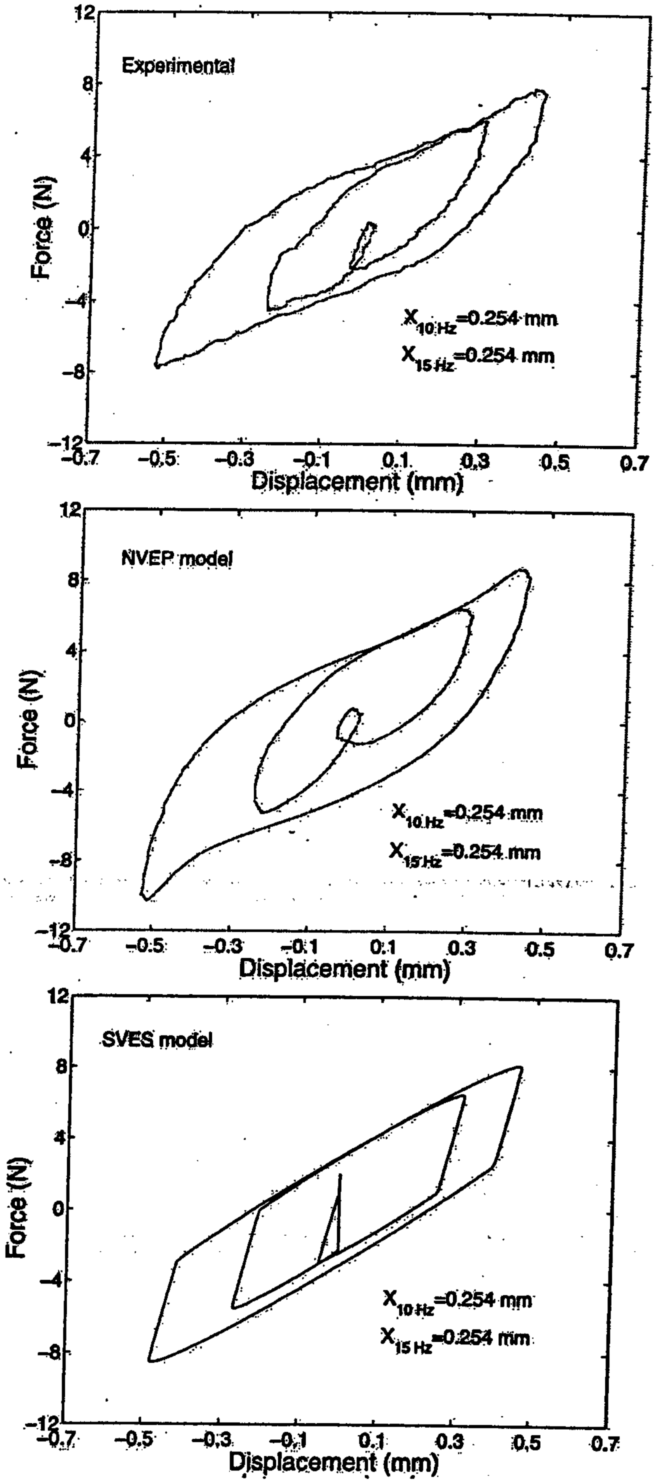

Figure 12. Dual frequency validation of SVES and NVEP hysteresis models for the preloaded MR ON case for a 10 Hz amplitude of 0.254 mm and a 15 Hz amplitude of 0.254 mm.

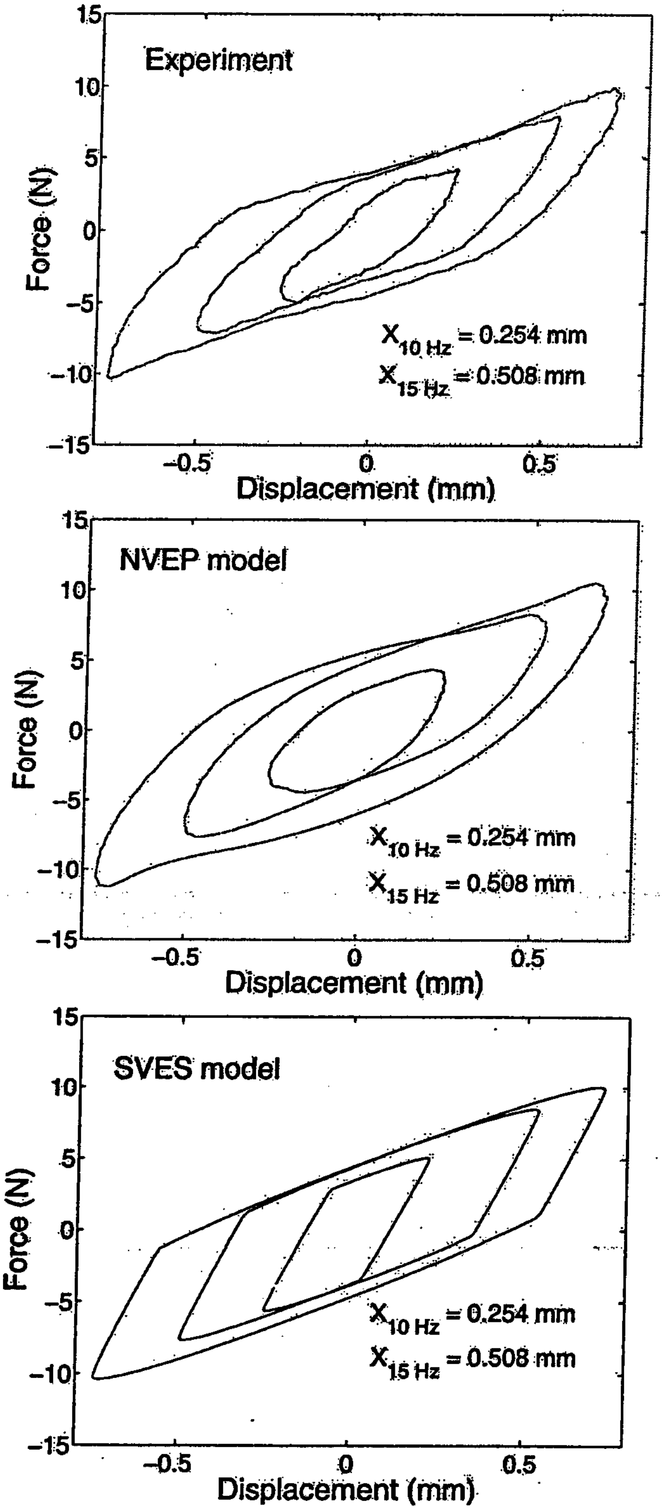

Figure 13. *Dual frequency validation of SVES and NVEP hysteresis models for the preloaded MR ON case for a 10 Hz amplitude of 0.254 mm and a 15 Hz amplitude of 0.504 mm.*

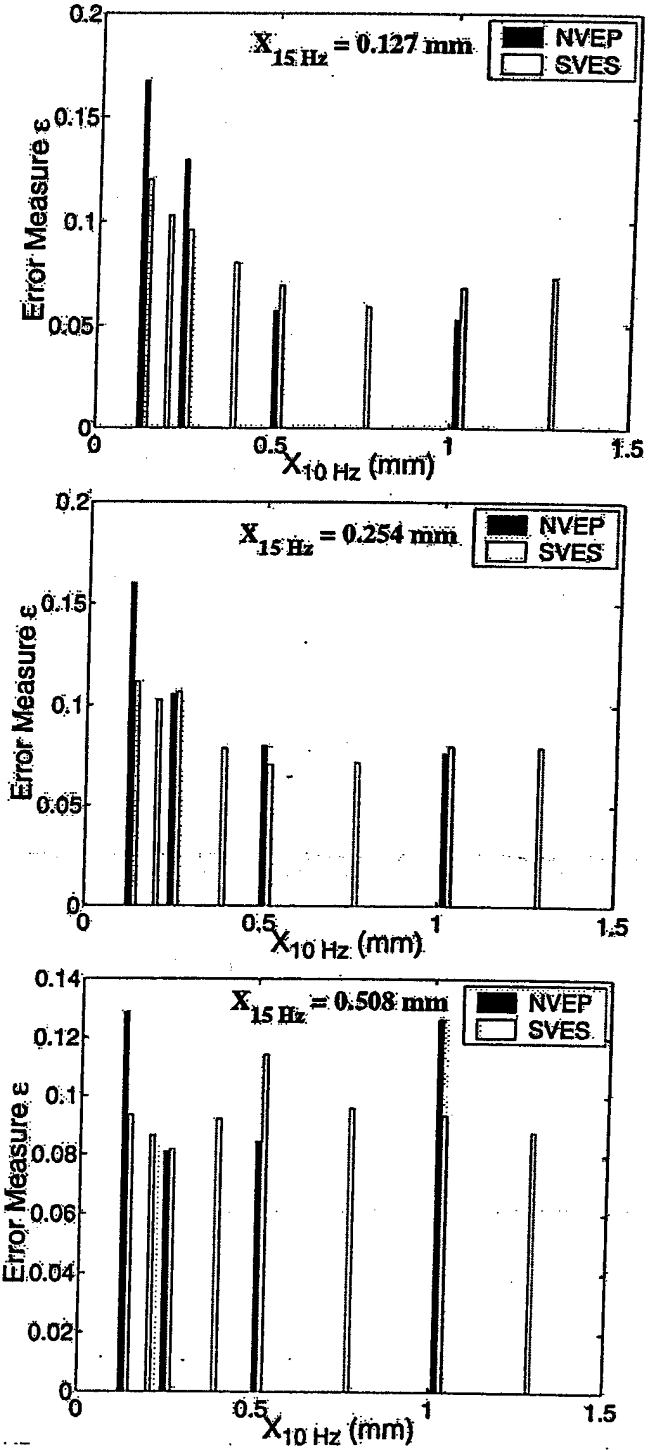

Figure 14. *Dual frequency validation errors of SVES and NVEP hysteresis models for the preloaded MR ON case.*

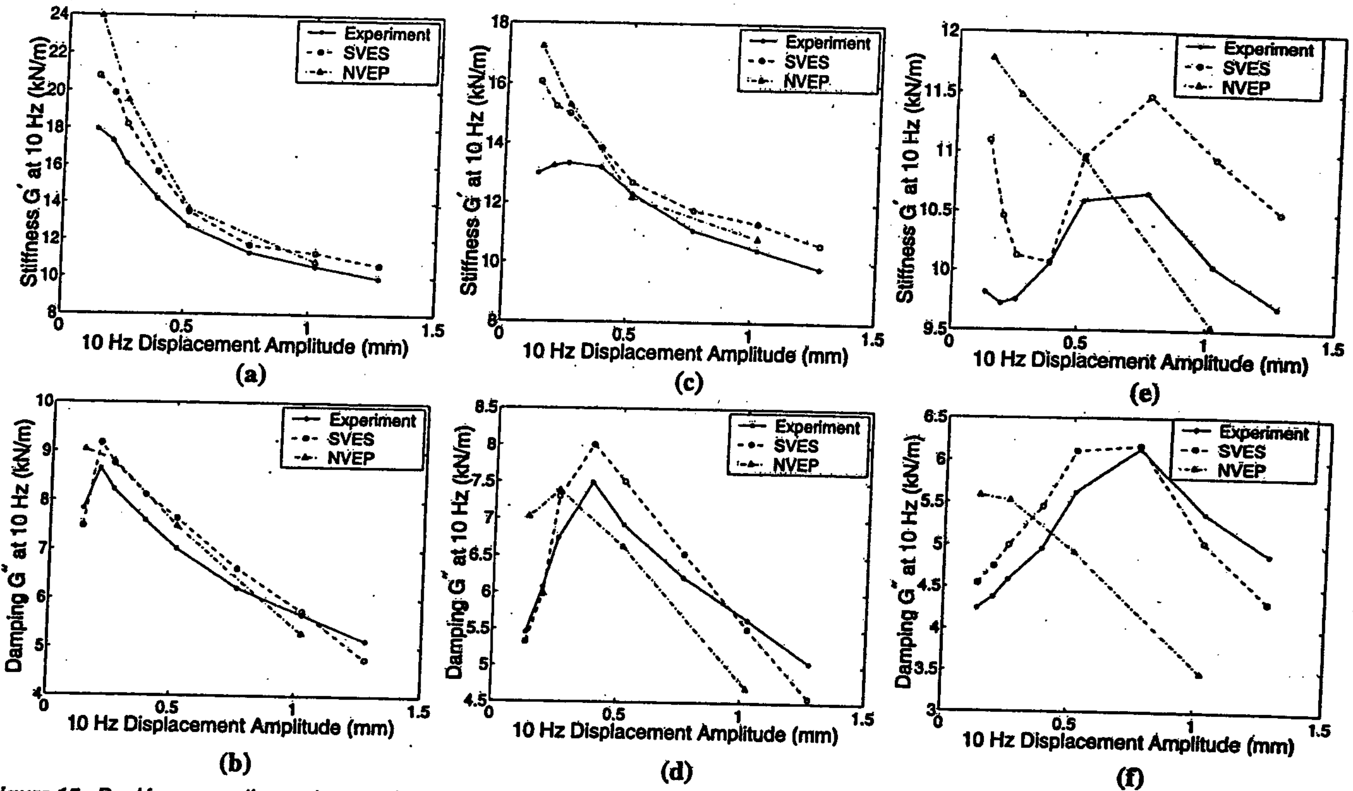

Figure 15. Dual frequency linear characterization results at 10 Hz for the MR(ON), preloaded case. (a) and (b) are for a 15 Hz amplitude of 0.127 mm. (c) and (d) are for a 15 Hz amplitude of 0.254 mm. (e) and (f) are for a 15 Hz amplitude of 0.508 mm.

have been presented for the sake of brevity. Generally, the nonlinear viscoelastic-plastic model performed better when representing the shape of the dual frequency hysteresis cycles.

A comparison of the prediction errors of the two models is shown in Figure 14. In both models, polynomial functions were fitted to the model's parameter values as a function of amplitude. It is seen that although the SVES model had uniformly lower prediction errors in the single frequency case, the errors of the two models are comparable in the dual frequency case. It therefore appears that the approach that we have used for dual frequency hysteresis modeling will yield comparable errors for any number of models that have a sufficient degree of nonlinearity to capture the single frequency behavior adequately.

A final interesting comparison is obtained by comparing the complex modulus at the lag frequency, Ω_{lag}, of the experimental data to the model predictions. Figure 15 shows the G' and G'' values at the lag/rev, when the amplitude of the 1/rev or 15 Hz signal is fixed and the lag/rev or 10 Hz signal is swept from 0.127 mm to 1.27 mm. We showed that the linearized G' and G'' values at lag/rev in the dual frequency case are lower than those in the single frequency case (Kamath, Wereley and Jolly, 1999). Therefore, in addition to accurate hysteresis cycle predictions, there are two other requirements, posed by the linear characterization studies when assessing the dual frequency hysteresis model: (1) the model must correctly capture the trends which indicate a loss in damping and stiffness compared to single frequency cases, and (2) the model must correctly capture the actual dual frequency stiffness and damping values. Both models do reasonably well on both counts as seen in Figure 15. Interestingly, the SVES stiffness and damping predictions are closer to the experimental values and seem to capture the trends better for both the stiffness and the damping values, even though the shape of the dual frequency hysteresis cycle is better captured by the nonlinear viscoelastic plastic model. The dual frequency prediction errors of both models are within 15% for most of the cases.

CONCLUSIONS

This study examined the hysteresis behavior of hybrid elastomeric and MR fluid dampers. A linear characterization of the damper response to sinusoidal displacements was conducted. The complex stiffness and equivalent viscous damping of the MR damper are strongly dependent on amplitude of excitation. In addition, the stiffness and damping increase when the magnetic field is turned ON. The force versus displacement hysteresis cycles of the dampers were also analyzed using two nonlinear models. The nonlinear viscoelastic plastic model is a nonlinear combination of linear elements while the stiffness-viscosity-elasto-slide model is a linear combination of nonlinear elements. The following conclusions were obtained:

1. In both the SVES and NVEP models, the model parameters are highly dependent on the amplitude of excitation. Both the SVES and NVEP models adequately capture the energy diagram of the MR damper as a function of amplitude for single and dual frequency excitation. Both models also capture the linear characterization behavior of the damper accurately.
2. Both models accurately predict damping performance for both single and dual frequency conditions, which suggests that the underlying hysteresis model is not unique when only damping is the performance metric.
3. The LMS errors of the two models, between the predicted and measured force time histories, were minimized to identify the model parameters. These errors were of comparable magnitudes for dual frequency conditions, although the SVES model performed slightly better in the single frequency condition. Thus, multiple models with sufficient degree of nonlinearity can adequately capture the single and dual frequency hysteresis behavior of these nonlinear MR dampers. Alternatively, the LMS error minimization between the predicted and measured force time histories does not yield a unique model.
4. The SVES stiffness and damping predictions are closer to the experimental values and seem to capture the trends better for both the stiffness and the damping values, even though the shape of the dual frequency hysteresis cycle is better captured by the nonlinear viscoelastic plastic model.

NOTATION

MR	magnetorheological
NVEP	nonlinear viscoelastic plastic model
OFF	MR damper in zero field condition
ON	MR damper in full field condition
SVES	stiffness viscosity elasto-slide model
$x(t)$	measured displacement of sinusoidal excitation
$\bar{x}(t)$	amplitude of sinusoidal excitation
$F(t)$	measured force
$\bar{F}(t)$	force amplitude measured over one cycle
$\hat{F}(t)$	predicted force
F_{es}	elasto-slide force for SVES model
F_d	damping force for SVES model
F_s	stiffness force for SVES model
F_{vi}	postyield viscous force for NVEP model
F_{ve}	preyield viscoelastic force for NVEP model
G^*	complex stiffness
G'	in-phase component of complex stiffness
G''	quadrature component of complex stiffness
S_{ve}	preyield weighting function
S_{vi}	postyield weighting function
Ω_{lag}	lag frequency (here, 10 Hz)
Ω	rotational frequency (here, 15 Hz)
$(\hat{\ })$	predicted quantity
$(\dot{\ })$	time derivative of quantity
$(\bar{\ })$	amplitude of quantity over a cycle

ACKNOWLEDGMENTS

Research supported under a grant by the U.S. Army Research Office Young Investigator Program, contract no. 38856-EG-YIP (Dr. Gary Anderson, technical monitor). Laboratory equipment support was provided under a grant by the FY96 Defense University Research Instrumentation Program (DURIP), contract no. DAAH-0496-10301 (Dr. Gary Anderson, technical monitor). The authors also thank Dr. Mark Jolly of the Lord Corporation Research Center in Cary, North Carolina, for fabricating and providing the dampers used in this study.

REFERENCES

1. Carlson, J.D., Catanzarite, D.M., and St. Clair, K.A. (1995). "Commercial Magneto-Rheological Fluid Devices," Presented at the *5th Int. Conf. on Electro-Rheological, Magneto-Rheological Suspensions and Associated Technology,* Sheffield, U.K.
2. Chopra, I. (1990). "Perspectives in Aeromechanical Stability of Helicopter Rotors," *Vertica,* Vol. 14, No. 4, pp. 457–508, 1990.
3. Felker, F.F., Lau, B.H., McLaughlin, S., and Johnson, W. (1987). "Nonlinear Behavior of an Elastomeric Lag Damper Undergoing Dual-Frequency Motion and Its Effect on Rotor Dynamics," *Journal of the American Helicopter Society,* Vol. 34, No. 4, October, pp. 45–53.
4. Kamath, G.M. and Wereley, N.M. (1997a). "A Nonlinear Viscoelastic-Plastic Model for Electrorheological Fluids," *Smart Materials and Structures,* Vol. 6, No. 3, pp. 351–359.
5. Kamath, G.M. and Wereley, N.M. (1997b). "Modeling the Damping Mechanism in ER Fluid Based Dampers," M3DIII: *Mechanics and Mechanisms of Material Damping,* ASTM STP 1304, A. Wolfenden and V.K. Kinra, Eds., American Society for Testing and Materials, pp. 331–348.
6. Kamath, G.M. and Wereley, N.M. (1997c). "Nonlinear Viscoelastic-Plastic Mechanisms-Based Model of an Electrorheological Damper," *AIAA Journal of Guidance, Control, and Dynamics,* Vol. 20, No. 6, Nov–Dec, pp.1125–1132.
7. Kamath, G.M., Wereley, N.M. and Jolly, M.R. (1999). "Characterization of Magnetorheological Helicopter Lag Dampers," *Journal of the American Helicopter Society,* Vol 44, No. 3, July, pp. 234–248.
8. Lazan, B.J. (1968). *Damping of Materials amd Members in Structural Mechanics.* Pergamon Press, New York.
9. Panda, B., Mychalowycz, E., and Tarzanin, F.J. (1996). "Application of Passive Dampers to Modern Helicopters," *Smart Materials and Structures,* Vol. 5, No. 5, October, pp. 509–516.
10. Panda, B. and Mychalowycz, E. (1997). "Aeroelastic Stability Wind Tunnel Testing with Analytical Correlation of the Comanche Bearingless Main Rotor," *Journal of the American Helicopter Society,* Vol. 42, No. 3, July, pp. 207–217.
11. Pang, L., Kamath, G.M., and Wereley, N.M. (1998). "Dynamic Characterization and Analysis of Magnetorheological Damper Behavior," 5th Symposium on Smart Structures and Materials, Passive Damping and Isolation Conference, San Diego, CA, March 1–5, SPIE Paper No. 3327–3325.
12. Spencer, B.F., Dyke, S.J., Sain, M.K., and Carlson, J.D. (1997). "Phenomenological Model of a Magnetorheological Damper," *ASCE Journal of Engineering Mechanics,* Vol. 123, No. 3, pp. 230–238.
13. Weiss, K.D., Carlson, J.D., and Nixon, D.A. (1994). "Viscoelastic Properties of Magneto- and Electro-Rheological Fluids," *J. Intelligent Material Systems and Structures,* Vol. 5, pp. 772–775.
14. Wereley, N.M., Pang, L., Kamath, G.M. (1998). "Idealized Hysteresis Modeling of Electrorheological and Magnetorheological Dampers," *Journal of Intelligent Material Systems and Structures,* Vol. 9, No. 8, August, pp. 642–649.

AIAA JOURNAL
Vol. 39, No. 7, July 2001

Characterization and Analysis of Magnetorheological Damper Behavior Under Sinusoidal Loading

Rebecca A. Snyder,* Gopalakrishna M. Kamath,† and Norman M. Wereley‡
University of Maryland, College Park, Maryland 20742

The hysteresis behavior of a linear stroke magnetorheological damper is characterized for several magnetic fields and sinusoidal excitations over a nominal operational frequency range of 1.0–3.0 Hz. The behavior of the damper is inadequately modeled using the equivalent viscous damping and the complex modulus. Therefore, four different nonlinear modeling perspectives are discussed for purposes of system identification procedures, including the 1) nonlinear Bingham plastic model, 2) nonlinear biviscous model, 3) nonlinear hysteretic biviscous model, and 4) nonlinear viscoelastic plastic model. The first three nonlinear models are piecewise continuous in velocity. The fourth model is piecewise smooth in velocity. The parameters for each model are identified from an identification set of experimental data; these parameters are then used to reconstruct the force vs displacement and the force vs velocity hysteresis cycles for the respective model. Model performance is evaluated by calculating equivalent viscous damping and force time history errors between the model fit and the experimental data. In addition to the identification study, a validation study was done. Model parameters were calculated for offset values of current and frequency. These intermediate parameters were used to calculate hysteresis cycles, which were compared with a second set of experimental data, a validation data set. Identification and validation study results including damping levels and force time history errors.

Nomenclature

$a(t)$ = acceleration input to damper shaft
C_{eq} = equivalent (linearized) viscous damping
C_{po} = postyield viscous damping [nonlinear hysteretic biviscous (NHBV)]
C_{pr} = preyield viscous damping (NHBV)
C_{ve} = preyield viscoelastic damping [nonlinear viscoelastic plastic (NVEP)]
C_{vi} = postyield viscous damping (NVEP)
E = energy dissipated by damper
F_c = yield force constant (NVEP)
F_y = yield force (NHBV)
$f(t)$ = force measurement
I = applied current
K_{ve} = preyield viscoelastic stiffness (NVEP)
K^* = damper complex stiffness
K' = damper in-phase or storage stiffness
K'' = damper quadrature or loss stiffness
S_c = yield force shape function
S_{ve} = preyield viscoelastic shape function
S_{vi} = postyield viscous shape function
$v(t)$ = velocity input to damper shaft
v_y = yield velocity
v_0 = zero force velocity intercept
v_1 = compressive yield velocity
v_2 = tensile yield velocity
X_0 = sinusoidal displacement amplitude
$x(t)$ = displacement input to damper shaft
ϵ_c = yield force shape function parameter (NVEP)
ϵ_y = yield shape function parameter (NVEP)
Ω = frequency of sinusoidal damper excitation

I. Introduction

ELECTRORHEOLOGICAL (ER) and magnetorheological (MR) fluids belong to the class of smart materials that have the unique ability to change properties when electric or magnetic field is applied. When field is applied to an ER or MR fluid, this change is primarily manifested as a substantial increase in the dynamic yield stress of the fluid, while the viscosity remains relatively constant.[1] When compared to ER fluids, MR fluids have superior properties, including an order of magnitude higher yield stress, typically 50–100 kPa, and a much wider operational temperature range, typically −40 to 150°C. High payoff can result by applying these materials in dampers for aerospace systems such as the lag mode damper for stability augmentation of helicopter rotor systems,[2] dampers for landing gear to enhance crashworthiness,[3,4] and shock and vibration isolation mounts for avionics packages.

A critical element in the design of such systems is the evaluation of system dynamics via simulation, for which the nonlinear behavior of the semiactive ER/MR damper must be properly represented. The damper model also plays an important role in the choice of the control strategy for a given application. Some of the existing semiactive control strategies assume a linear damper model (a purely viscous element or a Kelvin chain) with field-dependent coefficients.[5,6]

There are several potential pitfalls in assuming a linear damper model for the MR damper. The major problem with the linear model is the inability to capture the nonlinear dynamic behavior, or nonelliptical force vs displacement hysteresis cycle, exhibited during sinusoidal excitations. Linear models can predict equivalent viscous energy dissipation but are unable to predict force response. Although the damping is modeled well, these linear models represent the force response of the MR damper as a dashpot with a constant value for damping. However, the MR damper operates in two distinct regions, low speed and high speed, each with its own distinct value of damping.

Other problems with using a linear model to describe nonlinear dampers are discussed by Kunz,[7] as applied to helicopter lag dampers. The behavior of a lag damper is dependent upon amplitude and frequency of motion. These factors cause nonlinearities in the damper behavior, which linear models such as the equivalent viscous damping and the complex modulus cannot capture. Another drawback to the equivalent viscous damping and the complex

---

Presented as Paper 98-2040 at the AIAA/ASME/AHS Adaptive Structures Forum, Long Beach, CA, 20–23 April 1998; received 10 August 1998; revision received 18 March 1999; accepted for publication 25 September 2000. Copyright © 2001 by the authors. Published by the American Institute of Aeronautics and Astronautics, Inc., with permission.

*Graduate Research Assistant, Smart Structures Laboratory, Alfred Gessow Rotorcraft Center, Department of Aerospace Engineering; rebsny@glue.umd.edu. Member AIAA.

†Research Scientist, Smart Structures Laboratory, Alfred Gessow Rotorcraft Center, Department of Aerospace Engineering; currently Scientist, National Aerospace Laboratories, Bangalore 560 017, India.

‡Associate Professor of Aerospace Engineering, Smart Structures Laboratory, Alfred Gessow Rotorcraft Center, Department of Aerospace Engineering; wereley@eng.umd.edu. Member AIAA.

modulus is that they are frequency dependent; therefore, these linear models can only be used to predict the steady-state response of a linear damper.[8] Presented in this paper is a comparative analysis of models that can be used to describe ER/MR damper behavior in this context for steady state sinusoidal excitation.

We present four mechanisms-based modeling perspectives with which to analyze the nonlinear damper behavior: 1) the Bingham plastic model,[9,10] 2) the nonlinear biviscous model,[11,12] 3) the nonlinear hysteretic biviscous model,[13] and 4) the nonlinear viscoelastic plastic model.[8,14,15] In these models force vs velocity damper behavior is extrapolated from analogous shear stress vs shear rate constitutive behavior of ER/MR fluids. The first three models are piecewise continuous in velocity. These models increase in complexity by adding progressively more parameters. The fourth model, the nonlinear viscoelastic plastic model, is piecewise smooth in velocity. The nonlinear hysteretic biviscous model can be used to motivate our nonlinear viscoelastic plastic model[8,14,15] and to improve the parameter optimization procedures used to identify its parameters. Other generalized hysteresis models have been proposed for MR dampers of this type, such as Bouc–Wen hysteresis model.[16,17] However, our objective is to improve understanding of force vs displacement and force vs velocity damper behavior by developing a mechanisms-based modeling perspective.

Along with characterizing the behavior of the MR damper based on experimental data, we will demonstrate the ability of the nonlinear hysteretic biviscous and the nonlinear[8,14,15] viscoelastic plastic models to capture both the force vs displacement and force vs velocity behavior of the damper over its entire operating range. Model parameters for each of the four models are identified using an experimental data set. These parameters were used to both reconstruct the hysteresis cycles, which are compared with the experimental data from the identification data set, and to interpolate values for the model parameters for different frequencies and applied currents. The identified model is then validated using a second validation data set. Interpolated model parameters are used to reconstruct the hysteresis cycle data in the validation set. Again, the error between predicted and measured damping and force time histories is calculated. This allows an assessment of the model performance for data not used in its identification.

A systematic procedure with which to analyze the hysteresis behavior caused by steady-state sinusoidal excitation of MR dampers. Because the rheological behavior of ER fluids is qualitatively similar to that of MR fluids,[18] these results can also be extended to ER dampers. We will evaluate the performance of these models by comparing model identification and predictions with experimental force vs displacement and force vs velocity hysteresis cycle data.

II. Damper Testing

The magnetorheological (MR) linear stroke damper used for this study is a commercially available truck seat damper manufactured by the Lord Corporation. This damper was chosen in order to present a case study that can easily be replicated. A schematic of the nominal MR damper is shown in Fig. 1a. The hydraulic cylinder of the damper is nominally 102 mm (4 in.) in length and 45 mm (1.75 in.) in diameter. As shown in Fig. 1a, the hydraulic cylinder houses the damper piston, in which is mounted a magnetic circuit. At the base and inside the hydraulic cylinder is a nitrogen accumulator that is used to pressurize the approximately 50 ml of MR fluid to above atmospheric pressure. This is a standard technique used to prevent cavitation on the low pressure side of the piston while it is in motion. The MR fluid flows through an annular orifice in the piston head, where it can be activated by a current applied to the magnetic circuit. Additional discussions of this damper are given by Dyke et al.[16] and Spencer et al.[17]

The MR damper was tested in order to determine steady-state characteristics for sinusoidal velocity inputs. Testing of the MR damper was done at varying frequencies and magnetic fields, thus creating two separate test matrices. The first data set was used to identify model parameters. The identification data were collected using applied currents in the range of 0–1.0 A in increments of 0.2 A, with a sinusoidal excitation of the damper shaft through a frequency range of 1.00–3.00 Hz in increments of 0.25 Hz. To create a magnetic field inside the damper, electric current is used to activate a magnetic circuit. Measurements of magnetic field applied to the damper are not available; hence, applied current is used to gauge magnetic field strength. The validation, or second, data set is used to validate the hysteresis cycles reconstructed from interpolated model parameters of the nonlinear hysteretic biviscous and the nonlinear viscoelastic plastic models. For this test matrix the damper was tested using current ranging from 0–0.9 A in increments of 0.2 A. The frequencies tested for the validation data set range from 1.125–2.875 Hz in increments of 0.25 Hz. The test conditions for the identification and validation experimental matrices are shown in Tables 1 and 2, respectively.

Table 1 Tested 54 unique operating conditions to create an identification data set

Applied current I, A	Sinusoidal frequency Ω, Hz 1.00	1.25	1.50	1.75	2.00	2.25	2.50	2.75	3.00
0	×	×	×	×	×	×	×	×	×
0.2	×	×	×	×	×	×	×	×	×
0.4	×	×	×	×	×	×	×	×	×
0.6	×	×	×	×	×	×	×	×	×
0.8	×	×	×	×	×	×	×	×	×
1.0	×	×	×	×	×	×	×	×	×

Table 2 Tested 48 unique operating conditions to create a validation data set

Applied current I, A	Sinusoidal frequency Ω, Hz 1.125	1.375	1.625	1.875	2.125	2.375	2.625	2.875
0	×	×	×	×	×	×	×	×
0.1	×	×	×	×	×	×	×	×
0.3	×	×	×	×	×	×	×	×
0.5	×	×	×	×	×	×	×	×
0.7	×	×	×	×	×	×	×	×
0.9	×	×	×	×	×	×	×	×

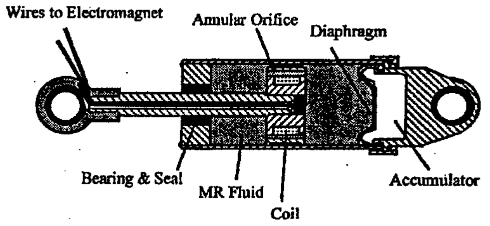

Fig. 1a Cross section of the Rheonetics SD-1000-2 MR damper. Courtesy of Lord Corporation.

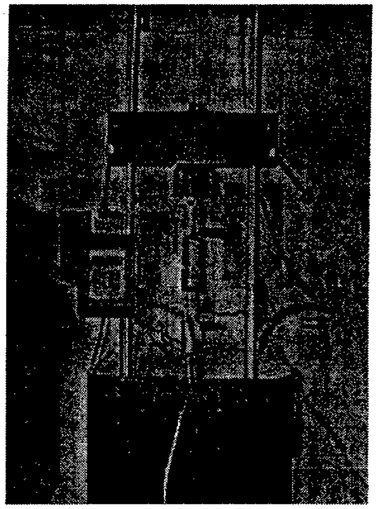

Fig. 1b Mechanical damper dynamometer used for damper testing.

MR damper testing was done using a 5-hp Roehrig Engineering mechanical damper dynamometer, as shown in Fig. 1b. A sinusoidal shaft displacement of 25.4-mm (1-in.) amplitude, measured using a linear variable differential transformer, was used to excite the dampers and the resulting force was measured using a load cell. The resulting force vs displacement and force vs velocity hysteresis cycles were measured for every test condition in each test matrix. Applied current, and hence magnetic field, was controlled using a power supply, which provided current to the electromagnet inside the damper.

III. Filtering of Data

During each test, nominally one cycle of force vs displacement data was measured, and the force vs velocity hysteresis cycle was calculated.

Calculating the velocity and acceleration signals using a finite difference method tended to accentuate noise, especially in the acceleration signal. Instead, the velocity and acceleration were calculated by differentiating a Fourier-series expansion. A periodic Fourier series was used to minimize the effects of this noise in the input displacement signal and the subsequent differentiations to obtain the input velocity and acceleration signals.[19]

The force signal was not filtered because the damper response was nonlinear and it could not be determined a priori exactly which harmonics contributed to the damper response and/or noise. Therefore, we conservatively used the measured (unfiltered) force data in both the model parameter identification and prediction studies.

IV. Experimental Results

Typical filtered hysteresis data is shown in Fig. 2. The force vs displacement [$f(t)$ vs $x(t)$] and the force vs velocity [$f(t)$ vs $v(t)$] hysteresis cycles show applied currents of 0.2, 0.4, 0.6, and 1.0 A at a frequency of $\Omega = 2.00$ Hz.

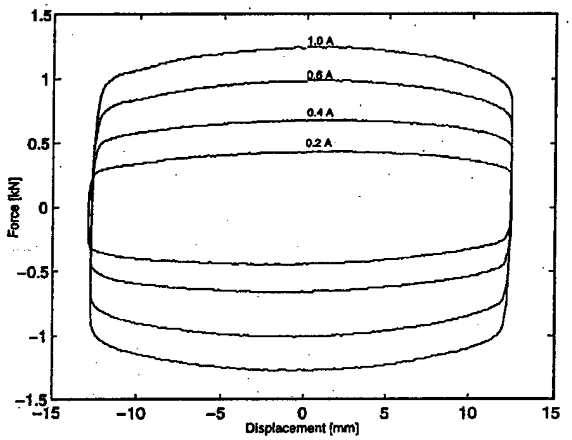

a) Force vs displacement

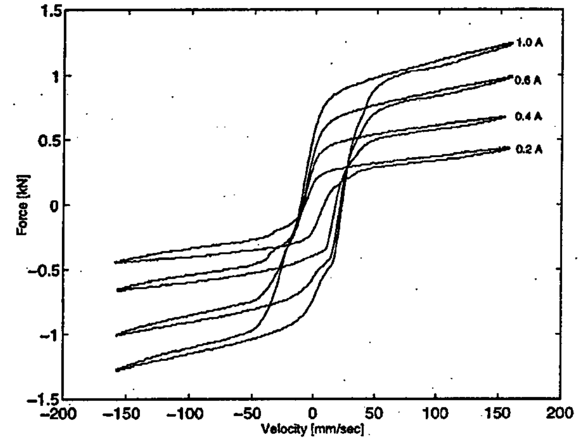

b) Force vs velocity

Fig. 2 Hysteresis cycles for the MR damper for sinusoidal excitation at 2 Hz.

As shown in Fig. 2a, as the applied current to the electromagnet is increased the magnetic field increases, and hence the amount of damping also increases, which is represented by the increasing area enclosed by the force vs displacement hysteresis cycle. The Bingham plastic-like behavior[20,21] of the MR damper can be seen in the force vs velocity hysteresis cycles as shown in Fig. 2b. Consider the high-velocity asymptote of an individual force vs velocity hysteresis cycle. If this asymptote is projected back to the force axis, this intercept gives the value of the yield force F_y. It is easily seen that this yield force increases as the applied current (magnetic field) increases. When the damper restoring force is less than this yield force, the damper is said to be operating in the preyield region. When the restoring force is greater than the yield force, the damper is said to be operating in the postyield region. The yield transition occurs as the damper restoring force transitions through the yield force value.

V. Linear Damper Models

A. Equivalent Viscous Damping

Equivalent viscous damping is a standard linearization technique that could be applied to a nonlinear damper such as this MR damper. Here, the damper restoring force $f(t)$ is proportional to damper shaft velocity $v(t)$ as

$$f(t) = C_{eq} v(t) \tag{1}$$

The equivalent viscous damping C_{eq} is computed by equating the energy dissipated over a cycle E at frequency Ω using

$$E = \oint F(t)\,\mathrm{d}x = \int_0^{2\pi/\Omega} F(t)v(t)\,\mathrm{d}t \tag{2}$$

and equating the dissipated energy of the nonlinear device to that of an equivalent viscous damper:

$$C_{eq} = E\big/\pi\Omega X_0^2 \tag{3}$$

The energy dissipated over one cycle is computed using the trapezoidal rule. The equivalent viscous damping is calculated using Eq. (3) for each test case. The results from the identification set are shown in Fig. 3. As a result of this characterization procedure, the damper is linearized to be an ideal dashpot at every operating condition so that C_{eq} is a function of both the input current I and the displacement amplitude X_0.

B. Complex Modulus

A second linear characterization approach is to characterize the complex damper stiffness K^* as the in-phase or storage stiffness K'

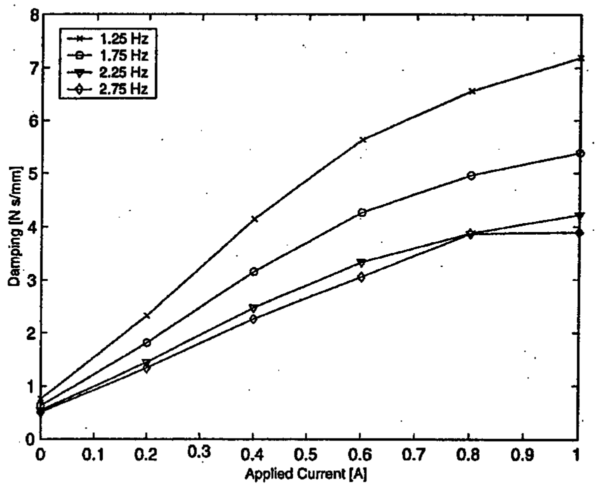

Fig. 3 Equivalent viscous damping is plotted vs applied current for several tested frequencies.

and quadrature or loss stiffness K'' so that

$$K^* = K' + jK'' = K'(1 + j\eta) \tag{4}$$

where η is the loss factor. This is a common approach in the characterization of elastomeric dampers.[2,22–24] To determine the damper force,

$$\begin{aligned} f(t) &= F_c \cos \Omega t + F_s \sin \Omega t \\ &= K'x(t) + (K''/\Omega)v(t) \end{aligned} \tag{5}$$

Here F_c and F_s are the cosine and sine Fourier coefficients of $f(t)$ at frequency Ω. We assume that the displacement is sinusoidal:

$$x(t) = X_c \cos \Omega t + X_s \sin \Omega t \tag{6}$$

where X_c and X_s are the cosine and sine Fourier coefficients of $x(t)$ at frequency Ω. Substituting $x(t)$ into the force equation and equating the sine and cosine terms yields the in-phase and quadrature stiffnesses as

$$K' = \frac{F_c X_c + F_s X_s}{X_c^2 + X_s^2}, \qquad K'' = \frac{F_c X_s - F_s X_c}{X_c^2 + X_s^2} \tag{7}$$

The storage stiffness K' is sometimes called the *effective* or *equivalent stiffness*. The loss stiffness K'' is approximately related to the equivalent viscous damping by

$$C_{\mathrm{eq}} \approx K''/\Omega \tag{8}$$

The relation is approximate because the complex stiffness considers only the harmonic of the force at frequency Ω, whereas the equivalent damping considers all harmonics of the force.

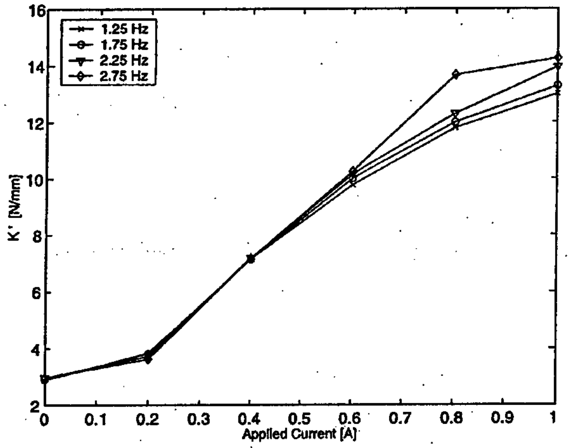

Fig. 4a Storage stiffness K' vs applied current.

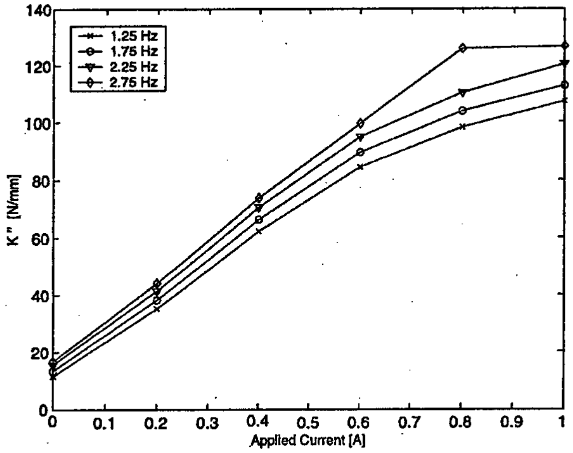

Fig. 4b Quadrature stiffness K'' vs applied current.

The estimated values for the equivalent stiffness and the loss stiffness for varying fields and shown in Figs. 4a and 4b. The damping and stiffness values increase as a quadratic function of the field.

VI. Nonlinear Damper Models

We discuss four perspectives with which to describe the behavior of the MR damper for oscillatory sinusoidal loading conditions: 1) nonlinear Bingham plastic model,[9,10] 2) nonlinear biviscous model,[11,12] 3) a nonlinear hysteretic biviscous model, and 4) nonlinear viscoelastic plastic model.[8,14,15] The first three models are piecewise continuous in velocity, and the fourth model is piecewise smooth in velocity.

A. Bingham Plastic Model

By adding a yield force to a linear damping model, the nonlinear Bingham plastic model results. This shear flow mechanism has been used to develop predictive models assuming both parallel plate geometry[25–27] or axisymmetric geometry.[20,21,28] Yield force F_y and postyield damping C_{po} are included in the model. A schematic of this model is shown in Fig. 5a. The equations describing this damper model are

$$f(t) = \begin{cases} C_{\mathrm{po}} v + F_y & v > 0 \\ -F_y < f(t) < F_y & v = 0 \\ C_{\mathrm{po}} v - F_y & v < 0 \end{cases} \tag{9}$$

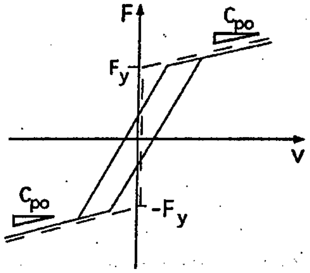

a) Nonlinear Bingham plastic

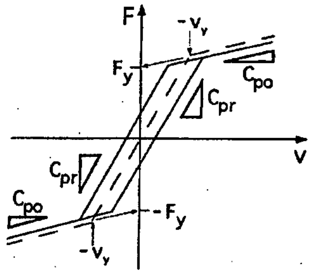

b) Nonlinear biviscous

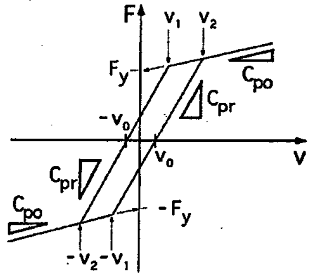

c) Nonlinear hysteretic biviscous

Fig. 5 Schematics of piecewise continuous nonlinear damper models. The idealized model force vs velocity behavior is represented by a - - -, whereas the —— is representative of actual damper behavior.

The nonlinear Bingham plastic model is often expressed as

$$f(t) = F_y \operatorname{sign}[v(t)] + C_{\text{po}} v(t) \tag{10}$$

The model assumes that in the preyield condition the material is rigid and does not flow; hence, when $|f(t)| < F_y$ the shaft velocity $v = 0$. Once the force applied to the damper exceeds the yield force, then the fluid begins to flow, and the material is essentially a Newtonian fluid with a nonzero yield stress, as shown in Fig. 5a. In this damper model the yield force is obtained from the postyield force vs velocity asymptote intercept with the force axis, as shown in Fig. 5a.

B. Nonlinear Biviscous Model

Rather than assuming that the MR fluid is rigid in the preyield condition, we adopt the nonlinear biviscous model developed by Stanway et al.,[11] where it is assumed the MR fluid is plastic in both the preyield and the postyield conditions. However, the preyield damping C_{pr} should be assumed to be much greater than the postyield damping C_{po} or $C_{\text{pr}} > C_{\text{po}}$. In this damper model the yield force is still represented by the postyield force vs velocity asymptote intercept with the force axis, as shown in Fig. 5b. The advantage of a plastic preyield mechanism is that it accounts for the preyield damping portion of the typical viscoelastic preyield behavior of an ER or MR fluid. Versions of this model have been adopted to analyze leakage in ER dampers.[12,29] The equations describing this model are

$$f(t) = \begin{cases} C_{\text{po}} v + F_y & v \geq v_y \\ C_{\text{pr}} v & -v_y \geq v \leq v_y \\ C_{\text{po}} v - F_y & v \leq -v_y \end{cases} \tag{11}$$

where the yield velocity is given by

$$v_y = F_y / (C_{\text{pr}} - C_{\text{po}}) \tag{12}$$

C. Nonlinear Hysteretic Biviscous Model

Based on damper behavior observed during testing, the force vs velocity behavior shows a distinct preyield hysteresis. A four-parameter nonlinear hysteretic biviscous model that has a clear physical motivation is introduced. The nonlinear hysteretic biviscous model is an extension of Stanway et al.'s nonlinear biviscous constitutive model[11] with an improved representation of the preyield hysteresis. The preyield hysteresis is modeled by adding a fourth parameter, that is, the zero force velocity intercept v_0 to the three prior parameters: the preyield viscous damping C_{pr}, the postyield viscous damping C_{po}, and the yield force F_y. The equations of the piecewise continuous nonlinear hysteretic biviscous model, schematized in Fig. 5c, are

$$f(t) = \begin{cases} C_{\text{po}} v - F_y & v \leq -v_1 & \dot{v} > 0 \\ C_{\text{pr}}(v - v_0) & -v_1 \leq v \leq v_2 & \dot{v} > 0 \\ C_{\text{po}} v + F_y & v_2 \leq v & \dot{v} > 0 \\ C_{\text{po}} v + F_y & v_1 \leq v & \dot{v} < 0 \\ C_{\text{pr}}(v + v_0) & -v_2 \leq v \leq v_1 & \dot{v} < 0 \\ C_{\text{po}} v - F_y & v \leq -v_2 & \dot{v} < 0 \end{cases} \tag{13}$$

where we have introduced the compressive yield velocity v_1 and the tensile yield velocity v_2, given by

$$v_1 = \frac{F_y - C_{\text{pr}} v_0}{C_{\text{pr}} - C_{\text{po}}}, \qquad v_2 = \frac{F_y + C_{\text{pr}} v_0}{C_{\text{pr}} - C_{\text{po}}} \tag{14}$$

The hysteresis cycle is separated into two groups of equations. The first group of three equations are for positive acceleration, whereas the second three are for negative acceleration.

D. Nonlinear Viscoelastic Plastic Model

As shown by the experimental force vs velocity hysteresis cycle data in Fig. 2b, there are two distinct rheological domains over which the dampers operate: the preyield and postyield regions. The preyield region exhibits a strong hysteresis, which is typical of a viscoelastic material. The postyield region is plastic with a nonzero yield force, as in the nonlinear Bingham plastic, biviscous, and hysteretic biviscous models. The yield force varies as a function of the applied current (magnetic field), as observed from Fig. 2. We now describe the structure of the nonlinear viscoelastic plastic model, a block diagram of which is depicted in Fig. 6.

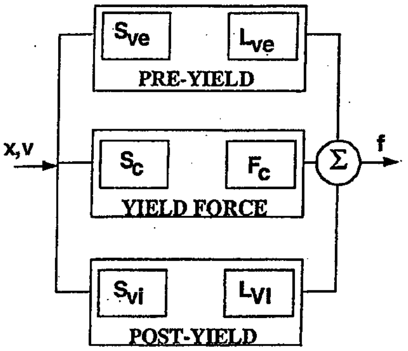

Fig. 6 Schematic of the nonlinear viscoelastic plastic model used to represent MR damper behavior.

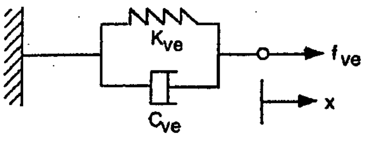

a) Viscoelastic mechanism L_{ve} in the preyield branch of the model

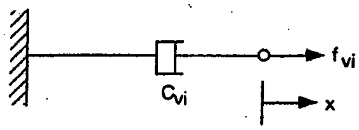

b) Viscous mechanism L_{vi} in the postyield branch of the model

Fig. 7 Mechanisms used in the viscoelastic plastic model.

1. Preyield Mechanism

The Kelvin chain element shown in Fig. 7a is used as the mechanical analog representing the viscoelastic behavior of the damper in the preyield region. The differential equation representing this mechanism in the time domain is

$$f_{\text{ve}}(t) = K_{\text{ve}} x(t) + C_{\text{ve}} v(t) \tag{15}$$

Here f_{ve} is the viscoelastic component of the damper force. The nonlinear shape function S_{ve} is the preyield switching function, which along with an analogous postyield switching function S_{vi} effects the smooth transition from the preyield phase to the postyield phase. The function S_{ve} is dependent on the yield velocity v_y that is chosen during the estimation process. S_{ve} is given by

$$S_{\text{ve}}(v) = \frac{1}{2}\left[1 - \tanh\left(\frac{|v| - v_y}{4\epsilon_y}\right)\right] \tag{16}$$

where $v(t)$ is the instantaneous velocity, and ϵ_y is a smoothening parameter. Thus, the force component caused by the preyield mechanism is given by

$$f_{\text{pr}}(t) = S_{\text{ve}}(v) f_{\text{ve}}(t) \tag{17}$$

2. Postyield Mechanism

In postyield the damper clearly behaves as a viscous damper with a nonzero yield force. The postyield mechanical analog, denoted by L_{vi} in Fig. 6, is the viscous mechanism, which can be represented as a damper in Fig. 7b. Thus, the postyield force component is given by

$$f_{\text{vi}} = C_{\text{vi}} v(t) \tag{18}$$

S_{vi} is similar to the shape function S_{ve}, where S_{vi} acts as a switching function to turn on the postyield viscous mechanism when the damper crosses the yield point. It is given by

$$S_{\text{vi}}(v) = \frac{1}{2}\left[1 + \tanh\left(\frac{|v| - v_y}{4\epsilon_y}\right)\right] \tag{19}$$

Thus, the force component caused by the postyield mechanism is given by

$$f_{\mathrm{po}}(t) = S_{\mathrm{vi}}(v) f_{\mathrm{vi}}(t) \tag{20}$$

3. *Yield Force*

The yield force F_c is a function of the applied field and is the field-dependent parameter that provides the damper with its semiactive capabilities. The Coulomb force or yield force effect seen in the damper behavior at low velocity are described using the yield force parameter F_c and the shape function S_c as given by the equation

$$S_c(v) = \tanh(v/4\epsilon_c) \tag{21}$$

where $v(t)$ is the velocity amplitude and ϵ_c is the smoothening factor that ensures smooth transition from the negative to positive velocities and vice versa. The force component caused by the yield force is given by

$$f_c(t) = S_c(v) F_c \tag{22}$$

4. *Mechanisms-Based Model*

For a sinusoidal displacement input the force output of the nonlinear viscoelastic plastic model is written as

$$\begin{aligned} f(t) &= f_{\mathrm{pr}}(t) + f_{\mathrm{po}}(t) + f_c(t) \\ &= S_{\mathrm{ve}}(v) f_{\mathrm{ve}} + S_{\mathrm{vi}}(v) f_{\mathrm{vi}} + S_c(v) F_c \end{aligned} \tag{23}$$

or, the total force is a nonlinear combination of the forces from each of the linear mechanisms.

The viscoelastic-plastic model combines linear mechanisms using nonlinear shape functions. In addition, the preyield and postyield mechanical analogs, the shape functions, the yield force effect, and nonlinear combination of these component forces to obtain the total predicted force, are based on observed damper behavior.

VII. Parameter Identification

The parameters associated with the nonlinear damper models are identified by minimizing the mean squared error between the measured force and the force predicted by the model, subject to constraints that the parameters be positive. The model parameters are determined only from the identification data set. These procedures are briefly described next.

A. Nonlinear Hysteretic Biviscous Model

The parameters of the three piecewise continuous models C_{pr}, C_{po}, F_y, and v_0 were identified as a function of applied current (magnetic field) and frequency, using a constrained least-mean-squared (LMS) error minimization procedure using MATLAB® subroutines. Only a single optimization procedure is required to identify the parameters of the nonlinear hysteretic biviscous model, the parameters of which are used for all three nonlinear models: Bingham plastic,

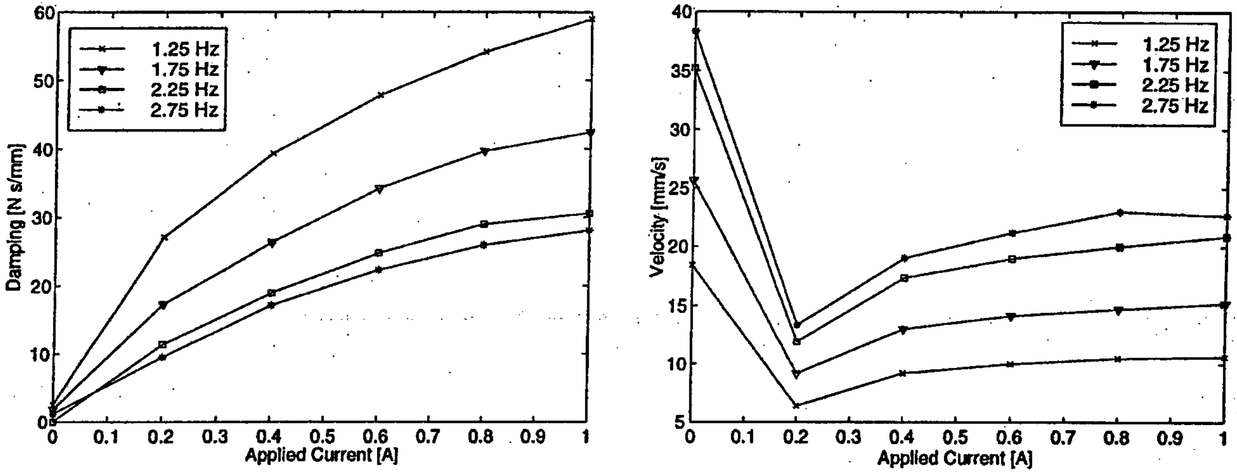

a) Preyield damping

c) Zero force velocity intercept

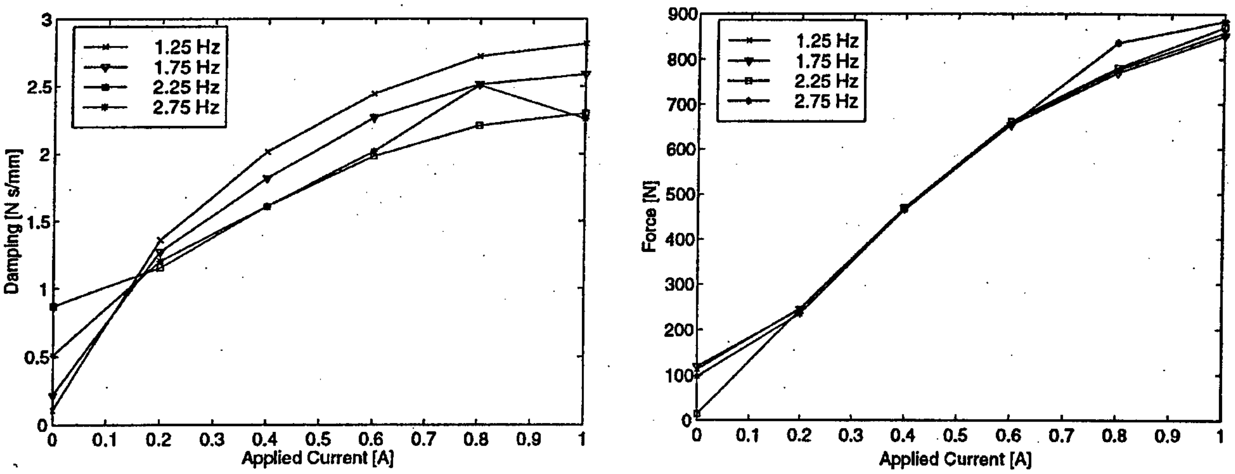

b) Postyield damping

d) Yield force

Fig. 8 Four parameters of preyield damping C_{pr}, postyield damping C_{po}, zero force velocity intercept v_0, and yield force F_y are plotted vs applied current for the linear stroke MR damper.

biviscous, and hysteretic biviscous. A cost function J was defined as

$$J(C_{\mathrm{pr}}, v_0, C_{\mathrm{po}}, F_y) = \sum_{k=1}^{N} [f(t_k) - \hat{f}(t_k)]^2 \tag{24}$$

where $\hat{f}(t_k)$ is the force calculated using the equations of the nonlinear hysteretic biviscous model from Eq. (13), $f(t_k)$ is the measured force, and t_k is the time at which the kth sample was taken. The four parameters of C_{pr}, C_{po}, F_y, and v_0 are estimated so as to minimize the cost function J. The values of C_{pr}, C_{po}, F_y, and v_0 are all constrained to be greater than zero, and $C_{\mathrm{pr}} > C_{\mathrm{po}}$. The parameter optimization is performed on each test case of the identification data set. In Fig. 8 the four parameters of preyield damping C_{pr}, postyield damping C_{po}, zero force velocity intercept v_0, and yield force F_y are plotted vs applied current.

B. Nonlinear Viscoelastic Plastic Model

The parameters of the nonlinear viscoelastic plastic model C_{ve}, K_{ve}, C_{vi}, F_c, v_y, ϵ_y, and ϵ_c are functions of both applied field and frequency. In this case the cost function J was defined as

$$J(C_{\mathrm{ve}}, K_{\mathrm{ve}}, v_y, \epsilon_y, F_c, \epsilon_c, C_{\mathrm{vi}}) = \sum_{k=1}^{N} [f(t_k) - \hat{f}(t_k)]^2 \tag{25}$$

where $\hat{f}(t_k)$ is the force calculated using the equations of the nonlinear viscoelastic plastic model, $f(t_k)$ is the measured force, and t_k

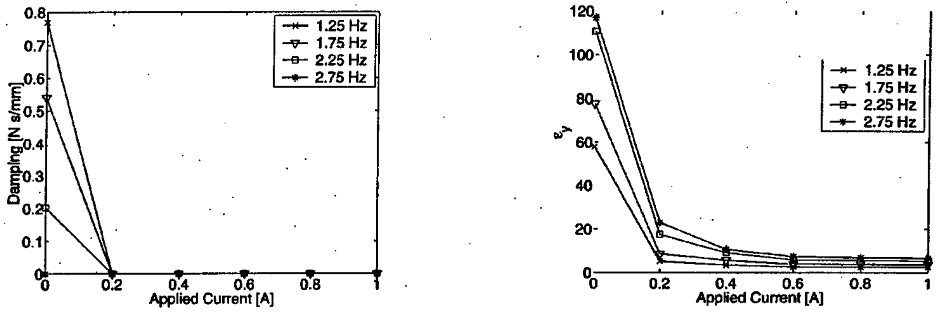

a) Preyield damping C_{ve}

d) Yield parameter ϵ_y

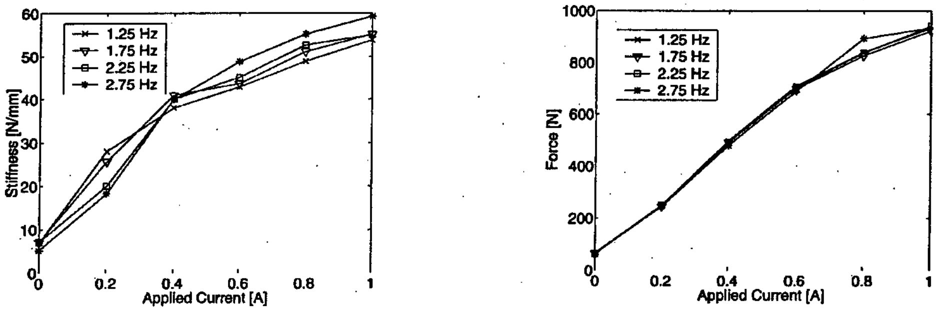

b) Preyield stiffness K_{ve}

e) Yield force F_y

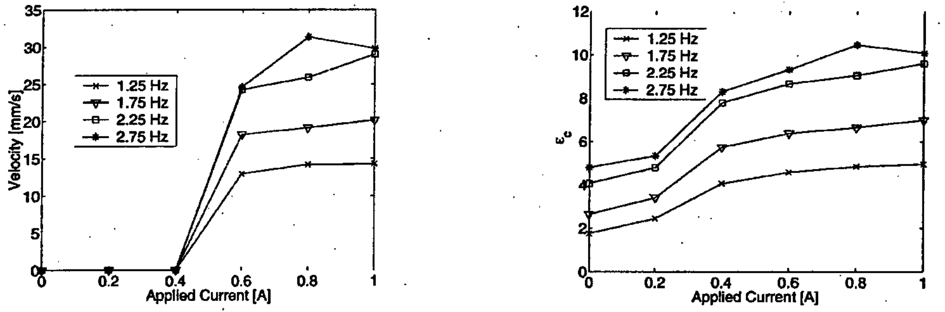

c) Yield velocity v_y

f) Yield force parameter ϵ_c

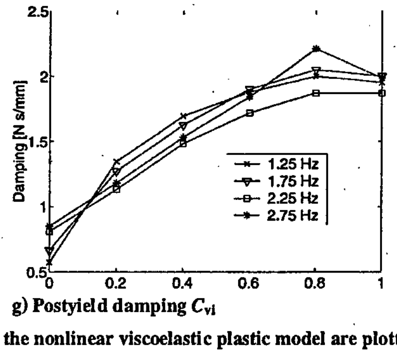

g) Postyield damping C_{vi}

Fig. 9 Parameters of the nonlinear viscoelastic plastic model are plotted vs applied current.

is the time at which the kth sample was taken. The seven parameters of the model are estimated so as to minimize the cost function J and are constrained to be greater than zero. The parameter optimization is performed for each tested condition of applied current and frequency.

An important problem is selecting the initial conditions for the optimizer. These initial conditions are based on the values calculated from the nonlinear hysteretic biviscous parameter optimization:

$$C_{\text{vi}} = C_{\text{po}}, \qquad F_c = F_y, \qquad v_y = v_0 \tag{26}$$

The initial conditions for the smoothening parameters ϵ_c and ϵ_y were typically chosen to be values between 0 and 10 depending on the test case. Initial conditions of the preyield mechanism parameters K_{ve} and C_{ve} were selected to be a small positive number and zero, respectively. In Fig. 9 the seven parameters of the viscoelastic plastic model plotted vs applied current.

VIII. Parameter Identification Results

The parameters obtained from the optimization procedure are used in their respective models to reconstruct hysteresis cycles. The force vs displacement and the force vs velocity cycles reconstructed from the parameters are then compared with the experimental data in the identification set.

A. Piecewise Continuous Models

The model parameters are used to reconstruct the force vs displacement and force vs velocity hysteresis cycles for each of the three piecewise continuous models. Figures 10–12 show the reconstructed hysteresis cycles using the optimized parameters for the nonlinear Bingham plastic, nonlinear biviscous, and the nonlinear hysteretic biviscous models. Applied currents of $I = 0.2$ and 1.0 A at a frequency of $\Omega = 2.0$ Hz are shown for each of the models.

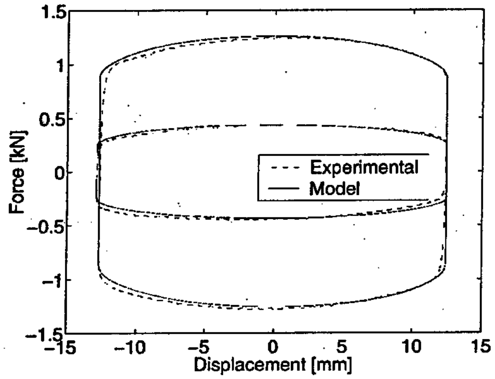

a) Bingham plastic force vs displacement

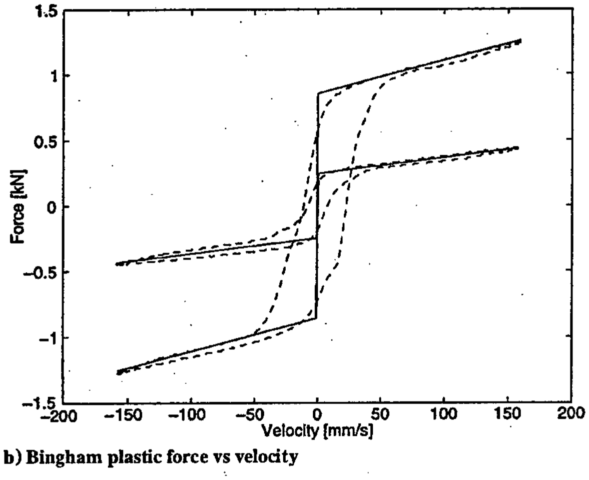

b) Bingham plastic force vs velocity

Fig. 10 Bingham plastic model reconstructions shown with experimental data. Test cases shown are $I = 0.2, 1.0$ A; $\Omega = 2.00$ Hz.

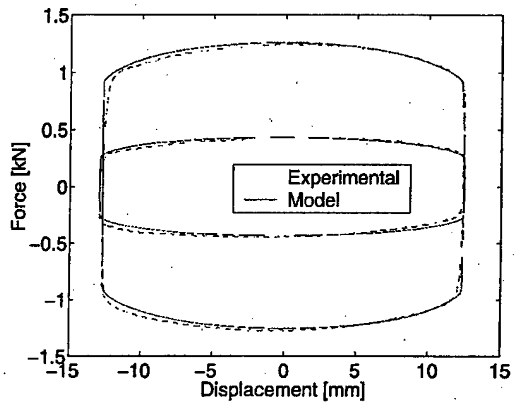

a) Biviscous force vs displacement

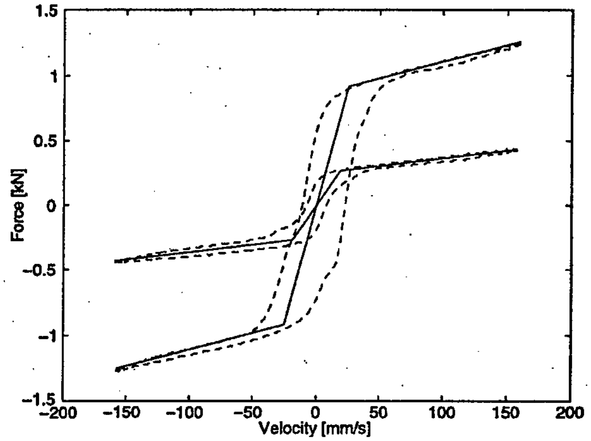

b) Biviscous force vs velocity

Fig. 11 Nonlinear biviscous model reconstructions shown with experimental data for test cases $I = 0.2, 1.0$ A; $\Omega = 2.00$ Hz.

For the nonlinear Bingham plastic model the comparison of modeled and experimental force vs displacement shown in Fig. 10a, the force vs velocity is shown in Fig. 10b. By adding a yield force to the postyield viscous damping, the Bingham plastic model accurately represents the postyield force vs velocity behavior. However, the rigid preyield characteristic is not representative of the measured preyield behavior.

For the nonlinear biviscous model the comparison of force vs displacement and force vs velocity is shown in Figs. 11a and 11b, respectively. The rigid preyield of the Bingham plastic model is replaced by a viscous preyield mechanism in order to have a more realistic preyield behavior. However, the preyield force vs velocity hysteresis is still not captured by this model.

For the nonlinear hysteretic biviscous model the force vs displacement and force vs velocity hysteresis cycles are shown in Figs. 12a and 12b. Of the piecewise continuous models the nonlinear hysteretic biviscous model most accurately represents the force vs velocity behavior, including the preyield hysteresis. The force vs displacement behavior is equally well represented by all of the piecewise continuous models.

B. Piecewise Smooth Model

The optimized parameter values are used to reconstruct the force vs displacement and force vs velocity hysteresis cycles for all of the tested conditions of the identification set. Shown in Figs. 13a and

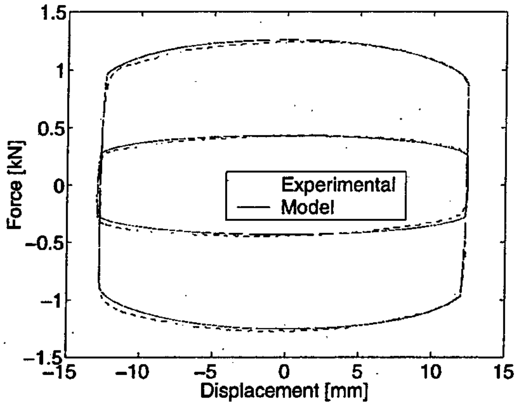

a) Hysteretic biviscous force vs displacement

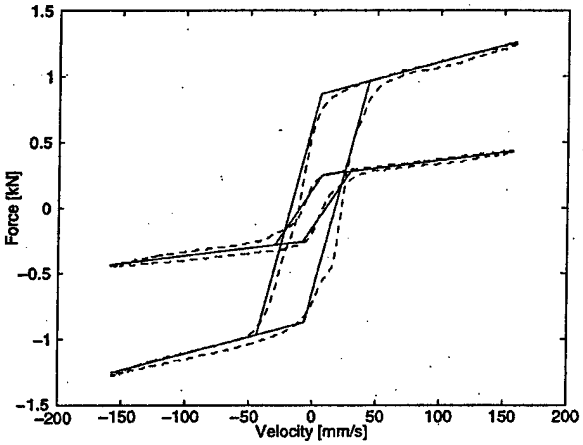

b) Hysteretic biviscous force vs velocity

Fig. 12 Hysteretic biviscous model reconstructions shown with experimental data for test cases $I = 0.2, 1.0$ A; $\Omega = 2.00$ Hz.

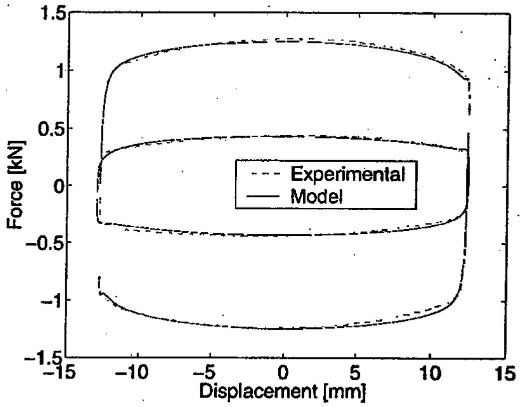

a) Viscoelastic plastic force vs displacement

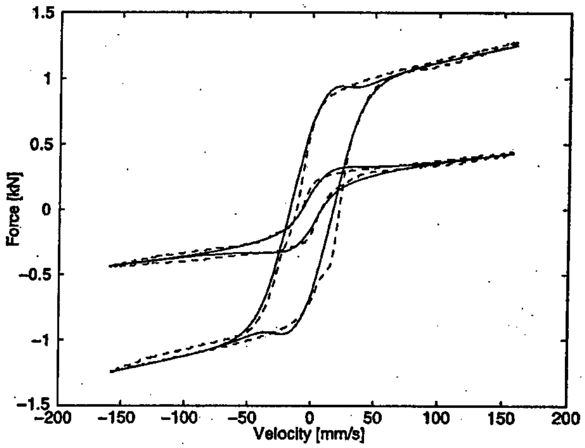

b) Viscoelastic plastic force vs velocity

Fig. 13 Viscoelastic plastic model reconstructions shown with experimental data for test cases $I = 0.2, 1.0$ A; $\Omega = 2.00$ Hz.

13b are the force vs displacement and force vs velocity hysteresis cycles for $\Omega = 2.0$ Hz for the applied current $I = 0.2$ and 1.0 A. This model very accurately reconstructs the force vs velocity behavior, including the preyield hysteresis. The force vs displacement data are also accurately reconstructed.

IX. Model Performance Assessment

To evaluate the performance of each of the four nonlinear models, the error between the experimental and the model values for the equivalent viscous damping and the force time history are calculated.

A. Equivalent Viscous Damping Error

Of critical importance is the modeling of damping or energy dissipation. Here we evaluate how well the nonlinear models identify the energy dissipation over one cycle because the cost function for the parameter optimization techniques was the LMS error in the prediction of the force time history and not the energy dissipation over a cycle. The force vs displacement hysteresis cycle behavior is represented accurately by the three nonlinear piecewise continuous models, but the nonlinear viscoelastic plastic model is a much improved model. The accuracy of the nonlinear models at matching the energy dissipation per cycle is fairly consistent, even though the force vs velocity hysteresis behavior varies significantly between the models. Essentially, the postyield behavior of the damper plays the largest role in describing the energy dissipation, where the velocity is greatest. All of the preyield behavior occurs at relatively lower velocity, making less of an impact on the damping performance.

To illustrate this, consider Figs. 14a and 14b, which show the error between the calculated damping from experimental data and the model during a single cycle of oscillation. Figure 14a shows the average equivalent viscous damping error for the Newtonian cases. The error for each model is obtained by taking the average error for the zero field, or Newtonian cases at all tested frequencies, and the standard deviation for each calculation is shown. As each model captures the hysteresis behavior more accurately, the equivalent viscous damping error is reduced. The overall performance for the Newtonian cases improves from 5.9% error for the Bingham plastic model to 0.1% for the viscoelastic plastic model.

Figure 14b shows the average equivalent viscous damping for the applied current cases, for which the damping error is much lower than for the Newtonian cases. This difference can be attributed to the asymmetric behavior seen in the damper when no field is applied. This effect is mainly caused by the nitrogen accumulator used to prevent cavitation. This asymmetry causes error in the identification of the model parameters, which are calculated using a symmetric model. As the applied field is increased, the hysteresis curves become symmetric because the effects of the accumulator diminish. At higher field strengths the model parameters can accurately be determined by the symmetric models, reducing the error. Figure 14b shows the average damping error for cases with applied field fall between 1.4% for the Bingham plastic model and 0.1% for the viscoelastic plastic model.

B. Force Error

As stated earlier, the postyield region behavior of the damper plays the largest role in the damper behavior. The ability of the

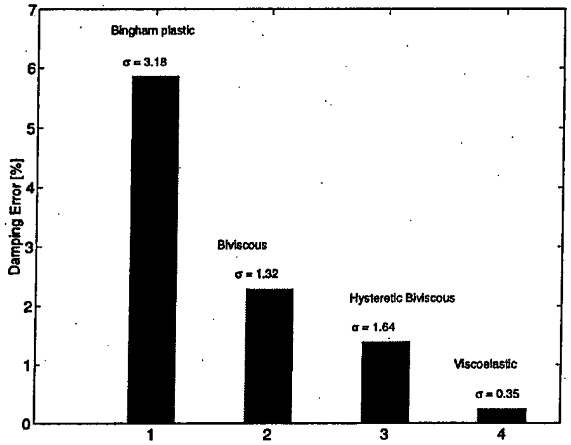

a) Zero field or Newtonian damping error

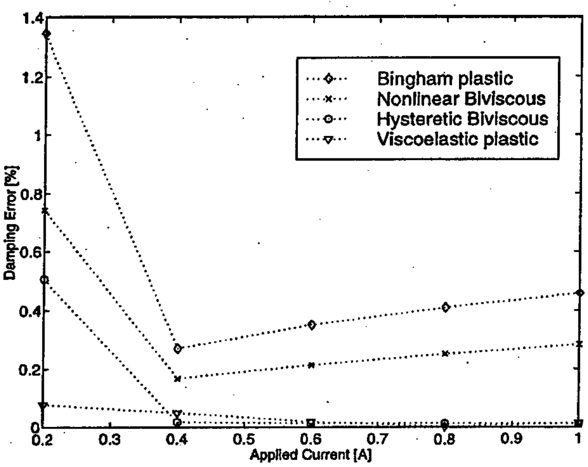

b) Damping error

Fig. 14 Average equivalent viscous damping errors for the identification data set.

nonlinear models to describe the force vs velocity hysteresis curves is extremely important in modeling the MR damper. To compare model performance in the identified force time history, the average error between the measured and identified force time histories is calculated. By calculating the force error for each model, we can get a quantitative measure of how well each model characterizes MR damper behavior. The force error was calculated using

$$\epsilon = \sqrt{\frac{1}{N}\sum_{k=1}^{N}[f(t_k) - \hat{f}(t_k)]^2 \bigg/ f_{\max}} \qquad (27)$$

where $\hat{f}(t_k)$ is the force time history calculated using the equations for each of the models, $f(t_k)$ is the measured force, and t_k is the time at which the kth sample was taken. The rms value is then nondimensionalized by the maximum measured force. For each test case of the identification set the force error was calculated for all four models. These values were then used to calculate an average error for value of field tested.

Figure 15a shows the force error for the Newtonian cases from the identification data set. Again the error is the largest for the Bingham plastic model and decreases as the modeling of the preyield region improves. The error for the Bingham plastic model was 29.5% while the error for the viscoelastic plastic model was 5.5%. The biviscous and the hysteretic biviscous models fall within the range of error between the Bingham plastic and the viscoelastic plastic models.

Figure 15b compares the average force error for non-Newtonian cases for each of the four nonlinear models. Once again the effects of the preyield modeling are seen in the force error. The Bingham plastic model has an average error of 19.4%; with the addition of parameters and smoothing functions to create the viscoelastic plastic model, the force time history error is reduced to 4.5%. These results were generally expected; however, the performance of the hysteretic biviscous model was better than expected with 6.6% error. For higher field cases the nonlinear hysteretic biviscous model performed almost as well as the viscoelastic plastic model.

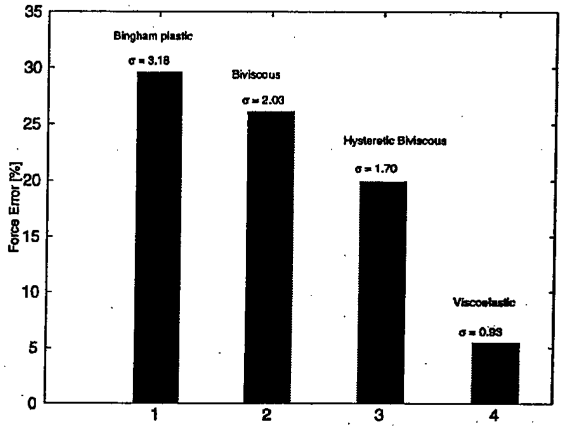

a) Zero field or Newtonian force error

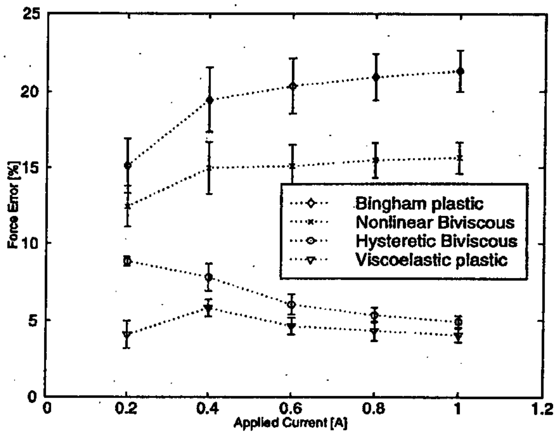

b) Force error

Fig. 15 Average force time history error for the identification data set.

X. Computational Expense

Determining the model parameters through an optimization scheme is both time consuming and costly. When considering which model optimization scheme to use, the tradeoff between model performance and computational time should be considered.

The nonlinear hysteretic biviscous model has four model parameters that must be optimized for every test case. These four model parameters are essentially LMS line fits to the preyield and postyield regions of the force vs velocity data. This optimization is fairly simple, and the optimization of the four model parameters is very efficient. In fact the model parameters of the hysteretic biviscous model can be determined graphically with great accuracy.

The nonlinear viscoelastic plastic model is a piecewise smooth model that has seven parameters. Increasing the number of parameters increases the computational time required to minimize the cost function. Optimization time is also increased because the viscoelastic plastic model is a more complex curve fit than the LMS line fit, which the hysteretic biviscous model uses.

To compare the two models, the CPU running time and the number of flops for each optimization scheme were determined for three test cases representing a low, medium, and a high field strength test. The applied current values were $I = 0.2$ A, 0.6 A, and 1.0 A; the frequency for each of these tests was $\Omega = 2.0$ Hz. Table 3 shows the results from the optimization cases for each model.

Typically the viscoelastic plastic model optimization is 16 times longer than the nonlinear hysteretic biviscous model optimization in terms of CPU processing time and uses three times as many more flops in order to minimize the cost function. The main difficulty that arises with this optimization scheme, other than actual running time, is choosing of initial conditions for each of the seven parameters.

Difficulties with the optimization are caused by incorrectly choosing initial values for each of the seven model parameters. Convergence for the parameters was unlikely to occur if even one of the initial values was chosen incorrectly. Because four of the model parameters are based on the four parameters of the hysteretic biviscous model, it is almost crucial that the nonlinear hysteretic biviscous optimization be run first to obtain values for those four parameters, which are in the correct range. As for the other three parameters, a trial and error method was used for these initial values. The sensitivity to initial conditions makes the nonlinear viscoelastic plastic model optimization scheme both more difficult and more time consuming to use. Quite often in this study test cases had to be run several times to obtain an acceptable fit with the experimental data.

Table 3 Computation effort comparison for the hysteretic biviscous and the viscoelastic models

Parameter	0.2 A	0.6 A	1.0 A
Hysteretic biviscous model optimization results			
Flops, M	4.6	4.5	5.8
CPU time, s	29	37	43
Viscoelastic plastic model optimization results			
Flops, M	12.9	13.3	16.6
CPU time, s	575	593	733

The results from the optimizations show that the viscoelastic plastic model gives slightly better results than the hysteretic biviscous in terms of modeling the damping and force, but a computational price is paid. The hysteretic biviscous model has an advantage with regard to optimization time because of its simplicity. Typically the performance of the hysteretic biviscous is fairly good with respect to the modeling of the hysteresis curves, making the hysteretic biviscous model better for some types of applications. When considering which model to use, performance as well as computational time and expense should be considered.

XI. Model Validation

The four nonlinear models require experimental data consisting of displacement, force, velocity, and acceleration in order to use the parameter optimization schemes. The prediction of hysteresis cycles from already identified model parameters is useful when experimental data are not available. To validate the model parameters over the operating range of the damper, a validation study was done. For this validation study the hysteretic biviscous and the viscoelastic plastic model parameters from the identification data set were used to determine offset model parameter values.

To determine the offset model parameters for the validation, a two-dimensional interpolation subroutine in MATLAB was used. Once

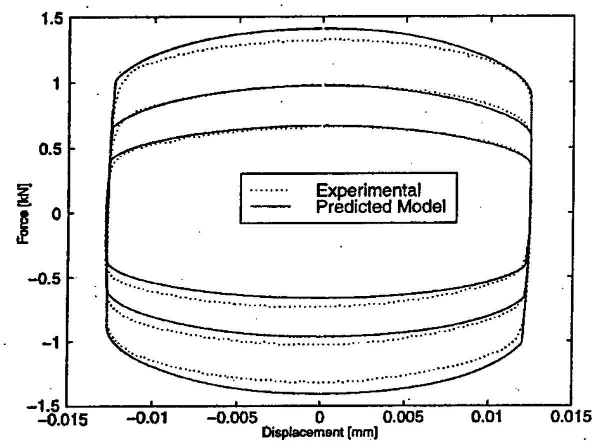

a) Hysteretic biviscous force vs displacement

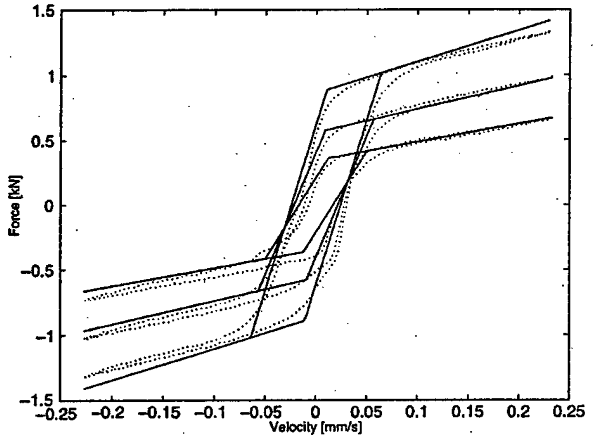

b) Hysteretic biviscous force vs velocity

Fig. 16 Predicted hysteresis cycles for the hysteretic biviscous model are compared to those from the validation data set. Test cases shown are $I = 0.3$, 0.5, and 0.9 A, all at 2.875 Hz.

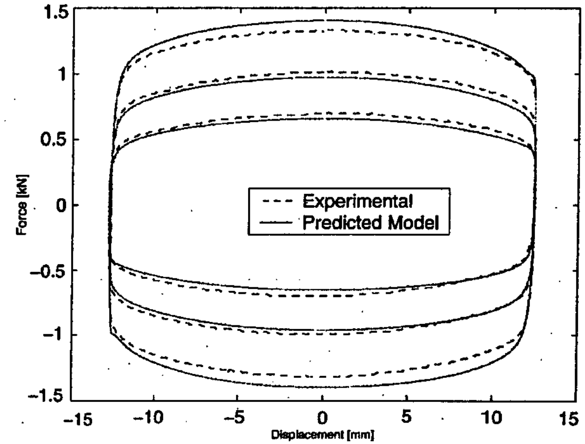

a) Viscoelastic plastic force vs displacement

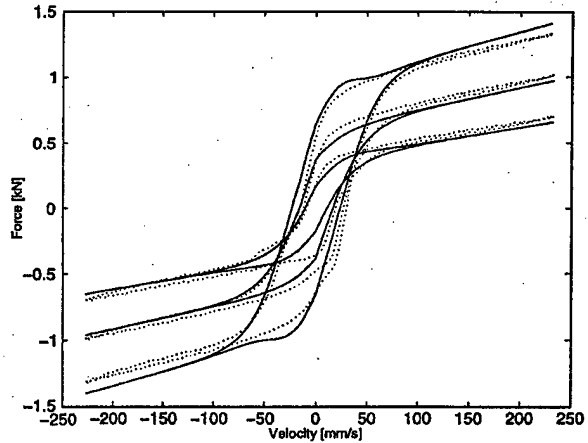

b) Viscoelastic plastic force vs velocity

Fig. 17 Predicted hysteresis cycles for the viscoelastic plastic model are compared to those from the validation data set. Test cases shown are $I = 0.3$, 0.5, and 0.9 A, all at 2.875 Hz.

the offset parameters were calculated, they were used to reconstruct force vs displacement and force vs velocity hysteresis cycles. The predicted hysteresis curves are compared with the experimental data from the validation data set. These data were collected at the same frequency and applied current as the predicted parameters.

Figures 16 and 17 show both the predicted and experimental hysteresis cycles for both the nonlinear hysteretic biviscous and the nonlinear viscoelastic plastic models. Each of the plots show applied current of 0.3, 0.5, and 0.9 A, at a frequency of $\Omega = 2.875$ Hz.

Figures 16a and 16b compare the measured force vs displacement and force vs velocity hysteresis cycle, with those predicted using the hysteretic biviscous model. Figures 17a and 17b do the same for the nonlinear viscoelastic plastic model. From these plots we can see that the correlation between the predicted and experimental hysteresis cycles is acceptable.

A. Model Prediction Error

To evaluate model performance, once again the equivalent viscous damping and the force time history errors are calculated. These errors will be used to compare the performance of the hysteretic biviscous and the viscoelastic plastic models in the validation study, which are compared with the results of the identification set.

B. Equivalent Viscous Damping Error

The equivalent viscous damping error for the prediction set is calculated using the same method that was used for the identification set. The Newtonian test cases were again separated from the applied field cases because the errors were higher as a result of the asymmetric behavior of the damper caused by the nitrogen accumulator.

First, examining the performance of each model in the prediction set in Figs. 18a and 18b shows the average Newtonian damping error for the nonlinear hysteretic biviscous and the viscoelastic plastic models. The zero field error for the viscoelastic plastic model is 29.1%; this is much higher than the error for the hysteretic biviscous model, which is 13.8%. Examining the non-Newtonian average damping errors, the 0.1 A case for both the hysteretic biviscous and the viscoelastic plastic has errors larger than the higher applied field cases. This is again caused by the asymmetric behavior of the damper at Newtonian and low field conditions. As the applied field increases, the average damping error decreases for both models, the average damping error for the nonlinear hysteretic biviscous model is 5.1%, and the average error for the nonlinear viscoelastic plastic model is 6.2%.

To compare the damping results from the identification set with those from the prediction set, consider Figs. 14 and 18. We can see that the equivalent viscous damping error is much higher in the prediction set than it is in the identification set for all field cases. The average Newtonian damping error of the prediction set is 13.8% for the hysteretic biviscous model; for the identification set this error is approximately 1.5%. For the applied field cases the average error for the equivalent viscous damping is 0.1% for the identification set; this error is on average 5.5% for the prediction data set.

Comparing the performance of the viscoelastic plastic model in the identification and prediction data sets, it is seen that the ability of the model to predict damping is not as good as the hysteretic biviscous model. The average damping error of the identification set was 0.1%, which is much lower than the average damping error for the validation set, which is 6.2%.

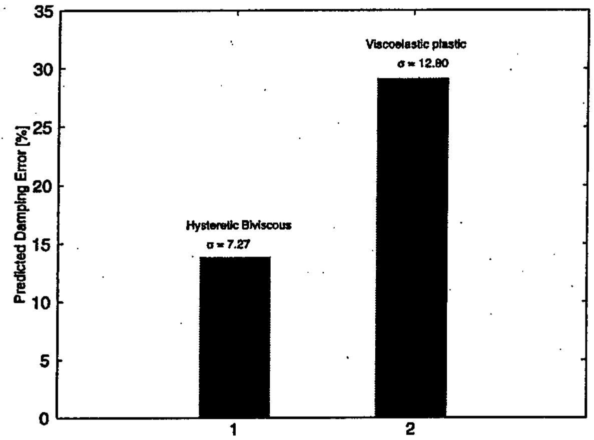

a) Newtonian prediction damping error

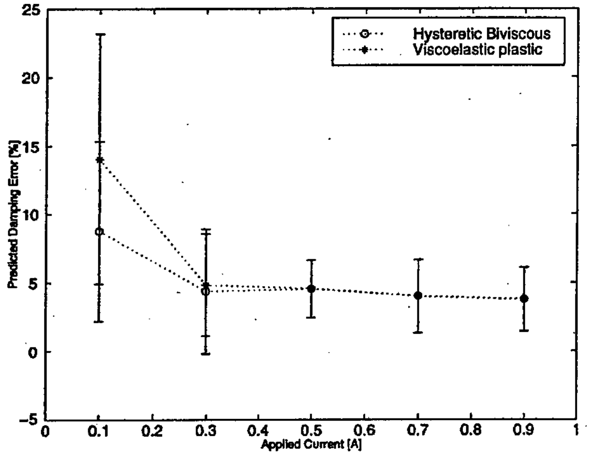

b) Prediction damping error

Fig. 18 Average damping error calculated from the predicted models and the experimental data.

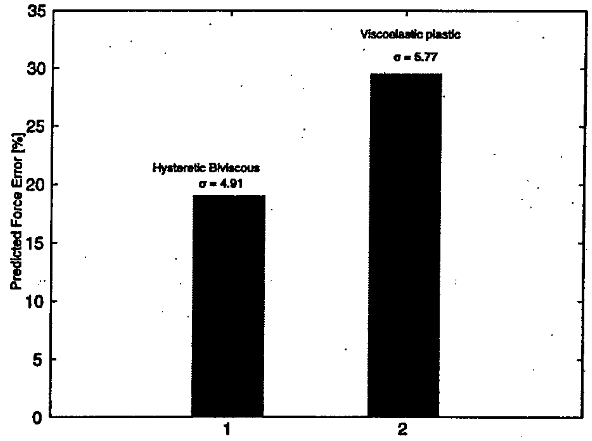

a) Newtonian prediction force error

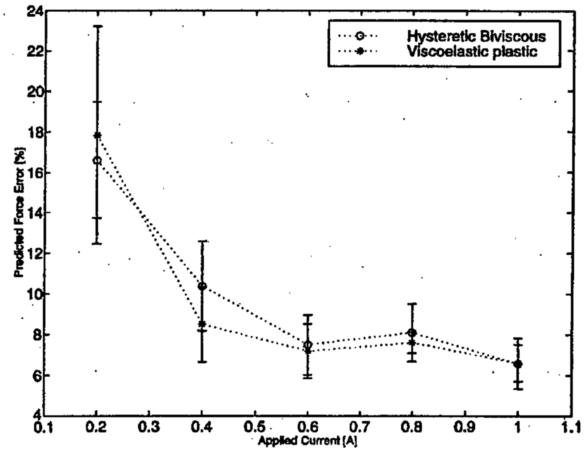

b) Prediction force error

Fig. 19 Average force time history error calculated from the predicted models and the experimental data.

C. Force Error

The force time history error between the predicted models and the measured force from the validation data set was calculated using Eq. (27). The results are shown in Figs. 19a and 19b.

The nonlinear hysteretic biviscous predicted model results were better than the viscoelastic plastic results for the Newtonian cases. The average Newtonian force error for the hysteretic biviscous model was approximately 19%, whereas the viscoelastic plastic Newtonian error was 29.5%. For the applied current cases the predictions were much better for both models. As the current increased the error decreased, and the models performed comparably. For the higher field strengths the average force error for both models is 9.5%. Comparing the force errors from the predictions with the force errors from the identification set, we see that the hysteretic biviscous model has about the same Newtonian force error in both studies. The viscoelastic plastic model percent error increased from 4.5% in the identification to 29.5% in the prediction. The two models perform comparably in both studies for applied field cases.

XII. Conclusions

An MR damper was characterized using equivalent viscous damping. This linear technique appropriately accounts for the energy dissipated over one oscillation cycle. This model describes the MR damper as an equivalent linear passive hydraulic damper via the equivalent viscous damping C_{eq}. C_{eq} was shown to be a function of both the applied magnetic field (current) and sinusoidal excitation. However, the equivalent viscous damping model does not accurately account for either the steady state force vs displacement or velocity hysteresis cycle behavior. Thus, the strong nonlinear behavior of the MR damper renders the linearized model nearly useless as a simulation model. However, C_{eq} is useful when comparing passive hydraulic or elastomeric dampers to MR dampers.

Four nonlinear models—the Bingham plastic, nonlinear biviscous, nonlinear hysteretic biviscous, and nonlinear viscoelastic plastic models—were proposed as the underlying model structure of a system identification procedure using experimental force vs displacement and force vs velocity hysteresis cycle data. These four models all describe the force vs displacement hysteresis cycles fairly well, but the nonlinear hysteretic biviscous and the nonlinear viscoelastic plastic models improve the reconstruction of the force vs velocity behavior. Improvements to the nonlinear Bingham plastic and the nonlinear biviscous model were made with additional model parameters and smoothing functions. A key conclusion of this study is that the preyield behavior has a small impact on the damping performance, but has a large impact in understanding the rheological behavior of the damper. For the four models the error in the damping performance was less than 6% for Newtonian cases and less than 1.4% for applied field cases.

The nonlinear hysteretic biviscous model has an advantage over the nonlinear viscoelastic plastic model in that the parameters can be estimated graphically from experimental data using linear or LMS fit procedures. Errors between the measured and model equivalent viscous damping were below 1%, whereas errors between the experimental force and the model force were typically around 6.6%. Because of the nonlinear hysteretic biviscous models ability to characterize damping, this model is the most appropriate as a simulation model for steady-state oscillations.

The nonlinear viscoelastic plastic (NVEP) model[8,14,15] is a piecewise smooth version of the nonlinear hysteretic biviscous model, which differs in that it is piecewise smooth in velocity. Force vs displacement and velocity hysteresis cycles were accurately reconstructed using this model. The energy dissipation error was far better for the NVEP model than for any of the other nonlinear models considered with a typical error less than 0.1%. The nonlinear viscoelastic plastic model also outperformed the nonlinear piecewise continuous models when reconstructing the force vs velocity hysteresis cycles. The average force time history error for the identification data set was 4.5%; this was on average 3% better than the nonlinear hysteretic biviscous model for higher field cases. The difference between the errors is even greater for low field cases.

A prediction study was also done using the nonlinear hysteretic biviscous and the nonlinear viscoelastic plastic models. These two models were chosen because of their superior performance over the Bingham plastic and nonlinear biviscous models in reconstructing the force vs velocity hysteresis cycles. Predicted model parameters were interpolated using the parameters identified using the identification data set. The values for the parameters were interpolated for intermediate current and frequency values. Hysteresis cycles were reconstructed from predicted parameters and compared with experimental data collected from the MR damper in the validation data set. Results of the prediction study show that the models performed comparably. Although prediction errors of equivalent viscous damping and force were higher than those errors in the identification set, the errors are still typically less than 10% for higher field cases.

Acknowledgments

Research was supported by the U.S. Army Research Office Young Investigator Program, Contract 38856-EG-YIP (Gary Anderson, Technical Monitor). Laboratory equipment was provided under a grant by the FY96 Defense University Research Instrumentation Program, Contract DAAH-0496-10301 (Gary Anderson, Technical Monitor). R. A. Snyder was supported in part under fellowships from the Vertical Flight Foundation. We also thank Mark Jolly, Lord Corporation, for his technical assistance.

References

[1] Carlson, J. D., Catanzarite, D. M., and St. Clair, K. A., "Commercial Magnetorheological Fluid Devices," *Proceedings of the International Conference on Electro-Rheological, Magneto-Rheological Suspensions and Associated Technology*, World Scientific Press, Rivers Edge, NJ, 1995, pp. 20–28.

[2] Kamath, G. M., Wereley, N. M., and Jolly, M. R., "Analysis and Testing of a Model-Scale Magnetorheological Fluid Helicopter Lag Mode Damper," *Journal of the American Helicopter Society*, Vol. 44, No. 3, 1999, pp. 234–248.

[3] Ervin, R. D., Lou, Z., Filisko, F. E., and Winkler, C. B., "Electrorheology for Smart Landing Gear," NASA CR-2000883 (N96-25313), April 1996.

[4] Lou, Z., Ervin, R. D., Filisko, F. E., and Winkler, C. B., "An Electrorheologically Controlled Semi-Active Landing Gear," Society of Automotive Engineers, Paper 93-1403, 1993.

[5] Leitmann, G., "Semiactive Control for Vibration Attenuation," *Journal of Intelligent Material Systems and Structures*, Vol. 5, No. 6, 1994, pp. 841–846.

[6] Leitmann, G., and Reithmeier, E., "A Control Scheme Based on ER-Materials for Vibration Attenuation of Dynamical Systems," *Applied Mathematics and Computation*, Vol. 70, 1995, pp. 247–259.

[7] Kunz, D. L., "Influence of Elastomeric Damper Modeling on the Dynamic Response of Helicopter Rotors," *AIAA Journal*, Vol. 35, No. 2, 1997, pp. 349–354.

[8] Kamath, G. M., and Wereley, N. M., "A Nonlinear Viscoelastic-Plastic Model for Electrorheological Fluids," *Smart Materials and Structures*, Vol. 6, No. 3, 1997, pp. 351–358.

[9] Prager, W., *Introduction to Mechanics of Continua*, Ginn and Co., New York, 1961, pp. 114–129.

[10] Phillips, R. W., "Engineering Applications of Fluids with a Variable Yield Stress," Ph.D. Dissertation, Mechanical Engineering, Univ. of California, Berkeley, CA, 1969.

[11] Stanway, R., Sproston, J. L., and El-Wahed, A. K. "Application of Electrorheological Fluids in Vibration Control: A Survey," *Smart Materials and Structures*, Vol. 5, No. 4, 1996, pp. 464–482.

[12] Wereley, N. M., and Lindler, J., E., "Biviscous Damping Behavior in Electrorheological Dampers," *ASME International Mechanical Engineering Congress and Exhibition: Adaptive Structures and Materials Symposium*, AD-Vol. 59/MD-Vol. 87, American Society of Mechanical Engineers, New York, 1999, pp. 67–75.

[13] Wereley, N. M., Pang, Li., and Kamath, K. M., "Idealized Hysteresis Modeling of Electrorheological and Magnetorheological Dampers," *Journal of Intelligent Material Systems and Structures*, Vol. 9, No. 8, 1998, pp. 642–649.

[14] Kamath, G. M., and Wereley, N. M., "Modeling the Damping Mechanism in Electrorheological Fluid Based Dampers," *M3DIII: Mechanics and Mechanisms of Material Damping*, edited by V. K. Kinra and A. Wolfenden, American Society for Testing and Materials, West Conshohocken, PA, 1997, pp. 331–348.

[15] Kamath, G. M., and Wereley, N. M., "Nonlinear Viscoelastic-Plastic Mechanisms-Based Model of an Electrorheological Damper," *Journal of Guidance, Control, and Dynamics*, Vol. 20, No. 6, 1997, pp. 1225–1332.

[16] Dyke, S. J., Spencer, B. F., Jr., Sain, M. K., and Carlson, J. D., "Modeling and Control of Magnetorheological Dampers for Seismic Response Reduction," *Smart Materials and Structures*, Vol. 5, No. 5, 1996, pp. 565–575.

[17]Spencer, B. F., Dyke, S. J., Sain, M. K., and Carlson, J. D., "Phenomenological Model of a Magnetorheological Damper," *Journal of Engineering Mechanics*, Vol. 123, No. 3, 1997, pp. 230–238.

[18]Weiss, K. D., Carlson, J. D., and Nixon, D. A., "Viscoelastic Properties of Magneto- and Electro-Rheological Fluids," *Journal of Intelligent Material Systems and Structures*, Vol. 5, No. 6, 1994, pp. 772–775.

[19]Bendat, J. S., and Piersol, A. G., *Random Data: Analysis and Measurement Procedures*, Wiley, New York, 1986, pp. 368–377.

[20]Kamath, G. M., Hurt, M. K., and Wereley, N. M., "Analysis and Testing of Bingham Plastic Behavior in Semi-Active Electrorheological Fluid Dampers," *Smart Materials and Structures*, Vol. 5, No. 5, 1996, pp. 576–590.

[21]Gavin, H. P., Hanson, R. D., and Filisko, F. E., "Electrorheological Dampers, Part I: Analysis and Design," *Journal of Applied Mechanics*, Vol. 63, No. 3, 1996, pp. 669–675.

[22]Felker, F. F., Lau, B. H., McLaughlin, S., and Johnson, W., "Nonlinear Behavior of an Elastomeric Lag Damper Undergoing Dual-Frequency Motion and its Effect on Rotor Dynamics," *Journal of the American Helicopter Society*, Vol. 32, No. 4, 1987, pp. 45–53.

[23]McGuire, D. P., "Fluidlastic Dampers and Isolators for Vibration Control in Helicopters," *50th Annual Forum of the American Helicopter Society*, American Helicopter Society, Alexandria, VA, 1994, pp. 295–304.

[24]Panda, B., and Mychalowycz, E., "Aeroelastic Stability Wind Tunnel Testing with Analytical Correlation of the Comanche Bearingless Main Rotor," *Journal of the American Helicopter Society*, Vol. 42, No. 3, 1997, pp. 207–217.

[25]Wereley, N. M., and Pang, Li, "Nondimensional Analysis of Semi-Active Electrorheological and Magnetorheological Dampers Using Approximate Parallel Plate Models," *Smart Materials and Structures*, Vol. 7, No. 5, 1998, pp. 732–743.

[26]Makris, N., Burton, S. A., Hill, D., and Jordan, M., "Analysis and Design of ER Damper for Seismic Protection of Structures," *Journal of Engineering Mechanics*, Vol. 122, No. 10, 1996, pp. 1003–1011.

[27]Lou, Z., Ervin, R. D., and Filisko, F. E., "A Preliminary Parametric Study of Electrorheological Dampers," *Electro-Rheological Flows*, FED-Vol. 164, American Society of Mechanical Engineers, New York, 1993, pp. 143–156.

[28]Gavin, H. P., Hanson, R. D., and Filisko, F. E., "Electrorheological Dampers, Part II: Testing and Modeling," *Journal of Applied Mechanics*, Vol. 63, No. 3, 1996, pp. 676–682.

[29]Lindler, J., and Wereley, N. M., "Parametric Analysis and Testing of an Electrorheological Fluid Damper," *Smart Structures and Materials 1999: Smart Structures and Integrated Systems*, edited by N. M. Wereley, Vol. 3668, *Proceedings of SPIE*, Society of Photo-Optical Instrumentation Engineers, Bellingham, WA, 1999, pp. 474–486.

A. Chattopadhyay
Associate Editor

Council of the European Communities (Brussels) (1989) On the approximation of the laws of the member states relating to machinery. Council directive (89/392/EEC). *Official Journal of the European Communities* June: 9–32.

Gemne G, Pyykko I, Taylor W and Pelmear P (1987) The Stockholm workshop scale for the classification of cold-induced Raynaud's phenomenon in the hand–arm vibration syndrome (revision of the Taylor–Pelmear scale). *Scandinavian Journal of Work, Environment and Health* 13 (4): 275–278.

Griffin MJ (1990) *Handbook of Human Vibration.* London: Academic Press.

Griffin MJ (1997) Measurement, evaluation and assessment of occupational exposures to hand-transmitted vibration. *Occupational and Environmental Medicine* 54 (2): 73–89.

Griffin MJ (1998) Evaluating the effectiveness of gloves in reducing the hazards of hand-transmitted vibration. *Occupational and Environmental Medicine* 55 (5): 340–348.

Griffin MJ, Seidel H, Bovenzi M and Benson AJ (1998) Vibration. In: Stellman JM (ed.) *Encyclopaedia of Occupational Health and Safety*, vol. 2, 4th edn. Geneva: International Labor Office, pp. 50.1–50.15.

International Organization for Standardization (1986), *Mechanical Vibration – Guidelines for the Measurement and the Assessment of Human Exposure to Hand-transmitted Vibration.* Geneva: International Standard ISO 5349.

International Organization for Standardization (1988) *Hand-held Portable Tools – Measurement of Vibration at the Handle – part 1: General.* Geneva: International Standard ISO 8662-1.

Taylor W and Pelmear PL (eds) (1975) *Vibration White Finger in Industry*. London: Academic Press.

HELICOPTER DAMPING

N M Wereley, R Snyder and R Krishnan,
University of Maryland at College Park,
College Park, MD, USA

T. Sieg, Paulstra Industries Inc., Carlsbad, CA, USA

Copyright © 2001 Academic Press

doi:10.1006/rwvb.2001.0022

The helicopter is one of the most severe vibration environments among aerospace vehicles, and vibration damping is of critical importance when enhancing aeromechanical stability and passenger comfort. The model 360 rotor hub (**Figure 1**) illustrates the typical hub configuration of an articulated rotor. The rotor blade has three degrees of freedom: (1) pitch, or rotation about the blade's longitudinal axis; (2) flap, or out-of-plane bending; and (3) lag, or in-plane bending. The need to augment damping is critical to mitigate aeromechanical instabilities, including pitch-flap, flag-lag, and ground and air resonance. Pitch-flap flutter is a modal coalescence of blade flap and torsion modes. Flap-lag flutter is an instability of primarily the lag mode, with participation from the flap mode. The flap mode is heavily damped aerodynamically, whereas the lag mode is very lightly damped. Ground resonance is a modal coalescence of the rotor lag mode with the landing gear modes of the helicopter, while the rotor is spinning up to its operational rotational frequency of 1/rev (typically 5–7.5 Hz). Air resonance is a modal coalescence of the lag mode with the rigid body modes of the helicopter while it is in high-speed forward flight. The latter three aeromechanical instabilities can be mitigated via damping augmentation, whereas pitch-flap flutter, as in fixed-wing flutter, must be mitigated in rotor design: the chordwise center of gravity must be kept at or ahead of the quarter-chord point (aerodynamic center) of the blade.

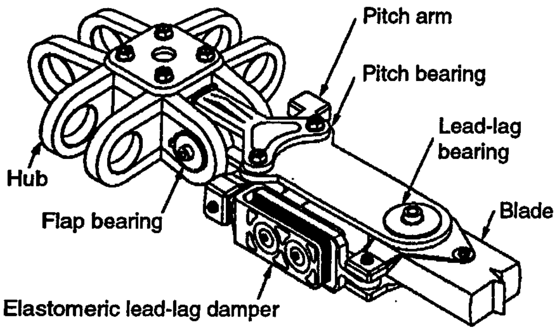

Figure 1 Rotor hub of the model 360 helicopter. Courtesy of Boeing Helicopters Inc.

In advanced rotor designs such as bearingless and hingless rotors, the lag and flap hinges, as well as the pitch bearing, are eliminated, and a flexure or flexbeam is introduced. The Comanche helicopter has such an advanced rotor (**Figure 2**). In conventional articulated rotors, ground resonance is typically mitigated using hydraulic or elastomeric dampers. Hingeless and bearingless rotors are designed to be soft inplane rotors, which implies that the lag mode or lag/rev frequency is less than the rotor rotational or 1/rev

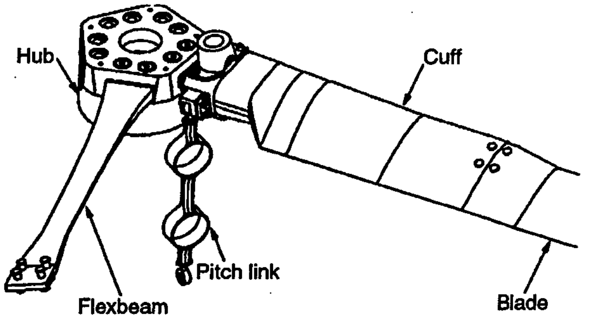

Figure 2 Wind tunnel model of the Comanche helicopter rotor hub. Courtesy of Boeing Helicopters Inc.

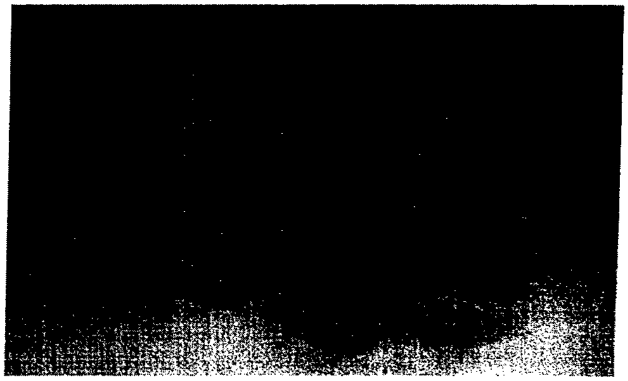

Figure 3 (See Plate 39). Laminated metal-elastomeric bearings for isolating transmission gear box vibrations in helicopters. Courtesy of Paulstra-Vibrachoc.

frequency. The rotor is soft in-plane due to stress considerations. As a result, elastomeric lag dampers are typically used to mitigate aeromechanical instabilities. Elastomeric dampers have some advantages: first, they have no moving parts, and second, the leakage problems that are present in hydraulic dampers are eliminated. However, a key disadvantage is that elastomeric damper behavior is nonlinear and highly dependent on frequency, temperature, and loading conditions such as preload and excitation amplitudes.

Elastomeric devices are added to the rotor hub to achieve two very different objectives: augmentation of flexibility, and augmentation of lag mode damping. Laminated metal-elastomeric bearings are used to increase the period of vibrations by softening, or introducing flexibility into, the rotor hub structures in order to isolate vibrations. Some examples of these type of bearings are shown in **Figure 3**. However, the primary focus of this article is to describe the behavior and analysis of elastomeric lag dampers used to augment stability of helicopter rotors with respect to air and ground resonance.

Damping Augmentation

The lag motion in helicopter rotors occurs at two frequencies: the lead-lag regressive frequency and the 1/rev frequency. Under these conditions, the damping in elastomers has been shown to degrade substantially at low amplitudes, thus causing undesirable limit cycle oscillations. In order to circumvent the problems associated with the elastomeric dampers, hybrid fluidic-elastomeric dampers have been used. Hybrid fluidic-elastomeric dampers use elastomers in conjunction with fluids. The fluid adds a viscous component to the energy dissipation mechanism in the dampers. Moreover, the inclusion of the fluid expands the dynamic range of forces generated by the damper. Hybrid fluidic-elastomeric lead-lag dampers were tested in a 1/6th Froude-scale rotor model and it was shown that the limit-cycle instabilities that were observed with elastomeric dampers can be substantially mitigated. A comparison between elastomeric and hybrid fluidic-elastomeric dampers shows that the former has stiffness and damping properties that are nonlinear functions of the displacement amplitude, whereas the latter exhibits relatively constant properties. Several lag dampers are shown in **Figure 4**.

The mechanical properties of lag mode dampers can vary from one damper to the next, so that they are carefully matched sets for a given rotor. Matched sets of dampers are used to minimize the impact of varying damper mechanical properties on rotor tracking conditions. The key to matching the properties of these dampers is to match their linearized damping and stiffness properties as a function of excitation amplitude, temperature, and stiffness. The methods for performing such a characterization will now be presented.

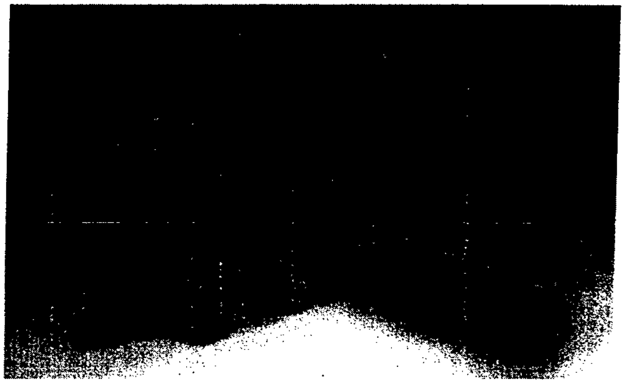

Figure 4 (See Plate 40). Lead-lag dampers are used to augment stability of helicopter rotor blade in-plane bending modes. Courtesy of Paulstra-Vibrachoc.

Example: Filled Elastomer Lag Damper

Rather than cataloging properties of various elastomers used in lag dampers, a primary objective of this article is to introduce how an elastomeric damper would be tested, characterized, and analyzed for use on a helicopter. The primary goal of such a testing program is to characterize the behavior of the damper due to steady-state sinusoidal excitation at the lag/rev frequency, and to assess the effects of the excitation at the rotor or 1/rev frequency on damping performance at the lag/rev frequency. This example is typical of what would be done for elastomeric dampers, as well as for fluidic, hybrid fluidic-elastomeric, and controllable fluid-based dampers.

Elastomeric Damper Testing

For our example, we will present the testing and characterization of double lap shear specimens incorporating Paulstra Industries material E136, which is a silicone-based filled elastomer. These specimens consist of three brass plates and a 10 mm (0.4 in) layer of damping material applied symmetrically across the center plate.

One of the important effects of a filler on viscoelastic material behavior is stress-softening. If a filled sample is stretched for the first time to 100% followed by a release in the strain and then stretched again to 200%, there is a softening in strain up to 100%, after which it continues in a manner following the first cycle. If this stress-strain is repeated in a third cycle, we can again see a softening up to 200% due to the previous strain history. This stress-softening or memory effect was first discovered by Mullins, and is called the Mullins effect. The Mullins effect was taken into account during these single-frequency tests. The material was first subjected to 300 cycles of sinusoidal excitation at 1 Hz at 5 mm (200 mil) of amplitude, which was the maximum amplitude in the chosen test matrix. All subsequent excitations were below this amplitude. During a test run, the material would be periodically excited for an amplitude of 5 mm (200 mil) at 1 Hz frequency to reinforce this memory effect. This was one of the ways in which consistency of results was ensured.

Because a viscoelastic material undergoes relaxation when subjected to loads, it requires a certain amount of time to stabilize and yield a steady value of force when a constant displacement is applied. Moreover, as an elastomeric damper is subjected to dynamic loading, the temperature of the damping material increases. This self-heating phenomenon is the result of energy dissipation via hysteresis. The temperature of the specimen can increase significantly in the first 30–50 s. Eventually, thermal equilibrium is established between the material, brass plates, and the environment. Based on preliminary tests, we concluded that, for these specimens, the dynamic relaxation, self-heating, and other unsteady effects require about 250 s to reach steady state. Data for characterization purposes were taken after the material properties had reached steady state.

The double lap shear specimens in this example were tested on a 5500 lb MTS servo-hydraulic testing machine. A schematic diagram of the system is shown in Figure 5.

Two types of excitation are typically studied: single-frequency sinusoidal displacement at the lag/rev frequency or a single frequency test, and the sum of two sinusoidal displacements at the lag/rev and 1/rev frequencies or a dual-frequency test.

Single-frequency testing To obtain consistent results, a sinusoidal input was applied at a given amplitude and displacement for 300 s and data were collected at the end of this period. These single-frequency tests are typically conducted at the lag/rev frequency, which was nominally $\Omega_{lag} \approx 5.0$ Hz for this example. Additional single-frequency testing is sometimes performed at the rotor rotational frequency or 1/rev, which in this case was $\Omega_1 = 7.5$ Hz. However, only sinusoidal testing at the lag/rev frequency will be

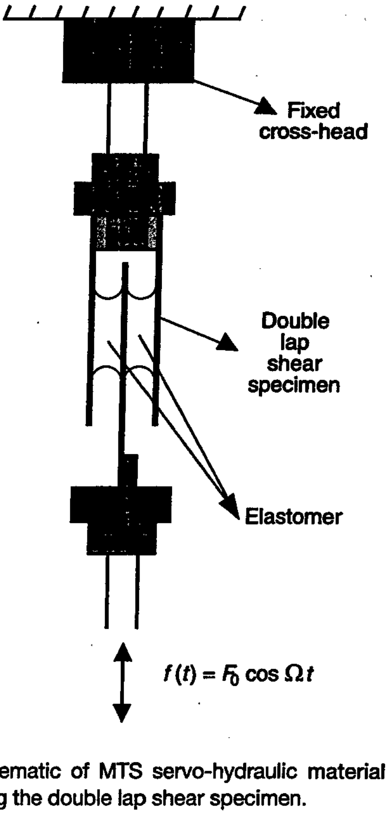

Figure 5 Schematic of MTS servo-hydraulic material testing system showing the double lap shear specimen.

considered. During each test, we measured 20 cycles of force vs displacement data and then calculated the force vs velocity hysteresis cycles for each test condition. The hysteresis cycle force and displacement data collected during each experiment were acquired on a PC-based data acquisiton system and were unavoidably noisy. However, the independent displacement variable was sinusoidal, so that a periodic Fourier series was used to eliminate, as much as possible, the effects of this noise in the input displacement signal, and the subsequent differentiations to obtain the input velocity and acceleration signals. The Fourier series expansion of the displacement was taken as:

$$x(t) = \frac{x_0}{2} + \sum_{k=1}^{\infty} \left(x_{c,k} \cos k\Omega_{\text{lag}}t + x_{s,k} \sin k\Omega_{\text{lag}}t\right) \quad [1]$$

where:

$$x_{c,k} = \frac{\Omega_{\text{lag}}}{\pi k} \int_0^{2\pi k/\Omega_{\text{lag}}} x(t) \cos k\Omega_{\text{lag}}t \, dt \quad [2]$$

$$x_{s,k} = \frac{\Omega_{\text{lag}}}{\pi k} \int_0^{2\pi k/\Omega_{\text{lag}}} x(t) \sin k\Omega_{\text{lag}}t \, dt \quad [3]$$

The bias and higher harmonics were then filtered out, and only the harmonic at the frequency of interest, Ω_{lag}, was retained, so that the displacement signal was reconstructed as:

$$x(t) = X_{c,1} \cos \Omega_{\text{lag}}t + X_{s,1} \sin \Omega_{\text{lag}}t \quad [4]$$

Calculating the velocity signal from the displacement signal using a finite difference method tends to accentuate any noise in the displacement signal. We can exploit the sinusoidal nature of the input displacement signal by differentiating the Fourier series expansion from eqn [4] to obtain:

$$\dot{x}(t) = -\Omega_{\text{lag}} X_{c,1} \sin \Omega_{\text{lag}}t + \Omega_{\text{lag}} X_{s,1} \cos \Omega_{\text{lag}}t \quad [5]$$

However, the force signal is typically not filtered because the damper response is nonlinear and it cannot be determined *a priori* exactly which harmonics contributed to damper response and/or noise. Therefore, it is typical to be conservative, and use the measured (unfiltered) force data in both characterization and model parameter identification studies.

Dual-frequency testing For the dual-frequency testing in this example, the 1/rev frequency was chosen as $\Omega_1 = 7.5$ Hz while the lag/rev was chosen as $\Omega_{\text{lag}} = 5$ Hz. In general, a dual-frequency displacement signal has the form:

$$x(t) = X_{\text{lag}} \sin \Omega_{\text{lag}}t + X_1 \sin \Omega_1 t \quad [6]$$

The resulting signal contains the product of two harmonics $\Omega_1 + \Omega_{\text{lag}}$ and $\Omega_1 - \Omega_{\text{lag}}$. It is periodic with a period equal to the frequency corresponding to the highest common factor of these two harmonics, which in this case is $\Omega = 2.5$ Hz. The displacement signal was filtered by expanding as a Fourier series expansion of many harmonics, N, with a base frequency of $\Omega = 2.5$Hz, or:

$$x(t) = \frac{X_0}{2} + \sum_{k=1}^{n} \left(X_{c,k} \cos k\Omega t + X_{s,k} \sin k\Omega t\right) \quad [7]$$

and setting the bias term, $X_0 = 0$. In this example, the second harmonic, $2\Omega = \Omega_{\text{lag}} = 5$ Hz, and the third harmonic, $3\Omega = \Omega_1 = 7.5$ Hz, so that only the first three harmonics need to be included in the above Fourier series expansion, or $n = 3$, and noise is eliminated from the displacement. The velocity in the dual-frequency case was determined by differentiating the Fourier series expansion of the displacement signal, so in general:

$$\dot{x}(t) = \sum_{k=1}^{n} \left(-k\Omega X_{c,k} \sin k\Omega t + k\Omega X_{s,k} \cos k\Omega t\right) \quad [8]$$

Again, in this case study, $n = 3$. As in the single-frequency case, the force signal is not filtered because the damper response is nonlinear. The measured (unfiltered) force data are used directly in both the dual-frequency characterization and model parameter identification studies.

Damper Characterization: Single-frequency

Two common approaches are described for a linear characterization of the damper behavior. First, the equivalent spring stiffness and equivalent viscous damping approach is presented. This is based on first characterizing the damping force based on force vs displacement data. The damping force is subtracted from the measured damper force to obtain a residual force signal, that is used to characterize the residual spring behavior. The second approach is the calculation of the complex modulus, K^*, in which a Fourier analysis is used to characterize the in-phase force or spring force, and the quadrature force or damper force, and hence the complex modulus.

Typical data used for such a characterization study are shown in **Figure 6**, for sinusoidal excitation at $\Omega_{\text{lag}} = 5\,\text{Hz}$, a 10% preload, for a range of amplitudes. The steady-state hysteresis cycle data are taken after stabilization of the material for a duration of 300 cycles at 1 Hz and 5 mm (200 mil) of sinusoidal excitation.

Equivalent spring stiffness and viscous damping The first characterization technique is that of equivalent spring stiffness and equivalent viscous damping. This is a standard linearization technique that can be applied to a nonlinear damper such as this elastomeric damper. Here, the damper restoring force, $f(t)$, is the sum of an equivalent spring or elastic stiffness force proportional to displacement, $f_s(t)$, and an equivalent viscous damping force proportional to velocity, $f_d(t)$:

$$f(t) = f_s(t) + f_d(t) \qquad [9]$$

where:

$$\begin{aligned} f_s(t) &= K_{\text{eq}} x(t) \\ f_d(t) &= C_{\text{eq}} \dot{x}(t) \end{aligned} \qquad [10]$$

where $x(t)$ and $\dot{x}(t)$ are the damper displacement and velocity, respectively. Here K_{eq} is the equivalent spring stiffness, and C_{eq} is the equivalent viscous damping. The equivalent viscous damping, C_{eq}, is computed by equating the energy dissipated over a cycle, E, at frequency Ω_{lag} using:

$$E = \oint F(t)\,\mathrm{d}x = \int_0^{2\pi/\Omega_{\text{lag}}} F(t) v(t)\,\mathrm{d}t \qquad [11]$$

and equating the dissipated energy of the nonlinear device to that of an equivalent viscous damper:

$$C_{\text{eq}} = \frac{E}{\pi \Omega_{\text{lag}} X_{\text{lag}}^2} \qquad [12]$$

where Ω_{lag} is the sinusoidal lag/rev test frequency, and X_{lag} is its amplitude. The energy dissipated over one cycle is computed using a numerical intregration technique such as the trapezoidal rule. In **Figure 7**, the hysteresis cycle is shown as the result of a sinusoidal input having nominal amplitude of $X_{\text{lag}} = 5\,\text{mm}$ (200 mil) and frequency of $\Omega_{\text{lag}} = 5\,\text{Hz}$. The damping force, $f_{\text{d}}(t)$, calculated as above, is plotted in **Figure 7** as a flat ellipse. The difference between the total force and the damping force is the elastic stiffness force, or:

$$f_s(t) = f(t) - f_d(t) \qquad [13]$$

This residual spring force is shown in **Figure 7**, and is characteristic of a nonlinear stiffening spring, or:

$$f_s(t) = K_1 x(t) + K_3 x^3(t) \qquad [14]$$

The parameters K_1 and K_3 are determined using a least mean squared error parameter optimization technique. The cost function J to be minimized in this procedure is expressed by:

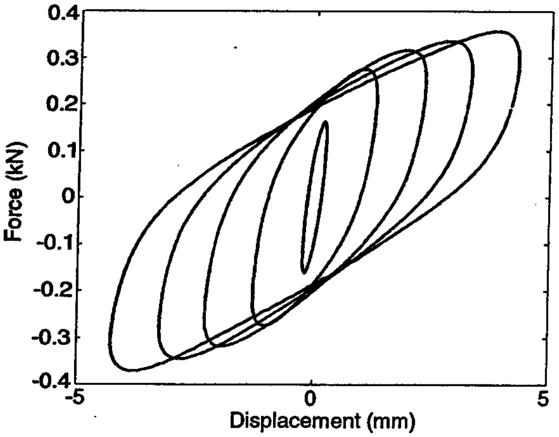

Figure 6 Hysteresis cycles for the double lap shear specimens at the lag/rev ($\Omega_{\text{lag}} = 5\,\text{Hz}$) frequency and 10% preload.

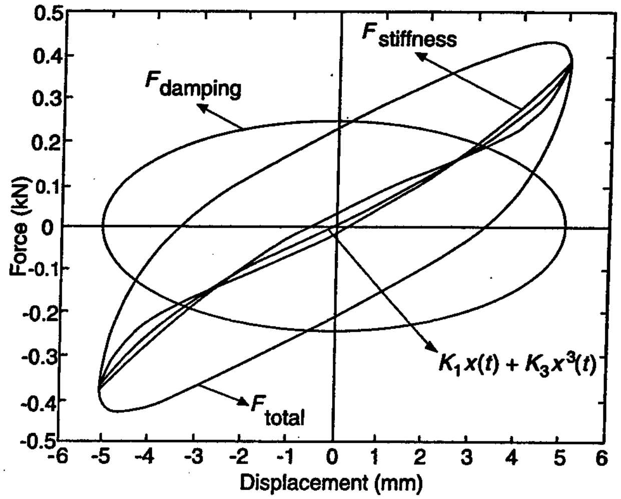

Figure 7 Contributions of the viscous damping force, and the elastic stiffness force to the total force.

$$J(K_1,K_3)=\sum_{i=1}^{m}\left(f_{s,i}-K_1x_i-K_3x_i^3\right)^2 \qquad [15]$$

where m is the number of datapoints taken over one period. Because the force and displacement data are sampled data with sampling period Δt, we define $x_i = x(i\Delta t)$, and $f_{s,i} = f(i\Delta t)$. The two necessary conditions that must be satisfied are:

$$\frac{\partial J}{\partial K_1}=0 \quad \text{and} \quad \frac{\partial J}{\partial K_3}=0 \qquad [16]$$

resulting in a solution of:

$$K_1=\frac{1}{\Delta}(\Sigma_1\Sigma_5-\Sigma_2\Sigma_4) \qquad [17]$$

$$K_3=\frac{1}{\Delta}(\Sigma_2\Sigma_3-\Sigma_1\Sigma_4) \qquad [18]$$

where:

$$\Sigma_1=\sum_{i=1}^{m}f_{s,i}x_i \qquad [19]$$

$$\Sigma_2=\sum_{i=1}^{m}f_{s,i}x_i^3 \qquad [20]$$

$$\Sigma_3=\sum_{i=1}^{m}x_i^2 \qquad [21]$$

$$\Sigma_4=\sum_{i=1}^{m}x_i^4 \qquad [22]$$

$$\Sigma_5=\sum_{i=1}^{m}x_i^6 \qquad [23]$$

$$\Delta=\Sigma_3\Sigma_5-\Sigma_4^2 \qquad [24]$$

The equivalent stiffness is then given by the formula:

$$K_{\mathrm{eq}}=K_1+\tfrac{1}{2}K_3X_{\mathrm{lag}}^2 \qquad [25]$$

We calculated the equivalent stiffness (Figure 8) and viscous damping (Figure 9) versus amplitude of sinusoidal excitation, ranging from 0.2 to 5 mm, using the above methods for the single frequency force vs displacement hysteresis cycle data. Clearly, both the equivalent stiffness and damping are strongly dependent on amplitude of excitation, as evidenced by the substantial decrease in these quantities as amplitude increases. The rate of change of equivalent stiffness and damping with amplitude is very large up to $X_{\mathrm{lag}} = 2\,\mathrm{mm}$, and becomes much more gradual for amplitudes $X_{\mathrm{lag}} > 2\,\mathrm{mm}$. In addition, comparing zero preload and 10% preload conditions at room temperature, the addition of preload tends to increase the equivalent stiffness and damping over the entire amplitude range. This effect is due to the compressive preload increasing the friction response of the filler in the elastomer. Comparing the preloaded cases at room temperature and at 50°C, an increase in temperature tends to decrease the equivalent stiffness and damping. This is a manifestation of the so-called softening effect as temperature is increased.

Complex stiffness A second approach is to characterize the complex damper stiffness, K^*, as the in-phase or storage stiffness, K', and quadrature or loss stiffness, K'', so that:

$$K^*=K'+jK''=K'(1+j\eta) \qquad [26]$$

where η is the loss factor. This is a common approach in the characterization of elastomeric dampers. Alternatively, is the effective or equivalent stiffness, while K''/Ω is related to the equivalent viscous damping of the damper. To determine the damper force:

$$\begin{aligned} f(t) &= F_c\cos\Omega_{\mathrm{lag}}t+F_s\sin\Omega_{\mathrm{lag}}t \\ &= K'x(t)+\frac{K''}{\Omega_{\mathrm{lag}}}\dot{x}(t) \end{aligned} \qquad [27]$$

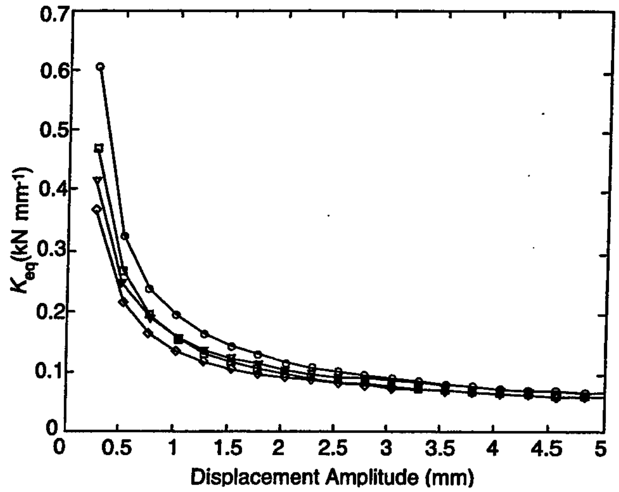

Figure 8 Single-frequency damper characterization of the equivalent elastic stiffness at $\Omega_{\mathrm{lag}} = 5\,\mathrm{Hz}$. Circles, preloaded; squares, zero preload; diamonds, zero preload at 50°C; triangles, preloaded at 50°C.

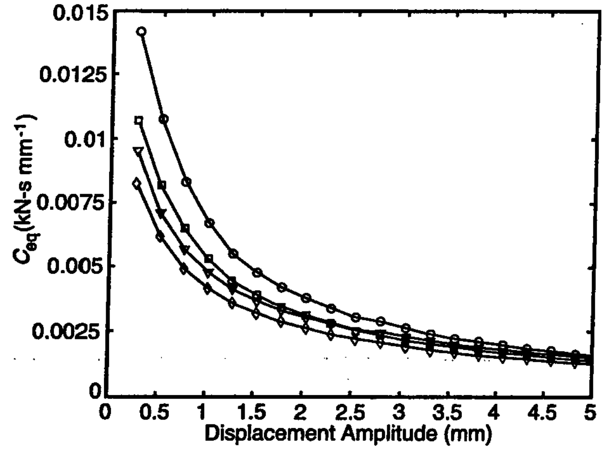

Figure 9 Single-frequency damper characterization of the equivalent viscous damping at $\Omega_{\text{lag}} = 5\,\text{Hz}$. Circles, preloaded; squares, zero preload; diamonds, zero preload at 50 °C; triangles, preloaded at 50 °C.

Here F_c and F_s are the cosine and sine Fourier coefficients of $f(t)$ at frequency Ω_{lag}. We assume that the displacement is sinusoidal:

$$x(t) = X_c \cos \Omega_{\text{lag}} t + X_s \sin \Omega_{\text{lag}} t \qquad [28]$$

where X_c and X_s are the cosine and sine Fourier coefficients of $x(t)$ at frequency Ω_{lag}. Substituting $x(t)$ into the force equation and equating the sine and cosine terms yields the in-phase and quadrature stiffnesses as:

$$\begin{aligned} K' &= \frac{F_c X_c + F_s X_s}{X_c^2 + X_s^2} \\ K'' &= \frac{F_c X_s - F_s X_c}{X_c^2 + X_s^2} \end{aligned} \qquad [29]$$

In general, this calculation would be performed for a sweep in the oscillation frequency, Ω, which included Ω_{lag} in its range. In our case, we are examining only a single harmonic excitation at Ω_{lag}. The quadrature stiffness of the damper is related to the equivalent viscous damping in an approximate way by:

$$C_{\text{eq}} \approx \frac{K''}{\Omega_{\text{lag}}} \qquad [30]$$

The relation is approximate because the complex stiffness considers only the harmonic at frequency Ω_{lag}.

The results of this linear characterization are shown in **Figures** 10–12. Clearly, both the in-phase stiffness and quadrature stiffness (damping) are strongly dependent on amplitude of excitation. Again, the rate of change of these quantities with amplitude is very large up to $X_{\text{lag}} = 2\,\text{mm}$, and becomes much more gradual for amplitudes $X_{\text{lag}} > 2\,\text{mm}$. In addition, comparing zero preload and 10% preload conditions at room temperature, the addition of preload tends to increase the complex modulus over the entire amplitude range, which is again because the compressive preload increases the friction response of the filler in the elastomer. The softening effect as temperature is increased can be observed by comparing the preload cases at room temperature and 50°C. This comparison shows that

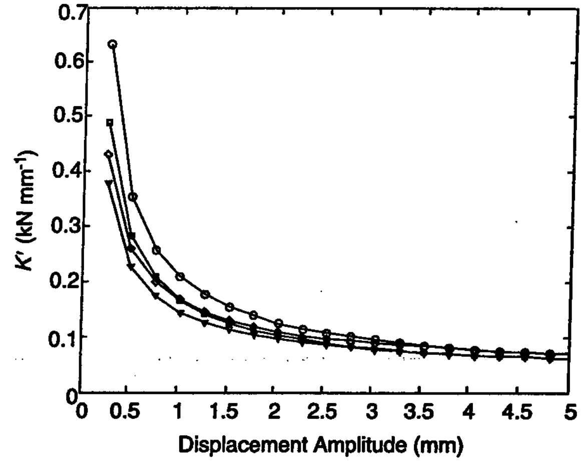

Figure 10 Single-frequency damper characterization of the stiffness at $\Omega_{\text{lag}} = 5\,\text{Hz}$. Circles, preloaded; squares, zero preload; triangles, zero preload at 50 °C; diamonds, preloaded at 50 °C.

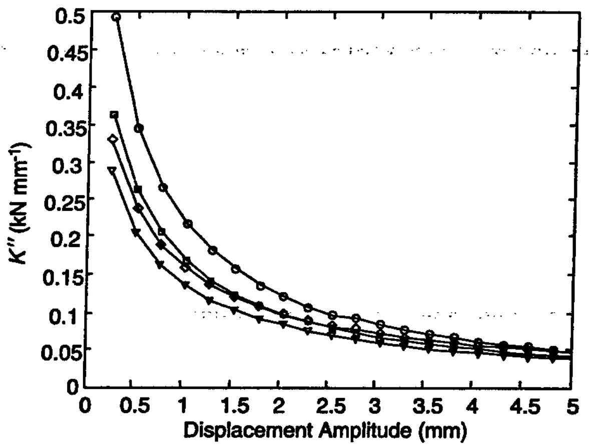

Figure 11 Single-frequency damper characterization of the damping at $\Omega_{\text{lag}} = 5\,\text{Hz}$. Circles, preloaded; squares, zero preload; triangles, zero preload at 50 °C; diamonds, preloaded at 50 °C.

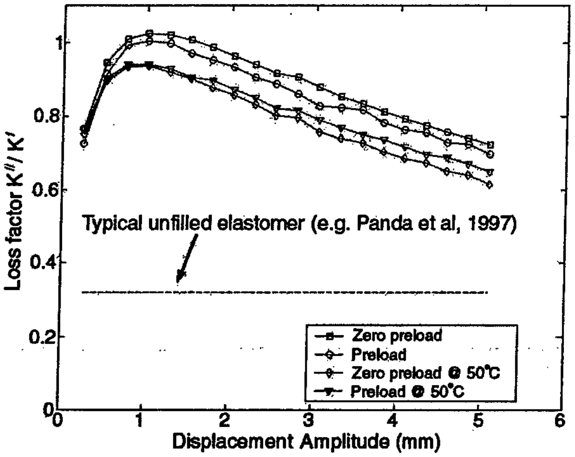

Figure 12 Single-frequency damper characterization of the loss factor at $\Omega_{\text{lag}} = 5$ Hz. Circles, preloaded; squares, zero preload; diamonds, zero preload at 50 °C; triangles, preloaded at 50 °C.

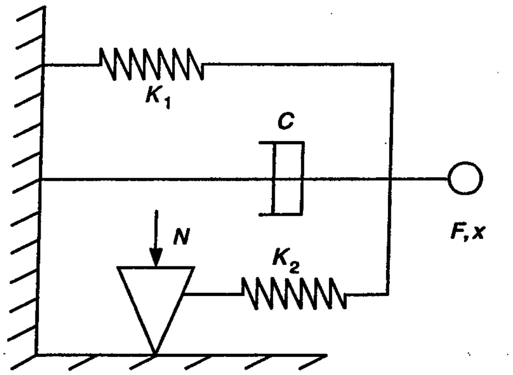

Figure 13 Schematic of the mechanisms-based stiffness-viscosity-elasto-slide analysis for the elastomeric damper.

an increase in temperature tends to decrease the complex modulus. A final useful comparison comes from the loss factor, which is the ratio of the quadrature stiffness to the in-phase stiffness, or:

$$\eta = \frac{K''}{K'} \qquad [31]$$

The loss factor, η, is a measure of the damping level relative to the stiffness, and it is desirable to have a high loss factor over a large amplitude range. The maximum value of the loss factor for this filled elastomer is as high as 1.025 for this material, which is much higher than the loss factor for elastomers used in existing dampers, which typically range from 0.4 to 0.8. A second observation is that the loss factor has its maximum effectiveness over a small amplitude range centered about an amplitude of 1 mm or, nominally, 10% shear strain, which is defined as the amplitude ($X_{\text{lag}} = 1$ mm) over the specimen thickness (10 mm or 0.4 in). These trends are fairly typical of elastomeric materials.

Single-frequency Hysteresis Modeling

The single-frequency force vs displacement hysteresis cycle data of these double lap shear specimens can be modeled using a mechanisms-based modeling approach. Figure 13 shows a schematic of the mechanical stiffness-viscosity-elasto-slide (SVES) model used for the elastomers. The model consists of three elements: (1) a linear stiffness; (2) a nonlinear elasto-slip or triboelastic element that models the rate-independent part of the hysteresis behavior; and (3) a linear viscous damping that characterizes the rate-dependent hysteresis behavior. The model includes various physical aspects seen in elastomer hysteresis behavior, such as: (1) strong amplitude dependence of linearized coefficients; (2) linear behavior at low amplitudes; (3) mild frequency dependence; (4) deviation in hysteresis behavior from the linearized elliptical behavior near the zero-velocity points of the hysteresis cycle; and (5) presence of a rate-dependent and rate-independent part. The SVES model is typical of the class of elastomeric mechanisms-based models, in that it contains a Kelvin chain element (a spring and damper in parallel) and a triboelastic element (an elasto-slide element).

Figure 14 shows the effect of each of these mechanisms on the hysteresis cycles of the dampers. The nonlinear elasto-slip element accounts for the almost vertical drop in force near the zero-velocity region. It is modeled as a combination of a spring and Coulomb force. The slip element, which represents the friction components of the model, will be modeled such that its parameters are independent of both amplitude and frequency. The linear stiffness parameter must be modeled such that it is amplitude-dependent but frequency-independent. The linear viscous damping parameter must be modeled such that it is dependent on both the amplitude and frequency.

The linear stiffness and linear dashpot parameters give the necessary slope and area to the force vs displacement hysteresis cycle shape. The elasto-slide element represents a stiffness in the region where the velocity of the damper changes its sign and the displacement is less than a certain value $2X_s$ from the maximum amplitude. In the remaining portion of the hysteresis cycle, the elasto-slide element is equivalent to a Coulomb element. Two parameters are required to characterize the elasto-slide element completely. The linear stiffness and linear viscous damping

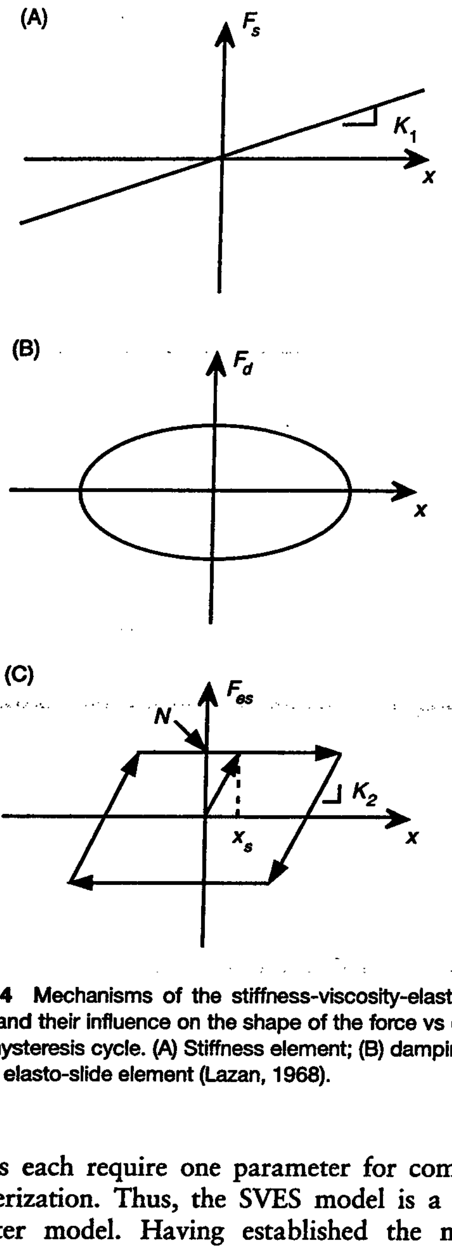

Figure 14 Mechanisms of the stiffness-viscosity-elasto-slide analysis and their influence on the shape of the force vs displacement hysteresis cycle. (A) Stiffness element; (B) damping element; (C) elasto-slide element (Lazan, 1968).

elements each require one parameter for complete characterization. Thus, the SVES model is a four-parameter model. Having established the model structure and model components, the parameters in the model need to be identified. The predicted force from the model is given by:

$$f(t) = f_s(t) + f_d(t) + f_{es}(t) \qquad [32]$$

where $f_s(t)$, $f_d(t)$ and $f_{es}(t)$ are the forces in the stiffness, viscous dashpot, and elasto-slide element at any time, t. The stiffness and damping forces are as below:

$$f_s(t) = K_1 x(t) \qquad [33]$$

$$f_d(t) = C\dot{x}(t) \qquad [34]$$

The elasto-slide element has four branches as below:

$$f_{es} = \begin{cases} -N & x = -\bar{x} & \dot{x} = 0 \\ -N + K_2(x + \bar{x}) & x < -\bar{x} + 2X_s & \dot{x} > 0 \\ N & x > -\bar{x} + 2X_s & \dot{x} > 0 \\ N & x = \bar{x} & \dot{x} = 0 \\ N + K_2(x - \bar{x}) & x > \bar{x} - 2X_s & \dot{x} < 0 \\ -N & x < \bar{x} - 2X_s & \dot{x} < 0 \end{cases} \qquad [35]$$

where $\bar{x}$ is the amplitude over the cycle, and the slide force is given by:

$$N = K_2 X_s \qquad [36]$$

The parameters N and K_2 of the elasto-slide element can be chosen *a priori* by careful observation of the force vs displacement hysteresis cycles. It was observed that, in the zero preload case, the value of the drop in force at maximum displacement was approximately 71.2 N. Hence, the Coulomb force corresponding to N was chosen to be 35.6 N. The stiffness K_2 was also fixed at 280.2 N mm^{-1}. Hence, the elasto-slide mechanism represents a Coulomb force of 35.6 N in parallel with a stiffness until the magnitude of the stiffening force becomes 35.6 N, but represents a Coulomb force of 71.2 N otherwise. This element is constant with respect to changing amplitude.

The remaining unknown parameters, K_1 and C, are estimated on the basis of minimizing the error between the predicted force, $\hat{f}$, and the measured force, f, obtained from experiments. The parameters of the model are obtained from a constrained minimization of the objective function, J, given by:

$$J(K_1, C) = \sum_{k=1}^{m} \left[\hat{f}(t_k) - f(t_k)\right]^2 \qquad [37]$$

where m is the number of data points for each hysteresis cycle. A constrained minimization was performed using design optimization tools (DOT), which uses the Broyden–Fletcher–Goldfarb–Shanno algorithm to minimize the above objective function in eqn [37]. To obtain physically meaningful results with this technique, the identified parameters are constrained to have positive values: $K_1 > 0$, and $C > 0$. The parameters K_1 and C were identified at each amplitude at the lag/rev frequency. The identified parameters are plotted versus amplitude in **Figure 15**.

Using the parameters estimated from the identification process, the force vs displacement hysteresis cycles were reconstructed. **Figure 16** shows the reconstructed hysteresis cycles for five different amplitudes at the lag/rev (5 Hz) frequency. The plots show that the model accurately captures the hysteresis behavior of the damper.

Dual-frequency Characterization

In addition to testing the dampers at the lag/rev frequency, experiments are typically conducted at dual frequencies of the lag/rev (5 Hz) frequency and the 1/rev (7.5 Hz) rotor frequency. These tests are intended to assess the potential loss of damping at the lag/rev frequency due to dual-frequency motion. In this section, such a dual-frequency test is described, and typical test results are presented for the filled elastomer of our case study.

The dual frequency tests in our case study were carried out on an MTS servo-hydraulic testing machine with a digital control system. The range of lag/rev amplitudes is the same as for the single-frequency tests, that is, 0.25–5 mm (10–200 mil) in increments of 0.254 mm (10 mil). The 1/rev amplitudes tested were 0, 0.508, 1.524, 2.54 and 3.55 mm (0, 20, 60, 100 and 140 mil). An HP 8904A multifunction synthesizer was used to generate and sum the sinusoidal signals with the two individual frequencies. A function generator was used to have as accurate as possible the desired dual-frequency sinusoidal excitations. The force input and the displacement response were measured using the load cell and LVDT of the MTS machine, respectively, as in the single-frequency characterization tests.

To characterize the dampers under dual-frequency excitation conditions, the components of the complex stiffness $K^* = K' + jK''$ were determined at the lag/rev frequency. The stiffness, K', and damping K'' at the

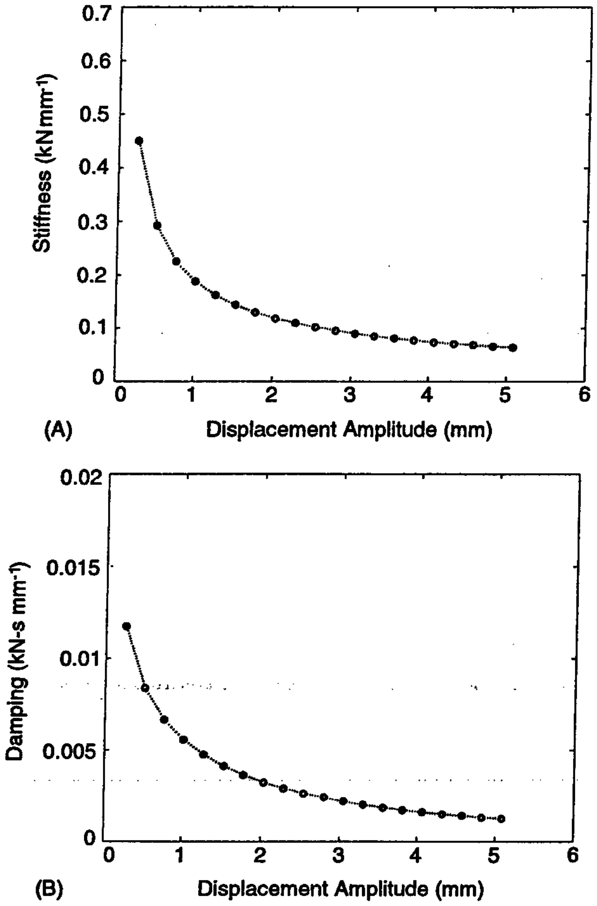

Figure 15 Identified stiffness and damping of the SVES model, assuming amplitude-independent elasto-slide element parameters, $N = 35.6$ N, and $K_2 = 280.2\ \mathrm{N\,mm^{-1}}$. (A) Stiffness parameter, K_1; (B) damping parameter, C.

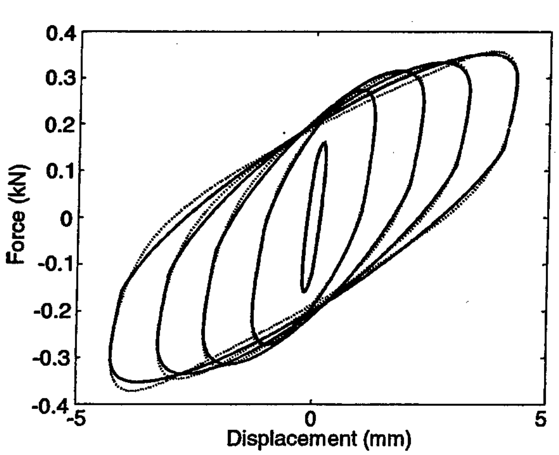

Figure 16 Validation of the mechanisms-based model at 5 Hz for different amplitudes. Continuous line, model; dashed line, experiment.

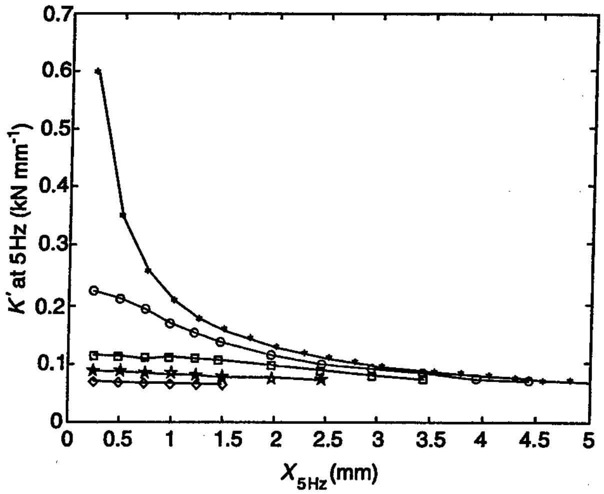

Figure 17 Dual-frequency damper characterization of stiffness at lag/rev = 5 Hz and 1/rev = 7.5 Hz. Amplitudes @ 7.5 Hz: Asterisks, 0 mm; circles, 0.508 mm (20 mil); squares, 1.524 mm (60 mil); stars, 2.54 mm (100 mil); diamonds, 3.556 mm (140 mil).

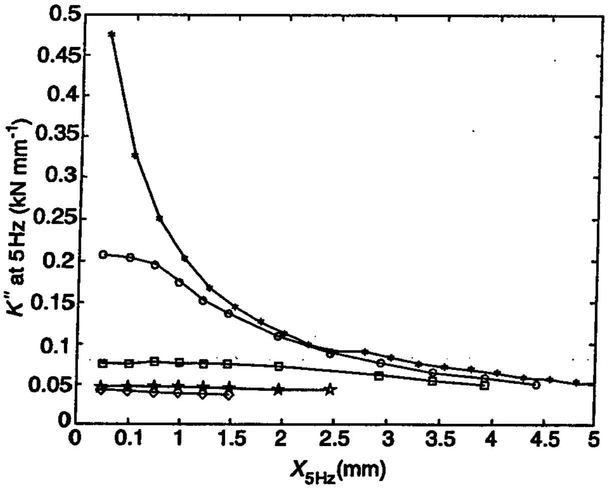

Figure 18 Dual-frequency damper characterization of the damping at lag/rev = 5 Hz and 1/rev = 7.5 Hz. Amplitudes @ 7.5 Hz: Asterisks, 0 mm; circles, 0.508 mm (20 mil); squares, 1.524 mm (60 mil); stars, 2.54 mm (100 mil); diamonds, 3.556 mm (140 mil).

lag/rev (5 Hz) frequency, shown in Figures 17 and 18, decrease as the 1/rev (7.5 Hz) amplitude increases. When the 1/rev (7.5 Hz) amplitude is 0.508 mm (20 mil), the reduction in stiffness and damping values is almost 50% compared to the single-frequency excitation at low 5 Hz amplitudes. The percentage reduction in these values gradually reduces with increasing amplitude of lag/rev (5 Hz) excitation and is not very significant (less than 10%) at high lag/rev (5 Hz) amplitudes. When the 1/rev (7.5 Hz) amplitude is 2.54 mm (100 mil), the stiffness and damping values at low lag/rev (5 Hz) amplitudes reduce by almost 80% and do not change substantially as the amplitude of 5 Hz excitation increases. Thus, it is clear that the 1/rev (7.5 Hz) excitation exerts a significant influence on the low-amplitude response at lag/rev (5 Hz). The elastomeric damper behavior exhibits strong nonlinearities and the nonlinearities degrade the performance of the damper. These effects of dual-frequency excitation are similar to the effects observed in other elastomeric damper studies.

Dual-frequency Hysteresis Modeling

To determine the dual frequency parameters, the Ω_{lag} (5 Hz) and $\Omega_{1/\text{rev}}$ (7.5 Hz) for each of the single frequency model parameters are used. First 10th order polynomials were used to fit the behavior of the linear damping and stiffness with respect to amplitude.

Once there are polynomials for both parameters at both the Ω_{lag} (5 Hz) and $\Omega_{1/\text{rev}}$ (7.5 Hz) frequencies, the polynomials are used to determine the parameter values for each frequency at the maximum displacement for the dual frequency test case. This value will be less than sum of the two amplitudes. This is due to the testing machine and its inability to match the desired amplitude of the input signal. This problem was present for the single frequency testing, but becomes more apparent in the dual frequency testing. The problem is most visible for larger amplitude excitations, in dual frequency testing the sum of the desired amplitudes is large enough that the machine was unable to match the desired output.

Using the single frequency polynomial fits, preliminary dual frequency parameters are calculated by revaluating the parameter curve at the maximum displacement of the dual frequency test. In order to calculate the dual frequency value for each parameter the values are scaled according to the amplitude for each frequency with respect to the maximum displacement for each test case. The equation used to determine the scaling for the damping and stiffness parameters can generally be written as

$$C = C(5\,\text{Hz}, \bar{X})\frac{X_{5\,\text{Hz}}}{\bar{X}} + C(7.5\,\text{Hz}, \bar{X})\frac{X_{7.5\,\text{Hz}}}{\bar{X}}$$

The dual-frequency correlation results for two dual-frequency excitation conditions are shown in Figures 19 and 20. Thus, the single-frequency model can be used to predict dual-frequency behavior.

Summary of Example

This example was presented describing how an elastomeric helicopter lag damper would be characterized and modeled using a mechanisms-based approach. The typical procedures used to character-

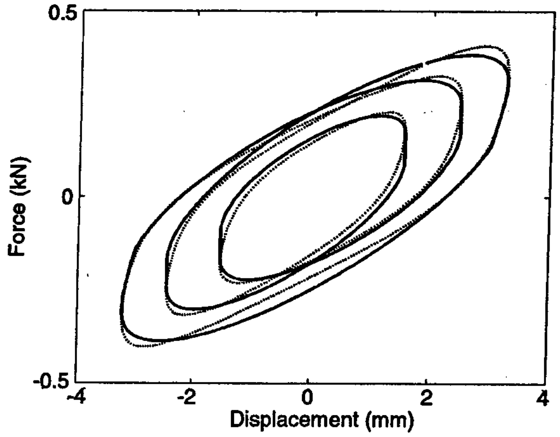

Figure 19 Dual-frequency damper analysis for 1/rev amplitude of 2.54 mm (100 mil) and lag/rev amplitude of 1 mm (40 mil). Continuous line, model; dashed line, experimental.

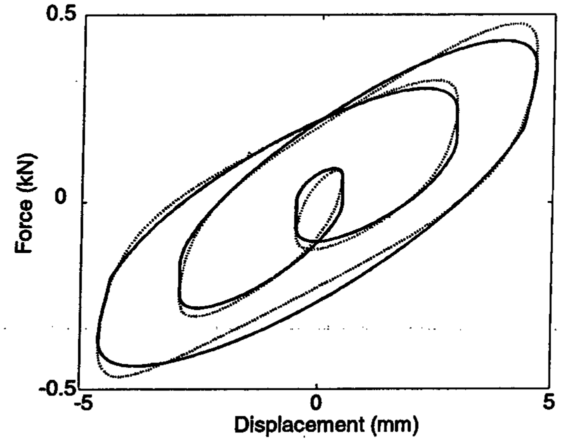

Figure 20 Dual-frequency damper analysis for 1/rev amplitude of 2.54 mm (100 mil) and lag/rev amplitude of 2.54 mm (100 mil). Continuous line, model; dashed line, experimental.

ize the steady-state behavior of elastomeric dampers under sinusoidal loading were described, including: (1) equivalent stiffness and equivalent viscous damping, and (2) complex stiffness and loss factor. The results of this linear characterization illustrated the amplitude-dependent nature of the linearized stiffness and damping. Additional effects of thermal softening, due to rising temperature, hardening due to lowering of temperature, and increases in stiffness and damping due to preload were illustrated using the linear stiffness and damping. A key component in the understanding of elastomeric helicopter lag dampers is the analysis of steady-state force response due to a sinusoidal displacement. A mechanisms-based tribo-viscoelastic analysis was outlined, specifically, the SVES analysis. Single-frequency (sinusoidal displacement at the lag mode frequency) and dual-frequency (sum of sinusoidal displacements at the lag mode frequency and the rotor rotational frequency) were analyzed. The SVES model worked well in predicting the behavior of the damper due to these classes of input displacement excitations.

Advanced Damper Concepts

New damping technologies are under development for application to the helicopter lag damping problem. Originally, hydraulic dampers were used to mitigate aeromechanical instabilities, where the damper force is proportional to the shaft velocity of the damper. However, these hydraulic dampers were prone to leakage problems. Because elastomeric dampers do not have comparable leakage problems, they were subsequently advocated for this application. The main problem, as described above, is that elastomeric damper properties are strongly dependent on amplitude and temperature. The linearized damping and stiffness of the elastomeric damper reduce substantially as amplitude is increased, or as temperature increases and the elastomer softens.

To reduce the impact of these amplitude-dependent damping and stiffness nonlinearities, hybrid fluid-elastomeric dampers have been proposed. The fluid which is passive, is used to linearize the damping and stiffness of the lag damper. As a result, the force vs displacement hysteresis cycles of these dampers are more linear, or elliptical in shape, as demonstrated for the Comanche model-scale wind tunnel damper (**Figure 21**). Using the same characterization methods described above, the equivalent viscous damping, C_{eq}, has been shown to be nearly constant as a function of excitation amplitude (**Figure 22**).

Another innovative concept is the introduction of adaptive or controllable fluids into lag dampers. Controllable fluids consist of a powder or particles dispersed in a carrier fluid. These fluids change their properties as electric field, as in electrorheological (ER) fluids, and magnetic field, as in magnetorheological (MR) fluids, is applied. This property change is manifested as a change in yield stress of the fluid, with a minimal change in plastic viscosity. This change in yield stress arises because the particles in the carrier fluid form chains, and resist shear stresses. The yield stress is the point in the shear stress versus shear rate behavior where the particle chains break or yield. This property of field-dependent yield stress can be exploited in the development of adaptive dampers.

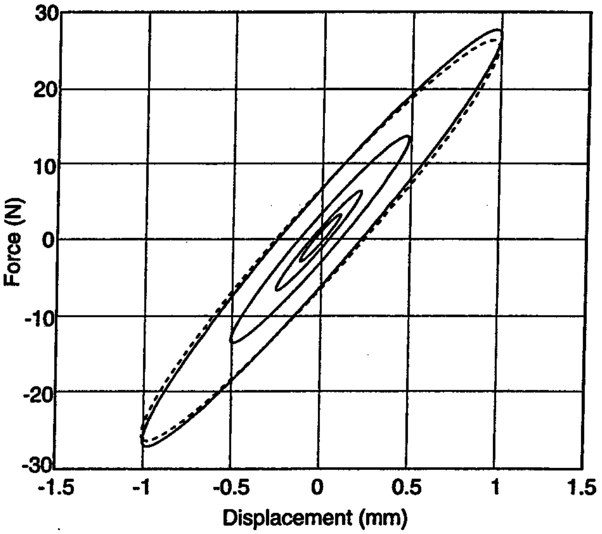

Figure 21 Force vs displacement hysteresis cycles of an elastomeric damper can be linearized via the addition of fluidic damping. Continuous line, model; dashed line, experiment.

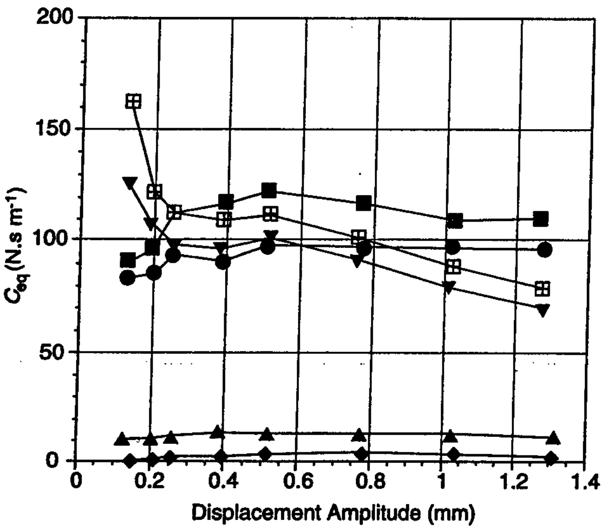

Figure 22 Linearized equivalent viscous damping constants for a pair of Comanche model-scale wind tunnel dampers under single-frequency excitation of the lag mode (in this case, 10 Hz). The MR on condition is comparable to a passive fluidic-elastomeric damper. The MR off condition has low damping. Circles, fluidlastic-zero preload; squares, fluidlastic-preloaded; diamonds, MR (off)-zero preload; triangles, MR (off)-preloaded; inverted triangles, MR (on)-zero preload; squares, MR (on)-preloaded.

To illustrate this, hybrid elastomeric MR lag dampers were fabricated for the Comanche wind tunnel model. The MR effect could be turned on and off in these dampers. The equivalent viscous damping for the MR on condition (Figure 22) is comparable to the fluidic-elastomeric case, however, the MR off condition has significantly reduced damping. This effect can have some interesting benefits.

Dampers must be matched sets for a given rotor so that it is balanced. However, due to manufacturing variations, dampers must be carefully matched, so that many dampers must be manufactured to achieve this matching of damper properties; that is, the properties of each damper are selected to be the same. Therefore, a damper that could adapt its properties to a fixed mechanical property specification would be of tremendous benefit. Damping augmentation is required only in certain flight regimes, which highlights the need for damping strategies that can be tailored to specific flight conditions. For example, when the helicopter is on the ground, and the rotor is spooling up to its operational rotational frequency of 1/rev, there are critical frequency ranges where the rotor can be marginally stable. Augmenting damping over these critical frequency ranges would be of benefit in increasing stability of the helicopter rotor. Also, the temperature-softening effect of elastomers can be mitigated by increasing the damping as temperature increases using an MR fluid-based damping component. Thus, controllable fluid dampers are attractive choices for augmenting lag mode damping in helicopter rotor systems.

Nomenclature

C_{eq}	equivalent viscous damping
f	measured force
$\hat{f}$	predicted force
$f(t)$	damper restoring force
K^*	damper stiffness
K'	storage stiffness
K''	loss stiffness
K_{eq}	equivalent spring stiffness
$x(t)$	damper displacement
$\Delta(t)$	sampling period

See Plates 39, 40.

See also: **Active control of vehicle vibration: Damping materials; Damping mounts.**

Further Reading

Aklonis JJ and McKnight WJ (1983) *Introduction to Polymer Viscosity*. New York: John Wiley.

Brackbill CR, Lesieutre GA, Smith EC and Govindswamy K (1996) Thermomechanical modeling of elastomeric materials. *Smart Materials and Structures* 5: 529–539.

Brackbill CR, Lesieutre GA, Smith EC and Ruehl LE (2000) Characterization and modeling of the low strain amplitude and frequency dependent behavior of elastomeric damper materials. *Journal of the American Helicopter Society* 45: 34–42.

Chopra I Perspectives in aeromechanical stability of helicopter rotors. *Vertica* 14: 457–458.

Felker FF, Lau BH, McLaughlin S and Johnson W (1987) Nonlinear behavior of an elastomeric lag damper undergoing dual-frequency motion and its effect on rotor dynamics. *Journal of the American Helicopter Society* 32: 45–53.

Gandhi F and Chopra I Analysis of bearingless main rotor aeroelasticity using an improved time domain nonlinear elastomeric damper model. *Journal of the American Helicopter Society* 41: 267–277.

Kamath GM, Wereley NM and Jolly MR Characterization of magnetorheological helicopter lag dampers. *Journal of the American Helicopter Society* 44: 234–248.

Kunz DL (1997) Influence of elastomeric damper modeling on the dynamic response of helicopter rotors. *AIAA Journal* 35: 349–354.

Lazan BJ (1968) *Damping of Materials amd Members in Structural Mechanics*. New York: Pergamon Press.

McGuire DP (1994) Fluidlastic dampers and isolators for vibration control in helicopters. Presented at the 50th Annual Forum of American Helicopter Society, Washington D.C., May 1994.

Panda B and Mychalowycz E (1997) Aeroelastic stability wind tunnel testing with analytical correlation of the comanche bearingless main rotor. *Journal of the American Helicopter Society* 42: 207–217.

HILBERT TRANSFORMS

M Feldman, Technion-Israel Institute of Technology, Haifa, Israel

Copyright © 2001 Academic Press

doi:10.1006/rwvb.2001.0057

Introduction

The Hilbert transform (HT), as a kind of integral transformation, plays a significant role in vibration signal processing. There are two common ways it can be used. First, the HT provides a direct examination of a vibration's instantaneous attributes: frequency, phase, and amplitude. It allows rather complex systems to be analyzed in the time domain. Second, the HT can find a system's real part of transfer function from the system's imaginary part and vice versa. This allows systems to be analyzed in the frequency domain. The HT can be used as an intermediate step in more elaborate system analysis. In addition to frequency response function analysis, it is useful for hysteretic damping characterizing and nonlinear system identification.

In the field of signal processing, the HT has also stimulated some progress. The classic example of this is signal demodulation, and also signal decomposition. Today the HT is taken as a standard procedure and has long been used widely in signal processing.

The Hilbert* transformation was first introduced to signal theory by Denis Gabor. He defined a generalization of the well-known Euler formula $e^{iz} = \cos(z) + i\sin(z)$ in the form of the complex function $Y = u(t) + iv(t)$, where $v(t)$ is the HT of $u(t)$. In signal processing, when the independent variable is time, this associated complex function is known as the analytic signal and the HT $v(t)$ is called quadrature (or conjugate) function of $u(t)$. For example, the quadrature function of $\cos(t)$ is $\sin(t)$ and the corresponding analytic signal is e^{it}.

The application of the HT to the initial signal provides some additional information about amplitude, instantaneous phase, and frequency of vibrations. This information can be useful when applied to analysis of vibrational motions, including an inverse problem – the problem of vibration system identification.

Notation

The HT of the function $u(t)$ is defined by an integral transform:

$$H[x(t)] = \tilde{x}(t) = \pi^{-1} \int_{-\infty}^{\infty} \frac{x(\tau)}{t-\tau} \, d\tau \qquad [1]$$

Because of the possible singularity at $t = \tau$, the integral is to be considered as a Cauchy principal value. The HT is equivalent to an interesting kind of filter, in which the amplitudes of the spectral components are left unchanged, but their phases are shifted by $-\pi/2$ (Figure 1).

Properties of the HT

The HT of a real-valued function $x(t)$ extending from $-\infty$ to $+\infty$ is a real valued function defined by eqn [1]. Thus, $\tilde{x}(t)$ is the convolution integral of $x(t)$ with $1/\pi t$, written as $\tilde{x}(t) = x(t) \cdot 1/\pi t$. The HT of a constant is zero. The double HT (the HT of a HT) yields the original function having the opposite sign, hence

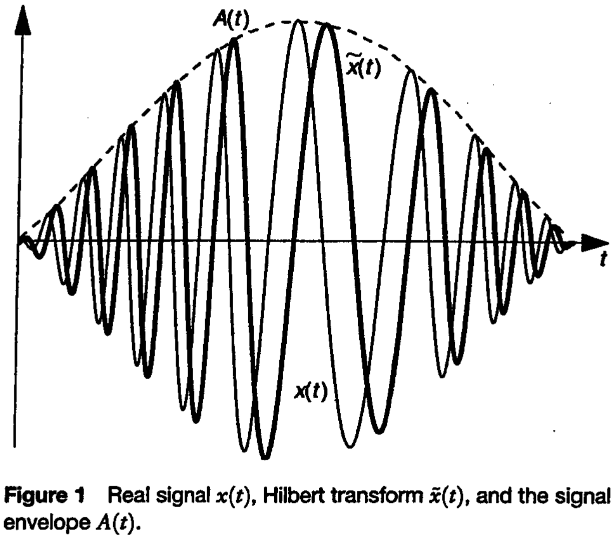

Figure 1 Real signal $x(t)$, Hilbert transform $\tilde{x}(t)$, and the signal envelope $A(t)$.

---

*David Hilbert, born 23 January 1862 in Königsberg, Prussia (now Kaliningrad, Russia), died 14 February 1943 in Göttingen, Germany. David Hilbert was one of the world's greatest mathematicians. Hilbert contributed to many branches of mathematics, including invariants, algebraic number fields, functional analysis, integral equations, mathematical physics, and the calculus of variations. He invented the space of wave functions used in quantum mechanics.

QUASI-STEADY BINGHAM BIPLASTIC ANALYSIS OF ELECTRORHEOLOGICAL AND MAGNETORHEOLOGICAL DAMPERS

Glen A. Dimock*, Jin-Hyeong Yoo†, and Norman M. Wereley ‡
Smart Structures Laboratory
Department of Aerospace Engineering
University of Maryland
College Park MD 20742 USA

ABSTRACT

Electrorheological (ER) and Magnetorheological (MR) fluids are characterized by an increase in dynamic yield stress upon application of a magnetic field. The Bingham plastic model has proven useful in modeling flow mode dampers utilizing ER and MR fluids. However, certain MR fluids can exhibit shear thinning behavior, wherein the fluid's apparent plastic viscosity decreases at high shear rates. The Bingham plastic model does not account for such behavior, resulting in over-prediction of equivalent viscous damping. We present a Bingham biplastic model that can account for both shear thinning and shear thickening behaviors. This approach assumes a bilinear post-yield viscosity, with a critical shear rate specifying the region of high shear rate flow. Furthermore, the model introduces non-dimensional terms to account for the additional parameters associated with shear thinning and thickening. A comparison is made between Bingham plastic and Bingham

---

*Graduate Research Assistant.

†Assistant Research Scientist.

‡Associate Professor. Tel: 301-405-1927. Fax: 301-314-9001. E-mail: wereley@eng.umd.edu

biplastic force responses to constant velocity input, and equivalent viscous damping is examined with respect to nondimensional parameters.

Keywords: ER(Electrorheological) Fluid, MR(Magnetorheological) Fluid, Shear Thinning, Shear Thickening, Bingham plastic model, Bingham biplastic model.

1. INTRODUCTION

Magnetorheological (MR) fluids and electrorheological (ER) fluids have been proposed for a wide variety of engineering devices requiring semi-active damping (Carlson *et al.*, 1999). These fluids, demonstrated to be qualitatively similar, are characterized by a field-dependent yield stress (Weiss *et al.*, 1994). Because of their field-dependent properties, ER and MR fluids have been utilized in a number of control studies to reduce transmissibility in civil structures (Spencer *et al.*, 1998; Hiemenz and Wereley, 1999), automotive systems, and other dynamical systems (Jeon *et al.*, 1999; Sharp *et al.*, 1986). This paper will focus on MR fluids, which respond to a magnetic field and have achieved greater commercial success in practical devices than their ER counterparts (Stanway *et al.*, 1996, Jolly *et al.*, 1999).

MR fluids are known to exhibit a number of nonlinear phenomena. A wide variety of nonlinear models have been used to characterize MR fluids and devices, including the Bingham Plastic model (Phillips, 1969), biviscous models (Stanway *et al.*, 1996), hysteretic biviscous models (Wereley *et al.*, 1998), and mechanism-based models (Kamath and Wereley, 1997; Sims *et al.*, 1999). One nonlinear phenomenon, shear thinning, refers to the reduction in apparent viscosity at high shear rates (Jolly *et al.*, 1999) and has traditionally been modeled with power-law or exponential functions (Wang *et al.*, 1999, and Wolff *et al.*, 1998). These models are complex, and a less complex alternative is to extend the widely-accepted Bingham plastic model.

The Bingham plastic model has been successfully used in previous studies to model field dependent rheological fluids (Kamath *et al.*, 1996; Block and Kelly, 1988). This model considers a fluid with a dynamic yield stress, beyond which a linear plastic viscosity is observed. When applied to flow between two parallel plates, the Bingham plastic model predicts a region of fluid that does not shear, having not reached the dynamic yield stress. Approaching the walls, the fluid shear rate increases as the shear stress increases. For high rod velocity and small gap size, this shear rate can reach values known to cause shear thinning (Jolly *et al.*, 1999). The Bingham plastic model predicts a constant plastic viscosity for all shear rates, but this assumption can be inaccurate at high shear rates.

This paper proposes a modified Bingham plastic model to account for shear thinning. Rather than fit an exponential curve to the post-yield viscosity, the Bingham biplastic approach considers biplastic post-yield behavior. This approach, while clearly a simplification, may be accurate enough to model MR fluid in most situations. Furthermore, the resulting model is simple enough to readily compare to the Bingham plastic case. For the new model, two parameters are added to the Bingham plastic model. Shear thinning is assumed to occur at a fixed *critical shear rate*, after which the fluid exhibits a *high shear rate viscosity*, and both of these parameters are assumed to be independent of field or shear rate. The new parameters are nondimensionalized for comparison to the Bingham plastic model. Finally, the Bingham biplastic relations are shown to reduce down to Bingham plastic equivalents when limiting cases suggest Bingham plastic flow.

2. DAMPER ANALYSIS

We will consider dampers, with an annular duct or valve in the piston head, that operate in the flow mode of operation, that is Poisieulle flow.

2.1. Flow mode

Fig. 1 depicts a magnetorheological damper operating in the flow mode. A force F is applied to the damper shaft, resulting in a pressure differential ΔP across an annular valve in the piston head.

As a result, fluid flows through the annular valve, resulting in shaft motion of velocity v_0. First, we assume that the annular gap, d, is very small relative to the inner radius of the annulus, R, so that the annular duct may be approximated by a rectangular duct or two parallel plates. The width of the rectangular duct is denoted by b, and is related to the circumference of the centerline of the the annular duct as below:

$$b \approx 2\pi \left(R + \frac{d}{2} \right) \tag{1}$$

A further consequence of the small gap assumption is that the velocity profile across the annular gap is response to a linear pressure gradient must be symmetric across the valve. Thus, we make the following assumptions: (1) the gap is assumed to be small relative to the annular radius (as above), (2) the fluid is incompressible; (3) the flow is fully developed along the entire finite active length of the valve, that is, the length over which the field is applied, so that we assume a 1D problem; (4) the flow is assumed to be steady or quasisteady, so that acceleration terms can be neglected; (5) a linear (shaft) axial pressure gradient is assumed, so that the pressure gradient is the pressure drop, ΔP, over the length of the valve, L. Therefore, we use a simplified form of the governing equation for Poiseuille flow in a rectangular duct as below (Wereley and Pang, 1998)

$$\frac{d\tau}{dy} = -\frac{\Delta P}{L} \tag{2}$$

where $\Delta P = P_{\text{in}} - P_{\text{out}}$. Here, P_{in} and and P_{out} are the pressures at the inlet and outlet of the MR valve, respectively.

2.2. Newtonian flow

The Newtonian constitutive relationship is

$$\tau = \mu \frac{du}{dy} \tag{3}$$

Differentiating Eq. 3 with respect to y and substituting the result into the governing Eq. 2 yields

$$\mu \frac{d^2u}{dy^2} = \frac{\Delta P}{L} \tag{4}$$

Integrating Eq. 4 twice with respect to y and applying the velocity boundary conditions at the walls of the valve,

$$u\left(-\frac{d}{2}\right) = 0 \tag{5}$$

$$u\left(\frac{d}{2}\right) = 0 \tag{6}$$

leads to the familiar Newtonian parabolic velocity profile

$$u\left(y\right) = \frac{\Delta P}{8\mu L}\left(d^2 - 4y^2\right) \tag{7}$$

Integrating the governing equation, Eq. 2, and applying the shear stress boundary condition, $\tau\left(0\right) = 0$, gives the shear stress profile between the two parallel plates of the valve as

$$\tau\left(y\right) = -\frac{\Delta P}{L}y \tag{8}$$

Integrating the velocity profile across the gap yields the total volume flux through the annulus

$$\begin{aligned} Q &= b\int_{-\frac{d}{2}}^{\frac{d}{2}} u(y)dy \\ &= \frac{bd^3\Delta P}{12\mu L} \end{aligned} \tag{9}$$

Noting that $Q = A_p v_0$, and that $\Delta P = \frac{F}{A_p}$, Eq. 9 can be expressed as

$$F = Cv_0 \tag{10}$$

where the Newtonian viscous damping, C, is given by

$$C = \frac{12A_p^2\mu L}{bd^3} \tag{11}$$

2.3. Bingham plastic flow

A Bingham plastic material is characterized by a dynamic yield stress, τ_y. In the presence of applied field, the fluid particles align with the applied field (Fig. 2). Fig. 3 shows an optical photomicrograph of MR particle chain formation. According to the idealized Bingham-plastic constitutive relationship, if the shear stress is less than the dynamic yield stress, then the fluid is in the preyield condition. In this preyield condition the fluid is assumed to be a rigid material. Shearing does not occur until the local shear stress, τ, exceeds the dynamic yield stress, τ_y. Once the local shear stress exceeds the dynamic yield stress, the material flows with a plastic viscosity of μ. Therefore, the post-yield shear stress can be expressed as

$$\tau = \tau_y \text{sign}\left(\frac{du}{dy}\right) + \mu\frac{du}{dy} \tag{12}$$

Thus, a Newtonian fluid can be viewed as a Bingham plastic material with a dynamic yield stress of zero (Fig. 4). For an MR fluid, the dynamic yield stress can be approximated by a power law function of the magnetic field.

Two distinct flow regions (Fig. 4) arise. The central plug region, or Region 1, is characterized by the local shear stress being less than the fluid yield stress τ_y, so that the shear rate or velocity gradient is zero. This width of the pre-yield region is denoted by the plug thickness, δ, which is nondimensionalized with respect to the gap between the two parallel plates of the valve as

$$\bar{\delta} = \frac{2L\tau_y}{d\Delta P} \tag{13}$$

The second region is the postyield region where the local shear stress is greater than the yield stress of the fluid. The velocity profile for Bingham plastic flow between parallel plates with uniform field is (Wereley and Pang, 1998):

$$u(y) = \begin{cases} \frac{\Delta P}{2\mu L}\left(\frac{d-\delta}{2}\right)^2 & \text{, if} \quad |y| \leq \delta/2 \\ \frac{\Delta P}{2\mu L}\left[\left(\frac{d-\delta}{2}\right)^2 - \left(|y| - \frac{\delta}{2}\right)^2\right] & \text{, if} \quad |y| > \delta/2 \end{cases} \tag{14}$$

The total Bingham plastic volume flux is

$$Q = \frac{bd^3\Delta P}{12\mu L}\left(1 - \bar{\delta}\right)^2\left(1 + \frac{\bar{\delta}}{2}\right) \tag{15}$$

Equating the volume flux displaced by the piston head to that through the annular duct, leads to

$$F = C_{eq} v_0 \tag{16}$$

where the equivalent viscous damping is given by

$$C_{eq} = \frac{1}{\left(1-\bar{\delta}\right)^2 \left(1+\frac{\bar{\delta}}{2}\right)} \tag{17}$$

2.4. Bingham biplastic flow

Shear thinning refers to the decrease of apparent viscosity at high shear rates and is an important characteristic of MR fluids, as shown in Fig. 5 (Jolly *et al.*, 1999). To account for this behavior, we will consider a Bingham biplastic material with two distinct linear post-yield viscosities. A critical shear rate, $\dot{\gamma}_t$, marks the boundary between the low shear rate viscosity, μ_0, and the high shear rate viscosity, μ_1. Fig. 6 shows the effects of shear thinning and shear thickening in this analysis.

By calculating force equilibrium across the gap, the shear stress can be obtained in terms of pressure drop, ΔP, as

$$\tau = -\frac{\Delta P}{L} y \tag{18}$$

This expression is useful when calculating the velocity profile. By inspection of Fig. 6, the shear stress can also be written in terms of the Bingham biplastic fluid parameters as

$$\tau = \begin{cases} \tau_y \text{sign}\left(\frac{du}{dy}\right) + \mu_0 \frac{du}{dy} & \text{, if} \quad 0 < \left|\frac{du}{dy}\right| < \dot{\gamma}_t \\ \left[\tau_y + (\mu_0 - \mu_1)\dot{\gamma}_t\right] \text{sign}\left(\frac{du}{dy}\right) + \mu_1 \left(\frac{du}{dy}\right) & \text{, if} \quad \left|\frac{du}{dy}\right| > \dot{\gamma}_t \end{cases} \tag{19}$$

Note that the high shear rate equation specializes to the Bingham plastic case for equal low and high shear rate viscosities, μ_0 and μ_1. Also, this analysis can account for shear thickening, where $\mu_1 > \mu_0$.

Bingham biplastic flow consists of three regions, each symmetric about the gap-center axis (Fig. 7). The central plug region or Region 1 or the pre-yield region, is identical to the Bingham plastic pre-yield plug, where the local shear stress has not yet exceeded the dynamic yield stress. Region 2, the post-yield, low shear rate region, consists of fluid that has yielded but has not reached the critical shear rate, $\dot{\gamma}_t$, or the onset of shear thinning or thickening. Region 3, the post-yield, high shear rate region, contains fluid exhibiting shear thinning or thickening behavior at high shear rates. The velocity profile is obtained by summing forces and applying the appropriate boundary conditions in each region.

In calculating the velocity profile, y is chosen to originate at the gap center, and the flow is examined on only one side of the gap. Because the velocity profile is symmetric about the gap-central axis in a parallel plate analysis, the resulting volume flux equations are doubled to obtain total volume flux. Note that this approach is a change from the original Bingham plastic analysis, where the y axis was measured from one side of the gap (Wereley and Pang, 1998).

Force equilibrium yields distances y_y and y_t, which define the flow regions as below

$$y_y = \frac{\delta_y}{2} = \frac{\tau_y L}{\Delta P} \tag{20}$$

$$y_t = \frac{\delta_t}{2} = \frac{\dot{\gamma}_t \mu_0 L}{\Delta P} + \frac{\tau_y L}{\Delta P} \tag{21}$$

It can be noted that y_t does not depend on the high shear rate viscosity, μ_1, and that this value approaches y_y as critical shear rate $\dot{\gamma}_t$ approaches zero.

Note that δ_y is equivalent to the Bingham plastic plug thickness, δ, and δ_t represents the low shear rate region. These parameters are nondimensionalized with respect to the gap width as

$$\bar{\delta}_y = \frac{2\tau_y L}{d\Delta P} \tag{22}$$

$$\bar{\delta}_t = \frac{2\dot{\gamma}\mu_0 L}{d\Delta P} + \frac{2\tau_y L}{d\Delta P} \tag{23}$$

2.4.1. Region 3: Postyield and high shear rate

The boundary condition for region 3 dictates zero flow at the walls

$$u_3\left(\frac{d}{2}\right) = 0 \tag{24}$$

In this region, Eq. 19 gives the shear stress as

$$\tau = -\left[\tau_y + (\mu_0 - \mu_1)\,\dot{\gamma}_t\right] + \mu_1 \frac{du}{dy} \tag{25}$$

The velocity profile in region 3 is obtained by integrating Eq. 25 across the region and substituting Eq. 18 for τ. Applying the aforementioned boundary condition gives

$$u_3\,(y) = \left(\frac{2y - d}{2\mu_1}\right)\left[-\frac{\Delta P}{4L}\,(2y + d) + \tau_y + \dot{\gamma}_t\,(\mu_0 - \mu_1)\right] \tag{26}$$

2.4.2. Region 2: Postyield and low shear rate

In region 2, the boundary condition requires flow continuity between regions 2 and 3:

$$u_2\,(y_t) = u_3\,(y_t) \tag{27}$$

Because region 2 does not experience shear thinning, Eq. 19 gives the shear stress as

$$\tau = -\tau_y + \mu_0 \frac{du}{dy} \tag{28}$$

Note that the shear stress in region 2 corresponds to that of a Bingham plastic material.

The region 2 velocity profile is calculated by integrating Eq. 28 across the region and applying the flow-continuity boundary condition. Eq. 20 and Eq. 21 define the locations of regions 2 and 3, and we obtain

$$\begin{aligned} u_2\,(y) =& \frac{1}{\mu_0}\left(\tau_y - \frac{\Delta P}{2L} y\right) y \\ &+ \frac{1}{2\mu_1}\left\{\frac{\Delta P}{4} d^2 - dL\left[\tau_y + \dot{\gamma}_t\,(\mu_0 - \mu_1)\right] + \frac{L^2}{\Delta P}\,(\tau_y + \dot{\gamma}_t \mu_0)^2\,(1 - \bar{\mu})\right\} \end{aligned} \tag{29}$$

where the viscosity ratio, $\bar{\mu}$, is defined as

$$\bar{\mu} = \frac{\mu_1}{\mu_0} \tag{30}$$

2.4.3. Region 1: Preyield

In region 1, the fluid flows with a uniform velocity, because the local shear stress throughout this region has not exceeded the yield stress. Thus, given the boundary condition of flow continuity between regions 1 and 2, the pre-yield plug velocity may be found by substituting Eq. 20 into Eq. 29 to give

$$u_1(y) = \frac{\tau_y^2 L}{2\mu_0 \Delta P} + \frac{1}{2\mu_1}\left\{\frac{\Delta P}{4} d^2 - L\left[\tau_y + \dot{\gamma}_t(\mu_0 - \mu_1)\right] d + \frac{L^2}{\Delta P}\left(\tau_y + \dot{\gamma}_t \mu_0\right)^2 (1 - \bar{\mu})\right\} \tag{31}$$

2.4.4. Flow rate

Total flow rate will be examined in terms of the flow properties, $\bar{\delta}_y$ and $\bar{\delta}_t$. These properties, in turn, depend on fluid parameters and applied pressure differential. Therefore, with knowledge of the fluid properties and damper geometry, flow rate can be predicted in terms of applied force.

The velocity profile is related to the flow properties by substituting Eqs. 20 and 21 into the velocity profile relations to obtain

$$\begin{aligned}
u_1(y) &= \frac{\Delta P}{8L}\left[\frac{(d-\delta_t)^2}{\mu_1} + \frac{(\delta_t - \delta_y)(2d - \delta_y - \delta_t)}{\mu_0}\right] \\
u_2(y) &= \frac{\Delta P}{8L}\left[\frac{(d-\delta_t)^2}{\mu_1} - \frac{4y(y-\delta_y) + 2d(\delta_t - \delta_y) + \delta_t^2}{\mu_0}\right] \\
u_3(y) &= \frac{\Delta P}{8L}\left[\frac{(d-2y)(2y + d - 2\delta_t)}{\mu_1} + \frac{2(d-2y)(\delta_t - \delta_y)}{\mu_0}\right]
\end{aligned} \tag{32}$$

Integrating the velocity profile across each region gives the flow rate in that region. Each region exists twice in the symmetrical gap, so the results are doubled to yield total flow.

$$\begin{aligned}
Q_1 &= 2b\int_0^{\delta_y} u_1(y)\,dy \\
Q_2 &= 2b\int_{\delta_y}^{\delta_t} u_2(y)\,dy \\
Q_3 &= 2b\int_{\delta_t}^{\frac{d}{2}} u_3(y)\,dy
\end{aligned} \tag{33}$$

Integrating after substitution of Eq. 32 yields

$$\begin{aligned}
Q_1 &= \frac{bd^3\Delta P}{8L}\left[\frac{(1-\bar{\delta}_t)^2}{\mu_1} + \frac{(\bar{\delta}_t - \bar{\delta}_y)(2 - \bar{\delta}_t - \bar{\delta}_y)}{\mu_0}\right]\bar{\delta}_y \\
Q_2 &= \frac{bd^3\Delta P}{8L}\left[\frac{(1-\bar{\delta}_t)^2}{\mu_1} + \frac{2(\bar{\delta}_t - \bar{\delta}_y)(3 - 2\bar{\delta}_t - \bar{\delta}_y)}{3\mu_0}\right](\bar{\delta}_t - \bar{\delta}_y) \\
Q_3 &= \frac{bd^3\Delta P}{8L}\left[\frac{2(1-\bar{\delta}_t)}{3\mu_1} + \frac{(\bar{\delta}_t - \bar{\delta}_y)}{\mu_0}\right](1-\bar{\delta}_t)^2
\end{aligned} \tag{34}$$

The total volume flux is then

$$Q = \frac{bd^3\Delta P}{12\mu_0 L}\left[\left(1-\bar{\delta}_y\right)^2\left(1+\frac{\bar{\delta}_y}{2}\right) - \left(1-\bar{\delta}_t\right)^2\left(1+\frac{\bar{\delta}_t}{2}\right)\left(1-\frac{1}{\bar{\mu}}\right)\right] \tag{35}$$

The velocity profile in the case of shear thinning is plotted as a function of field and viscosity ratio, $\bar{\mu}$, in Fig. 8. Note the effects of these parameters on the size of the pre-yield region, δ_y, and the location of the extent of shear thinning, the region outside δ_t. Increasing field widens the pre-yield region, δ_y, and a higher critical shear rate increases the size of low shear rate region, δ_t.

3. CONSTANT VELOCITY INPUT

For flow mode damper analysis, it is useful to consider force response for a given velocity. For Bingham plastic flow, this response depends on plastic viscosity, μ, yield stress, τ_y, and the damper geometry. However, in the event of shear thinning, several new parameters must be considered. The high shear rate behavior depends both on critical shear rate, $\dot{\gamma}_t$, and on the high shear rate viscosity, μ_1.

By noting that $Q = A_p v_0$ and that $\Delta P = \frac{F}{A_p}$, Eq. 35 can be manipulated to give a polynomial expression for applied force F with respect to rod velocity v_0

$$\begin{aligned} &F^3\left(\frac{-bd^3}{12\mu_1 A_p^2 L}\right) + F^2\left\{v_0 + \frac{bd^2}{4\mu_1 A_p}\left[\tau_y + \dot{\gamma}_t\left(\mu_0-\mu_1\right)\right]\right\} \\ &\qquad - \left(\frac{bA_pL^2}{3\mu_0}\right)\left[\tau_y^3 + \dot{\gamma}_t\left(\mu_0-\mu_1\right)\left(3\tau_y^2 + 3\dot{\gamma}_t\tau_y - \dot{\gamma}_t^2\mu_0^2\right)\right] = 0 \end{aligned} \tag{36}$$

The roots of this polynomial are solved numerically, and the single valid root is determined. For a Bingham plastic material, the fluid yield stress causes a yield force in the damper, and the post-yield plastic viscosity causes nearly linear post-yield damping. Shear thinning modifies this profile, due to a bilinear post-yield viscosity, characterized by a critical shear rate.

Fig. 9 depicts the theoretical effects of shear thinning and thickening on a typical MR damper filled with Lord MRF-336AG MR fluid. For this simulation, we chose nominal damper dimensions of $d = 0.8$ mm (gap), $L = 10.2$ mm (active length) and $b = 28.4$ mm (piston head diameter). The Lord

MR fluid has nominal properties of $\tau_y = 58$ kPa (yield stress at 1 Tesla) and $\mu = 1$ Pa-sec (viscosity at a 550/sec shear rate). The steady-state force response is plotted with respect to velocity, and the results are compared to the Bingham plastic case in various shear thinning/thickening scenarios. Both plots show the effects of shear thinning and thickening ($\bar{\mu} = 0.5$ and $\bar{\mu} = 5$, respectively) occuring at a critical shear rate of $\dot{\gamma}_t = 7000$/sec.

4. NONDIMENSIONAL ANALYSIS

For damper sizing purposes, we examine equivalent viscous damping, C_{eq}, in nondimensional terms, with and without shear thinning or thickening. The equivalent viscous damping is nondimensionalized with respect to Newtonian damping, C_n, and special considerations are made for shear thinning. The nondimensional damping term is compared to various nondimensionalized flow properties as follows.

4.1. Bingham plastic flow

Noting that $Q = A_p v_0$, and that $\Delta P = \frac{F}{A_p}$, Eq. 15 can be expressed as

$$F = C_{eq} v_0 \tag{37}$$

where C_{eq} represents the equivalent viscous damping for a Bingham plastic flow. The ratio of C_{eq} to the Newtonian damping constant, C, is

$$\frac{C_{eq}}{C} = \frac{1}{\left(1 - \bar{\delta}\right)^2 \left(1 + \frac{\bar{\delta}}{2}\right)} \tag{38}$$

The damping coefficient $\frac{C_{eq}}{C}$ indicates the dynamic range of the damper because it is the ratio of the field dependent damping to the zero field damping. Note that as the shear rate becomes very high or the applied magnetic field becomes very low, the nondimensional plug thickness approaches zero, and the damper exhibits a dynamic range of 1. In this case, the damper behaves as a passive viscous damper. Similarly, at low shear rates or high applied magnetic fields, the plug thickness increases, giving the damper a high dynamic range.

4.2. Bingham biplastic flow with Newtonian normalization

To determine the Bingham biplastic damping coefficient, an appropriate value of C must be chosen for the normalization. In the Bingham plastic case, C_{eq} is simply normalized with respect to Newtonian damping, C, which also corresponds to the zero-field Bingham plastic case. If we normalize Bingham biplastic damping, $C_{eq,t}$, with respect to Newtonian damping as illustrated in Fig. 10, we obtain the relation

$$\frac{C_{eq,t}}{C} = \frac{1}{\left(1-\bar{\delta}_y\right)^2\left(1+\frac{\bar{\delta}_y}{2}\right) - \left(1-\bar{\delta}_t\right)^2\left(1+\frac{\bar{\delta}_t}{2}\right)\left(1-\frac{1}{\bar{\mu}}\right)} \tag{39}$$

where Newtonian damping, C, is given by Eq. 11, and we have set the Newtonian viscosity equal to the low shear rate viscosity, μ_0. Note that this normalization is ineffective at high shear rates, where it indicates an unrealistic dynamic range for the damper. As the shear rate gets very large ($\bar{\delta}_y \to 0$), the damper should exhibit pure viscous damping, with a damping coefficient of 1. However, because this normalization does not allow for shear thinning in the Newtonian damping value, $C_{eq,t}$ does not approach C at high shear rates.

4.3. Bingham biplastic flow with zero-field damper normalization

Bingham biplastic damping, $C_{eq,t}$, is more appropriately normalized with respect to the zero-field biplastic case, C_t, which is defined as

$$C_t = C_{eq,t} \quad \text{as} \quad \bar{\delta}_y \to 0 \tag{40}$$

This normalization accurately predicts the damper's dynamic range at all shear rates, as illustrated in Fig. 11.

When $C_{eq,t}$ is compared to the equivalent zero-field case with shear thinning, C_t, the damping coefficient becomes

$$\frac{C_{eq,t}}{C_t} = \frac{1-\left(1-\bar{\delta}_t\right)^2\left(1+\frac{\bar{\delta}_t}{2}\right)\left(1-\frac{1}{\bar{\mu}}\right)}{\left(1-\bar{\delta}_y\right)^2\left(1+\frac{\bar{\delta}_y}{2}\right) - \left(1-\bar{\delta}_t\right)^2\left(1+\frac{\bar{\delta}_t}{2}\right)\left(1-\frac{1}{\bar{\mu}}\right)} \tag{41}$$

4.4. Variation of biplastic parameters

Bingham biplastic flow depends on two additional nondimensional parameters. First, the ratio of low and high shear rate viscosity is defined by the viscosity ratio, $\bar{\mu}$. Secondly, critical shear rate, $\dot{\gamma}$, will be nondimensionalized with a new parameter, $\bar{\epsilon}$.

From Eq. 22, it can be seen that the size of the low shear rate region depends on critical shear rate but not on the high shear rate viscosity. Therefore, a nondimensional term including δ_t will provide information about $\dot{\gamma}_t$ independently of $\bar{\mu}$. We define a ratio, $\bar{\epsilon}$, as

$$\bar{\epsilon} = \frac{1 - \bar{\delta}_t}{1 - \bar{\delta}_y} \tag{42}$$

where $\bar{\epsilon}$ represents the extent of shear thinning or thickening in the gap, which is the ratio of fluid exhibiting shear thinning to the total amount of post-yield fluid. When $\bar{\epsilon}$ approaches 1, all post-yield fluid is undergoing shear thinning. Similarly, as $\bar{\epsilon}$ approaches 0, no fluid exhibits shear thinning. It is important to use $\bar{\epsilon}$ instead of $\bar{\delta}_t$ when nondimensionalizing the damper properties, because $\bar{\delta}_t$ can never be smaller than $\bar{\delta}_y$; shear thinning does not apply within the pre-yield region. This would restrict the scope of the nondimensional analysis. Therefore, $\bar{\delta}_t$ is incorporated into a parameter that can vary independently of $\bar{\delta}_y$.

By substituting Eq. 42 into Eqs. 39 and 41, the damping coefficients can be expressed in terms of $\bar{\epsilon}$ as

$$\frac{C_{eq,t}}{C} = \frac{1}{\left(1 - \bar{\delta}_y\right)^2 \left\{1 + \bar{\delta}_y/2 - \bar{\epsilon}^2 \left[3 - \bar{\epsilon}\left(1 - \bar{\delta}_y\right)\right]/2\right\}} \times \frac{1}{\left(1 - 1/\bar{\mu}\right)} \tag{43}$$

$$\frac{C_{eq,t}}{C_t} = \frac{1 - \bar{\epsilon}^2 \left(1 - \bar{\delta}_y\right)^2 \left[3 - \bar{\epsilon}\left(1 - \bar{\delta}_y\right)\right]\left(1 - 1/\bar{\mu}\right)/2}{\left(1 - \bar{\delta}_y\right)^2 \left\{1 + \bar{\delta}_y/2 - \bar{\epsilon}^2 \left[3 - \bar{\epsilon}\left(1 - \bar{\delta}_y\right)\right]/2\right\}} \times \frac{1}{\left(1 - 1/\bar{\mu}\right)} \tag{44}$$

Given these relations, shear thinning behavior may be compared to Bingham plastic behavior, which is represented on all plots by a dashed line. Fig. 12 shows variation in viscosity ratio, $\bar{\mu}$ for low and high values of the shear thinning ratio, $\bar{\epsilon}$. This plot uses the $\left(\frac{C_{eq}}{C}\right)_t$ normalization and demonstrates the effect of shear thinning extent on damping coefficient. As would be expected, shear thinning and thickening are more noticeable at high values of $\bar{\epsilon}$, where they substantially impact the dynamic range of the damper. Note that shear thinning lowers the damping coefficient, while shear thickening raises the damping coefficient.

5. LIMITING CASES

The shear thinning relations can be shown to collapse down to equivalent Bingham plastic equations in various limiting cases.

5.1. Extreme shear rates

When the shear rate, $\frac{du}{dy}$, has not yet reached the critical shear rate, $\dot{\gamma}_t$, the fluid exhibits only two velocity profile regions. Here, $\bar{\delta}_t = 1$, and all the region 3 terms in the shear thinning equations approach zero. Therefore, these equations collapse down to Bingham plastic equivalents. Indeed, it can be seen from Fig. 6 that the fluid behaves as a Bingham plastic material at low shear rates.

When the shear rate is small, it may be seen from Eq. 22 that δ_t approaches δ_y. In this case, the fluid is dominated by shear thinning, as region 2 disappears. Similar to the low shear rate case, high shear rates result in a Bingham plastic material, where $\bar{\delta}_t = \bar{\delta}_y$. Again, the shear thinning equations collapse down to Bingham plastic equivalents, where the fluid exhibits a plastic viscosity μ_1.

5.2. Colinear post-yield viscosities

When the low shear rate viscosity, μ_0, approaches the high shear rate viscosity, μ_1, Eq. 30 demonstrates that the viscosity ratio, $\bar{\mu}$, approaches 1. Furthermore, it can be shown that all of the Bingham biplastic relations collapse down to equivalent Bingham plastic equations with viscosity $\mu_0 = \mu_1$.

6. CONCLUSIONS

MR fluids have been successfully modeled with the Bingham plastic model, but these fluids are known to exhibit shear thinning. In this analysis, the Bingham plastic model is extended to account for shear thinning or thickening, which is the respective decrease or increase of viscosity at high shear rates. Shear thinning or thickening over a given shear rate range is approximated by low and high shear rate regions, each of which is characterized by a unique linear plastic viscosity. A critical shear rate divides the two regions.

Nondimensional parameters are introduced to account for the ratio of low and high shear rate viscosity, as well as critical shear rate. When coupled with Bingham plastic nondimensional parameters, these relationships show the expected effects of shear thinning or thickening on MR damper performance. The damping coefficient indicates the dynamic range of the damper and is compared to the Bingham plastic case. With shear thinning, we observe that the damper exhibits a lower dynamic range and must be operated at higher magnetic fields or lower speeds to achieve a given damping coefficient. The opposite is true of shear thickening.

Acknowledgements

Research support was provided under a grant by the U.S. Army Research Office Young Investigator Program, contract no. 38856-EG-YIP. Laboratory equipment was provided under a grant by the FY96 Defense University Research Instrumentation Program (DURIP), contract no. DAAH-0496-10301. For both grants, Dr. Gary Anderson served as technical monitor. Glen A. Dimock was partially supported by a scholarship from the Vertical Flight Foundation.

REFERENCES

1. H. Block and J. Kelly (1988). "Electro-rheology," *Journal of Physics. D: Applied Physics,* Vol. 21, pp. 1661-1667.

2. J. Carlson, D. Catanzarite and K. St. Clair (1999). "Commercial magnetorheological fluid devices," *International Journal of Modern Physics B*, Vol. 10, Nos. 23–24, pp. 2857–2865.
3. H.P. Gavin (2001). "Annular Poiseuille flow of electrorheological and magnetorheological materials," Journal of Rheology, Volume 45, No. 4, July /August, pp. 983-994.
4. G. Hiemenz and N. Wereley (1999). "Seismic response of civil structures utilizing semi-active MR and ER bracing systems," *Journal of Intelligent Material Systems and Structures,* Vol. 10, pp. 646-651.
5. D. Jeon, C. Park and K. Park (1999). "Vibration suppression by controlling an MR damper," *International Journal of Moden Physics B*, Vol. 13, Nos. 14–16, pp. 2221–2228.
6. M. Jolly, J. Bender and J. Carlson (1999). "Properties and applications of commercial magnetorheological fluids," *Journal of Intelligent Material Systems and Structures,* Vol. 10, No.'1, pp. 5–13.
7. G. Kamath, M. Hurt and N. Wereley (1996). "Analysis and Testing of Bingham Plastic Behavior in Semi-Active Electrorheological Fluid Dampers," *Smart Materials and Structures,* Vol. 5, No. 5, pp. 576–590.
8. G. Kamath and N. Wereley (1997). "Modeling the damping mechanism in electrorheological fluid based dampers," *M^3D III: Mechanics and Mechanisms of Material Damping, ASTM STP 1304,* A. Wolfenden and V. K. Kinra, Eds., American Society for Testing and Materials, pp. 331–348.
9. R. Phillips (1969). "Engineering applications of fluids with a variable yield stress," Ph.D. thesis, Mechanical Engineering, U.C. Berkeley.
10. R. Sharp and S. Hassan (1986). "The relative performance capabilities of passive, active, and semi-active car suspension systems," *Proceedings of the Institution of Mechanical Engineers,* Vol. D200, pp. 219-228.
11. N. Sims, S. Peel, R. Stanway, A. Johnson, and W. Bullough (2000). "The electrorheological long-stroke damper: A new modelling technique with experimental validation," *Journal of Sound and Vibration* Vol. 229, No. 2, pp. 207-227.
12. B. Spencer, R. Christenson and S. Dyke (1998). "Next generation benchmark control problem for seismically excited buildings," *Proceedings of the 2nd World Conference on Structural Control,* Kyoto, Japan, 28 June–1 July.

13. R. Stanway, J. Sproston and A. El-Wahed (1996). "Application of electrorheological fluids in vibration control: a survey," *Smart Materials and Structures*, Vol. 5, No. 4, pp. 464-482.
14. X. Wang and F. Gordaninejad (2000). "Controllable fluid dampers in flow mode using Herschel-Bulkley model," *7th Annual SPIE Symposium on Smart Structures and Materials, Conference on Damping and Isolation,* Newport Beach, CA, 5-9 March, Paper No. 3989-23.
15. K. Weiss, J. Carlson and D. Nixon (1994). "Viscoelastic properties of magneto- and electro- rheological fluids," *Journal of Intelligent Material Systems and Structures,* Vol. 5, pp. 772–775.
16. N. Wereley and L. Pang (1998). "Nondimensional analysis of semi-active electrorheological and megnetorheological dampers using approximate parallel plate models," *Smart Materials and Structures,* Vol. 7, pp. 732–743.
17. N. Wereley, L. Pang and G. Kamath (1998). "Idealized Hysteresis Modeling of Electrorheological and Megnetorheological dampers," *Journal of Intelligent Material Systems and Structures,* Vol. 9, pp. 642–649.
18. C. Wolff-Jesse and G. Fees (1998). "Examination of flow behaviour of electrorheological fluids in the flow mode," *Journal of Systems and Control Engineering,* Vol. 212, No. 13, pp. 159–173.

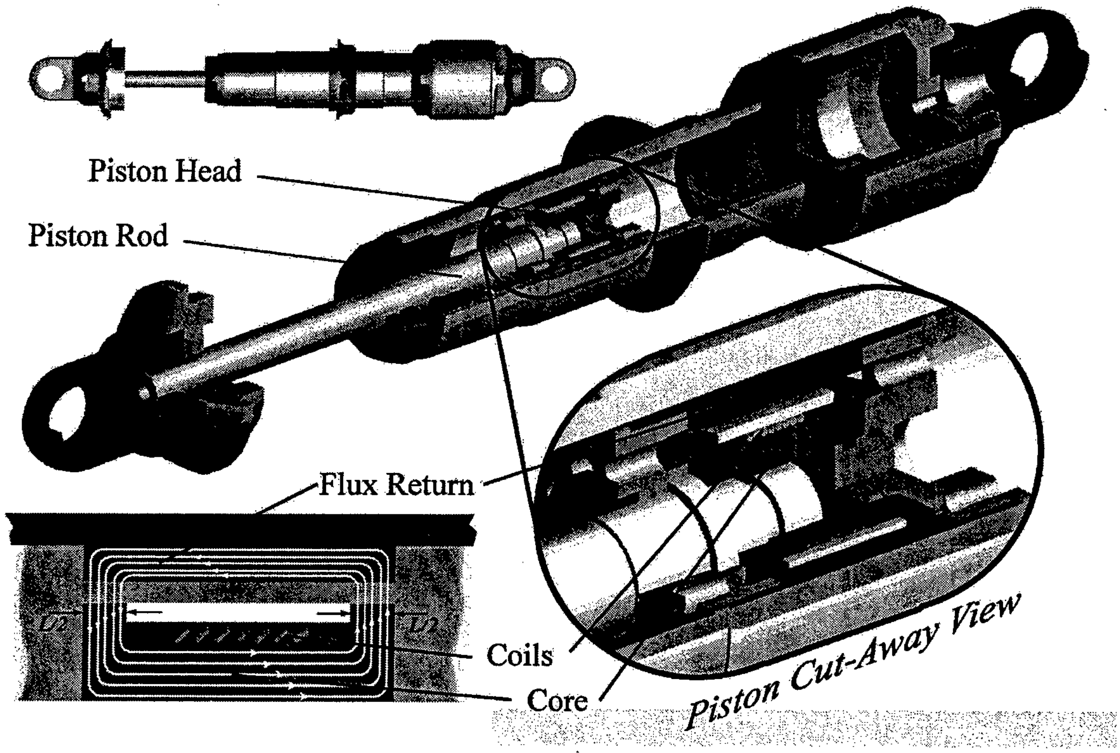
Piston Head
Piston Rod
Flux Return
L/2
L/2
Coils
Core
Piston Cut-Away View

Figure 1. Typical magnetorheological damper

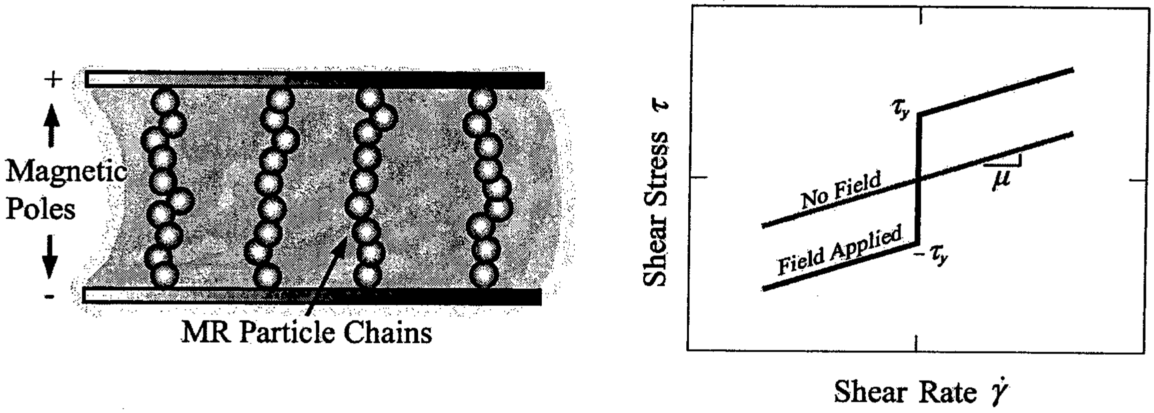
+
Magnetic Poles
-
MR Particle Chains
Shear Stress τ
τ_y
No Field
μ
Field Applied
$-\tau_y$
Shear Rate $\dot{\gamma}$

Figure 2. A schematic of particle chain formation in a magnetorheological fluid and traditional shear stress diagram for Bingam plastic model

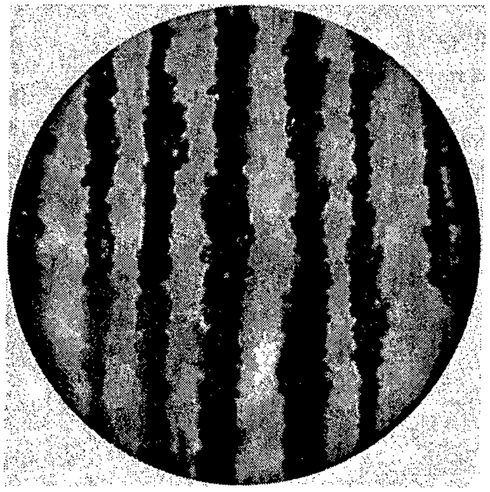

Figure 3. Optical photomicrograph of particle chain formation in a magnetorheological fluid under a passive magnetic field.

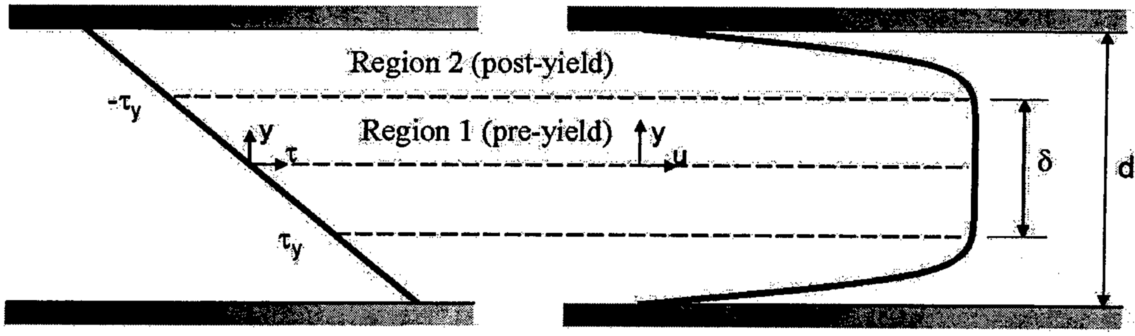
Region 2 (post-yield)
$-\tau_y$
y
τ
Region 1 (pre-yield)
y
u
δ
d
τ_y

Figure 4. Bingham plastic shear stress and velocity profiles across the gap in a MR rectangular duct valve.

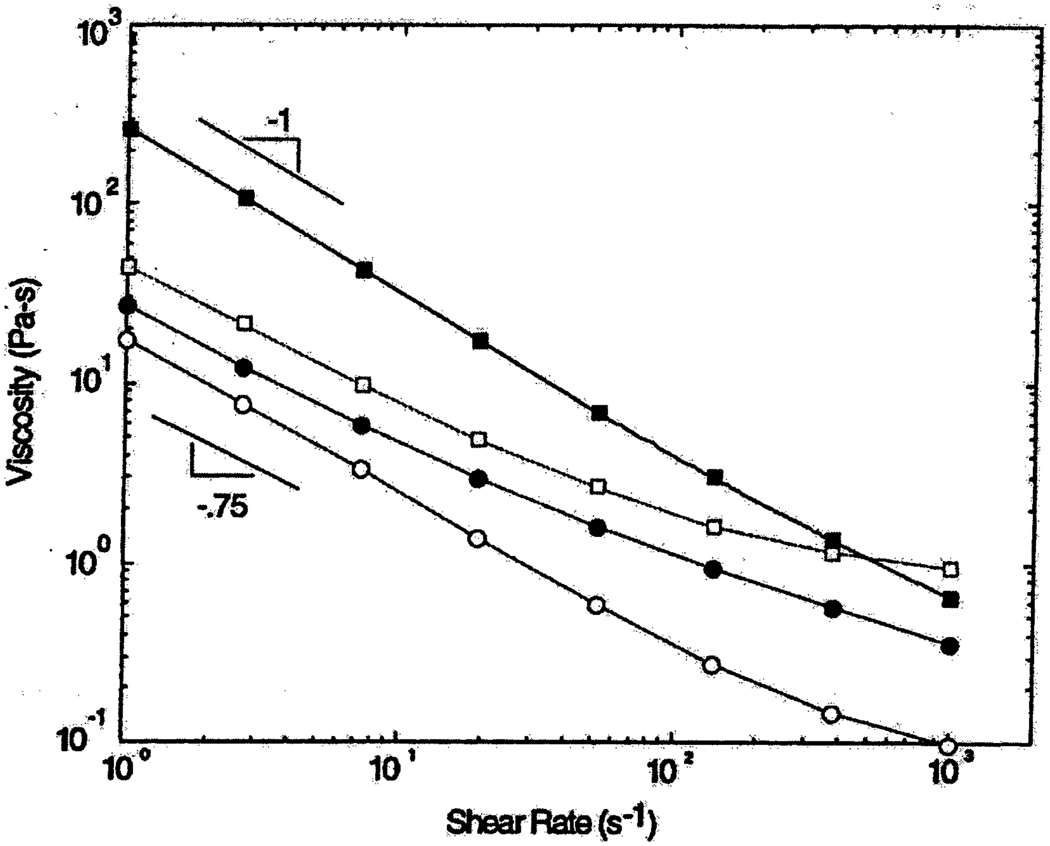

Figure 5. Viscosity as a function of shear rate at 25°C for MRX-126PD(○), MRX-242AS (●), MRX-140ND (□), and MRX-336AG (■). Figure provided courtesy of Dr. Mark Jolly (Lord Corporation).

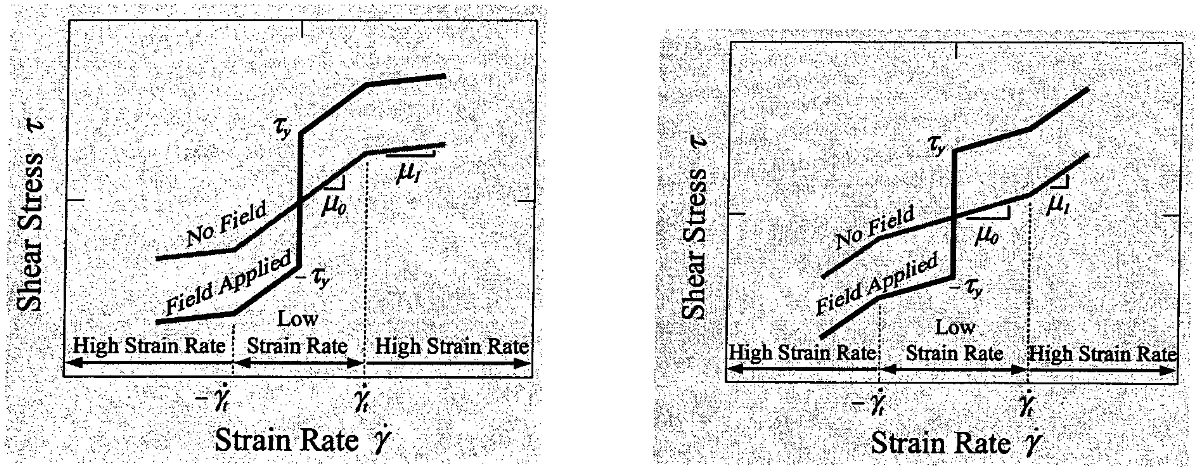

(a) Shear Thinning

(b) Shear Thickening

Figure 6. Bingham biplastic shear stress vs. shear rate for (a) shear thinning and (b) shear thickening

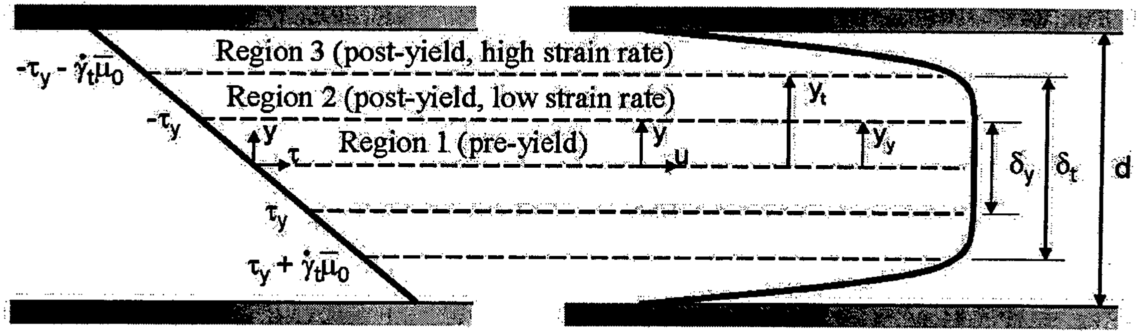
Region 3 (post-yield, high strain rate)
Region 2 (post-yield, low strain rate)
Region 1 (pre-yield)
$-\tau_y - \dot{\gamma}_t\bar{\mu}_0$
$-\tau_y$
τ_y
$\tau_y + \dot{\gamma}_t\bar{\mu}_0$
y
τ
y
u
y_t
y_y
δ_y
δ_t
d

Figure 7. Bingham biplastic shear stress and velocity profiles across the gap in a MR rectangular duct valve.

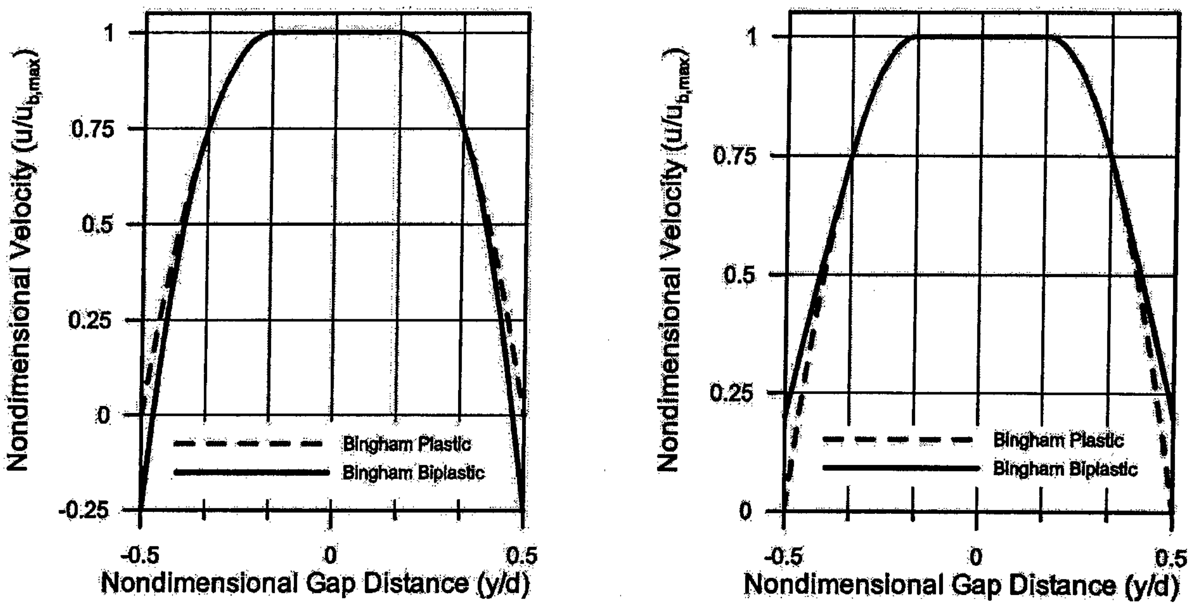

(a) Shear Thinning ($\bar{\mu}$=0.5) (b) Shear Thickening ($\bar{\mu}$=5)

Figure 8. The velocity profile of a Bingham biplastic material with (a) shear thinning and (b) thickening is compared to that of a Bingham plastic material

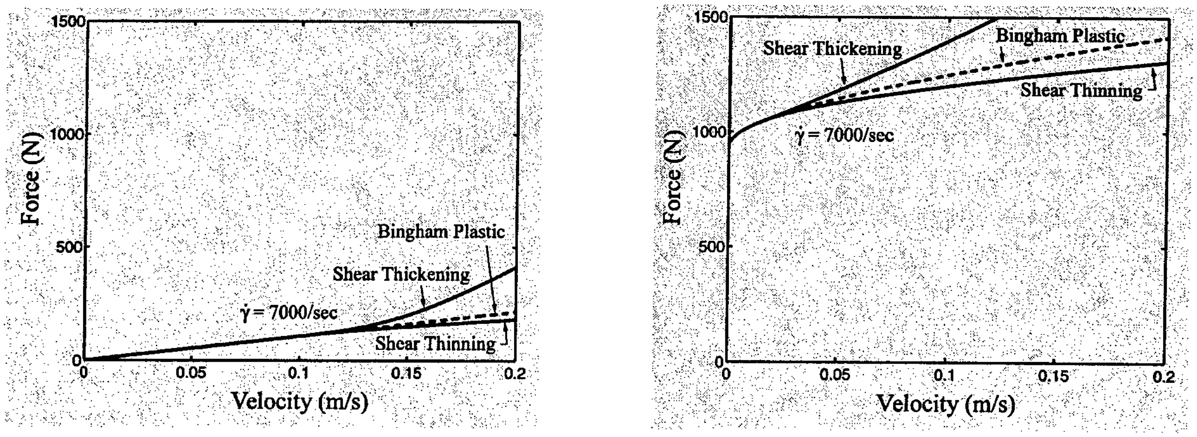

(a) Zero field (b) 1 Tesla

Figure 9. Force vs. Velocity for varying yield force, critical shear rate, and viscosity ratio for (a) zero field and (b) 1 Tesla

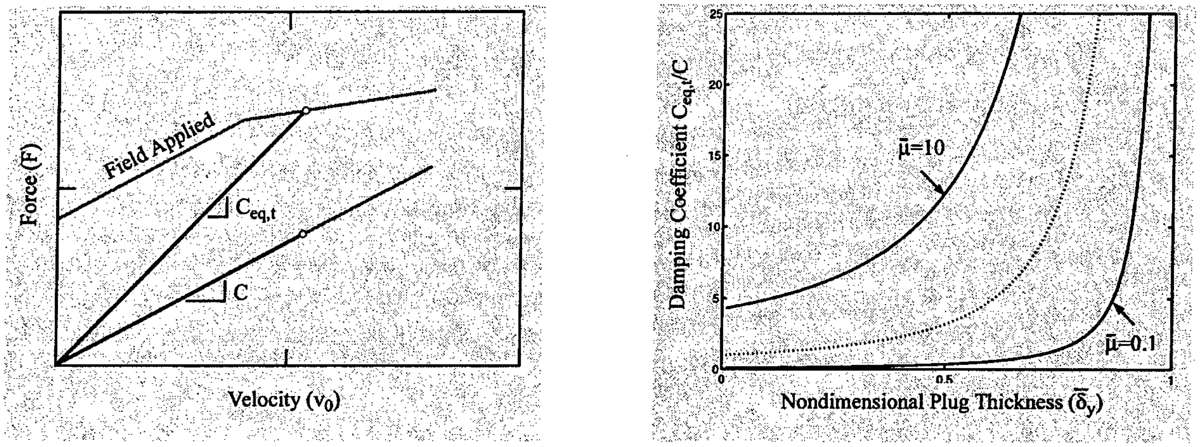

(a) Normalization with $C_{eq,t}$ and C (b) Damping Coefficient using Newtonian C

Figure 10. Normalization of damping force and damping coefficient with respect to Newtonian damping C

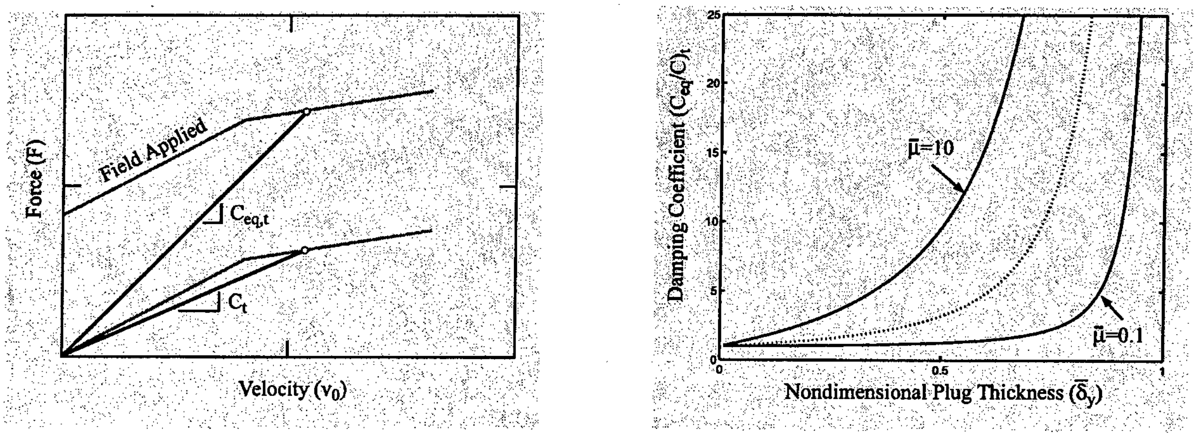

(a) Normalization with $C_{eq,t}$ and C_t (b) Damping Coefficient using Zero-Field C_t

Figure 11. Normalization of damping force and damping coefficient with respect to zero-field damping with shear thinning C_t

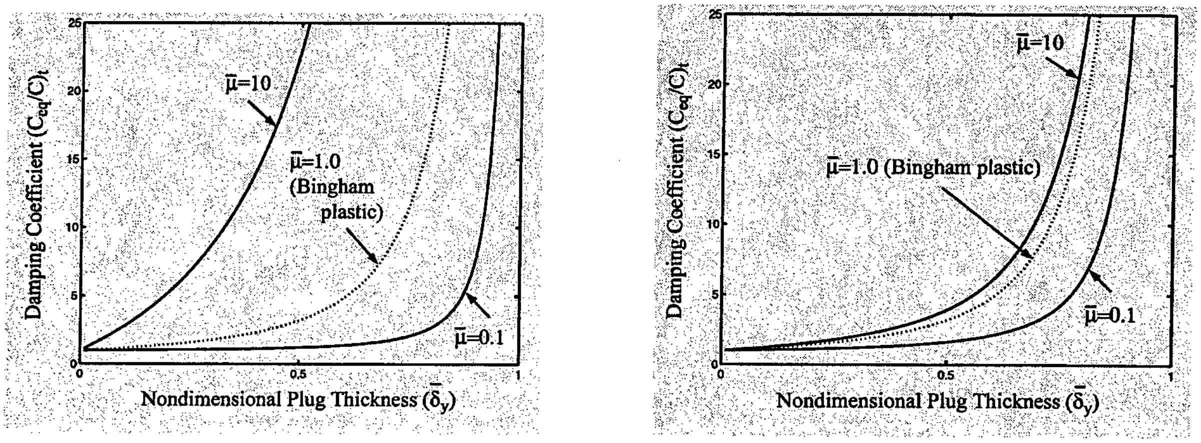

(a) High Critical Shear Rate ($\bar{\epsilon}$=1.0)

(b) Low Critical Shear Rate ($\bar{\epsilon}$=0.5)

Figure 12. $\left(\frac{C_{eq}}{C}\right)_t$ vs. $\bar{\delta}_y$ for varying $\bar{\epsilon}$ and $\bar{\mu}$